



Lecture Notes in Mechanical Engineering

Bhingole Pramod P.
Ulkes B. Desai
Sunkulp Goel *Editors*


Advances in Material Science and Metallurgy

Select Proceedings of ICFAMMT 2022

 Springer

Lecture Notes in Mechanical Engineering

Editorial Board

Francisco Cavas-Martínez , Departamento de Estructuras, Construcción y Expresión Gráfica Universidad Politécnica de Cartagena, Cartagena, Murcia, Spain

Francesca di Mare, Institute of Energy Technology, Ruhr-Universität Bochum, Bochum, Nordrhein-Westfalen, Germany


Mohamed Haddar, National School of Engineers of Sfax (ENIS), Sfax, Tunisia

Young W. Kwon, Department of Manufacturing Engineering and Aerospace Engineering, Graduate School of Engineering and Applied Science, Monterey, CA, USA

Justyna Trojanowska, Poznan University of Technology, Poznan, Poland

Series Editors

Fakher Chaari, National School of Engineers, University of Sfax, Sfax, Tunisia

Francesco Gherardini , Dipartimento di Ingegneria “Enzo Ferrari”, Università di Modena e Reggio Emilia, Modena, Italy

Vitalii Ivanov, Department of Manufacturing Engineering, Machines and Tools, Sumy State University, Sumy, Ukraine

Lecture Notes in Mechanical Engineering (LNME) publishes the latest developments in Mechanical Engineering—quickly, informally and with high quality. Original research reported in proceedings and post-proceedings represents the core of LNME. Volumes published in LNME embrace all aspects, subfields and new challenges of mechanical engineering. Topics in the series include:

- Engineering Design
- Mechanical Structures and Stress Analysis
- Engine Technology
- Nanotechnology and Microengineering
- Control, Robotics, Mechatronics
- MEMS
- Theoretical and Applied Mechanics
- Fluid Mechanics
- Engineering Thermodynamics, Heat and Mass Transfer
- Manufacturing
- Precision Engineering, Instrumentation, Measurement
- Tribology and Surface Technology

To submit a proposal or request further information, please contact the Springer Editor of your location:

Europe, USA, Africa: Leontina Di Cecco at Leontina.dicecco@springer.com

China: Ella Zhang at ella.zhang@springer.com

India: Priya Vyas at priya.vyas@springer.com

Rest of Asia, Australia, New Zealand: Swati Meherishi at swati.meherishi@springer.com

To submit a proposal for a monograph, please check our Springer Tracts in Mechanical Engineering at <https://link.springer.com/bookseries/11693>.

Indexed by SCOPUS and EI Compendex. All books published in the series are submitted for consideration in Web of Science.

Bhingole Pramod P. · Ulkesh B. Desai ·
Sunkulp Goel
Editors

Advances in Material Science and Metallurgy

Select Proceedings of ICFAMMT 2022

 Springer

Editors

Bhingole Pramod P.
Department of Mechanical and Aerospace
Engineering
Institute of Infrastructure, Technology,
Research and Management (IITRAM)
Ahmedabad, India

Ulkesh B. Desai
Microwave Payloads Mechanical Division
SSME Space Applications Centre
Indian Space Research Organisation
Ahmedabad, India

Sunkulp Goel
Herbert Gleiter Institute of Nanoscience
University of Science and Technology
Nanjing, China

ISSN 2195-4356

ISSN 2195-4364 (electronic)

Lecture Notes in Mechanical Engineering

ISBN 978-981-19-4917-3

ISBN 978-981-19-4918-0 (eBook)

<https://doi.org/10.1007/978-981-19-4918-0>

© The Editor(s) (if applicable) and The Author(s), under exclusive license to Springer Nature Singapore Pte Ltd. 2023

This work is subject to copyright. All rights are solely and exclusively licensed by the Publisher, whether the whole or part of the material is concerned, specifically the rights of translation, reprinting, reuse of illustrations, recitation, broadcasting, reproduction on microfilms or in any other physical way, and transmission or information storage and retrieval, electronic adaptation, computer software, or by similar or dissimilar methodology now known or hereafter developed.

The use of general descriptive names, registered names, trademarks, service marks, etc. in this publication does not imply, even in the absence of a specific statement, that such names are exempt from the relevant protective laws and regulations and therefore free for general use.

The publisher, the authors, and the editors are safe to assume that the advice and information in this book are believed to be true and accurate at the date of publication. Neither the publisher nor the authors or the editors give a warranty, expressed or implied, with respect to the material contained herein or for any errors or omissions that may have been made. The publisher remains neutral with regard to jurisdictional claims in published maps and institutional affiliations.

This Springer imprint is published by the registered company Springer Nature Singapore Pte Ltd.

The registered company address is: 152 Beach Road, #21-01/04 Gateway East, Singapore 189721, Singapore

Preface

The First International Conference on Futuristic Advancements in Materials, Manufacturing and Thermal Sciences (ICFAMMT 2022) was jointly organized by the Department of Mechanical and Aerospace Engineering, Institute of Infrastructure, Technology, Research and Management, Ahmedabad, India, and the Space Society of Mechanical Engineers (SSME), Space Applications Centre, ISRO, Ahmedabad. This conference aims to provide splendid opportunities for academicians, researchers, industrial persons, and young scientists to address new challenges and discuss futuristic advancements in materials, manufacturing, and thermal sciences. Further, ICFAMMT 2022 also aims to facilitate technical advancement and futuristic advancement in the field of machine design, nanotechnology, composites, processing of plastics, modelling and simulations, optimization, and fluid engineering.

This book includes select peer-reviewed proceedings of ICFAMMT 2022. The content provides an overview of the latest research in the area of material sciences such as metal casting, powder metallurgy, alloys, nano-composites, heat treatment processes, material properties and its characterization, process design and synthesis, modelling and simulation used for material science and metallurgy. The book has four major parts such as ‘Alloys and Composites’, ‘Design and Synthesis’, ‘Material Properties’ and ‘Modelling and Simulation’. The book is useful for researchers and professionals working in the field of material sciences, and readers will be able to develop a deep understanding of material behaviour and possible changes for future implementations.

Ahmedabad, India
Ahmedabad, India
Nanjing, China

Bhingole Pramod P.
Ulkes B. Desai
Sunkulp Goel

Contents

Alloys and Composites

Optimization of Concrete Mix Design for Thermal Energy Storage	3
Bhim Kumar Choure and Nishit Bedi	
Thermo-chemical Characterisation of Fe–Ni Alloys for Space Applications	15
Yogesh Ghotekar, Ravi Kumar Varma, V. M. Shah, H. M. Modi, A. P. Vora, A. K. Lal, and B. A. Makwana	
Stress Analysis of Carbon Composite Material for Space-Based RF Component Using CAE Simulation	29
Aaryan Shah, Ashish Soni, Dhaval Vartak, and Pina Bhatt	
RF Shielding Effectiveness of Nano-composites for Space Payload Applications	39
Nandini Deshpande, Manisha Upadhyay, Dhaval Vartak, Bhuwaneshwar Semwal, Anil Shah, and A. K. Lal	
Aluminium Metal Matrix Composites Fabricated by Powder Metallurgy Techniques: A Review	51
Guttikonda Manohar, K. M. Pandey, and S. R. Maity	
Processing Techniques of Magnesium Matrix Composites and Its Heat Treatment—A Review	63
Manan Shah, Ayush Pandya, Bhingole Pramod, and Neeraj Srivastava	
A Review on Heat Treatment of Magnesium Alloys and Its Effect on Various Properties	77
Ayush Pandya, Manan Shah, Bhingole Pramod, and Neeraj Srivastava	
Preparation of Bamboo-Based Nano-Cellulose by Ball Milling	89
Yogendra Kumar Verma, Amit Kumar Singh, and M. K. Paswan	

Design and Synthesis

Brush Plating on Aluminum for High-Reliable Use	101
Vaishali Umrana, Vimal M. Shah, and Sharad Shukla	

Numerical Synthesis of Bending Behaviour of Flexible Composite Tape Spring	113
Megha Thaker, Hemant Arora, Dhaval Patel, and Shashikant Joshi	

A Review on Different Mechanisms Used in Power Generation Through Speed Bumps	127
Kunj Patel, Parth Patel, Tejas Ghodasara, and Sumit Tripathi	

The Behavior of Pyro-Carbon Matrix Synthesized Through Isothermal Chemical Vapor Infiltration (I-CVI) Process	137
Dipoo Kumar, N. Gomati, Deepak Kumar Agarwal, and B. Santhosh	

Material Properties

Deformation Effect on Corrosion Resistance of 316 ASS—A Review	153
Sourabh Shukla, Abhay Kewati, Anshula Gaurkar, Tulika Bawankar, and Abhishek Gawai	

Experimental and Numerical Analysis of Diametric Compression Test of FRP Rings	167
T. K. Nagaraja, K. B. Yogesha, and M. Mruthunjaya	

Modelling and Simulation

Alternate Bicycle Freewheel Mechanisms: Design and Finite Element Analysis Under Different Loading Conditions	183
Mohammad Ahmed Basri, Talvinder Singh, and Anoop Aggarwal	

Design and Analysis of Composite Spur Gear	205
Aniket Oswal, Deepesh Bhalodia, Akshay Sunctankar, and Lokavarapu Bhaskara Rao	

Structural and Thermal Analysis of Modified Ventilated Paperboard Using Finite Element Analysis	219
Sagar Yanda, Jagadish, N. V. Swamy Naidu, Sathish Kumar Adapa, and Sivasankara Raju	

Dynamic Analysis of Helical Planetary Gearbox Using Simulation Software	227
Sumit Singh Rajput, Shreya A. Tripathi, C. Subiksha, and Lokavarapu Bhaskara Rao	

Electromechanical Instability Modeling of Particle-Reinforced Dielectric Elastomeric Actuators	245
Sankalp Gour, Deepak Kumar, and Vinod Yadav	

**An Advance Optimal Torque Control MPPT Technique
for Variable-Speed WECS 257**
Shailendra Kumar Gupta, Motilal Rinawa, Kishor Thakre,
Neeraj Garg, Ashwani Sharma, Harish Sharma, and Haris Arquam

**Mechanical Characterization and Numerical Modeling of Moso
Bamboo for a Collapsible Stretcher Cum Chair 271**
Mohammad Ahmed Basri, Vijay Gautam, Mukul Rai, and Nikhil Rajput

About the Editors

Dr. Bhingole Pramod P. is an Assistant Professor at Institute of Infrastructure, Technology, Research and Management (IITRAM), India. He holds a Ph.D. in Metallurgical and Materials Engineering, Indian Institute of Technology (IIT) Roorkee (2014) and Master's degree in Production Engineering. He has over seven years of experience in teaching and three years in research. His major areas of research include magnesium-aluminum alloy casting, composite materials, ultrasonic processing of magnesium and aluminum alloys and biomaterials. He has authored more than 15 research papers and completed one DST project.

Ulkesh B. Desai is currently functioning as the Head of Microwave Payloads Mechanical Division (MPMD). He has over 22 years experience in sensor configuration, mechanical design and analysis (structural and thermal), fabrication, assembly and space qualification testing for various microwave electronic packages at frequencies like L, S, C, Ku, Ka, V & W-bands. He has played a vital role in the design and successful realization of 250 W High Power SSPA and High Power EPC's. He has published more than 30 technical papers at national and international level.

Dr. Sunkulp Goel is an Assistant Professor at Herbert Gleiter Institute of Nanoscience, Nanjing University of Science and Technology, China where he also completed his post doctoral research. He holds a Ph.D. in Metallurgical and Materials Engineering, Indian Institute of Technology (IIT) Roorkee (2015). He has over three years of experience in teaching and three years in research. His major areas of research include bulk nanolammellar structured materials, deformation behavior of magnesium alloys and severe plastic deformation of bulk metallic glass. He has authored more than 32 research papers.

Alloys and Composites

Optimization of Concrete Mix Design for Thermal Energy Storage



Bhim Kumar Choure and Nishit Bedi

Abstract An experimental investigation conducted to determine optimum mix design concrete for better strength with least cost for thermal energy storage is presented in this paper. Several concrete mix design such as M20, M25, M30, M35, and M40 were identified for conducting the experimental test. Compressive strength test was performed on each of the concrete mix design. M30 was observed to be optimum mix. Split tensile strength test was also performed on this optimum mix design. The tensile strength of the order of 0.25–0.5 of the compressive strength was noticeable. The minimum uncertainty in the reading of data set was observed for M30 mix design. The results obtained in this study will be useful in design and development of large-scale sensible heat storage unit accompanied with charging and discharging cycle. Such storage units can be incorporated in real-time thermal power plants.

Keywords Concrete · Mix design · Compressive strength · Thermal energy storage

Nomenclature

M	Mix design
W/C	Water to cement ratio
IS	Indian Standard
kN	Kilo Newton
x_i	Particular value of observations
μ	Arithmetic mean
σ	Standard deviation
n	Number of observations
CV	Coefficient of variation
σ^2	Variance

B. K. Choure (✉) · N. Bedi
Mechanical Engineering Department, Ujjain Engineering College, Ujjain, MP, India
e-mail: bhimkumarchoure@gmail.com

<i>F</i>	Applied load
<i>L</i>	Length of the specimen
σ_x	Split tensile strength
C	Cement
FA	Fine aggregate
CA	Coarse aggregate
W	Water
OPC	Ordinary Portland cement
SHT	Sensible heat thermal
SHS	Sensible heat storage
ASTM	American Society for Testing and Material
UTM	Universal testing machine
<i>D</i>	Diameter of the cylinder

1 Introduction

The process of making concrete structures depends on many factors. The selection of fine aggregate (sand), coarse aggregate, cements, and proper water–cement ratio has always been an important parameter. Compressive strength and direct tensile strength behavior of the mix design having specific water to cement ratio as well as ratio of water, fine aggregate, and coarse aggregates are very important factors because they affect the cracking, deflections, delayed setting, improper strength, and bonding behavior of concrete. These factors not only affect the strength but also affect the life of concrete. The common problems associated with the manufacture of concrete structures are delayed setting, improper strength increase, and concrete cracking which all affect strength and durability of structure [1]. With the widespread use of concrete, various water–cement ratio has been applied in practice. The change of water–cement ratio will lead to the change of strength, thus providing higher strength under the condition of low water–cement ratio [2]. The influence of water–cement ratio has been extensively studied in the past few years [3–7]. It has also been observed that the compressive strength of fine sand is lower than that of coarse sand when water–cement ratio is relatively low [8]. Compressive strength studies have been conducted using different water cement ratio [3]. A direct tensile strength behavior of self-compacting concrete is studied, and a new procedure for determining the stress–strain behavior of self-compacting concrete is explored [9]. In addition, the methods to establish correlation between compressive strength and split tensile strength are also studied [10]. For thermal energy storage model, it is necessary to know the extent of compressive strength and split tensile strength so as the designer of thermal energy storage model should be aware about failure criteria of that model in compression and tension. The designed thermal energy storage model should have the lowest cost to obtain the best strength for optimal design.

Solid media concrete SHT energy storage with tubular heat exchanger was built, and thermal analysis was performed [11]. Analysis of concrete as high temperature heat storage material was performed [12]. A concrete ceiling deck with integrated water pipes was used as a heat storage device [13]. A heat storage SHS concrete model with a capacity of 10 MJ was studied in the temperature range of 523–673 K [14]. Heat transfer phenomenon of the concrete sensible heat storage prototype with a heat capacity of 15 MJ was studied [15]. Various applications of concrete-based thermal energy storage have been found in the literature. When designing concrete-based thermal energy storage model, the current concrete-based mixed design work can be used. The current focus of work is how to safely design thermal energy storage within the design stress range with the help of concrete mix design.

Concrete testing plays an important role in analyzing the strength of concrete. The strength of concrete can be analyzed by the compressive strength of cubes and the split tensile strength of the cylinder. With the growth of construction industry, there is need to develop such a model that would not fail in construction field especially when consider to be operated in thermal energy storage. The idea of applying maximum thermal stress on the model should be such that it should not lead to failure. If we have an idea of maximum compressive strength and maximum tensile strength, then we could apply the maximum stress within the limit for that particular concrete thermal energy storage model and thereof model would get operated within the designed safe limit.

2 Experimental Details

2.1 Details of Concrete

There are several types of concrete available in concrete industry namely ordinary concrete, standard concrete, and high strength concrete. Five concrete mixtures designated as M20, M25, M30, M35, and M40 were used in this study. OPC 43 grade cement was used in this study, which complies with IS 8112:1989. In this study, nominal maximum size of coarse aggregate of 8 mm was used, confirming compliance with IS 882:1992. For all the OPC 43 grade cements and coarse aggregate with a nominal maximum size of 8 mm, fine aggregate of 100% crushed sand was used in compliance with IS 882:1992. Potable water was used. The method, code, and instrument taken for compressive strength testing of concrete were gone through standard procedure.

2.2 *Experimental Setup*

The dimensions of the cube and cylinder were taken as $150 \times 150 \times 150$ mm and 150×300 mm for compressive and tensile strength test. Computerized universal testing machine with load rate controls of maximum capacity 1500 kN (150 tons) with loading accuracy within $\pm 1\%$ and load resolution 0.005% were used.

3 Experimental Methods and Test Procedure

3.1 *The Work to Make Concrete Cubes for Testing Has Been Completed*

According to the local supply situation, quantity of cement, coarse aggregate, and fine aggregate were arranged from different places. Quantity of gravel particles were sieved with the help of mesh. Quantity of cement, coarse aggregate, fine aggregate, and water for M20 design mix were estimated. All the quantities were mixed in exact proportion to fill in prepared mold cube boxes. With the help of concrete vibrator, filled cube boxes (7 in number) were vibrated to ensure uniform and perfect mixing. The filled cubes were immersed into a water tank for curing. After 7 days, cubes (3 pieces) were tested on compression testing machine, and then after 28 days, the compressive strength readings (3 pieces) were obtained. Same procedure was followed for other designs, i.e., M25, M30, M35, and M40.

Mix design strength with days of molding and testing are presented in Table 1.

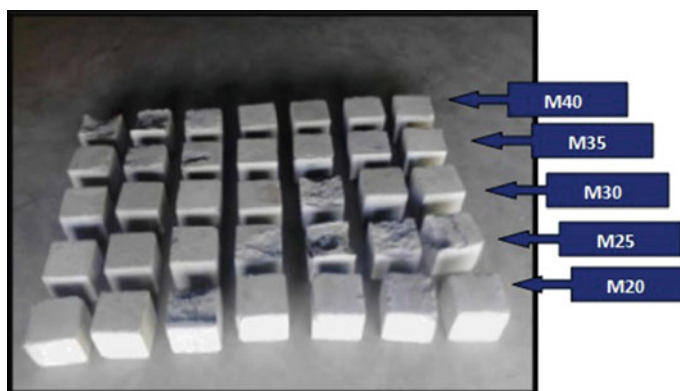
3.2 *Testing Procedure*

3.2.1 *Compressive Strength*

Different grades of compressive strength specimens were cured in a water bath for 7 and 28 days, and then taken out of the water bath for cleaning and then subjected to compressive strength test. Seven specimens were prepared for each mix design. Three specimens were tested after the age of 7 days, and remaining three were tested after the age of 28 days in a universal testing machine in accordance with IS 516 (1959). An additional sample was prepared for each mix design, and testing was performed only when any of the previously 6 test specimens shows an error in the measurement. All the concrete mix designs of cube specimens are shown in Fig. 1. The pictorial view of compression strength test of cube is shown in Fig. 2. Table 2 shows the compressive strength and average compressive strength of mix design.

Table 1 Mix design strength with days of molding and testing of cubes

Mix design	Peak load (kN)		Days of molding	Days of testing	
	After 7 days	After 28 days		After 7 days	After 28 days
M20	290	510	1st day	8th day	29th day
	310	520			
	330	560			
M25	440	760	6th day	13th day	34th day
	490	700			
	410	750			
M30	580	1000	12th day	19th day	40th day
	580	1010			
	590	1000			
M35	840	1150	18th day	25th day	46th day
	940	1150			
	850	1070			
M40	780	1210	24th day	31st day	52nd day
	760	1140			
	880	1050			

**Fig. 1** Concrete mix (M20–M40)

3.2.2 Split Tensile Strength

The seven specimen of a specific mix design were kept in a water bath for 7 and 28 days, and then removed from water bath for cleaning before the split tensile strength test. Three specimens were tested after the age of 7 days, remaining three were tested after the age of 28 days in a universal testing machine in accordance

Fig. 2 Compression strength test of cube



Table 2 Peak load, compressive strength, and average compressive strength testing of cubes

Mix design	Peak load (kN)		Compressive strength (MPa)		Average compressive strength (MPa)	
	After 7 days	After 28 days	After 7 days	After 28 days	After 7 days	After 28 days
M20	290	510	12.9	22.7	13.8	23.6
	310	520	13.8	23.1		
	330	560	14.7	24.9		
M25	440	760	19.6	33.8	19.8	32.8
	490	700	21.8	31.2		
	410	750	18.2	33.3		
M30	580	1000	25.7	44.4	25.9	44.6
	580	1010	25.7	44.8		
	590	1000	26.2	44.4		
M35	840	1150	37.3	51.1	38.9	49.9
	940	1150	41.8	51.1		
	850	1070	37.7	47.6		
M40	780	1210	34.7	53.8	38.9	50.4
	760	1140	33.8	50.7		
	880	1050	39.1	46.7		

with IS 516 (1959). Figure 3 shows the pictorial view of split tensile strength test of cylinder. The split tensile strength was calculated using the given equation

$$\sigma_x = \frac{2F}{\pi DL} \quad (1)$$

Fig. 3 Split tensile strength test of cylinder



4 Experimental Result and Analysis

4.1 Mix Design Optimization

Because of the fact that water to cement ratio in the M20 mix design was high resulting in lower compressive strength, but in M25, M30, M35, and M40 mix design, water to cement ratio tends to decrease and strength tends to increase, since water to cement ratio in the M25 mix design was high resulting in lower compressive strength. Therefore, in the M25, M30, M35, and M40 mix design, the water–cement ratio tends to decrease and the strength tends to increase. In the mix design M30, M35, and M40, though strength increases but water–cement ratio would further gets decrease, which affects the workability of concrete, since the mixture having less water to cement ratio results in immediate hardening of concrete at the time of concrete filling. To work in a mixture of low water–cement ratio, an additional adhesive was required to properly bond the material [16]. Therefore, the mixed design of M30 and M35 was chosen because of their high compressive strength and was not required any additional adhesive.

Taking into account the cost standard, the least cost mix design would be M20 and M25 since cement to sand ratio is 1:1.5 and 1:1.4, respectively. In the M30, M35, and M40 mix design, the ratio of cement–sand were 1:1.28, 1:1.27, and 1:1.05, respectively. Obviously, the amount of cement used in the M30 mix design was less than the cement used in the M35 and M40 mix design. Therefore, the cost of M40 mix design would be higher than the cost of M30 and M35 mix design. Hence, if the cost was the main criterion M20 or M25, mix design was preferable and if strength was the main criterion, M40 mix design was preferable. Since, the cost of lower grade concrete mix design was low due to its low cement content than the cost of the higher grade concrete mix design, for selecting the optimal mix design, compressive strength to cost ratio parameter was used that considers both compressive strength and cost as an ideal parameter. From the test result of M20, M25, M30, M35, and

Table 3 Cost estimation of mix design

Mix design	W/C ratio	C:FA:CA	F (kN)				Cost (\$)	F/cost (kN/\$)
			Testing 1	Testing 2	Testing 3	Average		
M20	0.55	1:1.80:3.62	510	520	560	530.00	0.33	1606.06
M25	0.52	1:1.60:3.40	760	700	750	736.67	0.37	1991.00
M30	0.49	1:1.50:3.20	1000	1010	1000	1003.33	0.41	2447.14
M35	0.46	1:1.38:3.01	1150	1150	1070	1123.33	0.46	2442.02
M40	0.43	1:1.25:2.79	1210	1140	1050	1133.33	0.49	2312.91

M40, the compressive strength–cost ratio was found to be 1606.06, 1991, 2447.14, 2442.02, and 2312.91, respectively. Among all the mix design of M20–M40, it was found that M30 had the highest compressive strength to cost ratio, so the M30 mix design was chosen. The detailed cost estimation of mix design is shown in Table 3.

4.2 Behavior of Mix Design

Figure 4 shows the behavior of the average compressive strength of the mix design from M20 to M40 after 7 and 28 days. For mix designs M20 and M25, the approximate percentage increase in average compressive strength was about 60%, M30 was 70%, and M35 and M40 were 30%. For mix design M35 and M40, the average compressive strength exhibits flat characteristics. The compressive strength and tensile strength of the selected mix design M30 were compared. The data showed that the compressive strength was approximately three times the tensile strength of the same age.

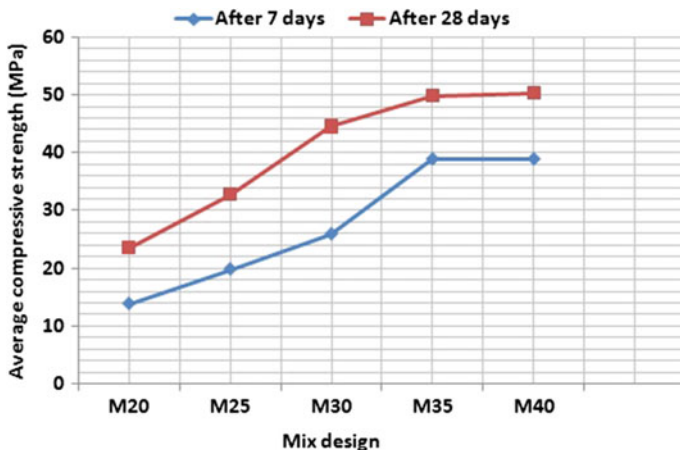


Fig. 4 Average compressive strength of mix design

4.3 Thermal Application of Mix Design

There was always need to develop such a model that would not fail in construction field especially when considered to be operated in thermal energy storage. The idea of putting maximum thermal stress on the SHT energy storage model should be such that it should not fail. Maximum compressive strength and maximum tensile strength reading of experimental result and calculated thermal stress using Eq. 2 help in designing the SHT energy storage model.

$$\sigma_{th} = \alpha \Delta t \cdot E \tag{2}$$

The applied thermal stress was within the limit of the maximum compressive and tensile stress, the model runs within the safe limit otherwise, and there may be chances of getting the failure of thermal energy storage model. The tensile strength experimental reading of M30 mix design is presented in Table 4. The data shows that the compressive strength is approximately three times the tensile strength under the same age. In addition, the mixed design data obtained may also help to compare experimental data of the same aggregate size obtained at different places.

Standard deviation and coefficient of variation for cubes indicating various mix design after 7 and 28 days are presented in Table 5. Standard deviation is an absolute measure of dispersion, so it cannot be used to compare the variability of two data sets with different means. Therefore, this type of comparison is done by using a measure of relative dispersion called the coefficient of variation (CV). When comparing data sets, a data set with a larger coefficient of variation value has greater variability than a data set with smaller coefficient of variation value. The standard deviation and coefficient of variation were calculated by using the Eqs. 3 and 4, respectively, whereas uncertainty and percentage uncertainty were calculated using Eqs. 5 and 6, respectively.

Table 4 Tensile strength of M30 mix design

Sample number	Peak load (kN)	Cross head travel (mm)	Tensile strength (MPa)
<i>After 7 days</i>			
S1	155.6	7.4	8.8
S2	149.9	5.4	8.4
S3	155.4	4.5	8.8
<i>After 28 days</i>			
S4	268.5	7.1	15.1
S5	242.8	7.1	13.7
S6	255.6	7.4	14.7

$$\sigma = \sqrt{\frac{n \sum x_i^2 - (\sum x_i)^2}{n^2}} \quad (3)$$

$$CV = \frac{\sigma}{\mu} \quad (4)$$

$$\text{Uncertainty} = \frac{\text{Maximum value} - \text{Minimum value}}{2} \quad (5)$$

$$\text{Uncertainty}(\%) = \frac{\text{Uncertainty}}{\text{Mean value}} \times 100 \quad (6)$$

The coefficient of variation for data set M40 is greater than data set M30 after 7 and 28 days; data set M30 is less variable compared to data set M40. The maximum uncertainty in the reading of data set was observed to be up to $\pm 9\%$ for M25 mix design, whereas minimum uncertainty was found for M30 mix design.

5 Conclusions

Different mix designs were studied, and M20, M25, M30, M35, and M40 mix design were selected for compressive strength test. The cost to strength ratio of M30 mix design was observed minimum among the various mix designs tested. M30 concrete mix was only experimentally investigated for its split tensile strength. Under same duration, the tensile strength of the order of 0.25–0.5 of the compressive strength was noticeable. The minimum uncertainty in the reading of data set was observed for M30 mix design. Analysis of the data performed in order indicated encouraging results. The value of coefficient of variation within 1% was noticeable for the data obtained after 28 days. The study will be useful in the design and development of large-scale sensible heat storage unit.

Table 5 Standard deviation and coefficient of variation for cubes after 7 and 28 days

Mix design	After 7 days						After 28 days					
	x_i	Uncertainty in x_i (%)	μ	$(x_i - \mu)^2$	σ	CV (%)	x_i	Uncertainty in x_i (%)	μ	$(x_i - \mu)^2$	σ	CV (%)
M 20	290	±6.45	310	400	16.32	5.26	510	±4.71	530	400	21.60	4.07
	310			0			520			100		
	330			400			560			900		
M 25	440	±9.00	446.67	44.49	32.99	7.38	760	±4.07	736.67	544.28	26.24	3.5
	490			1877.48			700			1344.68		
	410			1344.69			750			177.68		
M 30	580	±0.85	583.4	11.11	4.68	0.80	1000	±0.50	1003.33	11.08	4.71	0.46
	580			11.11			1010			44.48		
	590			43.56			1000			11.08		
M 35	840	±5.70	876.7	1344.5	44.96	5.12	1150	±3.56	1123.34	710.75	37.71	3.35
	940			4006.89			1150			710.75		
	850			712.89			1070			2845.15		
M 40	780	±7.43	806.67	711.28	52.49	6.5	1210	±7.00	1133.34	5876.75	65.48	5.77
	760			2178.08			1140			44.35		
	880			5377.28			1050			6945.55		

References

1. Shrivastava AK, Kumar M (2016) Compatibility issues of cement with water reducing admixture in concrete. *Perspect Sci* 8:290–292
2. Shen D, Jiang J, Wang W, Shen J, Jiang G (2019) Tensile creep and cracking resistance of concrete with different water-to cement ratios at early age. *Constr Build Mater* 146:410–418
3. Nikbin IM, Beygi MHA, Kazemi MT, Amiri JV, Rabbanifar S, Rahmani E (2014) A comprehensive investigation into the effect of water to cement ratio and powder content on mechanical properties of self-compacting concrete. *Constr Build Mater* 57:69–80
4. Bello L, Diaz EG, Rougeau P (2019) An original test method to assess water absorption/desorption of lightweight aggregates in presence of cement paste. *Constr Build Mater* 154:752–762
5. Yigiter H, Yazici H, Aydin S (2007) Effects of cement type, water/cement ratio and cement content on sea water resistance of concrete. *Build Environ* 42:1770–1776
6. Yasar E, Erdogan Y, Kılıc A (2004) Effect of limestone aggregate type and water–cement ratio on concrete strength. *Mater Lett* 58:772–777
7. Shamsai A, Peroti S, Rahmani K, Rahemi L (2012) Effect of water-cement ratio on abrasive strength, porosity and permeability of nano-silica concrete. *World Appl Sci J* 17(8):929–933
8. Lim SK, Tan CS, Chen V, Lee ML, Lee WP (2013) Effect of different sand grading on strength properties of cement grout. *Constr Build Mater* 38:348–355
9. Alhussainy F, Hasan HA, Rogic S, Sheikh MN, Hadi MNS (2016) Direct tensile testing of self-compacting concrete. *Constr Build Mater* 112:903–906
10. Gaedicke C, Torres A, Huynh KCT, Marines A (2016) A method to correlate splitting tensile strength and compressive strength of pervious concrete cylinders and cores. *Constr Build Mater* 125:271–278
11. Laing D, Bahl C, Bauer T, Lehmann D, Steinmann WD (2011) Thermal energy storage for direct steam generation. *Sol Energy* 85:627–633
12. Bai FW, Xu C (2011) Performance analysis of a two-stage thermal energy storage system using concrete and steam accumulator. *Appl Therm Eng* 31:2764–2771
13. Pomianowski M, Heiselberg P, Jensen RL (2012) Dynamic heat storage and cooling capacity of a concrete deck with PCM and thermally activated building system. *Energy Build* 53:96–107
14. Prasad L, Muthukumar P (2013) Design and optimization of lab-scale sensible heat storage prototype for solar thermal power plant application. *Sol Energy* 97:217–229
15. Rao CRC, Niyas H, Muthukumar P (2018) Performance tests on lab–scale sensible heat storage prototypes. *Appl Therm Eng* 129:953–967
16. Yu J, Li G, Leung CKY (2018) Hydration and physical characteristics of ultrahigh-volume fly ash-cement systems with low water/binder ratio. *Constr Build Mater* 161:509–551

Thermo-chemical Characterisation of Fe–Ni Alloys for Space Applications



Yogesh Ghotekar, Ravi Kumar Varma, V. M. Shah, H. M. Modi, A. P. Vora, A. K. Lal, and B. A. Makwana

Abstract In aerospace applications, Iron-Nickel (Fe–Ni) alloys are first choice of structural designers, whenever high strength and low thermal expansion are required for spacecraft subsystems. Fe–Ni alloy have an extraordinarily minimum thermal expansion, and dimensions were nearly invariable even at cryogenic temperatures, popularly it is called Invar. This alloy is used as a structural component in optical payloads and accelerometer in spacecraft systems. For enhancing the thermal conductivity of Fe–Ni alloys, Cobalt and Silver elements were added to alloy. Cobalt added in Invar alloy called as Kovar, whereas if silver is added, then it is called Silvar. Kovar acts as sealing alloys in space applications specific to commutation satellites. This paper highlights on the estimation of thermal properties and chemical constituents of Fe–Ni alloys. Study reveals that, Invar has 64.271% of Fe, 35.15% of Ni and total 0.608% of other constituents. As the temperature increases from -150 to 200 °C, thermal conductivity of Invar increased from the 12.567 to 18.420 W/(m K). Thermal conductivity of Fe–Ni alloy is enhanced up to 21.454 W/(m K) by addition of 17%

Y. Ghotekar (✉) · R. K. Varma · V. M. Shah · H. M. Modi
Process & Materials Quality Assurance Division-Mechanical (PMQD-M), Ahmedabad, India
e-mail: yogeshghotekar@sac.isro.gov.in

R. K. Varma
e-mail: rkv@sac.isro.gov.in

V. M. Shah
e-mail: vmshah@sac.isro.gov.in

H. M. Modi
e-mail: hmmodi@sac.isro.gov.in

A. P. Vora
Mechanical Quality Assurance Group, Ahmedabad, India
e-mail: anupvora@sac.isro.gov.in

A. K. Lal
Systems Reliability Area (SRA), Space Applications Centre (SAC-ISRO), Ahmedabad, India
e-mail: aklal@sac.isro.gov.in

B. A. Makwana
Kadi Sarva Vishwavidyalaya (KSV), Gandhinagar, India
e-mail: bhrtchem1@gmail.com

Cobalt, whereas addition of 32.2% of silver will enhance the thermal conductivity up to 51.084 W/(m K). For Invar, mean coefficient of thermal expansion (CTE) of 1.998 ppm/°C observed for 150 °C to 200 °C temperature range while in case of Kovar and Silvar alloy, mean CTE enhances up to 7.018 ppm/°C and 6.928 ppm/°C, respectively. Current study provides the valuable thermal data at sub-ambient and higher cryogenic temperature for thermal design of systems.

Keywords Iron–Nickel (Fe–Ni) alloy · Coefficient of linear thermal expansion (CTE) · Cryogenic temperature · Thermal conductivity (TC)

1 Introduction

In aerospace sector, Iron–Nickel (Fe–Ni) alloys used in spacecraft subsystems. Fe–Ni alloys with 35% Ni have very limited thermal expansion, and their dimensions are practically invariable around room temperature, hence the name as Invar alloy. Invar alloy (Fe 65% and Ni 35%) widely used in aeronautical and aerospace engineering, cryogenic engineering and other industrial applications where the high dimensional stability required over the temperature variation. The addition of 30–40% Ni to Fe reduces the coefficient of thermal expansion (CTE) and enhances magnetic permeability in the region of 50% and above. At high temperatures, a large quantity of Ni provides resistance to oxidation [1]. Addition of Ni in Fe alloy increases its machinability and corrosion resistance. Fe–36Ni Invar alloy was popular low expansion material [2]. The Invar effect refers to the unique low thermal expansion property of the Fe–36Ni alloy [3]. Invar has CTE less than $2 \times 10^{-6} \text{ K}^{-1}$. Invar is a ductile and easily weldable alloy, machinability is similar to austenitic stainless steel (SS304) and it does not suffer severe corrosion under normal atmospheric condition.

Whenever high strength and low thermal expansion required for spacecraft subsystems, Invar alloy is the first choice of structural designers. Invar alloy used as a structural component for support in optical payloads and accelerometer in spacecraft systems where high precision measurement required. Invar's low CTE (1.2 ppm/°C) is really useful for the opto-mechanical application where system needs to be dimensionally stable due to temperature change to meet desired performance requirement [4]. Invar CTE (1.2 ppm/°C) near about matches with Zerodur lens assembly CTE value (0.5 ppm/°C), therefore, ideal material for optical assembly. Invar alloy is also used for formulating moulds for the preparation of composite structures for aerospace applications where extremely tight tolerances required. Optical lens assembly brackets made from Invar alloy shown in Fig. 1.

Super-Invar constituents approximately 5% Cobalt element in place of 5% less nickel, and it is also popular Fe–Ni alloy for space use. Super-Invar has CTE around 1 ppm/°C, it has martensitic transformation temperature (Ms) which is around 223 K (–50 °C), and this is the main limitation for low temperature application of Super-Invar [5]. Super-Invar cannot be applied at temperatures below 243 K (–30 °C) considering safety margin [5]. Invar has low thermal conductivity around



Fig. 1 Electroless Nickel-plated Invar lens assembly bracket

14–15 W/(m K), improvement in the thermal conductivity of Fe–Ni alloy can be achieved by addition of Cobalt (Co) and Silver (Ag) elements to alloy. Cobalt around 17% added in Fe–Ni alloy then it called as Kovar, and if silver is added, then it termed as Silvar. Kovar acts as sealing alloys in space applications specific to commutation and microwave remote sensing satellites. Carrier plates were made from Kovar alloy, in a typical carrier plate assembly an alumina substrate is bonded to Kovar carrier plate using a solder preform. The carrier plates are used in different sizes and shapes so that micro-integrated circuit (MIC) substrate is properly soldered on them [6]. The CTE value of alumina (6.3 ppm/°C) substrate and Kovar is matching; therefore, Kovar is ideal alloy for carrier plates. Figure 2 showing carrier plates of different sizes and shapes, MIC substrate and MIC substrate mounted on carrier plates.

Researchers also trying to enhance thermal conductivity of Fe–Ni alloy by addition of 20–35% Ag. Silvar alloy is a unique composite material combination of Ag and Invar. The material has advantage to minimise thermal mechanical stresses due to unique mechanical and thermal properties to be used as carrier plate for microwave integrated circuits in satellites. The processing of MMCs (metal matrix composites)

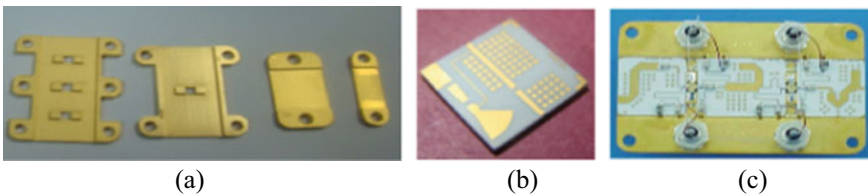


Fig. 2 **a** Gold-plated Kovar carrier plates, **b** MIC substrate and **c** MIC substrate mounted on carrier plates

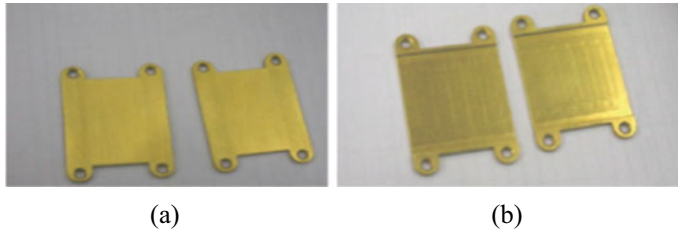


Fig. 3 **a** Bottom side and **b** top side of gold plated Silvar carrier plate

is carried out through sintered/infiltrated powder metallurgy processing. The material has advantage of thermal conductivity against Kovar material but the thermal expansion is little higher compare to Kovar. The addition of other elements (Co and Ag) in Fe–Ni alloys not only enhances the thermal conductivity but also alters the CTE value (Fig. 3).

This paper highlights on the thermal analysis techniques using high end thermal instruments. It also focuses on the evaluation of chemical constitution of Invar, Kovar and Silvar alloy and thermal properties of these alloys at higher cryogenic temperature ($-150\text{ }^{\circ}\text{C}$) and how the thermal properties varies with the increasing temperature up to $200\text{ }^{\circ}\text{C}$. Chemical constitution of Fe–Ni alloys evaluated by the inductively coupled plasma optical emission spectrometer. Thermal diffusivity evaluated using laser flash method, whereas specific heat capacity is evaluated using the differential scanning calorimeter for -150 to $200\text{ }^{\circ}\text{C}$ temperature range. Coefficient of thermal expansion estimated by the vitreous silica push rod dilatometer for -150 to $200\text{ }^{\circ}\text{C}$ temperature range.

2 Materials and Methods

2.1 Evaluation of Chemical Composition of Alloys

Evaluation of chemical composition of Invar, Kovar and Silvar alloys carried out by wet chemical analysis, for estimation 2–4 g weight of each alloy sample digested in acids using the microwave acid digestion system (Make-Anton Paar). After the digestion of samples, digested extract make up to appropriate volume with distilled water. Dilute digested sample used for the chemical constitution evaluation by inductively coupled plasma optical emission spectrometer (ICP-OES/Make-Amteck, Model-Arcos). The digested liquid samples are nebulized into an aerosol and introduced into the produced plasma's centre. The sample atoms are excited to a higher energy state by the plasma, which then relaxes to a lower energy state by generating light with an elementally specific wavelength. The intensity of these characteristic wavelengths is detected, measured and compared to intensities of recognised standards, and the quantitative elemental composition is then provided by the device.

2.2 Coefficient of Thermal Expansion (CTE) Evaluation

Coefficient of thermal expansion (CTE) evaluation made by CTE measurement set-up (Make-TA, Model-DIL 801) having linear variable differential transformer (LVDT) sensor (Fig. 4). CTE measurement carried out as per the test procedure mention in ASTM E 228 [7]. In this method, specimen is heated in the furnace, and the displacement of the ends of the specimen is transferred to the LVDT sensor through push rods.

Cylindrical rod samples of size 50 mm in length and diameter 5 mm prepared by the precise machining. Three samples of each alloy prepared and length of these samples accurately measured by the digital Vernier calliper. In the fused silica push rod dilatometer, a standard silica rod is loaded, instrument run at heating or cooling rate of 2 °C/min in temperature range –150 to 200 °C in air atmosphere. To achieve the low temperature, furnace is connected to the liquid nitrogen cylinder. Whole operation of instrument controlled through the operating software Win TA. After that change in length and corresponding temperature data obtain after the run, this data is corrected using standard quartz data set to avoid the instrumental bias. This correction file of fused silica rod standard used for the correcting the low thermal expansion materials like Invar. In similar way, standard aluminium oxide (Al_2O_3) rod also loaded in instrument and after analysis, data is corrected with standard Sapphire data set. Kovar and Silvar which are comparatively high thermal expansion materials for these correction file of standard Al_2O_3 rod used for the correction. In similar way, all the samples analysis carried out. Test data set obtain after each sample run is corrected by the standard fused silica or aluminium oxide (Al_2O_3) correction data set. After correction, corrected data set of change in length and corresponding temperature used for the CTE measurement. Instrument also provides the instantaneous Alpha (α or CTE) value with respect to ambient temperature. CTE value for the temperature range –150 to 200 °C determined by following formula.

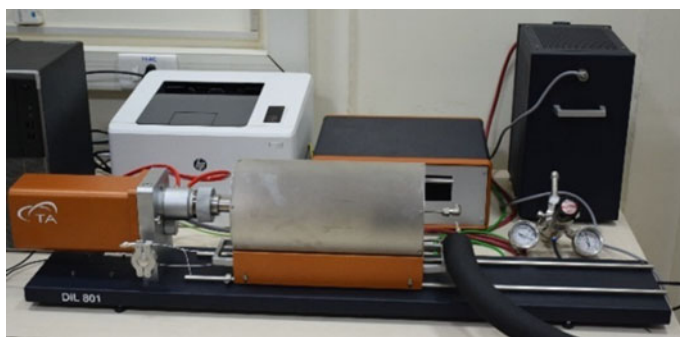


Fig. 4 CTE measurement set-up (Make-TA, Model-DIL 801)

$$\alpha = \frac{(L_2 - L_1)/L}{(T_2 - T_1)} = \frac{(\Delta L/L)}{\Delta T} \quad (1)$$

Here α represents coefficient of thermal expansion in ppm/°C or $10^{-6}/K$ or $10^{-6}/^{\circ}C$, L represents original length and L_1 and L_2 represent length of sample at temperature T_1 and T_2 , respectively. ΔL represents length change and ΔT represents temperature change. Three samples of each alloy are evaluated for CTE measurement.

2.3 Evaluation of the Thermal Conductivity (TC)

Thermal conductivity (λ) is derived from the alloys' density (ρ), thermal diffusivity (α) and specific heat capacity (C_p). It always represents in unit W/(m K). Specific heat capacity (C_p) of the alloys evaluated by the differential scanning calorimeter (DSC). DSC (Make-TA, Model-DSC-25/discovery series, Fig. 5) used for the C_p determination as per ASTM E 1269 [8]. Operation of the system controlled by the TRIOS software.

Two empty, clean specimen holder plus lids were sealed and record the weight. Weight of the both empty pan should be matched and position it on reference position of the DSC sample holder and another one kept on sample position. Sample were heat or cooled at constant rate of 20 °C/min and record the data for temperature range of -150 to 200 °C as the baseline thermal curve. To achieve the temperature below the room temperature, liquid nitrogen need to pour in the sample holder chamber. In second run, empty sample holder replace by the standard Sapphire holder and run the instrument in similar manner, record the standard Sapphire thermal curve. In third run, standard Sapphire holder replaces by sample. Sample weight of around 20 mg taken and run the instrument in similar manner and record the sample thermal curve.

Fig. 5 Differential scanning calorimeter (Make-TA, Model-DSC-25)



Fig. 6 Thermal conductivity measurement set-up (Make-TA, Model-Discovery Xenon Flash DXF 200)



Export the baseline, standard Sapphire and sample thermal curve to the software Speciality library and calculated the C_p at desired temperature by using software.

Thermal diffusivity (α) of the alloy samples measured by the laser flash method using the thermal diffusivity measurement set-up (Make-TA, Model- Discovery Xenon Flash DXF 200) (Fig. 6). Three samples of each alloy are evaluated for thermal diffusivity measurement. Evaluation of thermal diffusivity of samples carried out as per ASTM E 1461 (Clark Taylor Diffusivity) [9].

Cylindrical disc-shaped sample of size 12.5 mm diameter and 1.5 mm thickness or square block-shaped sample of length 10 and 1.5 mm thickness prepared by the machining operation. Dimensions and weight of the sample noted and loaded in the instrument. To achieve the temperature below the room temperature, liquid nitrogen cylinder connected with furnace of the instrument. Instrument fully controlled by the operating software DXF 200, instrument records the thermal diffusivity values for the temperature range of -150 to 200 °C. Thermal diffusivity measured by the instrument at the temperature -150 , -100 , -50 , 0 , 25 , 50 , 100 , 150 and 200 °C. Finally by using the density (ρ) value of the alloy, thermal diffusivity (α), specific heat capacity (C_p) and thermal conductivity (λ) of alloy at different temperature calculated by the formula,

$$\lambda = \alpha \cdot C_p \cdot \rho \quad (2)$$

Table 1 Chemical compositions of Fe–Ni alloys (wt%)

Elements	Elemental composition in percentage (%)		
	Invar	Kovar	Silvar
Carbon (C)	0.015	0.016	–
Silicon (Si)	0.125	0.130	0.250
Sulphur (S)	0.002	0.005	–
Phosphorus (P)	0.004	0.001	–
Manganese (Mn)	0.315	0.350	0.040
Nickel (Ni)	35.150	29.300	22.000
Chromium (Cr)	0.074	0.060	–
Molybdenum (Mo)	0.003	–	–
Copper (Cu)	0.033	–	0.120
Cobalt (Co)	0.025	17.00	–
Aluminium (Al)	0.012	–	0.030
Magnesium (Mg)	–	–	0.060
Silver (Ag)	–	–	32.200
Iron (Fe)	Balance	Balance	Balance

3 Results

3.1 Chemical Composition of Alloys

Chemical composition of Fe–Ni alloys measured by the instrument ICP-OES. Analysis results show that 35.15% Ni and total other elements 0.608% found in Invar alloy. In case of Kovar alloy 29.30% Ni, 17% Co and other elements 0.60% was found, whereas in case of Silvar alloy 32.20% Ag, 22% Ni and other elements 0.8% were observed. Detail elemental composition is given in Table 1.

3.2 Coefficient of Thermal Expansion (CTE) of Alloys

CTE of alloys evaluated from the data of change in length and corresponding temperature provided by the instrument. Change in length of test alloys sample and corresponding temperature is shown in Fig. 7.

Invar alloy contracts up to 16.376 μm at temperature $-150\text{ }^\circ\text{C}$ and at temperature $200\text{ }^\circ\text{C}$, it expands up to 18.669 μm . Invar alloy shows mean CTE 1.998 ppm/ $^\circ\text{C}$ for temperature range of -150 to $200\text{ }^\circ\text{C}$. In case of Kovar, alloy contracts up to 74.274 μm and at temperature $200\text{ }^\circ\text{C}$, it expands up to 48.848 μm and shows mean CTE 7.018 ppm/ $^\circ\text{C}$ for similar temperature range, whereas in case of Silvar, alloy contracts up to 65.440 μm at temperature $-150\text{ }^\circ\text{C}$ and it expands up to 55.910 μm

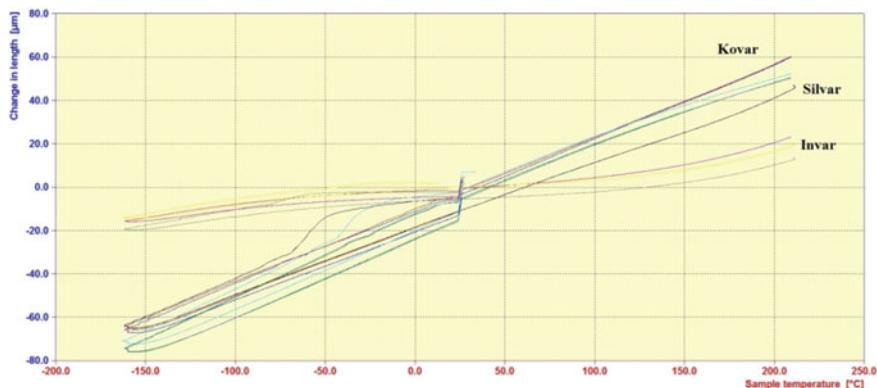


Fig. 7 Change in length of Invar, Kovar and Silvar alloys versus temp.

Table 2 Coefficient of thermal expansion (CTE) of Fe–Ni alloys

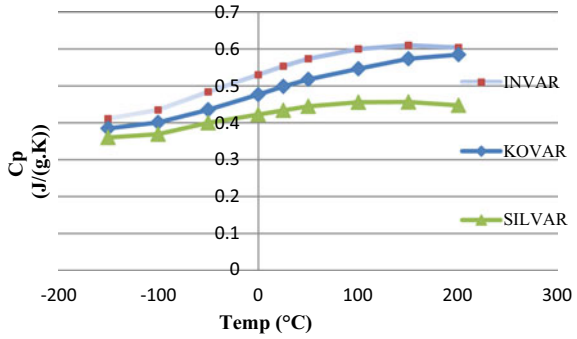
Fe–Ni alloy	Sample ID	CTE value for temp. range –150 to 200 °C	
		α (in $10^{-6}/^{\circ}\text{C}$)	Avg. CTE \pm STD devi.
Invar	Sample 1	1.750	1.998 ± 0.224
	Sample 2	2.059	
	Sample 3	2.185	
Kovar	Sample 1	7.049	7.018 ± 0.059
	Sample 2	6.951	
	Sample 3	7.055	
Silvar	Sample 1	6.959	6.928 ± 0.115
	Sample 2	6.800	
	Sample 3	7.024	

at temperature 200 °C, and it shows mean CTE 6.928 ppm/°C for temperature range –150 to 200 °C. Detail CTE evaluation data is given in Table 2.

3.3 Specific Heat Capacity of Alloys

Specific heat capacity of Invar at temperature –150 °C observed 0.411 J/(g °C), and it gradually increases up to 0.604 J/(g °C) at temperature 200 °C. In case of Kovar varies from 0.385 J/(g °C) at temperature –150 °C and it gradually increases up to 0.585 J/(g °C) at temperature 200 °C, whereas in case of Silvar alloy, specific heat capacity at temperature –150 °C observed 0.360 J/(g °C), and it gradually increases

Fig. 8 Specific heat capacity versus temp.



up to 0.447 J/(g °C) at temperature 200 °C. Graphical representation of specific heat capacity over the temperature range is shown in Fig. 8.

3.4 Thermal Conductivity of Alloys

Thermal conductivity of the Fe–Ni alloys evaluated using the thermal diffusivity provided by the thermal diffusivity instrument, and specific heat capacity provided by the DSC and density of the alloys. Density of Invar alloy 8.03 g/cm³, Kovar 8.36 g/cm³ and for Silvar 8.26 g/cm³ used for the calculation to evaluate thermal conductivity. Average thermal conductivity of Invar alloy increases from 12.567 W/(m K) at –150 °C to 18.420 W/(m K) at 150 °C, and it slightly decreased up to 17.180 W/(m K) at 200 °C (Fig. 9).

Average thermal conductivity of Kovar alloy increases from 19.452 W/(m K) at –150 °C to 23.013 W/(m K) at 150 °C, and it slightly decreased up to 22.908 W/(m K) at 200 °C, while in case of Silvar alloy, it increases from 46.375 W/(m K) at –150 °C

Fig. 9 Thermal conductivity of Invar alloy versus temp.

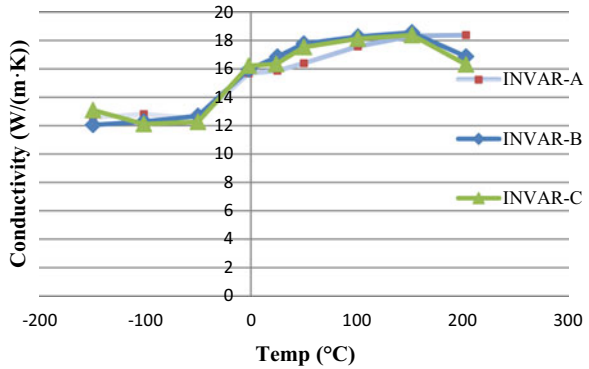
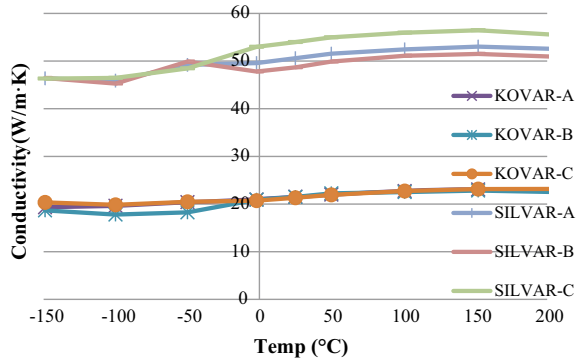


Fig. 10 Thermal conductivity of Kovar and Silvar alloy versus temp.



to 53.670 W/(m K) at 150 °C, and it slightly decreased up to 53.019 W/(m K) at 200 °C (Fig. 10).

4 Discussion

Study reveals that tested Invar sample has an average 64.271% of Fe, 35.15% of Ni and total 0.608% of other element constituents. As the temperature increased from -150 to 200 °C, thermal conductivity of Invar increased from the 12.567–18.420 W/(m K) and specific heat capacity also increased from 0.411 to 0.6037 J/(g °C). Thermal conductivity of Fe–Ni alloy enhanced up to 21.454 W/(m K) by addition of 17% Cobalt, whereas addition of 32.2% of silver enhanced the thermal conductivity up to 51.084 W/(m K). For Invar, mean coefficient of linear thermal expansion 1.998 ppm/°C observed in the temperature range of -150 to 200 °C. In case of Kovar and Silvar alloy, mean coefficient of linear thermal expansion enhances up to 7.018 ppm/°C and 6.9279 ppm/°C, respectively, for similar temperature range. The addition of 17% Cobalt element in Invar alloy increases the thermal conductivity, but CTE enhances up to 7 ppm/°C means enhancement of thermal conductivity need to sacrifice low CTE of Invar alloy. Study reveals that instead of Cobalt element addition of 32% silver element in Invar alloy is the better alternative to enhance thermal conductivity up to 51 W/(m K). It also gives the similar CTE value as Kovar (7 ppm/°C), but price of the silver element is the main constraint because it ultimately increases the production cost. Silvar alloy is the best alternative for high thermal conductivity requirement where another low CTE alloy alternatives were not available.

Researches also focus on the use of composite material as alternative for high density Fe–Ni alloys. Carbon fibre reinforced polymer (CFRP) is an excellent candidate having density (1.8–2.0 g/cm³) has potential to replace high density Fe–Ni alloys. Low CTE of CFRP attracts designer to build optical-mechanical subsystem of spacecraft with composite material instead of high density alloys which not only

provides benefits of low CTE but also reduces launch cost of spacecraft. Composite systems sustain property for temperature range -150 to 200 °C which is severe temperature range in space use proves to be suitable for space application instead of Fe–Ni alloys. Main disadvantage of CFRP material is its low electrical and thermal conductivity which limits its extensive use for space use. Addition of the high conductive fillers such as nanomaterials (Carbon nanotubes, graphene and nano-size high conductive metal particles) in the composite material is the possible solution to overcome the conductive issue of composite materials. Thermal characterisation data of Fe–Ni alloys for temp range -150 to 200 °C is also useful for compare the data with composite materials.

5 Conclusion

Current study is very useful for thermal designer for designing the aerospace systems which subjected the sub-ambient temperature condition during the operations. Generally ambient conditions thermal properties of materials use for the modelling and prediction due to the non-availability of thermal data at sub-ambient or negative temperature range. Estimation of thermal properties at cryogenic temperature is really challenging and time-consuming task due to the creating cryogenic environment during the testing, but nowadays using sophisticated instrumentation provides the good accuracy and precision even at cryogenic temperature.

Invar and Kovar are frequently used alloys for space use. Each alloy has its own benefit and limitations, therefore, modification in their properties carried out by addition of different elements. Invar has benefit of very low CTE but poor thermal conductivity. Kovar has comparatively high thermal conductivity due to the addition of Co element but due to addition Co enhances the CTE value up to 7 ppm/°C. Silvar is the new developed alloy prepared by addition of around 30–32% Ag in Fe–Ni alloy and Ag in Fe–Ni alloy enhance thermal conductivity up to 50 W/(m K).

Acknowledgements Authors are sincerely thankful to Director of Space Applications Centre (SAC), Ahmedabad for their guidance, support and constant encouragement.

References

1. Al-Dabbagh JB, Al-Falujji IK, Hashim YB (2012) Thermal expansion of ferromagnetic Fe–Ni INVAR alloy. *Int J Eng Sci* 1(1):47–50. ISSN: 2278-4721
2. Lomova NV, Shabanova IN (2004) The study of the electronic structure and magnetic properties of Invar alloys based on transition metals. *J Electron Spectrosc* 137:511–517
3. Hu Q, Wang JM, Yan YH, Guo S, Chen SS, Lu DP, Zou JZ, Zeng XR (2018) Invar effect of Fe-based bulk metallic glasses. *Intermetallics* 93:318–322
4. Gibb S (2013) An introduction to Invar. *J Inf Knowl Res Mech Eng* 02(02):436–451

5. Ona K, Sakaguchi N, Ohno H, Utsunomiya S (2020) The advanced super Invar alloys with zero thermal expansion for space telescopes. *Trans JSASS Aerosp Tech Jpn* 18(3):32–37. <https://doi.org/10.2322/tastj.18.32>
6. Vartak DA, Ghotekar Y, Satyanarayana B, Munjal BS, Bhatt PM (2020) Embedment of carbon nanotubes in carbon fiber reinforced polymer for carrier plates in space payload. *J Environ Nanotechnol* 9(4):01–07. <https://doi.org/10.13074/jent.2020.12.204421>
7. ASTM E228. Standard test method for linear thermal expansion of solid materials with a push rod dilatometer. ASTM International
8. ASTM E1269. Standard test method for determining specific heat capacity by differential scanning calorimetry. ASTM International
9. ASTM E1461. Standard test method for thermal diffusivity by the flash method. ASTM International

Stress Analysis of Carbon Composite Material for Space-Based RF Component Using CAE Simulation



Aaryan Shah, Ashish Soni, Dhaval Vartak, and Pina Bhatt

Abstract Radio frequency (RF) subsystems contain microwave integrated circuits (MIC) which are used as electrical interfaces between the components in the space payload. These subsystems are designed for wide band of microwave frequencies. The package consists of microwave integrated circuits mounted on carrier plates. Metallic carrier plate is used to support MIC which is etched on the substrate. Warpage in carrier plate is developed due to residual stress during the fabrication. The surface flatness of carrier plate plays an important role in failure of the substrate, leads to fail the transponder. Carbon composite can be promising material for carrier plate due to its less density and flexibility. This paper describes stress comparison between carbon fibre reinforced plastic (CFRP) and Kovar carrier plates. This study explores feasibility of CFRP carrier plates including the challenges and requirements to qualify for space use.

Keywords RF Subsystem · Microwave integrated circuit · Space payload · Kovar carrier plates · CFRP

1 Introduction

Radio frequency (RF) subsystems contain microwave integrated circuits (MIC) which are used as electrical interfaces between the components of the space payload.

A. Shah (✉)

Vishwakarma Government Engineering College, Ahmedabad, India
e-mail: aaryanshah4261@gmail.com

A. Soni · D. Vartak

Space Applications Centre (SAC-ISRO), Ahmedabad, India
e-mail: ashishsoni@sac.isro.gov.in

D. Vartak

e-mail: dhaval@sac.isro.gov.in

P. Bhatt

Silver Oak College of Engineering and Technology, Ahmedabad, India
e-mail: pmbhatt15@gmail.com

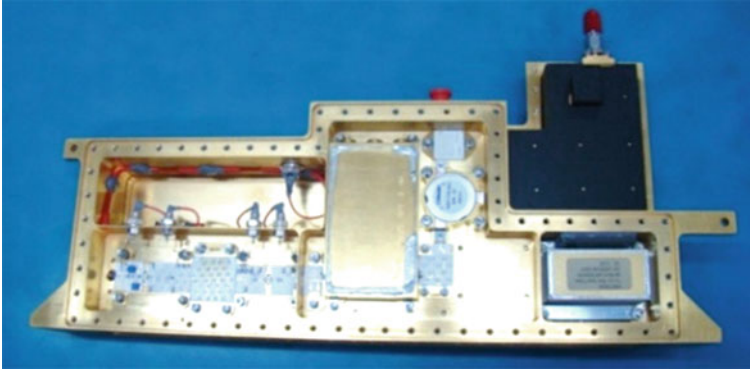


Fig. 1 MIC package

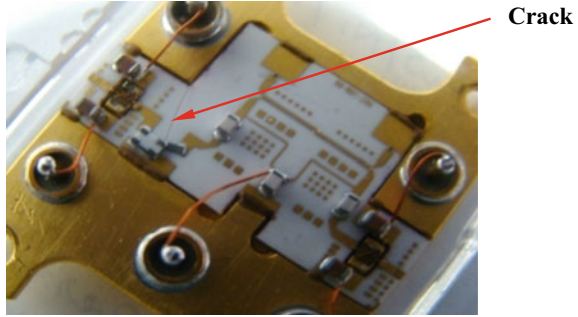
These subsystems are designed for wide band of microwave frequencies [1–3]. This package (Fig. 1) provides structural support to mount an electrical component like connectors, filters, receivers, RF cable, capacitors, resistors, carrier plates, (CP) etc.

These packages consist of alumina substrate brazed on Kovar carrier plates. Metallic carrier plate is used to support microwave circuit which is etched on the substrate. Kovar material has poor corrosion resistance. Carrier plate is gold plated for 4–6 μ thickness of gold (Au). Gold being noble in nature gives excellent corrosion resistance along with good electrical conductivity and good solderability for attaching gold plated alumina substrate. Alumina Al_2O_3 is an extremely brittle ceramic with hexagonal close packed crystal structure and more than 99.6% purity [4–7]. It is available from the size 6.35 mm \times 6.35 mm to 76.2 mm \times 76.2 mm with 0.635 mm thickness (Fig. 2). Surface co-planarity is important parameter to avoid the crack of the substrate.

Carrier plate is fabricated from the Kovar sheets. It is constrained by the mounting screws during machining, the stresses produced in the material causes deformation or undulation. Thermo-mechanical strains in substrates and carrier plates are induced due to the difference in the coefficient of thermal expansion (CTE) between Kovar and alumina. The strain gradient may be associated with deformation sometime, such as warping of carrier plates during mechanical assembly. During the assembly of carrier plate assembly and box, the maximum shear stress occurs at the carrier plate



Fig. 2 Kovar carrier plate and alumina substrate

Fig. 3 Substrate cracking

edges. This stress transfers to substrate contacting area, which ultimately transfers to alumina substrate. Due to weaker atomic bonding, alumina substrate is subjected to tensile stress and it fails at the boundaries. With increase in temperature, the stress to extend inherent flaws and substrate may develop a hairline crack resulting into a failure of circuit as shown in Fig. 3 [8].

These shows even though stress generated at every step of operation is less, but there may be incremental of stresses at the different stages of activities. Combined effect of these may be critical. Stress minimization at the functional area is necessary to prevent the cracking of substrate resulting into failure of electromechanical package. Failure or electromechanical packages leads to heavy penalty in terms of package cost and mission delay.

The material used for space applications is space qualified. For space use, aluminium alloy 6061T6 is used as packaging material, however, Kovar, Invar, magnesium alloy, and titanium are also used for specific design requirements. The lightweight materials are desirable to reduce the launching cost. Due to specific stiffness of carbon fibre reinforced plastic (CFRP), it has greater capabilities and prospective and thus used as best suitable structural material for space. Being the light weight material, use of CFRP carrier plate and microwave integrated circuit packages reduces the mass by more than 60% than traditional space-qualified materials [9]. CFRP has significantly lower conductivity compared to metals. The lower conductivity directly affects the electromagnetic shielding, thermal dispersion, and current carrying capability. CFRP is the suitable material for low frequency carrier plates, which can avoid warpage. Weight reduction nearly six times is achieved due to development of CFRP carrier plate, in comparison with existing topology [10–15]. This paper explains the comparison between Kovar and CFRP carrier plate in terms of stresses produced due to undulation using CAE simulation.

2 Finite Element Analysis (FEA)

The FEA is carried out on 37.6 mm × 25.6 mm carrier plate with alumina substrate as shown in Fig. 4. For the construction of 3D model, Autodesk Inventor V.11 CAD

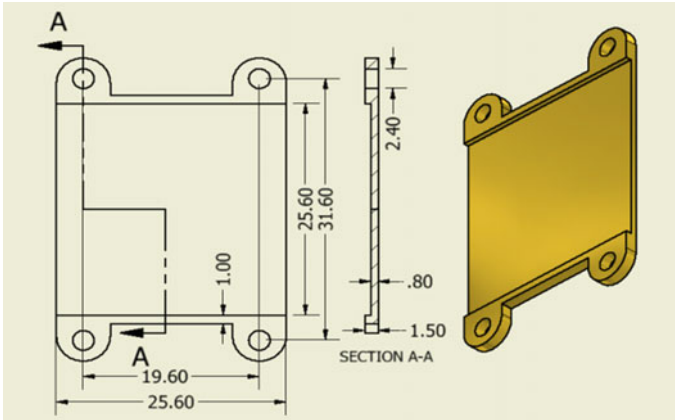


Fig. 4 Carrier plate model

software is used. This model is converted in STEP format and imported in Solid works 2018 for FE analysis. Solid Works is a high performance finite element pre- and post- processor software that allows building finite element and finite difference models, view their results, and perform data analysis.

CFRP composite is consider as anisotropic material. Meshing of each shell thickness is considered 0.25 mm, and the angle is considered 0 and 90° alternatively as it is bilateral directional fibres. Total numbers of six shells and three shells are considered at lug and at middle functional area, respectively. The quad element size 1.6991 mm is considered for both the materials. The number of nodes are 1345, whereas number of elements are 614.

2.1 Properties of Kovar and CFRP

The properties of Kovar and CFRP are taken for the analysis as per Table 1 [16, 17].

Table 1 Materials property

Material	Elastic modulus (E) (N/mm ²)	Poisson's ratio (μ)	Mass density (ρ) (kg/m ³)	Yield strength (N/mm ²)	CTE (mm/mm/°C)
Kovar	140×10^3	0.3	8100	276	5.2×10^{-6}
CFRP (bilateral direction)	80×10^3	0.28	1800	460	1×10^{-6}

2.2 Frequency Modes

The natural frequency should be above 100 Hz to prevent resonance coupling with the spacecraft structure. Hence, the first fundamental frequency is very much important for any space component/package. Natural frequencies and its modes of CP are shown in Table 2 and Fig. 5.

Table 2 Natural frequency mode

Mode	First mode	Second mode	Third mode	Fourth mode
Kovar CP frequency Hz	4143	5656	8786	10,452
CFRP CP frequency Hz	5533	7104	10,738	12,790

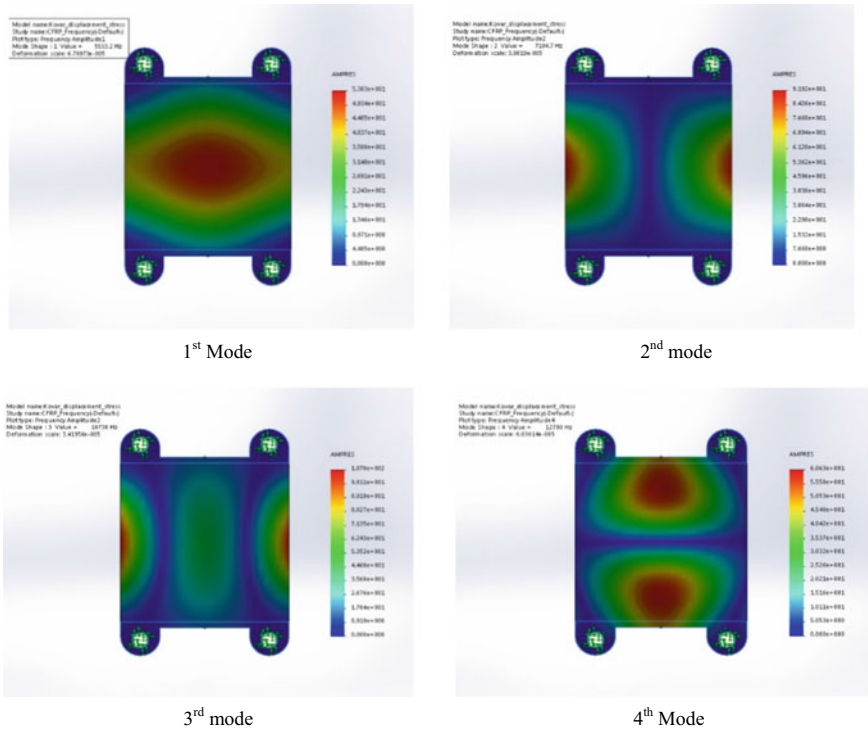


Fig. 5 Mode shape of CFRP carrier plates

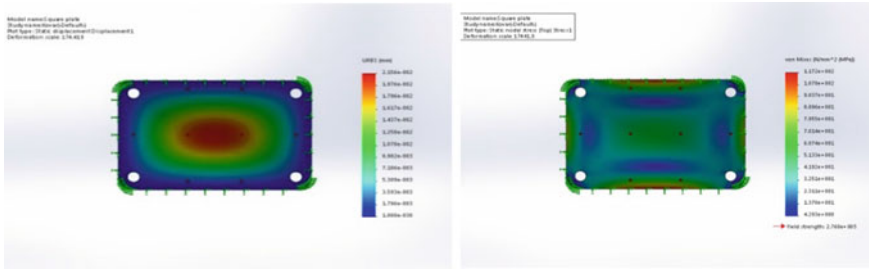


Fig. 6 Displacement and stress on CFRP plates

2.3 Validation of Model

Results of FE analysis are depending on various factors such as types and order of elements, boundary conditions, and assumptions but it is validated through numerical analysis. Carrier plate is of complex shape, and therefore, there is no direct equation for displacement, and stress analysis is available. Therefore, deflection and stress analysis are carried out basic on simple plate. The results obtained from numerical equation matches with the results obtained from CAE tool to validate the types and order of elements, boundary condition, assumptions considered in FE analysis.

2.3.1 FE Analysis (CAE Tool)

Boundary Condition: Second order shell quad elements, constrain all four edges (fixed), Uniform load: Pressure force: 1 N/mm^2 , Plate size: $37.6 \text{ mm} \times 25.6 \text{ mm} \times 1.5 \text{ mm}$ (Fig. 6).

Computational analysis shows maximum deflection at the centre of rectangular plate: $2.15 \times 10^{-2} \text{ mm}$ whereas maximum stress at the centre of longest edge of rectangular plate: 117 N/mm^2 .

2.3.2 Classical Analysis (Mathematical Formula)

Rectangular plate with all edges built in condition and uniform distributed load is considering for the analysis (same condition which consider for FE analysis given in previous para). Deflection and stress values under these conditions for rectangular plate are calculated. Equation is considered for thin rectangular plate with uniform load and all edges fixed [18].

Deflection at the Centre

Rectangular plate with $37.6 \times 25.6 \times 1.5 \text{ mm}$

$$W(\text{maximum deflection in plate at center}) = \frac{c_1 \times P \times \text{Min}(L_x \text{ or } L_y)^4}{D} \tag{1}$$

C_1 (constant depends on the ratio of length to width of plate) = 0.00214 for $\frac{b}{a} = \frac{37.6}{25.6} = 1.47$ (from table)

E (Modulus of elasticity) = 140 GPa

L_x (Length of plate) = 37.6 mm

L_y (width of plate) = 25.6 mm

h (Thickness of plate) = 1.5 mm

μ (Poisson Ratio) = 0.33 for Kovar

P (Load $\frac{N}{\text{mm}^2}$) = 1 N/mm²

D (Fractural Rigidity Nmm) = $\frac{140 \times 10^3 \times 1.5^3}{(1-0.3^2)} = 43.26 \times 10^3$ Nmm

$w = \frac{0.00214 \times 1 \times (25.6)^4}{43.26 \times 10^3} = 2.124 \times 10^{-2}$ mm (max) at middle.

Stress at the Centre of Longest Edge

$$\sigma(\text{Max Stress at the center of longest edge}) = \frac{6 \times M}{h^2} \tag{2}$$

$M = c_2 \times p \times \text{Min}(L_x, L_y)^2$

c_2 = constant depends on ratio of length to width

h = thickness of plate = 1.5 mm

M = moment at $x = 0, y = \frac{1}{2}$ for $\frac{b}{a} = \frac{37.6}{25.6} = 1.47$ (from table)

$M(y) = 0.0569 \times P \times \text{min}(L_x \text{ or } L_y)^2 = 37.30$ N

σ (Stress) = $\frac{6 \times 37.30}{1.5^2} = 100$ N/mm².

2.3.3 FE Analysis Results

Computational analysis and analysis by classical method are compared as shown in Table 3 in terms of deflection and stress for 1 N/mm² load.

FE analysis is carried out on rectangular plate of same size of 37.6 mm × 25.6 mm × 1.5 mm with boundary condition of second order quad shell elements with all edges are fixed. The value obtain from the analysis is very close to value obtained by mathematical formula for rectangular plate. Thus, the types, size and order of elements, and boundary condition assumed in FE analysis are validated for further analysis for carrier plate.

Table 3 Comparison of analysis results

Rectangular plate 37.6 mm × 25.6 mm × 1.5 mm	By analysis	By mathematical formula
Deflection in mm	2.15×10^{-2}	2.124×10^{-2}
Stress in N/mm ²	117	100

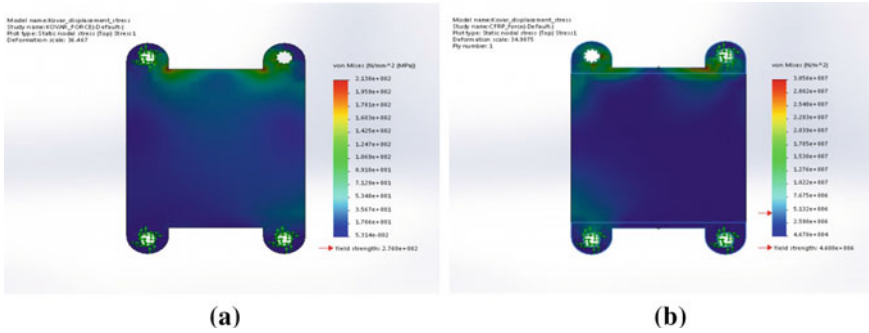


Fig. 7 a Stresses in Kovar CP and b stresses in CFRP CP

2.4 Stress with 0.1 mm Warpage on Carrier Plate

The warpage condition simulation is carried out by considering three lugs are fixed and one lug is given 0.1 mm displacement which is shown in Fig. 7a, b for Kovar and CFRP carrier plate, respectively.

3 Observation

Stress analysis is carried out for carrier plates (CPs) of Kovar and CFRP. The stress is induced in Kovar CP is 214 MPa, whereas 30.56 MPa in CFRP CP, when there is warpage in CP of 0.1 mm at lug. There is drastically reduction in stress (more than 85%) due to undulation in CFRP CP than that of Kovar CP. Figure 8 shows the stress induced in carrier plate of Kovar and CFRP at different warpage conditions and their comparison.

The maximum deformation generated with 1 N force at one lug in Kovar CP is 0.018 mm, whereas in CFRP CP is 0.08 mm for the same force at same location.

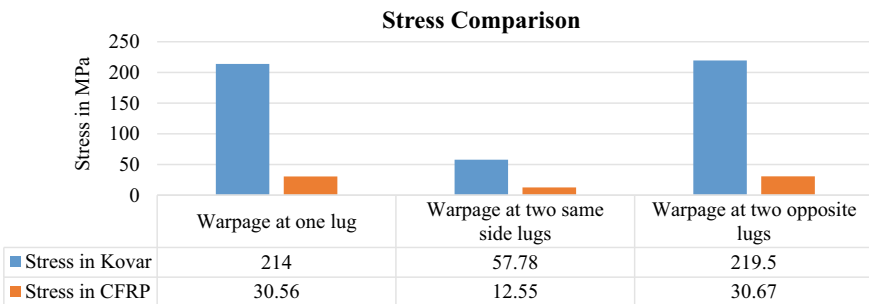


Fig. 8 Stress induced in different warpage conditions

Hence, more deformation is produced in CFRP material than Kovar material, which indicated that CFRP material gives more flexibility than Kovar material.

4 Conclusion

Stresses produced due to warpage (undulation) in one lug of CP can be reduced in CFRP material than that of Kovar. CFRP carrier plates refer adequate stiffness with flexibility, resulting to minimize the transfer of stresses from lug of CP to alumina substrate contacting area. These techniques are useful to reduce the stresses at the functional area (alumina substrate contact area) to help to avoid the crack. Moreover, CFRP carrier plate saves mass more than 40% Kovar materials, which reduces the weight of package. The impact of this study will be helpful to explore the possibilities of this composite as a carrier plate for space applications. However, there are certain limitations in properties of CFRP like thermal conductivity, coefficient of thermal expansion (CTE), and bulk electrical conductivity. Epoxy resin is thermally and electrically poor conductor and also has large CTE. However, these two problems can be solved by creating CFRP conductive by embedment of carbon nano fillers and considering bidirectional carbon fibres, respectively. Depending on the performance of the space payload component and requirement of a specific task, enhancement of the specific stiffness, improvement in thermal and electrical conductivity can be carried out. Further, study can be done on adoption of certain dispersion technique depending upon the type of carbon nano fillers and quantity of processed polymer.

Acknowledgements We are thankful to Shri. TVS Ram, Deputy Director-MISA, Shri Arup Hait, GD-MPMG/MESA, Shri Jaimin Desai, GD-ENTSG/ESSA of Space Applications Centre-ISRO for guidance and valuable suggestions. We would also like to extend our thanks to Shri Anand Pathak, GD-CNMG/MESA, Shri VM Shah, Eng.-SRA/SAC for their continuous technical support. We would also like to offer our sincere gratitude to Shri N.M. Desai, Director, Space Applications Centre, ISRO, Ahmedabad.

References

1. Kasturirangan K, Chakravarty SC (1999) Indian space program for the twenty first century. National seminar, PRL, Ahmedabad
2. Agrawal BN (1986) Design of geosynchronous spacecraft. Prentice-Hall, Englewood Cliffs, NJ
3. Michael P (1991) Handbook of electronics package design. Marcel Dekker Inc., New York
4. Ashish S et al (2008) Criticalities in space microwave package assembly and practical solutions Vaigyaniki'08. IIT, Bombay, Mar 2008
5. Ashish S (2008) M.Tech thesis report on design, simulation and optimization of microwave package for space communication payload
6. Ashish S (2004) Report on electro-mechanical compatibility and assembly aspects for communication subsystem packages, Doc. No. ISRO-SAC-MDFD-001, Dec 2004

7. Ashish S et al (2008) Simulation and optimization of microwave package for space communication payload. In: International conference on trends in product life cycle, modeling, simulation and synthesis, PLMSS-2008, Nov 2008
8. Vartak Dhaval A (2014) Failure analysis of substrate of carrier plate of electromechanical package for space payload. IJERT 3(3)
9. Vartak Dhaval A, Yogesh G, Satyanarayana B, Munjal BS, Bhatt Pina M (2020) Embedment of carbon nanotubes in carbon fibre reinforced polymer for carrier plates in space payload. J Environ Nanotechnol 9(4):01–07. ISSN (Print) 2279-0748, ISSN (online) 2319-5541
10. Vartak Dhaval A, Satyanarayana B, Munjal BS, Vyas KB, Bhatt Pina M, Lal AK (2020) Potential applications of advanced nano-composite materials for space payload. Aust J Mech Eng. <https://doi.org/10.1080/14484846.2020.1733176>
11. Prabhakaran R (2015) Nano-composites for space applications. [Online]. <https://www.researchgate.net/publication/275020661>
12. Vartak Dhaval A, Yogesh G, Bhatt PM (2021) Carbon nanotube polymer composites for microwave electronics package assembly of space payload: advantages and challenges. Int J Aerosp Syst Sci Eng. <https://doi.org/10.1504/IJASSE:2021.10036733>
13. Vartak Dhaval A, Yogesh G, Munjal BS, Bhatt Pina M, Satyanarayana B, Lal AK (2021) Characterization of tailored multi-walled carbon nanotubes based composite for geo-space payload components. J Electron Mater. <https://doi.org/10.1007/s11664-021-08978-6>
14. Vartak Dhaval A, Yogesh G, Nandini D, Munjal BS, Bhatt Pina M, Satyanarayana B, Lal AK (2021) New horizons of space qualification of single-walled carbon nano tubes-carbon fibre reinforced polymer composite. J Phys Conf Ser 1854:012001. <https://doi.org/10.1088/1742-6596/1854/1/012001>
15. Bhatt Pina M, Shah HN (2015) Computational and experimental analysis of nitride coated cutting tools. J Exp Appl Mech 6(3):1–8. ISSN 2230-9845 (online), ISSN: 2321:516x (print)
16. Non-ferrous metals & alloys (1997) ASM handbook, vol 2, American Society of Metals ISBN 0-87170-378-5
17. Declared material list (2014) SAC/SRA/QACMG/MQAD/TR/42/Nov 2014. Space Applications Centre, ISRO, Ahmedabad
18. Timoshanko S, Woinowsky-Krienger S (1987) Plates and shells, 2nd edn. McGraw-Hill

RF Shielding Effectiveness of Nano-composites for Space Payload Applications



Nandini Deshpande, Manisha Upadhyay, Dhaval Vartak,
Bhuwaneshwar Semwal, Anil Shah, and A. K. Lal

Abstract Embedment of nano-fillers like carbon nanotubes and Graphene in Carbon Fiber Reinforced Polymers (CFRP) is the recent research trend for improving electrical conductivity of CFRP laminates. Enhancement of electrical conductivity results into the improvement in shielding effectiveness, which is one of the essential property for electronics packages for space payloads. With the increased number of space systems in a closed vicinity, the challenges for electromagnetic interferences (EMI) has increased. Shielding effectiveness (SE) of any enclosure mainly depends upon its capability to prevent emission or to withstand interference coming from outside. Therefore, EMI shielding material selection is an important task. The paper is focused on suitable CFRP composite with different proportions of Multi-walled Carbon Nanotubes (MWCNT) and Graphene Oxide (rGO) in terms of SE. It describes different SE measurement techniques and discusses the result of waveguide-based measuring technique, which leads to the selection of appropriate composite for space payload applications.

Keywords Electromagnetic interferences · MWCNT · Nano-composites · rGO · Shielding effectiveness

N. Deshpande (✉) · D. Vartak · B. Semwal · A. Shah · A. K. Lal
Systems Reliability Area (SRA), Space Applications Centre (SAC-ISRO), Ahmedabad, India
e-mail: nandinigodhe@sac.isro.gov.in

D. Vartak
e-mail: dhaval@sac.isro.gov.in

B. Semwal
e-mail: bhuwan@sac.isro.gov.in

A. Shah
e-mail: akshah@sac.isro.gov.in

A. K. Lal
e-mail: aklal@sac.isro.gov.in

M. Upadhyay
Nirma University, Ahmedabad, India
e-mail: manisha.upadhyay@nirmauni.ac.in

1 Introduction

A space system is an integration of various electronics and mechanical subsystems. These independent or inter-dependent subsystems is working under varying electromagnetic environment. Each subsystem behaves as either a source of electromagnetic interference (EMI) or receptor. Shielding effectiveness (SE) of any enclosure mainly depends upon its capability to prevent emission or to withstand interference coming from outside. Demand for composite materials is increasing rapidly to cater to the requirement of lightweight components for the space missions. Multi-walled Carbon Nanotubes (MWCNT) and Graphene Oxide (rGO) being explored as a potential conductive filler with conductive Carbon Fiber Reinforced Polymers (CFRP) to increase the electrical conductivity of composite. The increase in conductivity will in-turn improve shielding effectiveness of the material. However, the SE value depends on the proportion of nano-fillers. Samples with different proportions of MWCNT and rGO fabricated and tested for EMI testing/SE testing. This experiment results into selection of an appropriate nano-composite with suitable proportion for electronic packages.

2 Shielding Effectiveness

Space systems are becoming more and more compact to reduce the weight and to accommodate more and more hardware in lesser space. The closely spaced subsystems are being affected by EMI/EMC problems. Either hardware becomes a source or victim of EMI. The best approach is to eliminate the radiation at the source level itself, so that all the subsequent stages may be protected. Shielding is an external enclosure, which provides a conductive barrier to an enveloping electrical circuit. It prevents the signals from propagating further by providing adequate isolation.

The basic mechanism by which a material provides shielding: reflections, absorptions and internal reflections [1] as in Fig. 1. To understand the shielding effectiveness (SE) concept, it is required to enhance the knowledge on the absorption and reflection phenomenon of materials. Shielding effectiveness of a barrier is defined as the ratio of radiated power received without the shield in place to the power received with the shield in place.

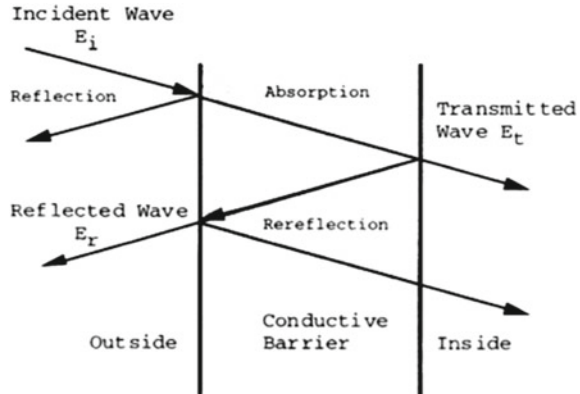
Shielding Effectiveness [3],

$$SE = SE_A + SE_R + SE_B$$

where A = attenuation loss due to absorption (in dB), R = loss due to reflection (in dB) and B = re-reflection correction.

Nano-fillers improve the conductivity of the parent material and hence the absorption shall necessarily increase while RF signal travels through the material. Also the

Fig. 1 Radiated wave through a shielding material [2]



reflection and re-reflection may also take place within the internal layers of the composite. Quantitative verification may be done with the measured S -parameters.

2.1 Challenges in Selecting Shielding Material

At higher frequencies, surface conductivity becomes critical as due to skin effect currents will tend to crowd into upper most layer and hence higher chances of leakage. In the thin shields, the absorption losses are very less thus signals can pass thin shields and hence re-reflection or multiple reflections cannot be ignored. Shields are frequency dependent. Shielding effectiveness of the enclosure plays an important role to achieve immunity against internal and external interferences. Hence, selection of an appropriate EMI shielding material is very important. The main purpose to achieve shielding in a material is to make that material conductive enough to provide adequate shielding. The type of material selected to provide shielding determines SE. Mainly, electrical properties contribute to formulate shielding effectiveness (SE) and in-turn have an effect on electromagnetic compatibility of the system. Conductivity, volume resistivity, permeability, permittivity, skin depth, intrinsic impedance and shielding effectiveness (SE) are the few important parameters to be considered for any conductive material to be studied for space. Shielding effectiveness (SE) is a numerical number derived from a set of values for each material.

2.2 SE Measurement Methods

Analytical, numerical/simulation and experimental methods are different measurement approaches to derive SE values. Assessment of test method and test apparatus for each of the methods will lead to help into taking decision on the applicable SE

measurement technique. The calculated values of SE can further be verified using any of the applicable measurement techniques.

Following formulae were used during the calculation of current work

$$SE_T = SE_A + SE_R + SE_B$$

$$SE_A = 10 \log 10(1/1 - |S_{11}|^2)$$

$$SE_R = 10 \log 10(1 - |S_{11}|^2)/|S_{12}|^2$$

$$SE_B = \text{Thickness is very small, hence not much contribution is expected}$$

where SE_T = total shielding (SE_T), absorption loss (SE_A) and reflection loss (SE_R).

Material samples can be measured with following measuring methods [4, 5]:

- (a) Open field or free space method
- (b) Shielded box method
- (c) Waveguide/coaxial transmission line method
- (d) Shielded room method

(a) **Open field or free space method**

This method is used to measure radiated emission from a complete electronic assembly.

Limitations: This method is not suitable for measuring any specific material, and the results greatly depend on the assembly and interfaces of the electronic assembly products (Fig. 2).

(b) **Shielded box method**

This method uses a metal box wherein which there is a sample port to hold sample. This metallic box connected with receiving antenna. A transmitting antenna is placed nearby with power fed from signal generator and amplifier. A receiver connected to receiving antenna to measure the emission from the sample as shown in Fig. 3. This method has limited frequency range of about 500 MHz. The specimen needs to have a perfect contact with the shielded box. As it completely depends on the contact of the sample with specimen; variation in results over different measurement setups is found.

Fig. 2 Open field SE measurement [2]

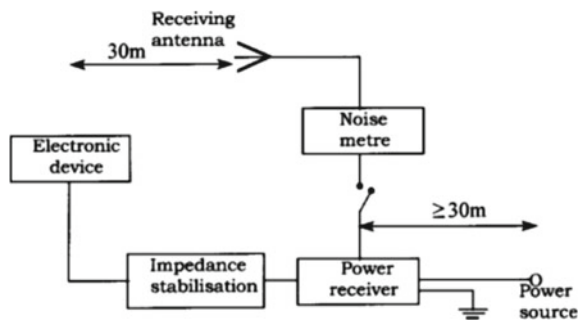
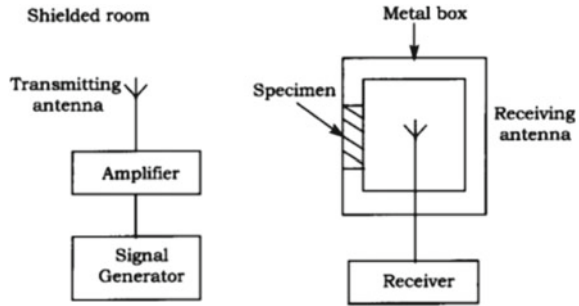


Fig. 3 Shielded box SE measurement [2]



(c) Shielded room method

The limitations of shielded box method can overcome with shielded room method. The basic working principle of both the methods remains the same except measuring instruments and transmit and receive antennae are kept isolated as shown in Fig. 4.

Limitations: The required size of the sample is quiet high app. 2.5 m² in area.

(d) Coaxial/Waveguide transmission line method

This method is useful for measuring material samples with smaller dimensions/thin sheets. This method used a flanged holder to place material sample and vector network analyzer (VNA) as a measuring equipment. *S*-parameters, *S*₁₁ and *S*₂₁—reflection and transmission coefficients are measured and absorption and reflection contributed by them are calculated (Fig. 5).

As the frequency of measurement increases, the sample size reduces and even the gaps between sample and holder become accountable. This method provides better solution to all these problems.

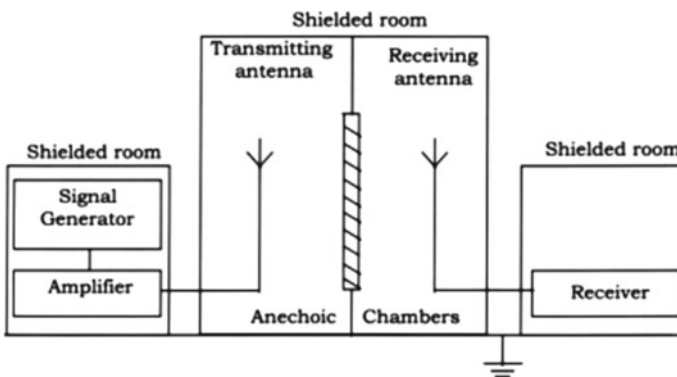
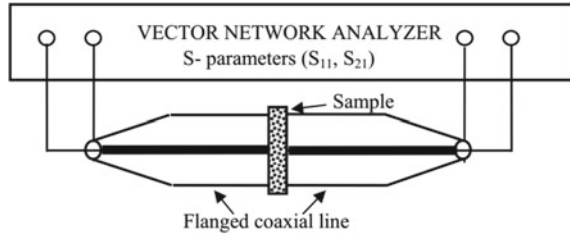


Fig. 4 Shielded room SE measurement [2]

Fig. 5 Coaxial/waveguide transmission line method



3 Composite Materials and Fabrication of Samples

Samples of composite are fabricated by solution mixing method by varying the concentration wt% of the MWCNT and rGO [6, 7]. Fabricated samples cured by vacuum bagging as shown in Fig. 6.

- Carbon fabric sheet: Bi-axial, plain weave, thickness 0.300 mm and density 1.7 g/cc
- Multi-walled Carbon Nanotube (MWCNTs): Purity 99%, diameter 5–20 nm and length 10 μm
- Reduced Graphene Oxide (rGO): Purity > 99%, thickness 0.8–2 nm and length 1–2 μm
- Epoxy: Density 1.3 g/cc
- Hardener: Density 0.9 g/cc
- Solvent: Acetone.

Three different variants fabricated are as below. Size of samples are of 100 \times 100 mm, whereas thickness each of the composite is kept 2 ± 0.150 mm.

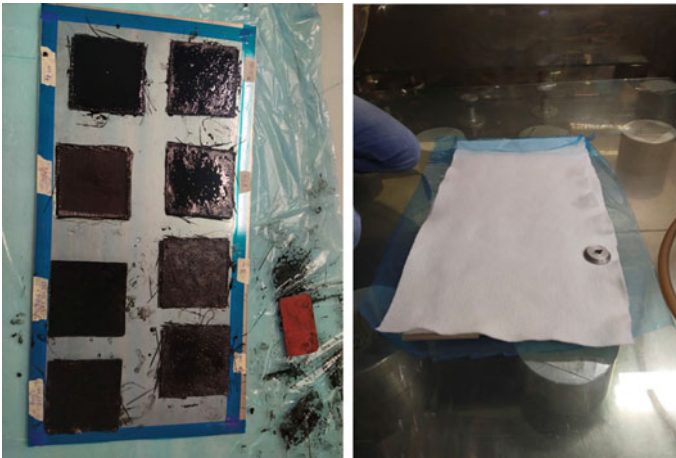


Fig. 6 Sample fabrication and vacuum

Table 1 Sample Configuration

Sr. No.	Nano-filler in CFRP	Composition of sample
1.	No filler	Bare CFRP
2.	Hybrid MWCNT + rGO	0.25 wt% + 0.25 wt%
3.	Hybrid MWCNT + rGO	0.25 wt% + 0.75 wt%
4.	Hybrid MWCNT + rGO	0.75 wt% + 0.25 wt%

Table 1 gives the ample details based on the concentration of nano-fillers in CFRP.

4 SE Measurement

Waveguide transmission line measurement method selected for SE measurement of the composite. In this measurement technique, sample is placed within the cavity of waveguide flanges, and then *S*-parameters are measured using vector network analyzer (VNA). Two port SOLT (short, Open, Load and Thru) calibration is performed before commencement of the measurement. With the material in place reflected (S_{11}) and transmitted signal (S_{21}) measured, which is used to calculate absorption and reflection of the material by equations. Measured *S*-parameters converted into absorption and reflection losses by computation.

Two numbers of back-to-back connected waveguide to coaxial adaptors used wherein the sample under test fixed inside the cavity as shown in Fig. 8. An Aluminum sample holder of the thickness same as that of sample thickness placed in between two flanges to fix the material sample. The samples were prepared with appropriate machining so that the sample fit tightly into the cavity of the holder as shown in Fig. 7.

PNA-X series VNA is used for this measurement as shown in Fig. 9. Frequency calibration was done thru E-Cal kit. Calibration of VNA is done at the reference

Fig. 7 Measurement accessories. A: W/R to coaxial adaptor, B/C/D: intermediate Al plate for WR28/WR51/WR75 with and E: composite sample fixed within the flange cavity

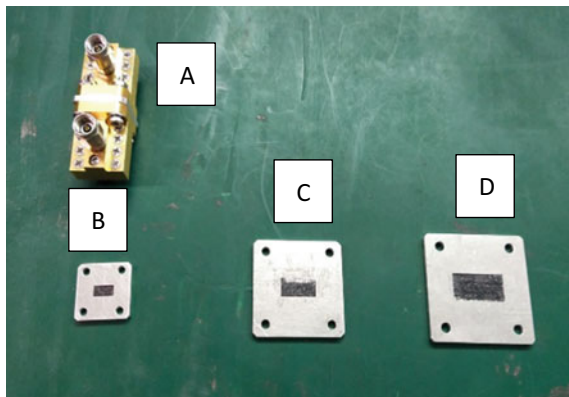
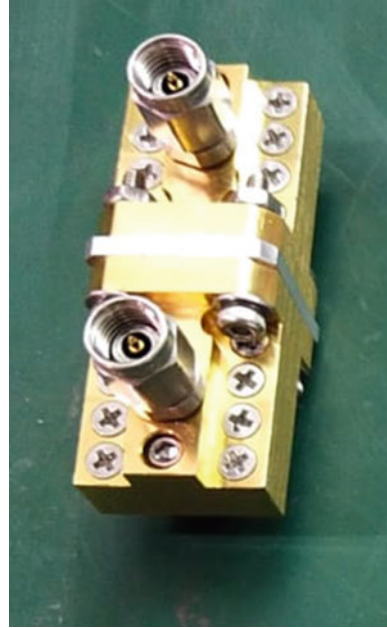


Fig. 8 Back-to-back connected WR51 waveguide to coaxial adaptors having an aluminum sample holder plate fixed between two flanges carries sample



plane where the material under test (MUT) is to be connected. After the successful completion of calibration, MUT is placed in the holder with minimum air gaps to improve measurement accuracy.

Also de-embedding of the waveguide to coaxial adaptor along with the intermediate Aluminum holder plate is done first. After calibration, first the S -parameters of empty sample holders are measured. The measured value is used for the de-embedding of the sample holder performance from the MUT performance [8].

Measurement are done using three different types of waveguide configurations over frequency band ranging from 10 to 40 GHz (Table 2).

1. WR75 (10–15 GHz),
2. WR51 (15–26.5 GHz),
3. WR28 (26.5–40 GHz).

Each of the above sample is tested with all three waveguide configurations WR75 (10–15 GHz), WR51 (15–26.5 GHz) and WR28 (26.5–40 GHz), and the results were compared with bare CFRP.

5 Observations

Based on the S -parameters measured; broadband SE value is calculated for each of the filler composition over 10–40 GHz and compared with CFRP as shown in Fig. 10.

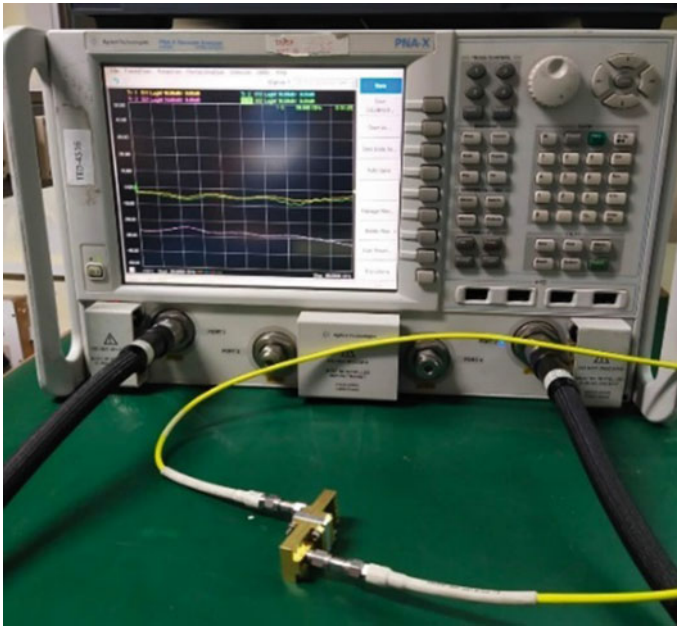


Fig. 9 VNA measurement setup

Table 2 Test configuration details

Sr. No.	Nano-filler	Composition	Test configuration		
			WR75 (10–15 GHz)	WR51 (15–26.5 GHz)	WR51 (15–26.5 GHz)
1.	No filler	Bare CFRP	✓	✓	✓
2.	Hybrid MWCNT + rGO	0.25 wt% + 0.25 wt%	✓	✓	✓
3.	Hybrid MWCNT + rGO	0.25 wt% + 0.75 wt%	✓	✓	✓
4.	Hybrid MWCNT + rGO	0.75 wt% + 0.25 wt%	✓	✓	✓

Calculations indicated that the total shielding effectiveness value is governed by the shielding due to absorption; however, the reflection has very less contribution in overall SE value. For these nano-fillers absorption appears to be the dominant shielding phenomena.

SE is measured on the samples with different concentrations of rGO and MWCNT, using the waveguide method.

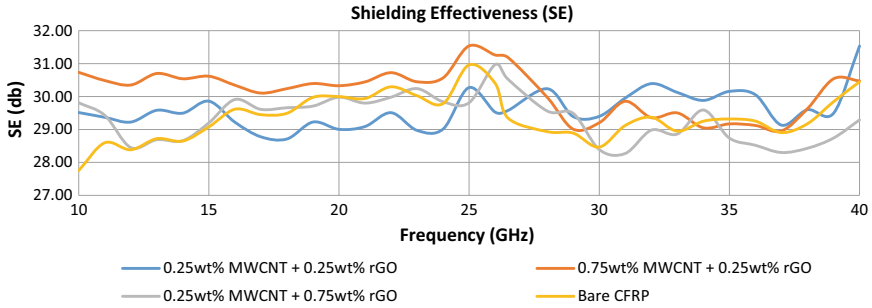


Fig. 10 SE value comparison of various nano-fillers over 10–40 GHz

Table 3 Assessment of SE values measured for various nano-fillers

Sr. No.	Sample details	Observations
1.	0.25 wt% MWCNT and 0.25 wt% rGO	Improvement observed over 10–15 GHz and 27–36 GHz frequency range
2.	0.25 wt% MWCNT and 0.75 wt% rGO	No improvement
3.	0.75 wt% MWCNT and 0.25 wt% rGO	Improvement observed over 10–27 GHz frequency range

Assessment of the measured SE value is listed in Table 3.

0.75 wt% MWCNT and 0.25 wt% rGO appears to have better SE as compared to other two configurations. Absorption is observed to be the dominant shielding mechanism for studied nano-fillers.

6 Conclusion

- Nano-fillers of MWCNT + rGO (0.75 wt% + 0.25 wt%) embedded with CFRP has an improved electrical conductivity which results in shielding effectiveness.
- This improvement in SE explored CFRP material with nano-fillers as a material for space components.
- Moreover, space components fabricated by CFRP saves mass over conventional material space components.
- Also improvement in electrical conductivity may lead to electroplate the composite without surface activation. This is an added advantage in reflector designing terms of expediting the current fabrication process.

Acknowledgements We are thankful Shri. Sharad Shukla Head STPD, Shri. Nitin Sharma Head CDFG and Shri. Yogesh Ghotekar Engr. MQAG of Space Applications Centre-ISRO for the technical support. We would also like to offer our gratitude to Shri N. M. Desai, Director Space Applications Centre (ISRO) for his kind support and constant encouragement.

References

1. EMI shielding engineering handbook. Chomerics
2. NASA Contractor Report 4784. Design guidelines for shielding effectiveness, current carrying capability, and the enhancement of conductivity of composite materials
3. Geetha S, Satheesh Kumar KK, Rao CRK, Vijayan M, Trivedi DC, Violette JLN, White DRJ, Violette MF. EMI Shielding: methods and materials—a review
4. (1987) Electromagnetic compatibility handbook. Van Nostrand Reinhold Company, New York
5. Miller HK (1997) Mater Eval 55:994
6. Vartak DA, Ghotekar Y, Munjal BS, Bhatt PM, Satyanarayana B, Lal AK (2021) Characterization of tailored multi-walled carbon nanotubes based composite for geo-space payload components. J Electr Mater. <https://doi.org/10.1007/s11664-021-08978-6>
7. Vartak DA, Ghotekar Y, Deshpande N, Munjal BS, Bhatt P, Satyanarayana B, Vyas KB, Lal AK (2021) New horizons of space qualification of single-walled carbon nano tubes-carbon fibre reinforced polymer composite. J Phys. <https://doi.org/10.1088/1742-6596/1854/1/012001>
8. Al-Saleh MH, Saadeh WH, Sundararaj U. EMI shielding effectiveness of carbon based nanostructured polymeric materials: a comparative study
9. TR 1006 EN 0206. Test report shielding effectiveness per ASTM 4935

Aluminium Metal Matrix Composites Fabricated by Powder Metallurgy Techniques: A Review



Guttikonda Manohar, K. M. Pandey, and S. R. Maity

Abstract Nowadays composite materials are at top in material selection process because of its superior mechanical, chemical and corrosive properties. But, predicting the behaviour of composites with different reinforcements and their content levels is complex because of different fabrication techniques give different properties. To use reinforcements up to its fullest in a metal matrix, suitable processing techniques have to be select so that composite with good interface bond strength and better mechanical properties can be obtained. Interface bond strength plays a major role in robustness of the composite material. Interface bond strength depends on many factors like type of reinforcement, sintering temperature, intermetallic compounds formed, etc. In this paper, a very good review is presented about composites with different reinforcements and their content levels, processing techniques, sintering temperatures, strengthening mechanisms along with theoretical equations and robustness of the composites obtained by each and every technique is included for comparison purpose.

Keywords Powder metallurgy · Composite materials · Ball milling · Intermetallic compounds · Sintering

1 Introduction

Composites play a major role in the present generation by adopting properties from added reinforcements. There are various reinforcement materials used depend on type of matrix or type of applications, generally used reinforcement materials are boron carbide (B_4C), silicon carbide (SiC), graphene, graphite, CNT, tungsten carbide (WC), titanium carbide (TiC), zirconium carbide (ZrC), etc. [1–6]. The interface binding strength between the matrix and the hard ceramic reinforcements is a crucial

G. Manohar (✉)

NBKR Institute of Science and Technology, Vidyanagar, Nellore 524413, A.P, India
e-mail: manohar317k@gmail.com

K. M. Pandey · S. R. Maity

National Institute of Science of Technology Silchar, Silchar 788010, Assam, India

component that affects the characteristics of composite materials, especially in metal matrix materials particle reinforcements give better properties along with ductility when compared to fibre reinforcements, the reason for this is that generated contacts between matrix and reinforcements act as dislocation movement barriers [7–9], which reduces deformation capability while applying load. Compared to fibres, particle reinforcements make less interface regions and also decreased particle sizes makes high surface to volume ratios so that better load transfer mechanisms are possible. Among different available reinforcement particles, B_4C and SiC are majorly used. B_4C is used in structural applications due to high brittle nature that protects from shocks localized at high strain rates [10]. The strength of the composite increases by the addition of hard ceramic reinforcements by sacrificing the ductility nature of the material [11]. Majorly there are two methods to make nanomaterials or nanocomposites those are (a) by using external energy changing the structure of the material (conventional methods) and (b) from the powders by using mechanical alloying technique [12]. By conventional methods, agglomeration of the reinforced particles in the molten metal was the major problem due to their high surface energies which are readily to react and also factors like particle size, shape and formation of an electrical charge while stirring lead to agglomeration effects [13]. In mechanical alloying process, ball milling is the technique used to reduce particle size of reinforcements and for effective dispersion of reinforcements in matrix material. In powder metallurgy, properties of the composites mainly depend upon the quality of the green compact specimen, and this quality depends upon the densification behaviour of powders. While compaction, the compressibility of the composite powder's declines compared to its unreinforced ones [14]. Density of the green compact decides the quality of the composite while consolidating from composite powders [15], relative density increases with sintering temperature up to some level after that there are no significant changes was observed in case of plasma arc sintering (PAS) [16]. At the initial stage of compaction, sliding and rearrangement of particles are more, after that at high pressure rates, plastic deformations are predominant. At high pressure rates, densification behaviour was low compared to low pressures rates, because of hard ceramic particles clusters cause poor densification and also differences in their deformation capabilities of matrix and reinforcements [17]. As the volume fraction increases in the matrix material, agglomeration of reinforcements leads to small pores in matrix-reinforcement network. The advantage of powder metallurgy process is that chances of segregation and generation of intermetallic compounds are low. By conventional methods, sedimentation of added reinforcements was major drawback, and it affects the consistent dispersion of the reinforcement particles in the matrix material. Blended powder semisolid forming (BPSF) is a new technique which holds the advantages of casting, semisolid forming and powder metallurgy processes, in case of BPSF wetting behaviour between matrix and reinforcements was good because of liquid phase matrix [18]. Adding of Ti in the molten metal of Al increase the wettability between Al and B_4C leads to better bonding properties [19]. In traditional procedures, a temperature of around 1100 °C is required for improved

bonding between Al and B₄C. There is a substantial risk of forming unneeded inter-metallic compounds at that temperature, which can damage the composite material's mechanical qualities. [20].

2 Major Reported Works in Al Composites

Graphene is the most widely used reinforcement material and has very superior mechanical properties when compared to other Al composites. GNP's have high strength compared to matrix Al and its alloys, but reinforced composites show relatively low strengths. It is because of pores left during cold compaction and initiate crack propagation during fracture and also huge difference in the compressive strength and melting points makes rearrangement of particles and diffusion process difficult while sintering process makes composite porous. GNP's particle size also effects porosity levels directly and sintering temperatures decreases the porosity levels, correlation between sintering and diffusion coefficient is explained as in Eq. 1 [21].

$$D = D_o \exp(-Q/RT) \quad (1)$$

D = diffusion coefficient, D_o = diffusion constant, Q = activation energy, R = Boltzmann's constant, T = sintering temperature.

Graphene-reinforced Al composites are stronger than other composites because of graphene strength. Al₄C₃ intermetallic's are formed at interfaces for Al/Graphene composites and also dislocation pileups at the grain boundaries of Al matrix also strengthen the composite material that are shown by TEM images represented in Fig. 1 [22].

Casted Al-GNP composite fabricated by ball milled, spark plasma sintered and melted along with Al melts along with subsequent rolling shows superior mechanical properties due to good interface bond strength, micro cracks are generated by rolling process at interfaces, that are shown in Fig. 2. Nano GNPs are embedded in to Al matrix, and stacking faults are generated in Al grains help in enhancement in tensile

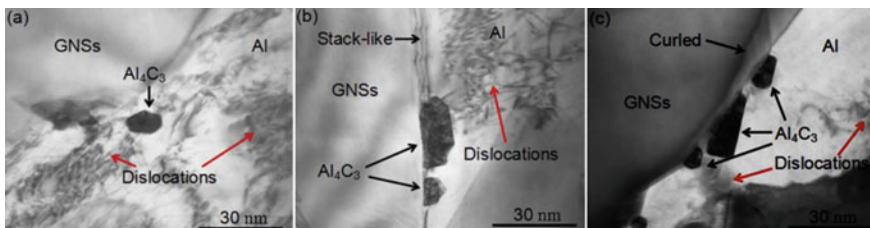


Fig. 1 Graphene-reinforced Al MMC. **a** 0.25% reinforced. **b** 0.5% reinforced. **c** 1% reinforced composites [22]

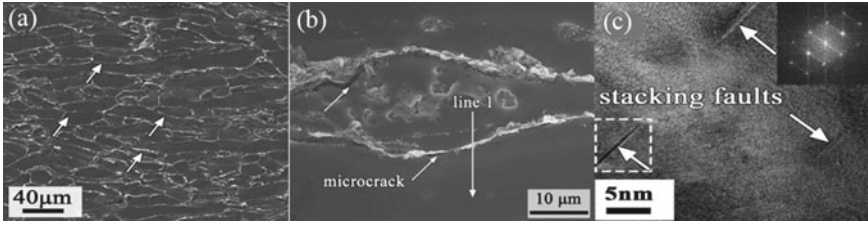


Fig. 2 a Uniform distribution of GNP in spark plasma sintered Al powder. b SEM image of composite along rolling direction. c Stacking faults in Al grain [23]

strength of the composite material. Nanotwin interface is also an important factor in altering the mechanical properties of the composite, and addition of graphene and rolling operations leads to generation of nanotwins in Al grains [23].

Graphene-reinforced Al composites are another trend in composites history because of its reinforcement strength (tensile strength—130GPa, elastic modulus—0.5–1 TPa). About 1 wt% reinforced graphene in Al matrix dispersed by magnetic stirring (ethanol as stirring medium) method after that cold compaction and sintering followed by hot extrusion techniques showed the mechanical properties better by 46% compared to unreinforced ones. Researches revealed that grain boundary pinning by graphene particles leads to high volume of grain boundaries which hinders the dislocation movements by this strength of the composite increases tremendously [24]. By adding graphene as reinforcement, good interface bond was formed with matrix material and Al_4C_3 compound formed at interface this phenomenon was increasing with graphene content leads to declining of its tensile strength, among the investigated reinforcement contents of 0.25, 0.5 and 1%, composite with lowest compounds formation shows better mechanical properties which is 0.25% and its tensile strength was 164 MPa [22]. By the addition of GNPs experimental density of the composite increases compared to its theoretical densities, it is because of the formation of Al oxides during sintering process. For 0.3% addition of graphene in Al matrix, there is an enhancement in UTS of 11.1%, in compression it was -7.8% and in Vickers hardness it was 11.8%. Thermal mismatch and hindered dislocations help in strengthening of composite, smaller the particle size greater the dislocation densities [21]. Few layers graphene (FLG) reinforced Al alloy shows tremendous increment in tensile strength from 350 to 700Mpa with a reinforcement content of 0.7% and elongation at failure is 4%. This was attributed to its large surface area enable to share its strength with the matrix material by effective load transfer mechanism, because of its high interfacial surface areas relation was established to predict the strength of composite as in Eq. (2) [25].

$$\sigma_c = V_r \left(\frac{S}{A} \right) \left(\frac{\tau_m}{2} \right) + \sigma_m V_m \quad (2)$$

where σ_c and σ_m = yield strength of composite and matrix, V_r and V_m = volume fraction of reinforcement and matrix, S = interfacial area, A = cross section area of FLG, τ_m = shear strength of the matrix.

GNP dispersed in Al matrix via ultrasonication and spark plasma sintering shows good dispersibility up to 1% content after those agglomerations are came in to effect due to their high surface energies, added GNP helps in pinning action of grain boundaries and restrict the grain growth while sintering process but after 3% reinforcement content average grain size increases and relative density decreases after 1% this was due to agglomeration effect. No intermetallic's were detected, this was due to low temperature and short time consolidation by spark plasma sintering process. Hardness was improved by 21.4% with 1% addition of GNP, but elastic modulus did not show any significant change, this was attributed to that major strengthening effect was by obstructing the dislocation movements rather than load transfer mechanism [26]. Another novel technique to disperse graphene in Al matrix was by coating Al particles with hexadecyl trimethyl ammonium bromide (CTAB) to obtain positive charge and graphene oxide with negative charge synthesized by modified hummers method, and then electrostatic self-assembly was used to combine graphene oxide aqueous dispersion with Al powder suspension to produce GO-Al particles. Another interesting phenomenon in this process is charge attraction between CTAB-Al powders and GO sheets which is greater than Vander Waals force makes uniform dispersion by adsorption of GO sheets on CTAB-Al particles. Structural integrity was also not affected by this process makes strength of the composite superior [27]. Another method to disperse graphene in molten Al was by preparing master alloy (Al-GNP) with graphene in it fabricated by ball milling and spark plasma sintering and then melting the master alloy along with Al melts which makes it to overcome difficulties in casting process along with subsequent rolling makes composite more strengthen and good interface bond strength. By rolling process grain refinement and GNP fibres are oriented in the rolled direction which captures the advantage of 2D graphene properties [23]. GNP dispersed by mechanical milling shows amorphous structure in the matrix material because of high impacts through ball milling defects density increases similar to this diamond and graphite also shows amorphous structures after 5000 h of milling time and in case of single walled carbon nanotube it is 50 h, compared to high energy ball milling low energy ball mills are advantageous in terms of structural integrity of the reinforcement. In the composite powder milling process, ductile phase of Al protects the GNP from collisions which delays the transformation time in to amorphous state [28]. Cold drawing also helps in dispersion of GNP effectively and creates good interface bond by eliminating GNP dense zones, but with increasing the content of GNP dispersion efficiency reduces. For 0.4% GNP after cold drawing, dense agglomerates breaks into fragments and dispersed along the drawing direction [29]. Corrosion resistance of Al-GNP composites decreases with increase in GNP content, added GNP acts as obstacles to continuous oxide film above Al particles cause initiation of corrosion from that spot. Generally, high corrosion potential and low corrosion current density represent good corrosion resistance to a material. In case of Al-GNP composites, tests revealed low corrosion resistance characteristics, this is due to cathodic behaviour of graphene particles with respect to matrix which

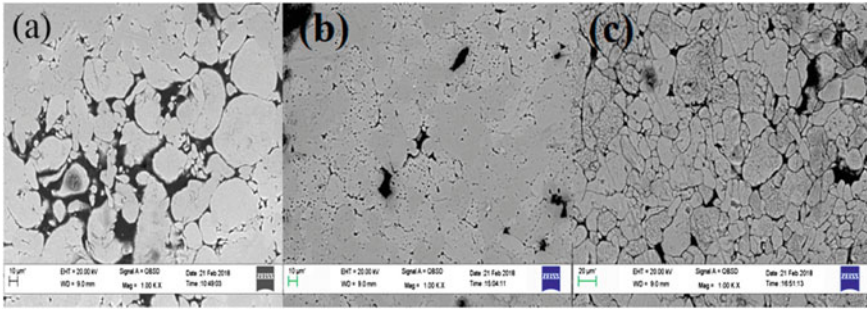


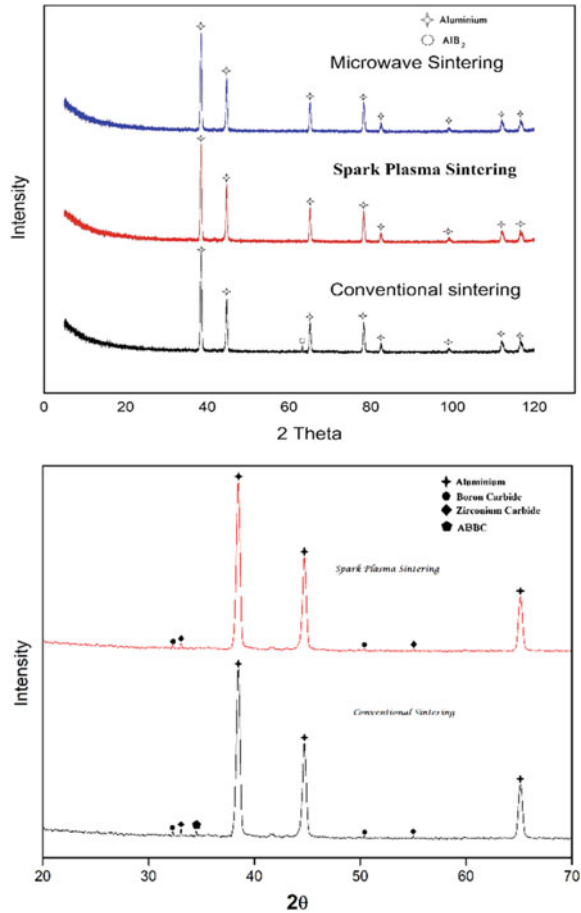
Fig. 3 SEM morphology of composites sintered by **a** conventional, **b** microwave and **c** spark plasma techniques [31]

leads to galvanic corrosion in electrolyte solution [30]. To reduce so many defects that caused by the conventional sintering processes researchers reported that microwave sintering helps in eliminating so many defects like low level intermetallic compounds generation and excellent mechanical properties. In this direction, Manohar et al. [31] conducted experiments on Al/B₄C composites with different sintering mechanisms. Microstructural tests of microwave and spark plasma sintered (SPS) composites revealed excellent increase in mechanical properties, as well as uniform distribution of reinforcements and clean interfaces without any detection of intermetallic phases through XRD analysis. Represents the XRD analysis of Al/B₄C composite subjected to different sintering mechanisms, no intermetallic's were detected in microwave and SPS composites, but AlB₂ intermetallic compound was detected in conventionally sintered composite. Fig. 3 shows the microstructural morphology of Al-B₄C composite subjected to different sintering mechanisms.

Low sintering temperatures, short sintering periods and rapid heating rates are all advantages of microwave sintering for improving the mechanical characteristics of composite materials. Experiments on AA7075/B₄C/ZrC hybrid nano composites revealed that those sintered using microwave method had improved mechanical properties and that no intermetallic compounds were discovered using XRD analysis, but Al₃BC intermetallic phase was detected in conventionally sintered composite. Formation of these brittle intermetallic phases degraded the mechanical properties of conventionally sintered composite. Addition of Nano ZrC particles and microwave sintering helped in enhanced mechanical properties [32]. In a similar manner, microwave sintering on AA7075/graphite/SiC hybrid composite showed excellent mechanical properties. As graphite and SiC ceramic particles are more respond to microwaves and have high magnetic permeabilities, so that resultant mechanical properties also showed superior enhancement. Additionally, strengthening mechanisms help in strengthening the composite material. Because of the temperature mismatch between the matrix and the reinforcement particles, Orowan

strengthening takes effect through appropriate dispersion of reinforcement particles and improved dislocation density strengthening. A schematic diagram representing enhanced dislocation strengthening is shown in Fig. 4 [33]. In this direction, several researchers investigated microwave sintering and the effect of different types of reinforcement particles on Al matrix composites. Different reinforcement particles include TiC [34], Al-Cu-Li particles [35], Inconel625 [36], CeO₂ [37], SiC [38], Aluminium/Tin-Bismuth [39], SiC-ZrO₂ [40], SiC-TiO₂ [41], Si₃N₄ [42], NiTi (Nitinol) [43] and Y₂O₃ [44–46] (Fig. 5).

Fig. 4 XRD analysis of Al composites subjected to different sintering techniques



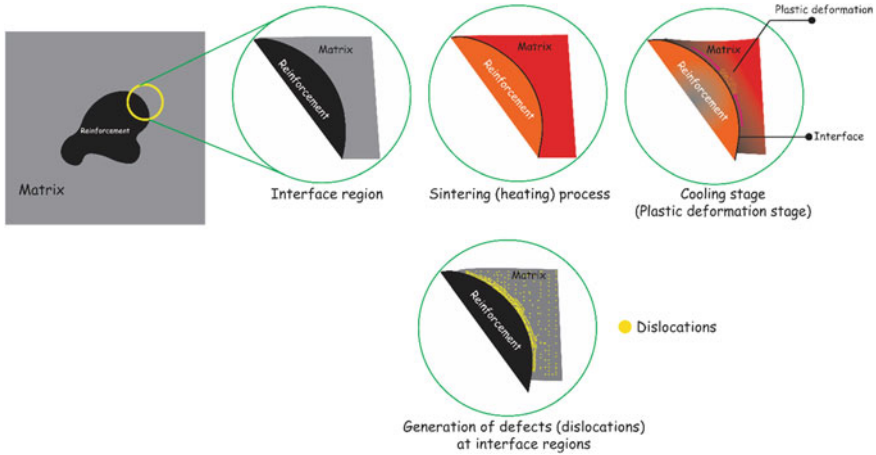


Fig. 5 Schematic diagram showing the enhanced dislocation density strengthening mechanism [33]

3 Conclusion

From the above observations and literature, it is observed that majority of the works reported by adding different reinforcement materials and fabricated through conventional sintering process showed enhanced mechanical behaviour. Intermetallic compounds generation was reported in majority of works, where fabrication process was performed through conventional sintering process. When comparing micro and nanocomposites, nanocomposites showed superior mechanical performance due to their high surface--to-volume ratios. To enhance the performance of the composites and to retain the ductility nature of the composite materials, researchers choose advanced sintering mechanisms like microwave sintering and spark plasma sintering (SPS) as alternative to conventional sintering process. Some investigators reported that implementation of microwave sintering is recommended in case of hybrid nanocomposite where chances for the formation of intermetallic compounds.

References

1. Manohar G, Dey A, Pandey KM, Maity SR (2018) Fabrication of metal matrix composites by powder metallurgy: a review. In: AIP conference proceedings, vol 1952. American Institute of Physics Inc. <https://doi.org/10.1063/1.5032003>
2. G Manohar KM Pandey SR Maity 2020 Aluminium (AA7075) metal matrix composite reinforced with B 4 C nano particles and effect of individual alloying elements in Al fabricated by powder metallurgy techniques J Phys: Conf Ser 1451 012024 <https://doi.org/10.1088/1742-6596/1451/1/012024>
3. Manohar G, Pandey KM, Maity SR (2020) Effect of china clay on mechanical properties of AA7075/B4C hybrid composite fabricated by powder metallurgy techniques. In: Materials

- today: proceedings. <https://doi.org/10.1016/j.matpr.2020.10.740>
4. A Tan J Teng X Zeng D Fu H Zhang 2017 Fabrication of aluminium matrix hybrid composites reinforced with SiC microparticles and TiB₂ nanoparticles by powder metallurgy Powder Metall 60 1 66 72 <https://doi.org/10.1080/00325899.2016.1274816>
 5. Manohar G, Maity SR, Pandey KM (2021) Effect of Sintering temperatures on mechanical properties of AA7075/B4C/graphite hybrid composite fabricated by powder metallurgy techniques. In: Pandey KM, Misra RD, Patowari PK, Dixit US (eds) Recent advances in mechanical engineering. Singapore, Springer Singapore, pp 343–350
 6. Manohar G, Pandey KM, Ranjan Maity S (2020) Effect of compaction pressure on mechanical properties of AA7075/B4C/graphite hybrid composite fabricated by powder metallurgy techniques. In: Materials today: proceedings. <https://doi.org/10.1016/j.matpr.2020.05.194>
 7. Manohar G, Pandey KM, Maity SR (2021) Effect of processing parameters on mechanical properties of Al7175/Boron Carbide (B4C) composite fabricated by powder metallurgy techniques. In: Materials, computer engineering and education technology, vol 105. Trans Tech Publications Ltd, pp 8–16
 8. R Harichandran N Selvakumar 2016 Effect of nano/micro B4C particles on the mechanical properties of aluminium metal matrix composites fabricated by ultrasonic cavitation-assisted solidification process Archiv Civ Mech Eng 16 1 147 158 <https://doi.org/10.1016/j.acme.2015.07.001>
 9. VSS Venkatesh AB Deoghare 2021 Effect of particulate type reinforcements on mechanical and tribological behavior of aluminium metal matrix composites: a review KM Pandey RD Misra PK Patowari US Dixit Eds Recent advances in mechanical engineering Springer Singapore Singapore 295 303
 10. CYH Lim SC Lim M Gupta 2003 Wear behaviour of SiCp-reinforced magnesium matrix composites Wear 255 1–6 629 637 [https://doi.org/10.1016/S0043-1648\(03\)00121-2](https://doi.org/10.1016/S0043-1648(03)00121-2)
 11. E Ghasali M Alizadeh T Ebadzadeh AH Pakseresht A Rahbari 2015 Investigation on microstructural and mechanical properties of B4C-aluminum matrix composites prepared by microwave sintering J Mater Res Technol 4 411 415 <https://doi.org/10.1016/j.jmrt.2015.02.005>
 12. AE Nassar EE Nassar 2017 Properties of aluminum matrix Nano composites prepared by powder metallurgy processing J King Saud Univ Eng Sci 29 295 299 <https://doi.org/10.1016/j.jksues.2015.11.001>
 13. Liu R, Wu C, Zhang J, Luo G, Shen Q and Zhang L 2018 Microstructure and mechanical behaviors of the ultrafine grained AA7075/B4C composites synthesized via one-step consolidation. J Alloys Compd 748:737–44. <https://doi.org/10.1016/j.jallcom.2018.03.152>
 14. A Alizadeh E Taheri-Nassaj HR Baharvandi 2011 Preparation and investigation of Al-4 wt% B4C nanocomposite powders using mechanical milling Bull Mater Sci 34 1039 1048 <https://doi.org/10.1007/s12034-011-0158-5>
 15. H Alihosseini K Dehghani J Kamali 2017 Microstructure characterization, mechanical properties, compressibility and sintering behavior of Al-B4C nanocomposite powders Adv Powder Technol 28 2126 2134 <https://doi.org/10.1016/j.appt.2017.05.019>
 16. Atrian A, Majzoobi G (2015) Characterization of Al7075-B 4 C composite fabricated by powder compaction techniques under different 1–11; Vanmeensel K, Laptev A, Hennicke J, Vleugels J and Van Der Biest O (2005) Modelling of the temperature distribution during field assisted sintering Acta Mater 53:4379–88. <https://doi.org/10.1016/j.actamat.2005.05.042>
 17. Javdani A, Daei-Sorkhabi AH (2018) Microstructural and mechanical behavior of blended powder semisolid formed Al7075/B4C composites under different experimental conditions. Trans Nonferrous Met Soc China (English Ed. 28 1298–310). [https://doi.org/10.1016/S1003-6326\(18\)64767-3](https://doi.org/10.1016/S1003-6326(18)64767-3)
 18. Ş Karabulut U Gökmen H Çinici 2016 Study on the mechanical and drilling properties of AA7039 composites reinforced with Al₂O₃/B4C/SiC particles Compos Part B Eng 93 43 55 <https://doi.org/10.1016/j.compositesb.2016.02.054>
 19. S Ozkaya A Canakci 2016 Effect of the B4C content and the milling time on the synthesis, consolidation and mechanical properties of AlCuMg-B4C nanocomposites synthesized by mechanical milling Powder Technol 297 8 16 <https://doi.org/10.1016/j.powtec.2016.04.004>

20. L Zhang Z Wang Q Li W Junyan G Shi F Qi X Zhou 2018 Microtopography and mechanical properties of vacuum hot pressing Al/B4C composites *Ceramic Int* 44 3048 3055
21. M Rashad F Pan A Tang M Asif 2014 Effect of graphene nanoplatelets addition on mechanical properties of pure aluminium using a semi-powder method *Prog Nat Sci Mater Int* 24 101 108
22. G Li B Xiong 2017 Effects of graphene content on microstructure and tensile property of graphene-nanosheets/aluminium composites *J Alloy Compd* 697 31 36
23. M Li 2018 Microstructure evolution and properties of graphene nanoplatelets reinforced aluminium matrix composites *Mater Charact* 140 172 178
24. Niteesh Kumar SJ, Keshamurthy R, Haseebuddin MR, Praveennath, Koppad G (2017) Mechanical properties of aluminium-graphene composite synthesized by powder metallurgy and hot extrusion. *Trans Indian Inst Met* 605–613
25. SE Shin DH Bae 2015 Deformation behaviour of aluminium alloy matrix composites reinforced with few-layer graphene *Compos Part A* 78 42 47
26. A Bisht 2017 Strengthening mechanism in graphene nanoplatelets reinforced aluminium composite fabricated through spark plasma sintering *Mater Sci Eng A* 695 20 28
27. X Gao 2016 Preparation and tensile properties of homogeneously dispersed graphene reinforced aluminum matrix composites *Mater Des* 94 54 60
28. R Perez-Bustamante 2014 Microstructural and hardness behaviour of graphene-nanoplatelets/aluminum composites synthesized by mechanical alloying *J Alloys Compd* 615 S578 S582
29. J Li X Zhang L Geng 2018 Improving graphene distribution and mechanical properties of GNP/Al composites by cold drawing *Mater Des* 144 159 168
30. M Rashad 2015 Investigation on microstructural, mechanical and electrochemical properties of aluminium composites reinforced with graphene nanoplates *Prog Nat Sci Mater Int* 25 460 470
31. G Manohar KM Pandey SR Maity 2021 Effect of sintering mechanisms on mechanical properties of AA7075/B4C composite fabricated by powder metallurgy techniques *Ceram Int* 47 11 15147 15154 <https://doi.org/10.1016/j.ceramint.2021.02.073>
32. G Manohar KM Pandey SR Maity 2021 Effect of microwave sintering on the microstructure and mechanical properties of AA7075/B4C/ZrC hybrid nano composite fabricated by powder metallurgy techniques *Ceram Int* 47 23 32610 32618 <https://doi.org/10.1016/j.ceramint.2021.08.156>
33. G Manohar SR Maity KM Pandey 2021 Microstructural and mechanical properties of microwave sintered AA7075/Graphite/SiC hybrid composite fabricated by powder metallurgy techniques *SILICON* <https://doi.org/10.1007/s12633-021-01299-7>
34. MP Reddy MA Himyan F Ubaid RA Shakoor M Vyasraj P Gururaj M Yusuf AMA Mohamed M Gupta 2018 Enhancing thermal and mechanical response of aluminum using nanolength scale TiC ceramic reinforcement *Ceram Int* 44 8 9247 9254 <https://doi.org/10.1016/j.ceramint.2018.02.135>
35. MP Reddy V Manakari G Parande RA Shakoor AMA Mohamed M Gupta 2019 Structural, mechanical and thermal characteristics of Al-Cu-Li particle reinforced Al-matrix composites synthesized by microwave sintering and hot extrusion *Compos Part B: Eng* 164 June 2018 485 492 <https://doi.org/10.1016/j.compositesb.2019.01.063>
36. MR Mattli A Khan PR Matli M Yusuf AA Ashraf RA Shakoor M Gupta 2020 Effect of Inconel625 particles on the microstructural, mechanical, and thermal properties of Al-Inconel625 composites *Mater Today Commun* 25 March 101564 <https://doi.org/10.1016/j.mtcomm.2020.101564>
37. H Mohammed MP Reddy F Ubaid A Shakoor AMA Mohamed 2018 Structural and mechanical properties of CeO2 reinforced Al matrix nanocomposites *Adv Mater Lett* 9 8 602 605 <https://doi.org/10.5185/amlett.2018.2030>
38. MP Reddy RA Shakoor G Parande V Manakari F Ubaid AMA Mohamed M Gupta 2017 Enhanced performance of nano-sized SiC reinforced Al metal matrix nanocomposites synthesized through microwave sintering and hot extrusion techniques *Prog Nat Sci: Mater Int* 27 5 606 614 <https://doi.org/10.1016/j.pnsc.2017.08.015>

39. Khan A, Matli PR, Nawaz M, Mattli MR, Parande G, Manakari V, Shakoor A, Aljaber AS, Gupta M (2020) Microstructure and mechanical behavior of hot extruded aluminum/tin-bismuth composites produced by powder metallurgy. *Appl Sci* (Switzerland), 10(8). <https://doi.org/10.3390/APP10082812>
40. A Khan MW Abdelrazeq MR Mattli MM Yusuf A Alashraf PR Matli RA Shakoor 2020 Structural and mechanical properties of Al-SiC-ZrO₂ nanocomposites fabricated by microwave sintering technique *Curr Comput-Aided Drug Des* 10 10 1 12 <https://doi.org/10.3390/cryst10100904>
41. Mattli MR, Matli PR, Khan A, Abdelatty RH, Yusuf M, Ashraf A Al, Kotalo RG, Shakoor RA (2021) Study of microstructural and mechanical properties of al/sic/tio₂ hybrid nanocomposites developed by microwave sintering. *Crystals* 11(9). <https://doi.org/10.3390/cryst11091078>
42. PR Matli F Ubaid RA Shakoor G Parande V Manakari M Yusuf AM Amer Mohamed M Gupta 2017 Improved properties of Al-Si₃N₄ nanocomposites fabricated through a microwave sintering and hot extrusion process *RSC Adv* 7 55 34401 34410 <https://doi.org/10.1039/c7ra04148a>
43. PR Matli V Manakari G Parande MR Mattli RA Shakoor M Gupta 2020 Improving mechanical, thermal and damping properties of niti (Nitinol) reinforced aluminum nanocomposites *J Compos Sci* 4 1 18 21 <https://doi.org/10.3390/jcs4010019>
44. MR Mattli A Shakoor PR Matli AMA Mohamed 2019 Microstructure and compressive behavior of Al-Y₂O₃ nanocomposites prepared by microwave-assisted mechanical alloying *Metals* 9 4 1 9 <https://doi.org/10.3390/met9040414>
45. Manohar G, Pandey KM and Maity SR (2022) Effect of variations in microwave processing temperatures on microstructural and mechanical properties of AA7075/SiC/Graphite hybrid composite fabricated by powder metallurgy techniques silicon 15–7. <https://doi.org/10.1007/s12633-021-01554-x>
46. G Manohar KM Pandey SR Maity 2021 Characterization of boron carbide (B₄C) particle reinforced aluminium metal matrix composites fabricated by powder metallurgy techniques—a review *Mater Today Proc* 45 6882 6888 <https://doi.org/10.1016/j.matpr.2020.12.1087>

Processing Techniques of Magnesium Matrix Composites and Its Heat Treatment—A Review



Manan Shah, Ayush Pandya, Bhingole Pramod, and Neeraj Srivastava

Abstract The present study covers the different processes to manufacture different magnesium matrix composites (MMCs) and different conditions for its heat treatment. Based on diverse researches taken place in this area, this study depicts the effects of T4 and T6 heat treatment conditions on different magnesium MMCs on microstructure, various mechanical properties like tensile strength, ductility, hardness, damping capacity and wear resistance.

Keywords Magnesium metal matrix composites · Heat treatment · Microstructure · Processing techniques

1 Introduction

In the present era, the demand for lightweight materials has increased in various sectors of industries. Magnesium, being one of the lightest in alkaline earth metals, has potential in its widespread applications. Also, magnesium, which is having two-third of its density that of aluminium, has been weight-saving material for many industries [1]. Magnesium has some limitations like high flammability, low corrosion and wear resistance. Some alloying elements like aluminium (Al), zinc (Zn), manganese (Mn), and zirconium (Zr) are added to pure magnesium metal for overcoming these limitations and improvements like increase in its castability, uniform grain size, corrosion resistance and machinability have been observed [2]. Magnesium alloys are having low density, high strength to weight ratio and high stiffness

M. Shah · A. Pandya

B-Tech-Mechanical Engineering, Institute of Infrastructure Technology Research and Management, Ahmedabad, India

B. Pramod (✉)

Mechanical and Aerospace Engineering Department, Institute of Infrastructure Technology Research and Management, Ahmedabad, India

e-mail: pramod_bhingole@yahoo.com

N. Srivastava

Department of Mechanical Engineering, SVNIT Surat, Surat, India

compared to the aluminium alloy. Similarly, they have a higher thermal conductivity which is efficient in heat transfer applications along with properties like easily to recycle and hence they are environment friendly. Due to lightweight property of magnesium alloys, they become attractive structural material for military vehicles and heavy armours can be accommodated easily [1]. However, at elevated temperature applications, it has some limitations. With the increase in temperature, the strength and wear resistance properties of Mg alloys deteriorate, so it is not practical where higher temperatures are encountered [3]. Composites have shown some promising results and thus help overcome these shortcomings.

Generally, metal matrix composites (MMCs) of Mg alloys are developed with many reinforcements to improve related properties along with new and developed processing approaches. Some of the mechanical properties of Mg MMCs are discussed, which mainly included high strength, better resistance to wear, good damping characteristics with high stiffness and being lightweight it is suitable for majority of applications in automotive, defence and aerospace sectors [4, 5]. Different properties of reinforcements like size, shape, type, distribution, and bonding are responsible for varying mechanical properties of Mg MMCs. Most commonly, SiC, Al_2O_3 , CNTs, B_4C , fly ash, and TiC are reinforcements which played a major role in improving properties of the base metals like Mg and Al. Abhijit Dey et al. [3] had proposed a study of these reinforcements and their effects on the properties of Mg alloys. SiC particulates are used to increase the wear and creep resistance of Mg and its alloy [6]. The addition of CNTs in the Mg matrix showed improvement in properties like wettability and bonding strength of the composite. In hybrid composites, boron carbide (B_4C) particulates help in increasing the flexural strength and also the interfacial bonding strength. Some of the fibre reinforcements are responsible for increment in tensile strength of the material. An Al_2O_3 as reinforcement helped to improve the tensile strength, wear resistance and hardness of the materials [7]. Also, by the use of low-cost fly ash shows a noticeable effect on hardness, compressive strength, yield strength and tensile strength [8]. Fly ash is also recyclable and hence can be helpful in the sustainable development of Mg base composites [9]. In recent days, in situ composite making is also recognized effective processes for introducing nano-size reinforcement in the Mg alloy matrix [13].

However, many applications require contradicting combination of properties like high hardness and moderate ductility and are not quite possible with only preparation of Mg MMCs. Hence, to achieve these properties, homogenization in the microstructure of MMCs is quite promising. In line with lacuna observed and possible solutions were focused in this study in relation to Mg MMCs. This study focused on representative techniques reported in the field of Mg alloys MMCs preparation and improved mechanical properties by heat treatments and its effect on microstructure along with its properties were elaborated.

2 Techniques for Preparation for Mg MMCs

Many techniques such as powder metallurgy, spray deposition, disintegrated melt deposition, stir casting, electroplating, squeeze casting, in situ fabrication technique, selective laser melting, etc., are used for the processing of Mg matrix composites. However, this study focuses on those processes which are usually followed by heat treatment process of Mg MMCs.

2.1 *Disintegrated Melt Deposition (DMD) Technique*

DMD is a primary processing technique to make a composite. In this technique, firstly molten metal is taken in the crucible and a determined quantity of reinforcement particles are added, followed by continuous stirring for a predetermined time with the help of a mechanical stirrer. This slurry of composite is then poured or made to exit from the bottom of that crucible according to the facility available in the setup [11]. At the top surface of molten melts in the crucible, an inert atmosphere is maintained in a closed system. One or multiple jets of Argon or any other inert gas is positioned at the sides of the system between the top side of the crucible and substrate. When the slurry is poured from the bottom of the crucible, the jet of Argon gas is used to protect the melted slurry from oxidation [12]. The slurry is then collected in a metal substrate located at some fixed distance from the base of the crucible and allowed to solidify for a certain time. This process is generally followed by hot extrusion [11, 13].

This technique was used to fabricate Mg-SiC composite in which the molten slurry was disintegrated with two argon jets at a constant flow rate of $4.17 \times 10^{-4} \text{ m}^3/\text{s}$ [13]. Ugandhar et al. [14] also utilized the DMD technique to reinforce micro-sized SiC particulate in 99% pure magnesium to prepare Mg/SiC composite. This liquid state processing technique has some advantages over conventional methods such as oxide formation is negligible, the problem of settling of dense reinforcements at the bottom is resolved, and the solidification rates become higher due to this technique [11]. DMD technique with hot extrusion is effective in enhancing microstructural behaviour and helps in achieving higher tensile properties [12].

2.2 *Squeeze Casting*

Squeeze Casting is also an innovative method for fabricating composites, which generally is a combination of casting and forging methods. In this method, the base metal or alloy is melted in a furnace and the melt is transferred to bottom half of a die. The molten metal is then squeezed by the upper half of die with a certain amount

of hydraulic pressure [16]. The solidification of melt happens under pressure of the upper die [17, 18].

Balasubramanian [19] applied this technique with a squeeze pressure of 392.6 kN to prepare AZ91D/SiC Mg composite. Also, squeeze casting was used to manufacture short alumina fibre reinforced AZ91 matrix composite. An inert ($\text{CO}_2 + \text{SF}_6$) atmosphere was created for this technique for making alumina-AZ91 MMC by reinforcing safill alumina fibres [1]. Some salient features, which can be obtained using squeeze casting are good surface finish, the precision of dimensions in composite [17]. This technique also helps in reducing phase agglomerations [11], improving mechanical properties like toughness due to equiaxed microstructure [17].

2.3 *Selective Laser Melting (SLM)*

Selective laser melting is one of the most advanced and innovative methods of additive manufacturing, which is used to fabricate complex parts easily having approximately 99.9% density. It has been used for fabricating metals like aluminium, stainless steel, magnesium, and copper and has many related research opportunities [20]. In this technique, basically, a high-intensity laser is directed on the specific region of a very thin layer of powder. The particular path of the laser, which is predefined on the basis of the CAD model, melts the metal powder. Then another very thin layer of powder is overlapped on the first one and the laser melts the specific area similar to the first iteration. Likewise, the number of layers is being overlapped and the high-intensity laser continues to melt the metal powder. During the successive iterations, the heat produced by the laser to melt the particular layer also fuses the two layers leading to the dense product. This whole process is being done in an inert atmosphere only.

Wang et al. [21] used this SLM technique to fabricate TiB_2 reinforced Al-Cu-Mg-Si composite, in which TiB_2 particles were rigorously mixed with Al-Cu-Mg-Si alloy powder using a drum hoop mixer. With a scanning speed of 165 mm/s and thickness of layer as 0.04 mm as optimized parameters, SLM was used to prepare rectangular specimens of this composite under argon atmosphere. Similarly, bulk magnesium parts are being produced with the SLM technique, which has good corrosion resistance and superior mechanical properties [22]. It was noticed that with an increase in laser intensity, the density of the sample increases and the microstructure of sample is enhanced with the refinement in grains using SLM [23]. While studying magnesium powder, Mojtaba et al. [24] concluded that magnesium powder evaporates vigorously, and there is a development of micro cracks in a sample due to quick oxidation of magnesium during SLM.

2.4 Stir Casting

One of the easiest to use and economical methods for the preparation of composite is Stir Casting [25]. For stir casting, firstly the base matrix of magnesium alloy or pure magnesium is melted at very high temperatures in an electric furnace. To avoid the oxide formation and agglomeration of reinforcements due to high-temperature differences, reinforcements are preheated. Then the preheated reinforcements are added to the molten base matrix. For homogenous mixing of reinforcements particulates, a mechanical stirrer is used. The most mechanical stirrers are made of graphite material to withstand high-temperature conditions [26, 27]. The mixture is stirred for a certain time period with a specified speed while keeping the stirrer below the surface of the molten matrix [25]. After that, the cast is allowed to solidify and then quenched in liquid after some time. This whole process is done in a protective atmosphere of inert gas argon or in a $\text{CO}_2 + \text{SF}_6$ atmosphere.

Anil Kumar et al. [26] used this method to fabricate SiC reinforced AZ91 composite in a vacuum chamber. This method has some limitations when performed in inadequate controlled protective environment. There are some problems which occur while using this technique, which mainly includes entrapment of gas into melt and also slag formation which may lead to micro cracks in composite during solidification [11]. Some unavoidable chemical interactions may also take place at the interface. Also, one of the common defects encountered in the composite is formation of an oxide layer on the surface while using stir casting [26]. However, these limitations can be mitigated by using proper atmosphere and optimum parameters for Stir Casting.

3 Heat Treatment of Magnesium Matrix Composites

In the earlier section, it is observed that there were many techniques have been tried to manufacture magnesium matrix composites. To overcome some of the challenges like the non-homogenous distribution of reinforcements in the matrix can be faced while preparing the composite. One of the most common problems, as reported by researchers, is deterioration of mechanical properties of magnesium matrix composite due to agglomeration of reinforcements in the matrix [8]. Also, there is a need to improve some of the mechanical properties like hardness, ductility, tensile strength, damping behavior, corrosion resistance, etc., as per the demand of application of Mg composites. This need can be catered by performing heat treatment of Mg MMCs. The heat treatment comprises of two main parameters-Temperatures and Time.

The main objective of studying Mg MMCs heat treatment is to optimize the time and temperature of the heat treatment, thereby modifying the microstructure of composite to get the desired properties. Heat treatments are mainly classified as solutionizing or T4 heat treatment, annealing, age hardening or T6 heat treatment and

stress relieving in relation to Mg MMCs heat treatments. Out of the above-mentioned treatments, this section mainly focuses on T4 and T6 heat treatment of different magnesium MMCs and their effects on mechanical properties and microstructure.

3.1 T4 Heat Treatment

The T4 or solutionizing heat treatment is a method in which manufactured composites are heated to high temperatures, however, below their melting point and holding for a fixed interval of time. This is then followed by liquid quenching or air cooling according to requirements. During the heating cycle, the phases present in the microstructure of MMCs, get either dissolved or modified. The agglomerated particle reinforcements in the MMCs distribute evenly all over the matrix. Also, there are significant changes observed in grain morphology at certain high temperatures. In short homogenization of composite takes place. During the cooling cycle, the changes in the position of reinforcements or any modification in phases or grain structure freeze as it was in the heating cycle and no changes occur in the composite after the cooling stage at room temperatures. As observed in manufacturing in situ Mg MMCs [28], the mechanical properties of composites enhance or deteriorate due to these modifications in microstructure as per the time and temperature of the T4 heat treatment process.

In this section, the different conditions of heat treatments on different composites will be discussed based on some literature reviews. Basically, there are three temperatures ranges reported in the literature for heat treatment of Mg and its alloy MMCs. The first range is around the recrystallization temperature (± 150 °C). In this range, Mg/SiC [14], Mg-(5.6 Ti + 3 Al) [26] and AZ31-Al₂O₃-Cu [30] were isothermally heat treated for 5 h. The second temperature range is around 400–420 °C and generally, at this temperature range, the heat treatment time is much higher for about 16–24 h. It was reported that Al₂O₃p/AZ91D [31], SiC/AZ61 [32] and CNT/AZ31 [33] are the Mg MMCs treated around this temperature range for a period of 16–24 h. The last temperature range is around 520–580 °C, which is very close to the melting point of magnesium metal. Liu et al. [34] reinforced fly ash cenospheres in AZ91D alloy and performed its heat treatment at 520–580 °C for 40 min. The T4 heat treatment conditions applied and processing techniques adopted for the fabrication of different Mg MMCs are summarized in the Table 1.

3.1.1 Effect of T4 Heat Treatment on Microstructure

As seen in Table 1, three different temperature ranges for T4 heat treatment of Mg MMCs were used. And for homogenizing Mg/SiC composite at 150 °C, it has been found that the grains are equiaxed [14]. Due to this low temperature, significant energy is not provided and thus migration of grain boundaries is not possible and so grain morphology does not change as seen in Mg/SiC composite microstructure

Table 1 Solution heat treatment (T4) of magnesium matrix composites

S No.	Composite	Base matrix	Reinforcements	Processing technique	Heat treatment (T4) temperature (°C)	Heat treatment (T4) time
1	Mg/SiC [14]	99% pure magnesium	0.6 μ m SiC	Disintegrated melt deposition	150	5 h
2	RZ5/TiB ₂ [28]	RZ5 alloy	4; 6 ;8% wt TiB ₂	In situ synthesis	330	2 h
3	Mg-(5.6 Ti + 3 Al) [29]	99% pure magnesium	Ti – 5.6% wt Al – 3% wt Al ₂ O ₃ – 2.5% wt	Disintegrated melt deposition	200	5 h
4	Al ₂ O ₃ p/AZ91D [31]	AZ91D	Al ₂ O ₃	Disintegrated melt deposition	415	16 h
5	SiC/AZ61 [32]	AZ61	10 μ m diameter SiCp	Stir casting	410	24 h
6	CNT/AZ31 [33]	AZ31	0–1% wt CNT	Stir casting	400	24 h
7	Fly Ash cenospheres/AZ91D [34]	AZ91D	Fly ash cenospheres	Stir casting	520 550 570 580	40 min
8	WC/AZ91 [35]	AZ91	1.5; 3% wt WC	Stir casting	420	10 h
9	AZ61/SiCp [36]	AZ61	0.5, 1, 2% wt SiCp	Melt stirring	400	10 h
10	SiCp/AZ80 [37]	AZ80	1% wt SiCp	Melt stirring	420	6 h
11	SiCw/AZ91 [38]	AZ91	SiCw	Squeeze casting	415	24 h
12	SiCp/AZ91 D [39]	AZ91	SiCp	Rheocasting	415	18 h
13	TiC/AZ91 [40]	AZ91	8% wt TiC	Remelting and dilution	420	–

[39] and the same microstructure change observed in Mg-(5.6 Ti + 3 Al) [29] Mg MMCs.

The solutionizing of composites around 420 °C leads to the dissolution of Mg₁₇Al₁₂ phase in the base matrix [32, 35, 36]. Also, the dendrite structure was eliminated, and secondary phases were found to be densely populated and distributed all over the matrix. A similar observation was reported after T4 Heat treatment in SiCp/AZ80 [37] composite for 6 h at 400 °C and SiC particles homogeneously distributed in the matrix. And when T4 heat treatment temperature increases around 420 °C, phases in the matrix precipitate slowly [35].

In continuation with the increase in temperature up to the eutectic point (520 °C), β phase along with eutectic phase dissolves and formation of tiny liquid droplets is

seen in the grain structure. Further increasing temperature up to 550 °C, the liquid phase increases and also they concluded that Mg₂Si phases changes to spheroidal structure from polygon at these higher temperatures were reported [34].

3.1.2 Effect of T4 Heat Treatment on Mechanical Properties

This section discusses the effects of T4 heat treatment on various mechanical properties of Mg MMCs. At recrystallization temperature, there is increment seen in tensile strength of Mg MMCs post heat treatment due to breakdown of secondary phases [14, 29]. Also, significant improvement was found in tensile strength at a temperature around 410 °C due to the homogenization of particles in the matrix [31, 36, 37]. And there is an increment in ductility of the composite because of the dissolution of brittle β phase [38]. The T4 heat treatment has an influence on the hardness of the Mg MMCs reported in the literature. It is observed that due to its solution hardening effect, microhardness increases rather but then due to combined effect of solutionizing and strain relaxation of reinforcement particles leads to a decrease in the interfacial hardness [39]. These facts were reported when as-cast condition AZ61 alloy was compared with SiC reinforced MMCs of AZ61 after T4 heat treatment [32]. Whereas marginal reduction is seen in hardness in Mg-(5.6 Ti + 3 Al) [29] and WC/AZ91 [35] MMCs post T4 heat treatment. Besides hardness and tensile properties, the damping capacity of composite also gets affected after heat treatment. As an example, the damping capacity of TiC/AZ91 composite improved as there was a decrease in activation energy by T4 heat treatment [40].

On solutionizing fly ash cenospheres/AZ91D composite at temperatures above 500 °C, it was found that damping capacities are dependent on strain rates. An improved damping capacity can be found out at temperatures around 520 °C when the strain rate is lesser than 8.8×10^{-5} and above that strain rate, and its damping capacity was found maximum at 580 °C. The dislocation damping is the main reason for higher damping capacities at 580 °C and interface damping is the cause for higher damping capacities at 520 °C [34]. Also, the wear rate was increased after T4 heat treatment of WC/AZ91 MMCs and the probable mechanism behind this was found out to be the third body abrasion [35].

3.2 T6 Heat (Age Hardening) Treatment

T6 or age hardening treatment is usually done after T4 heat treatment. In this, the composite is reheated up to lower temperatures than that in T4 treatment. Generally, after T4 treatment the hardness and strength of composite decreases, so to improve that, T6 heat treatment is done. The main mechanism behind increasing the hardness of composite is due to T6 heat treatment, the precipitation of phases occurs and are evenly distributed at elevated temperatures, thereby increasing the number of

Table 2 Ageing of different magnesium matrix composites

S No.	Composite	Base matrix	Reinforcements	Processing technique	Ageing temperature (°C)	Ageing time
1	RZ5/TiB ₂ [28]	RZ5 alloy	4; 6; 8% wt TiB ₂	In situ synthesis	180	16 h
2	AZ31-Al ₂ O ₃ -Cu [30]	AZ31	Nano Al ₂ O ₃ ; sub-micron Cu	Disintegrated melt deposition	150	5 h
3	Al ₂ O ₃ p/AZ91D [31]	AZ91D	Al ₂ O ₃	Disintegrated melt deposition	170	16–40 h
4	SiC/AZ61 [32]	AZ61	10 μm diameter SiCp	Stir casting	200	12–48 h
5	CNT/AZ31 [33]	AZ31	0–1% wt CNT	Stir casting	200	10 h
6	WC/AZ91 [35]	AZ91	1.5; 3% wt WC	Stir casting	175	20 h
7	SiCp/AZ80 [37]	AZ80	1% wt SiCp	Melt stirring	170	2–12 h
8	Nano SiC/AZ61 [41]	AZ61	1% wt nano SiC	Ultrasonic processing	200, 250, 300	70 h
9	Safill alumina short fibres/AM 100 [42]	AM100	Safill alumina short fibres	Squeeze casting	225	–
10	Safill alumina short fibres/ZC 63 [42]	ZC63	Safill alumina short fibres	Squeeze casting	190–210	–

dislocations causing an increase in the dislocation density in the matrix and hence leading to an increase in hardness of the composite.

For age hardening, generally, a temperature ranges of 170–210 °C is chosen. The ageing time varies as per the requirement of the properties of the individual composite. As it is reported by Lin et al. [31], ageing of Al₂O₃p/AZ91D composite for different intervals of time (16, 24, 32 and 40 h) and examined the effect of ageing at each time interval while SiCp/AZ80 was aged from 2–12 h [37]. Sometimes over ageing is done to verify the properties for a moderate period of time, and this time increase up to 70 h. The study of Nano, SiC/AZ61 was determined at temperature 200, 250 and 300 °C for 70 h each [41]. Likewise, different researches were carried out to achieve the desired properties of a different time and temperatures for optimizing T6 heat treatment for Mg MMCs and summarized in Table 2.

3.2.1 Effect of T6 Heat Treatment on Microstructure

As seen in the previous section, after T4 heat treatment, secondary β phase gets dissolved in the matrix but the age hardening of that composite after solutionizing

leads to uniform precipitation of it is seen [35]. The formation of $Mg_{17}Al_{12}$ precipitates in alumina fibres/AM100 composite and spheroidization of α -Mg phase of ZC63 Mg MMC was found near the grain boundaries after ageing.

At the start of ageing, discontinuous precipitates are seen, whereas nucleation of continuous precipitates starts near the grain boundary with the increase in temperature [42]. A similar phenomenon was observed of SiCp/AZ61 composite [32], where continuous lamellar structures of secondary phases started to form from discontinuous phases with an increase in ageing time. Also, it is seen that intermetallic phases get diffused at grain boundaries due to ageing [43] and also T6 heat treatment of CNT/AZ31 leads to refinement in its grain size and enhancing microstructure [33]. It was concluded that in AZ61 matrix, the distribution of precipitates is homogeneous and they are smaller in size at the optimal ageing time, but precipitates become coarser as the time of ageing increases up to 70 h [41].

3.2.2 Effect of T6 Heat Treatment on Mechanical Properties

This section depicts the effects of T6 heat treatment on various mechanical properties of different Mg MMCs. There is significant improvement seen in ultimate tensile strength in Al_2O_3 p/AZ91D [31] after T6 heat treatment. Due to marginal increase in grain size, ductility gets improved in AZ31- Al_2O_3 -Cu [30] MMC and reduction in inter particulate spacing led to increase in its UTS and yield strength. Also, in SiCp/AZ80 composite [34], highest yield strength and tensile strength is establishing at optimal ageing time of 10 hours. Further, T6 heat treatment has a major impact on hardness and is explained in AM100 composite, due to formation of β precipitates at grain boundaries leads to increase in hardness post ageing treatment. Also, it is observed that with the increase in ageing temperatures from 200 to 300 °C, hardness of the composite increased [42].

Huang et al. [37] and Lin et al. [31] also concluded that T6 heat treatment improves hardness of Mg MMCs. T6 treatment performed on WC/AZ91 Mg MMC after T4 treatment gives increment in hardness value by 30–40% was reported. The wear resistances can also be improved as the microstructure gets modified and moreover as there is diffusion in phases in aged castings [43]. Due to precipitation of β phase after ageing, improvement of 32% in wear resistance was observed in WC/AZ91 composite. It is explained that wear in T6 heat treated composite is based on ploughing mode when operated at moderate speed and low load conditions [35].

4 Conclusions

After reviewing the literature available on Mg MMCs processing and heat treatment the following conclusions have been derived:

1. Mg MMCs have the potential to be an attractive choice for automotive and due to their special properties like high strength to weight ratio, high stiffness and low density.
2. For the processing of Mg MMCs, various techniques were used and still needs improvement.
3. Heat treatment showed a promising effect on mechanical properties.
4. Heat treatments like T4 and T6 play a major role in modifying the microstructure and help in achieving the desired mechanical properties in the Mg MMCs.

References

1. Gupta N, Luong D, Kyu C (2012) Magnesium matrix composite foams—density, mechanical properties, and applications, *metals* 238–252
2. Habibnejad-Korayem M, Mahmudi R, Poole WJ (2009) Enhanced properties of Mg-based nano-composites reinforced with Al₂O₃ nano-particles. *Mater Sci Eng A* 519:198–203. <https://doi.org/10.1016/j.msea.2009.05.001>
3. Dey A, Krishna MP (2015) Magnesium metal matrix composites—a review. *Rev Adv Mater Sci* 42:58–67
4. Koli DK, Agnihotri G, Purohit R (2015) Advanced aluminium matrix composites: the critical need of automotive and aerospace engineering fields. *Mater Today: Proc* 2:3032–3041
5. Gui M, Li P, Han J (2003) Fabrication and characterization of cast magnesium matrix composites by vacuum stir casting process. *J Mater Eng Perform* 12:128–134. <https://doi.org/10.1361/105994903770343259>
6. Muley SV, Singh SP, Sinha P, Bhingole PP, Chaudhari GP (2014) Microstructural evolution in ultrasonically processed in situ AZ91 matrix composites and their mechanical and wear behaviour. *Mater Des* 53:475–481
7. Yadav SD, Bhingole PP, Chaudhari GP, Nath SK, Sommitsch C (2015) Hybrid processing of AZ91 Magnesium alloy/nano-Al₂O₃ composites. In: *Key engineering materials*. Trans Tech Publications, Switzerland, pp 651–653
8. Chand R, Swamy DR, Characterization of magnesium based fly-ash reinforced composite using powder metallurgy. *J Eng Res Appl* (full detail)
9. Qaflesh M, Kryeziu DR, Misini M, Aliko L (2013) Physical and mechanical properties of Fly ash of kosava BTTP for utilization as product for partial cement. *Int J Modern Eng Res (IJMER)* 3(6):3323–3327
10. Bhingole PP, Chaudhari GP, Nath SK (2014) Processing, microstructure and properties of ultrasonically processed in situ MgO–Al₂O₃–MgAl₂O₄ dispersed magnesium alloy composites. *Compos Part A: Appl Sci Manuf* 66
11. Jayalakshmi S, Arvind Singh R (2013) Synthesis of light metal nanocomposites: challenges and opportunities. *Indian J Adv Chem Sci* S1:283–288
12. Gupta M, Srivatsan TS (1999) Microstructure and grain growth behavior of an aluminum alloy metal matrix composite processed by disintegrated melt deposition. *J Mater Eng Perform* 8:473–478. <https://doi.org/10.1361/105994999770346792>
13. Gupta M, Lai M, Saravananathan D (2000) Synthesis, microstructure and properties characterization of disintegrated melt deposited Mg/SiC composites. *J Mater Sci* 35:2155–2165
14. Ugandhar S, Gupta M, Sinha SK (2006) Enhancing strength and ductility of Mg/SiC composites using recrystallization heat treatment. *Compos Struct* 72:266–272. <https://doi.org/10.1016/j.compstruct.2004.11.010>
15. Soon LP, Gupta M (2001) Synthesis and recyclability of Al/SiC and Mg/SiC composites using an innovative disintegrated melt deposition technique. *J Mater Sci Lett* 20:323–326. <https://doi.org/10.1023/A:1006717231509>

16. Balasubramanian I, Maheswaran R, Manikandan V (2018) Mechanical characterization and machining of squeeze cast acturing engineering society international conference, MESIC 2017, 28–3. In: 2nd international conference on materials manufacturing and design engineering, vol 20. Procedia Manufacturing, pp 97–105
17. Natrayan L, Senthil KM (2018) Study on squeeze casting of aluminum matrix composites—a review. *Adv Manuf Mater Sci* 75–83. https://doi.org/10.1007/978-3-319-76276-0_8
18. Bakkar A, Neubert V (2010) Corrosion characterisation of alumina–magnesium metal matrix composites. *Corrosion Sci* 49:1110–1130. <https://doi.org/10.1016/j.corsci.2006.07.002>
19. Purazrang K, Kainer KU, Mordike BL (1991) Fracture toughness behaviour of a magnesium alloy metal-matrix composite produced by the infiltration technique. *Composites* 22(6):456–462. [https://doi.org/10.1016/0010-4361\(91\)90205-U](https://doi.org/10.1016/0010-4361(91)90205-U)
20. Yap CY, Chua CK, Dong ZL (2015) Review of selective laser melting: materials and applications. *Appl Phys Rev* 2:041101
21. Wang P, Gammmer C (2018) A heat treatable TiB₂/Al-3.5Cu-1.5Mg-1Si composite fabricated by selective laser melting: microstructure, heat treatment and mechanical properties. *Compos Part B*. <https://doi.org/10.1016/j.compositesb.2018.04.026>
22. Manakari V, Parande G, Gupta M (2017) Selective laser melting of magnesium and magnesium alloy powders: a review. *Metals* 1–35. <https://doi.org/10.3390/met7010002>
23. Li R, Wang M (2017) Selective laser melting of a novel Sc and Zr modified Al-6.2 Mg alloy: processing, microstructure, and properties. *Powder Technol* 319:117–128. <https://doi.org/10.1016/j.powtec.2017.06.050>
24. Salehi M, Maleksaeedi S, Farnoush H (2018) An investigation into interaction between magnesium powder and Ar gas: implications for selective laser melting of magnesium. *Powder Technol* 333:252–261. <https://doi.org/10.1016/j.powtec.2018.04.026>
25. Shahin Soltani R, Zari Khosroshahi R, Mousavian RT (2017) Stir casting process for manufacture of Al–SiC composites. *Fac Eng Inf Sci: Part A Rare Metals* 36(7):581–590
26. Kumar A, Kumar S, Mukhopadhyay NK (2018) Introduction to magnesium alloy processing technology and development of low-cost stir casting process for magnesium alloy and its composites. *J Magnes Alloys* 6:245–254. <https://doi.org/10.1016/j.jma.2018.05.006>
27. Chauhan H, Irfan CA (2017) Variation of mechanical properties (tensile strength & microstructure) of Al 6061/(Al₂O₃ and fly-ash), hybrid metal matrix composite produced by stir casting. *Int Res J Eng Technol (IRJET)* 2407–2414
28. Meher A, Mahapatra MM, Samal P, Vundavili PR (2020) Abrasive wear behaviour of TiB₂ reinforced in-situ synthesized magnesium RZ5 alloy based metal matrix composites. *Met Mater Int*. <https://doi.org/10.1007/s12540-020-00746-1>
29. Sankaranarayanan S, Jayalakshmi S, Gupta M (2013) Effect of nano-Al₂O₃ addition and heat treatment on the microstructure and mechanical properties of Mg-(5.6Ti+3Al) composite. *Mater Character* 75:150–164. <https://doi.org/10.1016/j.matchar.2012.10.005>
30. Nguyen QB, Tun KS, Lim CYH (2013) Influence of Nano-alumina and sub-micron copper on mechanical properties of magnesium alloy AZ31. *Compos Part B* 55:486–491. <https://doi.org/10.1016/j.compositesb.2013.06.041>
31. Lin PC, Huang S-J, Hong P-S (2010) Formation of magnesium metal composites Al₂O₃/AZ91D and their mechanical properties after heat treatment. *Acta Metallurgica Slovaca* 16(4):237–245
32. Huang S-J, Ali AN (2017) Effects of heat treatment on the microstructure and microplastic deformation behavior of SiC particles reinforced AZ61 magnesium metal matrix composite. *Mater Sci Eng, A*. <https://doi.org/10.1016/j.msea.2017.11.020>
33. Abbas A, Huang S-J (2020) Qualitative and quantitative investigation of as-cast and Aged CNT/AZ31 metal matrix composites. *JOM* 78(6):2272–2282. <https://doi.org/10.1007/s11837-020-04114-7>
34. Liu EY, Yu SR (2018) Effects of semi-solid isothermal heat treatment on microstructures and damping capacities of fly ash cenosphere/AZ91D composites. *Acta Metallurgica Sinica (English Letters)*. <https://doi.org/10.1007/s40195-018-0722-8>
35. Karuppusamy P, Lingadurai K, Sivananth V (2020) Effects of T4 and T6 Heat treatments on the wear behaviour of WC-reinforced Mg alloy matrix composite. *Trans Indian Inst Met* 73(3):521–530

36. Zhao W, Huang S-J (2017) Particle size and particle percentage effect of AZ61/SiCp magnesium matrix micro-and nano-composites on their mechanical properties due to extrusion and subsequent annealing. *Metals* 7(293):1–15. <https://doi.org/10.3390/met7080293>
37. Huang S-J, Li S-R, Yan K-L (2013) Particle reinforcement of magnesium composites SiCp/AZ80 and their mechanical properties after heat treatment. *Kovove Mater* 51:45–52. https://doi.org/10.4149/km_2013_1_45
38. Zheng MY, Zhang WC, Wu K, Yao CK (2013) The deformation and fracture behavior of SiCw/AZ91 magnesium matrix composite during in-situ TEM straining. *J Mater Sci* 38:2647–2654. <https://doi.org/10.1023/A:1024486619379>
39. Poddar P, Mukherjee S, Sahoo KL (2009) The microstructure and mechanical properties of SiC reinforced magnesium based composites by rheocasting process. *J Mater Eng Perform* 18(7):849–855. <https://doi.org/10.1007/s11665-008-9334-1>
40. Xiuqing Z, Liao L, Naiheng M, Haowei W (2006) The effect of heat treatment on damping characterization of TiC/AZ91 Composite. *Mater Lett* 60:600–604. <https://doi.org/10.1016/j.matlet.2005.09.038>
41. Hong Y, Xiaowu H, Qiao N, Lei C (2011) Aging behavior of nano-SiCp reinforced AZ61 magnesium matrix composites. *China foundry* 8(3):269–273
42. Jayalakshmi S, Singh RA, Xizhang C, Konovalov S, Srivatsan TS, Seshan S, Gupta M (2020) Role of matrix microstructure in governing the mechanical behavior and corrosion response of two magnesium alloy metal matrix composites. *Jom* 72. <https://doi.org/10.1007/s11837-020-04166-9>
43. Huang S-J, Abbas A, Ballóková B (2019) Effect of CNT on microstructure, dry sliding wear and compressive mechanical properties of AZ31 magnesium alloy. *J Mater Res Technol* 8(5):4273–428. <https://doi.org/10.1016/J.JMRT.2019.07.037>

A Review on Heat Treatment of Magnesium Alloys and Its Effect on Various Properties



Ayush Pandya, Manan Shah, Bhingole Pramod, and Neeraj Srivastava

Abstract This study is based on literature reviews which mainly covers the available types of magnesium alloys and enhancement of their required properties with the help of heat treatments. The demand of magnesium alloys has significantly increased in various sectors due to their low density and higher specific strength characteristics. However, some of their properties Mg alloys show limitations in certain applications. These limitations can be mitigated by heat treatment of these alloys at optimized time and temperature conditions. A review of different heat treatments like T4, T5, and T6 is performed on these magnesium alloys, and its effects on microstructure and mechanical properties are thoroughly being discussed.

Keywords Magnesium alloys · Heat treatment · Age hardening · Solutionizing · Microstructure

1 Introduction

The reason for increasing popularity of magnesium and its alloys as an engineering material can be attributed to its low density and high specific strength. Apart from this, magnesium and its alloys also possess good castability, high specific stiffness, good machinability, good damping characteristics, and good recycle ability [1–6]. Due to their high specific strength, magnesium alloys have found applications in automobile, aircraft, and aerospace industries where weight reduction is a priority; besides this,

A. Pandya · M. Shah

B. Tech-Mechanical Engineering, Institute of Infrastructure Technology Research and Management, Ahmedabad, India

B. Pramod (✉)

Mechanical and Aerospace Engineering Department, Institute of Infrastructure Technology Research and Management, Ahmedabad, India

e-mail: pramod_bhingole@yahoo.com

N. Srivastava

Department of Mechanical Engineering, SVNIT Surat, Surat, India

© The Author(s), under exclusive license to Springer Nature Singapore Pte Ltd. 2023

B. Pramod P. et al. (eds.), *Advances in Material Science and Metallurgy*, Lecture Notes in Mechanical Engineering, https://doi.org/10.1007/978-981-19-4918-0_7

they are also used in electronics, medical, and civil construction applications [3–13]. However, their potential use is limited due to their lower mechanical properties like strength, fatigue properties, corrosion and wear resistance, cold workability and toughness, creep resistance, high reactivity, and strengthening response [1–4, 7, 10, 14]. These drawbacks and lower cost of aluminum alloys contribute to the preference of aluminum alloys over magnesium alloys [5]. For eliminating these drawbacks of magnesium alloys two primary methods: use of advanced fabrication techniques and heat treatment of magnesium alloys may be implemented. Conventionally, the magnesium alloys and their products are fabricated by various casting processes like sand casting and die casting and by forming processes like rolling, extrusion, and forging. They can also be processed by using advanced fabrication methods like squeeze casting, semi-solid casting, stir casting, spray forming, friction stir processing, equal channel angular processing, selective laser melting, and high strain rate forming processes [15–23]. Generally, fabricating magnesium alloys via these advanced processing techniques result in alloys having better properties compared to the conventionally processed alloys. However, the aim of this paper is to explain the various heat treatment processes used for magnesium alloys and the effect of these heat treatment processes on property enhancement of the magnesium alloys.

They can be broadly classified in two groups: cast magnesium alloys and wrought magnesium alloys [1]. The cast magnesium alloys can be classified into two groups that is rare earth free and rare earth magnesium alloys. Rare earth free cast Mg alloys mainly include Mg-Al-Zn-Mn, Mg-Al-Mn, Mg-Al-Si, Mg-Zn-Zr, Mg-Mn, and Mg-Zr alloys [1, 5, 24]. However, rare earth magnesium alloys mainly include Mg-RE-Zr and Mg-Al-RE alloys. Apart from these, many other alloying elements like Ca, Sb, Cu, Sr, Ce, Sc, Nd, Gd, and Th can also be added to magnesium for making an alloy [24]. AZ, AS, and AM alloy series are widely used as commercial Mg cast alloys. AZ91 is a very popular as Mg-Al-Zn cast alloy due to its high strength and good castability and is used extensively in the automobile industry [1, 2, 25, 26]. Commercial Mg-Al-Mn alloys that is AM60 and AM50 alloys have lesser strength compared to AZ91 but have higher ductility and toughness [5]. A major drawback of the AZ and AM magnesium alloys is that they form $Mg_{17}Al_{12}$ that is β phase, whose less thermal stability results in low creep properties, thus these alloys cannot be used for high-temperature applications [1, 2, 24]. Mg-RE alloys possess excellent mechanical properties at both ambient and elevated temperatures compared to rare earth free magnesium alloys [1, 2, 14]. The rare earth alloying elements Gd, Nd, Ce, and Y are generally used for magnesium alloys. These rare earth magnesium alloys fabricated using advanced processing techniques and treated with heat treatment give the best mechanical properties [3, 24]. However, due to the addition of the rare earth elements, their cost increases and they also have higher density compared to rare earth free magnesium alloys [2, 13, 25]. Therefore, Mg alloys with Si, Ca, Sr, Sb, and Sn as alloying elements are used instead of rare earth alloys for increasing the creep resistance and strength while making them more economical and maintaining the lower density of alloy [1, 24]. In automobile industries, cast alloys are preferred over wrought magnesium alloys because production of magnesium alloys by casting is faster, easier, and cheaper [2, 26]. Due to this, production and use in industry

for cast magnesium alloys are higher than for wrought magnesium alloys [1, 27]. Disadvantage of the cast alloys is that their mechanical properties are worse because of the internal porosities present due to the casting process, and this also reduces the heat treatment response of the cast alloys. For eliminating these drawbacks, advanced casting methods like semi-solid casting are also used [11].

Commercial wrought magnesium alloys mainly include AZ, ZK, and WE series alloys. Rare earth free wrought magnesium alloys mainly include Mg-Al-Zn, Mg-Al-Mn, Mg-Al-Si, Mg-Zn-Mn, and Mg-Zn-Ca alloys; rare earth wrought magnesium alloys mainly include Mg-Zn-RE and Mg-Zr-RE alloys [27]. AZ and AM series alloys like AZ31, AM50, and AM60 are among the most popular commercial magnesium wrought alloys due to their good strength, corrosion resistance, and ductility [28–30]. Most of the wrought magnesium alloys are preferred for structural applications overcast magnesium alloys; due to the porosity defects and less energy absorption ability, cast alloys are not preferred for structural and high-stress applications [2, 11, 26, 31]. The disadvantage of AZ and AM series wrought alloys is due to Mg₁₇Al₁₂ β phase, the creep resistance is poor which restricts them to be used in high-temperature applications. Rare earth wrought alloys similar to cast alloys provide superior properties at room and elevated temperatures, but due to the rare earth element addition, they are uneconomical and increase the density of the alloy [25]. Mg-Zn-Zr alloys possess high strength but have poor high-temperature mechanical properties due to the formation of MgZn₂ phase [27]. Alloys like Mg-Zn-Ca and Mg-Zn alloys with only trace quantities of rare earth elements have also been developed to get both high mechanical properties and reduced costs. Those, processed using advanced forming techniques combined with strengthening heat treatments, very high strength rare earth wrought magnesium alloys can be produced [25, 28, 32].

2 Heat Treatment of Magnesium Alloys

As explained in the earlier section, some of the disadvantages of magnesium alloys are less strength, less toughness, and less corrosion resistance. These disadvantages can be easily eliminated by heat-treating the magnesium alloy [7]. The main heat treatments of magnesium alloys include solutionizing (T4), artificial aging (T5), annealing, and stress relieving. Stress relieving and annealing are mainly used in wrought alloys to reduce stresses from forming processes and to allow the alloy to be worked further. Age hardening or T6 heat treatment is one of the most widely used methods to improve the mechanical properties of magnesium alloys. It is a combination of solutionizing and aging heat treatments [11, 31].

2.1 Solutionizing Heat Treatment

In solutionizing heat treatment for magnesium alloys also known as homogenizing or T4 heat treatment, in this treatment, they are heated to a predefined high temperature below its melting point and soaked for a particular time. Due to this the different phases present in the microstructure dissolve in the α -magnesium matrix; after this, the alloy is quenched which locks in the microstructure which was present at higher temperature [11, 31]. Now, the alloy will contain a α -magnesium matrix which is supersaturated with other alloying elements, since precipitates of other phases which were present before are now dissolved in the matrix. Now, there will be less restriction to the flow of dislocations in the material, which generally results in increase of ductility, elongation, and tensile properties of the alloy with a reduction in hardness.

There are various ranges of temperature for performing the solutionizing heat treatments. Generally, the temperature range of 413–420 °C is implemented for most AZ series cast alloys because of the $Mg_{17}Al_{12}$ β phase which can fully dissolve into the α -magnesium matrix above 413 °C [11]. The temperatures below 400 °C are usually applied for the cases in which only partial dissolution of phases are required and for wrought alloys in some cases [10, 11, 33]; this partial dissolution is done to maintain a good combination of ductility and strength in the alloy [10, 11]. Higher temperatures above 450 °C are generally used for rare earth alloys and other alloys which are meant to be more stable at elevated temperatures [30, 34]. The phases present in this type of alloys require a higher temperature to dissolve into the matrix, so for their solutionizing, high temperatures are required. While heating magnesium above 400 °C, magnesium can react with the oxygen present in the atmosphere and oxidize, therefore, contact with the atmosphere has to be prevented; this is mainly done by either providing a protective atmosphere or performing the heat treatment in a vacuum furnace. The Ar [35–37], CO_2 [32, 38], and other various gases and gas mixtures [11, 30, 39] have been implemented as protective atmospheres. Huang et al. [10] and Wang et al. [11] have used carbon powder on the surface to protect the alloy against the atmosphere. Various solutionizing treatment, one of the important parameter is treatment time, ranging from 10 to 48 h and that have been implemented by many researchers were summarized in Table 1. The time for which alloy has to be soaked depends on the composition and phases present in the alloy, the amount of phase dissolution required and the amount of grain growth required in the final microstructure.

2.1.1 Effect of Solutionizing Heat Treatment on Alloy Microstructure

Before the heat treatment of both cast and wrought magnesium alloys containing Al consists of the α -magnesium matrix and a $Mg_{17}Al_{12}$ β phase [11, 35, 36, 38–40]. The β phase is generally found to be distributed along the grain boundaries in the microstructure [36, 39, 40, 43]; some studies also found an $\alpha + \beta$ eutectic adjacent to the β phase [35, 39, 42]. Liu et al. [6] noticed that due to other aluminum-containing

Table 1 Summary of solution heat treatment parameters for different Magnesium alloys

S No.	Alloy	Fabrication and processing techniques	Solutionizing temperature (°C)	Solutionizing time (h)
1	AZ91D [35]	Casting	445	24
2	AZ91 [40]	Casting	420	48
3	Mg-5Al-0.5Ca [6]	Casting	415	0.25–48
4	Mg-6Gd-3Y-0.5Zr [30]	Low pressure sand casting	475–515	12
5	AZ91 [10]	Cast-spray formed	415 365	12 2
6	AZ91D [11]	Rheo die casting	413 365	24 2
7	AZ61-0.7Si [38]	Casting	420	Up to 48
8	AZ80 [33]	Extruded	360	12
9	Mg-3Nd-0.2Zn [41]	Casting	540	10
10	AZ91D [39]	Casting	413	16
11	AZ91D [42]	Casting	420	24
12	Mg-Al-Zn [36]	Casting	430	10
13	AZ61 [37]	Wrought	Up to 400	–

phase Al_2Ca in Mg-5Al-0.5Ca alloy, the amount of $Mg_{17}Al_{12}$ phase present in the microstructure decreases. Yang et al. [38] found that in AZ61-0.7Si alloy, along with the α and β phases, the Chinese script phase (Mg_2Si) was also present due to slow solidification rates. In various studies, it was found that the microstructure of the magnesium alloy before heat treatment consisted of the α -magnesium matrix and phases which contained the other alloying elements of the alloy in appropriated concentration [6, 30, 34, 38, 44]. AZ80 extruded alloy was found to have elongated α grains with band-shaped β $Mg_{17}Al_{12}$ and Mg-Al-Zn phases [33].

The microstructure is supposed to be more homogenized after the solution heat treatment due to the dissolution of phases into the α matrix. Most of the studies with alloys containing the β - $Mg_{17}Al_{12}$ phase found that β phase dissolves into the α matrix making a supersaturated α matrix with aluminum and only a trace quantity of β remains left mostly at the grain boundaries after solutionizing heat treatment [10, 32, 35, 36, 38–42]. Liu et al. [6] reported that due to the less content of β - $Mg_{17}Al_{12}$ in the as-cast microstructure of Mg-5Al-0.5Ca alloy, after the heat treatment of 1 h the β phase dissolved completely at 415 °C, and the Al_2Ca network breaks because of the dissolution of the Al_2Ca phase into the matrix and takes spherical shape, while the Ca content in the matrix increases. The solutionizing of AZ61-0.7Si alloy dissolved the β phase in the matrix. Although only a small amount of Al_2Si and Al-Mn phases was dissolved and the continuous Chinese script structure of the Mg_2Si broke into short poles and block shapes for heat treatment up to 48 h at 420 °C [38]. However, solution heat treatment of the Mg-6Gd-3Y-0.5Zr rare earth magnesium alloy at 190 °C and

12 h was able to dissolve almost all eutectic phases; increasing temperature above 500 °C and treatment time to 16 h resulted in grain growth while 475 °C temperature treatment was not able to dissolve the eutectic compounds [30]. As the solution time increases, the grain size was also found to increase due to the grain growth [11, 30, 32]. The atomic diffusion capacity is larger for extruded alloys compared to cast alloys, therefore, solutionizing is possible at relatively lower temperatures for extruded alloys compared with the cast alloys [32].

Effect of Solutionizing Heat Treatment on Alloy Properties

The solutionizing heat treatment generally increases the elongation [11, 30, 42, 45], while decreasing the hardness [6, 10]. Y. Wang et al. [11] and Q. Wang et al. [32] reported a decrease in tensile strength, while some other studies reported an increase of tensile strength from a solution heat treatment [36, 42, 45]. In Mg-Al alloys, brittleness of the β phase tends to reduce the ductility, however, it provides hardness to the alloy [6, 11, 44]; therefore, dissolution of the β phase during the solution heat treatment reduces the alloy's hardness and increases its ductility. As the solution treatment progresses, the β phase dissolves into the α matrix and the hardness of the alloy decreases; when β is completely dissolved, the hardness becomes almost constant with increasing treatment time [6, 10]. It was found that a solution heat treatment below 400 °C near solvus temperature can break up the β network without completely dissolving it. This results in an alloy with a good combination of strength and ductility from T4 heat treatment without aging [10, 11]. Wang et al. found an increase in impact toughness of Mg-6Gd-3Y-0.5Zr alloy with an increase in elongation and decrease in yield and ultimate tensile strength after solutionizing [30]. Yang et al. showed that for AZ61-0.7Si alloy due to the breaking of the Chinese script structure of the Mg_2Si phase, the solution heat treatment improved both hardness and tensile strength [38]. Zhao et al. found that due to the grain growth and dissolution of the β phase, the strength and elongation for extruded AZ80 alloy decreased after solution heat treatment [32]. Zhou et al. reported an increase in tensile strength, elongation, and hardness from solution heat treatment of the AZ91 alloy [42]. Dobrzański et al. showed that by reducing the cooling rate by using air and furnace cooling instead of water quenching after solution heat treatment of AZ91 alloy, the tensile strength increased while the elongation decreased with decreasing cooling rate [36].

2.1.2 Aging Heat Treatment

In artificial aging heat treatment T5, magnesium alloys are heated at relatively lower temperatures compared to solutionizing and then air-cooled. When this aging treatment is performed after T4 solutionizing heat treatment, it is called T6 age hardening or precipitation hardening heat treatment [11, 30]. Aging heat treatments are widely used to increase the hardness and strength of magnesium alloys. After the T4 heat treatment, the α matrix becomes supersaturated with other alloying elements; these

alloying elements start to precipitate out, on the other hand, it takes a long time in doing so which is called natural aging. In artificial aging due to the elevated temperatures, these precipitates now form faster compared to natural aging. The new distribution of these precipitates acts as obstacles to dislocation motion, which generally causes the alloy's hardness to increase [38]. A disadvantage of magnesium alloys is also that they have a worse precipitation hardening response compared to aluminum alloys [7].

The different aging temperatures used, produce different effects on the microstructure of different alloys; but as observed from Table 2, the temperature is generally kept below 250 °C for all magnesium alloys and at this relatively lower temperature compared to solutionizing heat treatment there is no need for using a protective atmosphere while performing the heat treatment. The aging time, however, depends on the extent of hardness and ductility required. Generally, with an increase in aging time, first the hardness increases, then reaches a peak value and then starts to decrease [11, 30, 32, 38]; therefore, for achieving the best hardness, the alloy has to be peak aged. Due to this, a lot of studies have focused on finding the optimum aging temperature or time that gives the best-desired properties [10, 11, 30, 32, 35, 38, 39].

Effect of Aging Heat Treatment on Alloy Microstructure

Aging in the T6 heat treatment causes the alloying elements which were dissolved during the solutionizing heat treatment to precipitate out in the form of different phases in the microstructure of the alloy. In the Mg-Al alloys, the β Mg₁₇Al₁₂ phase

Table 2 Aging heat treatment parameters for different magnesium alloys

S No.	Alloy	Fabrication and processing techniques	Aging temperature (°C)	Aging time (h)
1	AZ91D [35]	Casting	200	8,16,24
2	AZ91 [10]	Extruded-spray formed	175	Up to 36
3	Mg-6Gd-3Y-0.5Zr [30]	Low pressure sand casting	175,200,212,225	Up to 100
4	AZ91D [11]	Rheo die casting	216	144
5	AZ61-0.7Si [38]	Casting	180,200	Up to 24
6	AZ80 [33]	Extruded	150,190,230	24
7	Mg-3Nd-0.2Zn [34]	Casting	200	14
8	AZ91D [39]	Casting	168	4,8,12
9	AZ91D [42]	Casting	200	24
10	Mg-Al-Zn [36]	Casting	190	15
11	ZK60 [44]	Extruded	170	10
12	AZ91 [45]	Extruded	70	16
13	AZ91 [46]	Cast	175	16

precipitates in two forms, first the lamellar shaped discontinuous precipitates form along the grain boundaries and with increasing aging time, discontinuous precipitates cease to grow and the continuous precipitates start forming inside the grains in regions unoccupied by discontinuous precipitates [10, 11, 33, 39]. The discontinuous and continuous precipitates depend upon the aging temperature and the aluminum content in the α matrix; while with an increase of aging time, continuous and discontinuous precipitates grow occupying a larger area [10, 11, 33, 39]. In magnesium alloys, the β precipitates directly transform without any Guinier–Preston (GP) zones or intermediate phase and produces coarse discontinuous precipitates along the grain boundaries during the aging heat treatment; due to this their strengthening, response from aging treatment is lower compared to the aluminum alloys [10, 11, 32]. Huang, et al. reported that a heat treatment near the solvus temperature without solutionizing suppresses the discontinuous precipitates, and only continuous precipitates are observed in the microstructure [10]. Daziadon et al. showed that the microstructure of T6 treated AZ91 alloy contains precipitations that are more continuous with a more regular distribution compared with T5 heat-treated alloy and that both alloys contain discontinuous precipitates along the grain boundaries [46].

Effect of Aging Heat Treatment on Alloy Properties

The main objective behind performing the aging treatment on magnesium alloys is to increase the strength and hardness of the alloy [10]. Due to the aging treatment different phases, which were previously dissolved into the matrix, precipitate out as explained earlier, these fine precipitates at grain boundary try to hinder the motion of dislocations, which in turn increases the strength, and hardness of the material [38]. The aging heat treatment increases the hardness of a material [11, 30, 33, 36, 42, 45], and with an increase in the aging time, the hardness value first increases, then reaches a maximum peak value and after that starts decreasing [11, 30, 33, 38]. The aging heat treatment generally decreases the ductility and elongation of the alloy [10, 11, 30, 36, 42]. Generally, the strengthening effect given by the fine precipitates is better compared to the coarse precipitates, but finer precipitates also tend to reduce the ductility of the alloy [10]. The aging heat treatment was also found to increase the tensile properties of the alloy in most of the studies [30, 36, 38, 42, 45]; however, aging caused an increase in ultimate tensile strength and a decrease in yield strength of Rheo die-cast AZ91 alloy [11]. An increase in fatigue strength, hardness and strength with a reduction in elongation was also found for T6 treated AZ91 alloy [42]. The aging treatment can increase the hardness, tensile strength, fracture toughness, and impact toughness for the Mg-6Gd-3Y-0.5Zr alloy but with a reduction in elongation; they also showed that impact toughness, tensile strength, and elongation had an inverse trend with hardness while the hardness decreased with an increase in aging temperature [30]. Increasing the aging temperature can accelerate the aging response of an alloy; they also reported that T5 heat treatment for extruded AZ80 alloy gives best tensile strength but worst elongation, while T6 heat treatment gives a good combination of strength and elongation [33]. The T6 treatment

of wrought and cast AZ91 alloys, respectively, gives better mechanical properties compared to the T5 heat treatment for the same aging time and temperatures used [30, 40]. And for extruded ZK60 alloy, the tensile strength and yield strength were higher for T5 heat treatment compared to T6 heat treatment while the elongation was lower [44].

3 Conclusions

1. Heat treatment of the magnesium alloys can eliminate some of the disadvantages and improves the properties of magnesium alloys. The heat treatments of the magnesium alloys mainly include the T4 solutionizing heat treatment, T5 aging heat treatment, and the T6 heat treatment.
2. In the T4 heat treatment, alloy is heated and soaked at a high temperature to dissolve the phases present in its microstructure, which increases the alloy's ductility and elongation at a sacrifice of its hardness.
3. T5 and T6 heat treatments are done to increase the hardness and strength of the alloy. In T5 heat treat, the alloy is heated at a relatively lower temperature compared to the T4 heat treatment; in the T6 heat treatment, the same T5 treatment is applied to the already T4 treated alloy.
4. T5 and T6 treatments cause the phases to precipitate out more in the microstructure, which increases the strength and hardness of the alloy with a decrease in elongation.
5. T5 and T6 heat treatments produce different effects for different alloys but generally T6 heat treatment gives better mechanical properties due to the more homogeneously spread precipitates compared with the T5 treatment.

References

1. Yang Z, Li JP, Zhang JX, Lorimer GW, Robson J (2008) Review on research and development of magnesium alloys. *Acta Metallurgica Sinica (English Letters)* 21:313–328. [https://doi.org/10.1016/S1006-7191\(08\)60054-X](https://doi.org/10.1016/S1006-7191(08)60054-X)
2. Kemal KM (2008) Magnesium and its alloys applications in automotive industry. *Int J Adv Manuf Technol* 39:851–865. <https://doi.org/10.1007/s00170-007-1279-2>
3. Luo Q, Guo Y, Liu B, Feng Y, Zhang J, Li Q, Chou K (2020) Thermodynamics and kinetics of phase transformation in rare earth-magnesium alloys: a critical review. *J Mater Sci Technol* 44:171–190. <https://doi.org/10.1016/j.jmst.2020.01.022>
4. Mordike BL, Ebert T (2001) Magnesium: properties-applications-potential. *Mater Sci Eng, A* 302:37–45. [https://doi.org/10.1016/S0921-5093\(00\)01351-4](https://doi.org/10.1016/S0921-5093(00)01351-4)
5. Pan F, Yang M, Chen X (2016) A Review on casting magnesium alloys: modification of commercial alloys and development of new alloys. *J Mater Sci Technol* 32:1211–1221. <https://doi.org/10.1016/j.jmst.2016.07.001>

6. Manping L, Qudong W, Liu Z, Yuan G, Wu G, Zhu Y, Ding W (2002) Behaviour of Mg-Al-Ca alloy during solution heat treatment at 415 °C. *J Mater Sci Lett* 21:1281–1283. <https://doi.org/10.1023/A:1016567421956>
7. Cepeda-Jiménez CM, Castillo-Rodríguez M, Pérez-Prado MT (2019) Origin of the low precipitation hardening in magnesium alloys. *Acta Mater* 165:164–176. <https://doi.org/10.1016/j.actamat.2018.11.044>
8. Pan H, Ren Y, Fu H, Zhao H, Wang L, Meng X, Qin G (2016) Recent developments in rare-earth free wrought magnesium alloys having high strength: a review. *J Alloys Comp* 663:321–331. <https://doi.org/10.1016/j.jallcom.2015.12.057>
9. Leszek D, Tański T, Čížek L (2007) Heat treatment impact on the structure of die-cast magnesium alloys. *J Achiev Mater Manuf Eng* 20:431–434
10. Huang J, Yu H, Li Y, Cui H, He J, Zhang J (2009) Precipitation behaviours of spray formed AZ91 magnesium alloy during heat treatment and their strengthening effect. *Mater Des* 30:440–444. <https://doi.org/10.1016/j.matdes.2008.06.001>
11. Wang Y, Liu G, Fan Z (2006) Microstructural evolution of rheo-diecast AZ91D magnesium alloy during heat treatment. *Acta Mater* 54:689–699. <https://doi.org/10.1016/j.actamat.2005.09.033>
12. Tomasz R, Andrzej K (2007) Microstructure of WE43 casting magnesium alloy. *J Achiev Mater Manuf Eng* 21:31–34
13. Bhingole PP, Chaudhari GP (2012) Synergy of nano carbon black inoculation and high intensity ultrasonic processing in cast magnesium alloys. *Mater Sci Eng, A* 556:954–961
14. Ali Y, Qiu D, Jiang B, Pan F, Zhang M (2015) Current research progress in grain refinement of cast magnesium alloys: a review article. *J Alloy Compd* 619:639–651. <https://doi.org/10.1016/j.jallcom.2014.09.061>
15. You Z, Jiang A, Duan S, Qiao G, Gao J, Guo L (2020) Effect of heat treatment on microstructure and properties of semi-solid squeeze casting AZ91D. *China Foundry* 17:219–226. <https://doi.org/10.1007/s41230-020-9103-9>
16. Chang Z, Su N, Wu Y, Lan Q, Peng L, Ding W (2020) Semisolid rheoforming of magnesium alloys: a review. *Mater Des* 195:108990. ISSN 0264-1275
17. Kumar A, Kumar S, Mukhopadhyay NK (2018) Introduction to magnesium alloy processing technology and development of low-cost stir casting process for magnesium alloy and its composites. *J Magnes Alloys* 6:245–254. ISSN 2213-9567
18. Li Y, Chen Y, Cui H, Xiong B, Zhang J (2009) Microstructure and mechanical properties of spray-formed AZ91 magnesium alloy. *Mater Character* 60:240–245. ISSN 1044-5803
19. Luo XC, Kang LM, Liu HL, Li ZJ, Liu YF, Zhang DT, Chen DL (2020) Enhancing mechanical properties of AZ61 magnesium alloy via friction stir processing: effect of processing parameters. *Mater Sci Eng A* 797:139945. ISSN: 0921-5093
20. Martynenko NS, Lukyanova EA, Serebryany VN, Gorshenkov MV, Shchetinin IV, Raab GI, Dobatkin SV, Estrin Y (2018) Increasing strength and ductility of magnesium alloy WE43 by equal-channel angular pressing. *Mater Sci Eng A* 712:625–629. ISSN 0921-5093
21. Ding S, Chang C, Kao P (2009) Effects of processing parameters on the grain refinement of magnesium alloy by equal-channel angular extrusion. *Metall Mater Trans A* 40:415. <https://doi.org/10.1007/s11661-008-9747-3>
22. Manakari V, Parande G, Gupta M (2017) Selective laser melting of magnesium and magnesium alloy powders: a review. *Metals* 7:1–35. <https://doi.org/10.3390/met7010002>
23. Jiang J, Wu J, Ni S, Yan H, Song M (2018) Improving the mechanical properties of a ZM61 magnesium alloy by pre-rolling and high strain rate rolling. *Mater Sci Eng A* 712:478–484. ISSN 0921-5093
24. Baghni I, Wu Y, Li J, Du C, Zhang W (2003) Mechanical properties and potential applications of magnesium alloys. *Trans Nonferrous Metals Soc China (English Edition)* 13:1253–1259
25. Pan H, Ren Y, Fu H, Zhao H, Wang L, Meng X, Qin G (2016) Recent developments in rare-earth free wrought magnesium alloys having high strength: a review. *J Alloy Compd* 663:321–331. <https://doi.org/10.1016/j.jallcom.2015.12.057>

26. Easton M, Beer A, Barnett M, Davies C, Dunlop G, Durandet Y, Blacket S, Hilditch T, Beggs P (2008) Magnesium alloy applications in automotive structures. *JOM* 60. <https://doi.org/10.1007/s11837-008-0150-8>
27. You S, Huang Y, Kainer KU, Hort N (2017) Recent research and developments on wrought magnesium alloys. *J Magnes Alloys* 5:239–253. <https://doi.org/10.1016/j.jma.2017.09.001>
28. Patel B, Chaudhari GP, Bhingole PP (2012) Microstructural evolution in ultrasonicated AS41 magnesium alloy. *Mater Lett* 66:335–338
29. Vyshak TP, Sankar R, Babu A, Harilal M, Devasia J (2020) A review on heating and rolling effect of AZ31 magnesium alloy. *Int Res J Eng* 07. ISSN: 2395-0056
30. Bhingole PP, Patel B, Chaudhari GP (2012) Ultrasonic processing and microstructural analysis of AZ91 magnesium alloy. *Mater Sci Forum* 702(703):975–978
31. Wang Q, Xiao L, Liu W, Zhang H, Cui W, Li Z, Wu G (2017) Effect of heat treatment on tensile properties, impact toughness and plane-strain fracture toughness of sand-cast Mg-6Gd-3Y-0.5Zr magnesium alloy. *Mater Sci Eng A* 705:402–410. <https://doi.org/10.1016/j.msea.2017.08.100>
32. Bhingole PP, Chaudhari GP (2012) Effect of ultrasonic treatment on the grain refinement and mechanical properties of AZ91 magnesium alloy. *Mater Sci Forum* 710:463–468
33. Nie JF (2012) Precipitation and hardening in magnesium alloys. *Metal Mater Trans A* 43:3891–3939. <https://doi.org/10.1007/s11661-012-1217-2>
34. Zhao D, Wang Z, Zuo M, Geng H (2014) Effects of heat treatment on microstructure and mechanical properties of extruded AZ80 magnesium alloy. *Mater Des* 1980–2015(56):589–593. <https://doi.org/10.1016/j.matdes.2013.11.072>
35. Zhou W, Shen T, Aung NN (2010) Effect of heat treatment on corrosion behaviour of magnesium alloy AZ91D in simulated body fluid. *Corros Sci* 52:1035–1041. <https://doi.org/10.1016/j.corros.2009.11.030>
36. Dobrzański LA, Tański T (2009) Influence of aluminium content on behaviour of magnesium cast alloys in bentonite sand mould. *Solid State Phenom* 147–149:764–769. <https://doi.org/10.4028/www.scientific.net/ssp.147-149.764>
37. González-Martínez R, Göken J, Letzig D, Timmerberg J, Steinhoff K, Kainer KU (2007) Influence of heat treatment on damping behaviour of the magnesium wrought alloy AZ61. *Acta Metallurgica Sinica (English Letters)* 20:235–240
38. Yang M, Liang X, Li H, Pan F (2010) Effects of solution heat treatment on microstructure and mechanical properties of AZ61–0.7Si magnesium alloy. *Trans Nonferrous Metals Soc China* 20:s416–s420. [https://doi.org/10.1016/S1003-6326\(10\)60509-2](https://doi.org/10.1016/S1003-6326(10)60509-2)
39. Zhang Z, Zeng X, Ding W (2005) The influence of heat treatment on damping response of AZ91D magnesium alloy. *Mater Sci Eng A* 392:150–155. <https://doi.org/10.1016/j.msea.2004.09.056>
40. Chelliah NM, Padaikathan P, Kumar R (2019) Evaluation of electrochemical impedance and biocorrosion characteristics of as-cast and T4 heat treated AZ91 Mg-alloys in Ringer's solution. *J Magnes Alloys* 7:134–143. <https://doi.org/10.1016/j.jma.2019.01.005>
41. Li ZM, Luo AA, Wang QG, Peng LM, Fu PH, Wu GH (2013) Effects of grain size and heat treatment on the tensile properties of Mg–3Nd–0.2Zn (wt%) magnesium alloys. *Mater Sci Eng A* 564:450–460. <https://doi.org/10.1016/j.msea.2012.12.008>
42. Bag A, Zhou W (2001) Tensile and fatigue behaviour of AZ91D magnesium alloy. *J Mater Sci Lett* 20:457–459
43. Dobrzański LA, Tański T, Trzaska J (2007) Modeling of the optimum heat treatment conditions of Mg–Al–Zn magnesium cast alloys. *Int J Comput Mater Sci Surf Eng* 1:540–554
44. Chen J, Tan L, Yang K (2017) Effect of heat treatment on mechanical and biodegradable properties of an extruded ZK60 alloy. *Bioactive Mater* 2:19–26
45. Reguła T, Edward C, Fajkiel A, Krzysztof S, Marzena L, Bronicki M (2010) Application of heat treatment and hot extrusion processes to improve mechanical properties of the AZ91 alloy. *Arch Found Eng* 10:141–146
46. Dziadon A, Bicki T, Porzucek P (2018) The effect of non-equilibrium solidification on the structure and mechanical properties of AZ91 alloy. *Archiv Found Eng* 18:120–125

Preparation of Bamboo-Based Nano-Cellulose by Ball Milling



Yogendra Kumar Verma, Amit Kumar Singh, and M. K. Paswan

Abstract The main objective of this work was the use of bamboo fiber for the preparation of nano-size filler which used as filler in nano-composite. The present paper concerns with the bamboo fibers as the main source for the preparation of nano-cellulose by the process of high-energy planetary ball milling at different speed of milling, different milling time, and different size of ball and its vital application as filler in biodegradable Nano-composite plastics used in automotive, agriculture, and packaging applications. The impact of the various milling condition as milling time, milling speed, ball mill size and on the basis of particle size distribution and morphology of obtained bamboo nanoparticles, nature of milling are studied. Wet milling in the presence of phosphoric acid resulted high yield bamboo nano-cellulose. During the dissolution of cellulose, the phosphoric acid plays vital role as swelling agent. Bamboo fibers easily were successfully pulverized into nano-size by the wet milling in the presence of deionized water. Due to sticking nature of material for the milling media, dry milling of bamboo fibers is difficult.

Keywords Bamboo fibers · Nano-cellulose · Ball milling

1 Introduction

The natural fibers are biodegradable, easily available, and removable materials. The aspect ratio and the strength-to-weight ratio of the natural fibers are high, and they have low density, but they have good tensile strength and modulus. This type's property makes them those type materials (textile type) which are traditionally used for manufacturing yam by the process of spinning. Spinning process is not good suitable for very efficient process and result into the waste due the shorter fibers of the bamboo and due to the some limitation of the spinning process with the shorter

Y. K. Verma · A. K. Singh (✉)
National Institute of Technology Nagaland, Dimapur, Nagaland, India
e-mail: amit.kumar965@yahoo.com

M. K. Paswan
National Institute of Technology, Jamshedpur, Jharkhand, India

fibers of the bamboo. Due to this reason, new way is searched for the process of the short fibers which can used in the some intrinsic properties [1]. Shear grinding, cryo-crushing, steam explosion, and high pressure turbulence are the good techniques which are mostly used for fibrils or crystal separation from the fibers. Now days, due to environmental consciousness, fossil fuels depleting and ecological concerns growing in societies greater demands of greener materials. The suppliers and industries should become more aware about facing the challenges for the better future because resources of the availability, sustainable and materials which are also renewable they should use for the better future. In future, cellulose will become very vital role in the material because cellulose abundance, versatility as biopolymer, several different forms and potential applications. The matrix regenerated the cellulose and also matrix dissolved, but the reinforcement partially dissolved or undissolved cellulose in the all-cellulose composites which is the class of bio [2]. In nano-composites, a great deal of attention has been paid recently to cellulosic nanofibrillar structure as a components because of their outstanding mechanical properties, their renewable, their wide abundance, and environmental friendly in nature. Wood, agricultural residues, or bacterial cellulose are the main source which liberate cellulosic fibrils. In various composites materials water swell able nature of cellulose main concern now days in non-crystalline regions [3]. Cellulose is most abundant in the form of polysaccharide on earth which is obtained from several sources as from the wood and plants cell walls (banana tree, bamboo grass, palm tree, etc.) Cellulose exists in the morphological forms of fibers, micro-fibril or nano-fibril, and micro- or nano-crystalline cellulose due to the physical properties or features, dimensions, and shapes of the cellulose [4]. The aspect ratio and the strength-to-weight ratio of the nano-cellulose material are high, and they have low density, but they have good tensile strength and modulus and good optical properties and unique morphology; due to these properties, nano-cellulose is now a days using for the better future. Mainly, cellulose contains two types of structure; one is crystalline (highly ordered), and second one is amorphous (disordered). Which cellulose extracted from micro-fibrillated cellulose of the crystalline region generally results in the form of nano-cellulose. In the fields of nano-composites such as food additive, in rubber industries for the filling materials and in the field of drug delivery, nano-cellulose are used now a days vitally [5]. By the combined action of the chemical treatments and the high speed of the planetary, ball milling preparation of the nano-cellulose is done in this current paper. In the bamboo fibers, cellulose, hemicellulose, and lignin are the main composition. The lignin and the hemicellulose are removed from the bamboo fibers due to the chemical treatment of the bamboo fibers. The high-speed planetary ball milling makes the bamboo fibers in the power form which is known as nano-cellulose. High stiffness is show in the obtained nano-cellulose from the bamboo fibers which are prepared by the ball milling; thus, they vitally used as good reinforcement in the preparation of fiber reinforcement composites. And by this good properties of the nano-cellulose, they have lots of application because they are renewable, biodegradable, low cost, less weight [6]. Ball milling is a grinder which grind the fibers into powder form. Ball milling is cost-effective green technology with a good potentials and also simple. The energy is released in the ball milling due the collisions between the grinding balls,

and also, high energy of grinding is created due to the friction of the balls with the grinding jar walls. Due to centrifugal force, ball rotates when the mill rotates. With respect to mill, a reverse rotation of the disk applied a centrifugal force in opposite direction which leads to transit the balls in the opposite walls of mill by this effect of impact given. In a planetary ball mill, most of the reduction is carried out by impact. Synthesis of bamboo-based nano-particle by ball milling is low cost, very simple, and in high yield has been a great challenge since the very early development of nano-science. In an inert atmosphere, high-speed ball milling is very widely used for the preparation of the various nanomaterials, nano-alloy, nano-composites, and nano-quasicrystalline materials among all top down approaches. During ball milling, the temperature depends on the kinetic energy of the ball and characteristics of the materials which is in the jar of ball milling machine for synthesis of material into powder and milling media. Phase transfer and diffusivity is occurring by the temperature of the powder. Formation of nano-crystalline phases and amorphous phases can also enhance at low temperature if energy is sufficient [7]. The final particle size has no impact by the variation of the empty space. The movement of ball during ball milling is free if the empty space increases [8]. Phosphoric acid is mostly used in the preparation of the cellulose nano-particle because it is non-corrosion and non-toxic in nature; it is low cost and safe use as compared to other inorganic mineral acids. Commonly, sulfuric acid used in the preparation of nano-cellulose but due to hydrolysis of sulfuric acid corrosion in equipment (Table 1).

Table 1 Specification of planetary ball mill

Model	PULVERISETTE 7 premium line
Final fineness (μm)	$\leq 0,1$
Material feed size (mm)	< 5
Max. sample volume (ml)	70
Batch/sample volume (ml)	0.5–70
Speed (min^{-1})	100–1100
Speed ratio	1–2
Grinding jar volumes (ml)	20, 45, 80
Grinding chamber material	Agate, sintered corundum, silicon nitride, zirconium oxide, stainless steel, hardened steel, tungsten carbide
Grinding time setting (min)	3
Power consumption (W)	1100
Power supply	240 V, 50–60 Hz
W \times D \times H (mm)	400 \times 580 \times 360
Weight (kg)	44

2 Materials and Methods

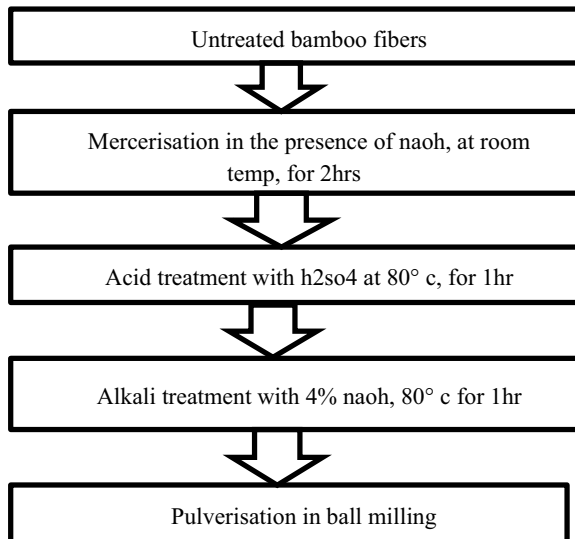
2.1 Materials

Bamboo fibers are prepared by mechanochemical processing methods in micro-size. After that for the removal of the lignin and hemicellulose from the bamboo fibers, chemical treatment is done. Bamboo fibers were sequentially undergone for mercerization with 18% concentration of NaOH at room temperature for 2 h. Other chemical also used ethanol, phosphoric acid.

2.2 Methods

Ball milling of the treated bamboo fibers done after the treatment of the bamboo fibers in the planetary ball milling which contain zirconia balls 10 mm diameters and name of this ball mill is Fritsch pulverisette 7. Ball milling of the treated bamboo fibers is done initially only 10 min of the dry milling, and 3 mm diameter of the ball is used for the milling of the bamboo fibers in the wet condition for 1.5–3.5 h in the presence of phosphoric acid, phosphotugstic acid at 400 and 1000 rpm, respectively. The ratio of ball and material in the ball milling is taken 10:1. The rotation speed 400 rpm of the planet carrier taken. By the phosphoric acid, transparent solution is obtained. During dissolution of cellulose and facilitated the disintegration of cellulose fibers into nano-fibers by the phosphoric acid. However, the nano-particle can be prepare by ball in the presence of normal water in wet condition of ball milling (Fig. 1).

Fig. 1 Chemical treatment of bamboo fibers



The manufacturing of bamboo nano-particle by ball milling in the presence of phosphoric acid, in this method, first, we cut the bamboo pulp in the small size and then take 1.5 g cellulose pulp and 45 g phosphoric acid in desire concentration then put this solution in the ball milling jar. After ball milling, this solution kept at 40–60°C in the water bath and stirred at 400 rpm for 1.5–3.5 h which is in Fig. 2. After that formation of the transparent cellulose is obtained [9]. However, we can prepare the bamboo nano-cellulose by the ball milling only without using the water bath for stirrer of the mixture. Preparation of the bamboo cellulose in the presence of phosphotungstic acid (PTA) is giving the better result than the phosphoric acid in the manufacturing of the bamboo nano-cellulose by the ball milling because this methods improve the hydrolysis efficiency, avoid lengthy separation on process, and very important things is that its reduces the preparation time. Due to the low toxicity, high acidic, easy recycling, and high thermal stability PTA can used (as solid acid catalyst) in many field. This experimental method is similar as phosphoric acid methods only difference in between them is that for hydrolysis acids is used different in between them [10]. Particle size distributions of milled material were carried out after every 1 h of milling by FESEM, TEM. And the crystallinity index of particle is investigated by XRD. The medium of dispersion was deionized water. With bandelin ultrasonic probe for 0.5 h, dispersion was ultrasonicated.

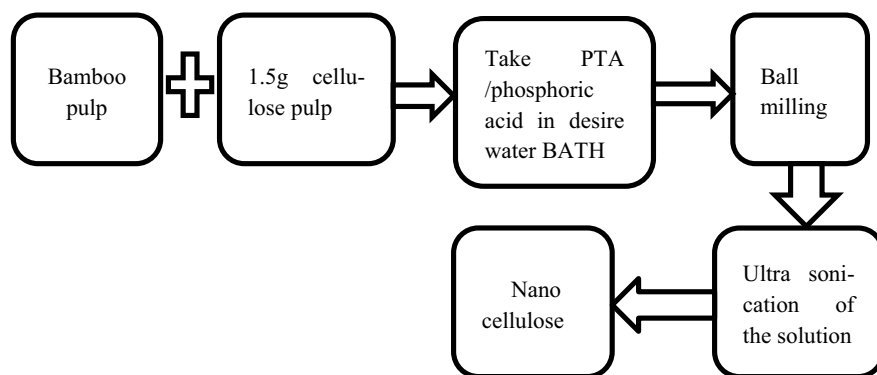


Fig. 2 Extraction of nano-cellulose

3 Results and Discussion

3.1 *Effect of Reaction Conditions on the Yield of Bamboo Nano-Cellulose*

The phosphoric acid and phosphotungstic acid concentration, reaction time, reaction temperatures are the main factor which influence on the yield of the bamboo nano-cellulose. Effect of the phosphoric acid concentration and phosphotungstic acid on the yield of bamboo nano-cellulose. With increasing the concentration of phosphoric acid and phosphotungstic acid yielding of the bamboo nano-cellulose increases, this phenomenon occurs due to the swelling nature of the phosphoric acid for the cellulose. The yielding value of the bamboo nano-cellulose in the presence of phosphoric acid concentration (77–80%) increases from 9.85 to 77.37% with increasing the concentration of phosphoric acid. The yielding of the bamboo nano-cellulose decreases if the concentration of the phosphoric acid is 85%. This occurs due to the over-swelling of the cellulose, and due to the high viscosity of the solution, some difficulty occurs in milling which can return the degradation of cellulose into fibers that is why the yielding value of the bamboo nano-cellulose decreases at the concentration of the phosphoric acid is 85% [11]. Yielding of the bamboo nano-cellulose increases when the concentration of the phosphotungstic acid increases from 10 to 15% [12].

3.2 *Milling Effect on the Properties of Nano-Cellulose*

The properties of the materials are highly influenced on microscopic and macroscopic properties such as structure of the materials, morphology of the materials, thermal stability of the materials, and also crystallinity of the materials in ball milling after the treatment of the nano-cellulose. The crystallinity transformation occurs from cellulose I to cellulose II in the presence of the specific amount of water in the ball milling process. The most effective transformation of cellulose I to cellulose II at 30 wt.% of water due to the interaction between the cellulose chain and water molecule [13]. During ball milling, transformation of morphology from short rod like to spherical shape of cellulose under the combined effect of agglomeration regime and breakage. As we increases the milling time, then size of particle and crystallinity index of cellulose decline. The molecular and chemical properties of cellulose not changing with milling time and speed. If cellulose nano-crystal is prepared in shorter time, then it has better thermal stability. In the measurements of rheological of the cellulose crystal, suspensions show that entangled network structure in all blended paste shear thinning and weak elastic gel like viscoelastic properties over the all investigated range exhibited behavior of the cellulose. The rheological properties of cellulose decrease with increases milling time and size of cellulose playing vital role in the composite properties suspension with this behavior a possible network is proposed in cellulose suspension [14]. The thermal stability and activation energy of cellulose are

reduced in the ball milling. Due to the pre-treatment of cellulose in the ball milling disruption of crystalline cellulose to amorphous effectively. So, cellulose which is obtained by ball milling process becomes a vital source of chemical and energy than crystalline cellulose easily [15]. Nano-cellulose which is obtained by ball milling is environmentally friendly applications which are biodegradable and biocompatible nano-composites and biosensors [16]. The ball milling time effect on the properties of nano-cellulose mainly influences on the yield of the nano-cellulose, but the size of milling ball is influenced on the nano-cellulose very less which is negligible [17]. If milling time increases, then thermal degradation of crystalline cellulose decreases. This occurs due to the substances of the denaturing of non-cellulosic such as lignin and hemicellulose. Ball milling broke the crystalline cellulose in different small crystals and amorphous cellulose, and finally, it fully destroyed by ball milling [18]. The efficiency of the preparation of cellulose is very effective now days by ball milling because explore rate acceleration in ball milling is low reactive. In the ball milling, the effective mechanical forces break the covalent bonds as c-c bonds also can break by mechanical forces which is in ball milling [19]. Ball milling size, milling time, mass ratio of cellulose pulp, and ball mill are the various factors in the preparation of the cellulose by the ball milling and their some complicated interactions, which effect on the prepared cellulose. Mostly, the yield of the cellulose is effect by milling time and speed of ball milling, but the effect of the milling ball is negligible. Milling ball size is considered during in the interaction between mass ratios to cellulose pulp [20]. During ball milling, energy consumption varies according to the process parameters, such as time, ball milling size and also milling speed, the particle size, and the properties of fibers. The properties of milling nano-particles (particle size distribution, shape of the particle, area of the specific surface, level of the agglomeration particle) obtained in the entire configuration were compared in relation to process consumption of energy. Agglomeration of nano-particles decreases the milling efficiency of the ball milling [21]. When the milling time increases, then the particle size of metal decreases, and magneto caloric effect of particle also decreases, and the size of bamboo nano-particles also depends on milling time and size of the milling ball size [22]. By the planetary ball milling with some acid hydrolysis, nano-cellulose is extracted from cellulose pulp and cellulose powder which are types of general cellulose feedstocks. High quality of nano-cellulose with high yield is obtained by the ball milling of cellulose feedstock could be very effective in the hydrolysis process. Due to the removal of amorphous phase from the structure of cellulose, the crystallinity and crystal size of nano-cellulose increases when we comparing with nano-cellulose and ball-milled nano-cellulose materials [23]. The chemically treated bamboo fibers losses the modulus and tenacity with some chemically treated bamboo fibers in the mechanical properties of the chemically treated bamboo fibers. Due to the acid hydrolysis, rupture formation occurs in the obtained chemically treated fibers which are totally responsible for the rupture of the bonds which leading the deterioration of the tensile strength to be very useful for the milling of the bamboo fibers. Bundles strands which are individual with each other by lignin but after acid treatment and mercerization, lignin partly cleaned off and defibrillated the structure obtained before

Table 2 Size of the particle at different speed, milling time [10, 13, 18, 27]

Ball milling	Milling time	Milling speed	Size of particle
Ball milling is done in the presence of water/toluene	hrs	200 rpm	5–10 μm
Ball milling is done in the presence of 30–50% water	2 h	400 rpm	100 nm
Ball milling is done in the presence of phosphoric acid	hrs	400 rpm	100–200 nm in length and 13–30 nm in width
Ball milling is done in the presence of phosphotungstic acid	hrs	400 rpm	200–300 nm in length and 25–50 nm in width
Ball milling is done in the presence of sulfuric acid	1.5–2.5 h	270 rpm	135 nm in length and 6 nm in width
Ball milling is done in the presence of TEMPO reagent	24 h	1000 rpm	100–200 nm in dia and 3–7 nm in height

the chemical treatment of the fibers [24]. The different nature of the fillers or additives can be applied for the better properties (rheological behavior or hydrophobic nature of the product, cellulosic bamboo fibers, activated in different degree or defibrillated or chemically treated or modified) of the nano-cellulose. The main objective of this work was the use of bamboo fiber for the preparation of nano-size filler which used as filler in nano-composite. The present paper concerns with the bamboo fibers as the main source for the preparation of nano-cellulose by the process of high-energy planetary ball milling at different speed of milling, different milling time, and different size of ball and its vital application as filler in biodegradable nano-composite plastics used in automotive, agriculture, and packaging applications [25]. Cellulose is the mainly the mixture of crystalline and amorphous material. On the ratio of these components, chemical, biochemical, and physical properties of cellulosic materials depend. Amorphous materials are more reactive, and they have less tensile strength. Ball milling is the vital part for increasing the ratio of amorphous materials. The fibers (bamboo, jute, banana, etc.) are divided into two parts such as open and broken into small bits, the molecular weights of the fibers decreases and on small-scale cellulose oxidized. Lots of pores and higher surface area of the ball milling resulted by this nature of the fibers. By this, water absorption increases, and thermal stability decreases [26] (Table 2).

4 Conclusion

Ball milling is a unique technique which is used for the preparation of nanoparticles of any kind of material like bamboo fiber, textile fibers, and agricultural waste material. Ball milling is simple, cost-effective green technology with enormous potentials. This techniques have number of scope to become industrially applicable as one of

them is it can produce nanoparticles in large quantity. Due to sticking nature of material for the milling media, dry milling of bamboo fibers is difficult. In ball milling method, ball-to-material ratio increases, small size of balls, and increased milling time by the some modification in the wet milling process by adding some active agent which reduces the size of particle below 100 nm. Small percentage of inorganic nanoparticles contaminations introduced from the milling media (milling time, ball size, and speed) in dispersion. Wet milling in the presence of phosphoric acid resulted high-yield bamboo nano-cellulose. During the dissolution of cellulose, the phosphoric acid plays vital role as swelling agent. Bamboo fibers easily were successfully pulverized into nano-size by the wet milling in the presence of deionized water.

References

1. Yuen CWM, Cheng YF, Li Y, Hu JY (2009) Preparation and characterisation of nano-scale cotton powder. *J Text Inst* 100(2):165–172. <https://doi.org/10.1080/00405000701660970>
2. Baghaei B, Skrifvars M (2020) All-cellulose composites: a review of recent studies on structure, properties and applications. *Molecules* 25(12). <https://doi.org/10.3390/molecules25122836>
3. Hubbe M, Rojas OJ, Lucia LA, Sain M (2008) Cellulosic nanocomposites: a review. no. August
4. Seddiqi H, Oliaei E, Honarkar H, Jin J (2021) Cellulose and its derivatives : towards biomedical applications, vol 28(4). Springer Netherlands
5. Phanthong P, Guan G, Ma Y, Hao X, Abudula A (2016) J Taiwan Institute of Chem Eng Effect of Ball Milling on the Production of Nanocellulose using Mild Acid Hydrolysis Method. 60:617–622. <https://doi.org/10.1016/j.jtice.2015.11.001>
6. Baheti V, Abbasi R, Militky J (2012) Ball milling of jute fibre wastes to prepare nanocellulose. *World J Eng* 9(1):45–50. <https://doi.org/10.1260/1708-5284.9.1.45>
7. Prasad Yadav T, Manohar Yadav R, Pratap Singh D (2012) Mechanical milling: a top down approach for the synthesis of nanomaterials and nanocomposites. *Nanosci Nanotechnol* 2(3):48. <https://doi.org/10.5923/j.nn.20120203.01>
8. Supriyono S, Susilo B (2019) Characterization of bamboo Tutul charcoal particle produced by high energy ball milling shaker type. *Media Mesin Maj Tek Mesin* 20(2):41–46. <https://doi.org/10.23917/mesin.v20i2.8534>
9. Lu Q, Lin W, Tang L, Wang S, Chen X, Huang B (2014) A mechanochemical approach to manufacturing bamboo cellulose nanocrystals. *J Mater Sci* 50(2):611–619. <https://doi.org/10.1007/s10853-014-8620-6>
10. Lu Q, Cai Z, Lin F, Tang L, Wang S, Huang B (2016) Extraction of cellulose nanocrystals with a high yield of 88% by simultaneous mechanochemical activation and phosphotungstic acid hydrolysis. *ACS Sustain Chem Eng* 4(4):2165–2172. <https://doi.org/10.1021/acssuschemeng.5b01620>
11. Mosier N et al (2005) Features of promising technologies for pretreatment of lignocellulosic biomass. *Bioresour Technol* 96(6):673–686. <https://doi.org/10.1016/j.biortech.2004.06.025>
12. Zhu Y et al (2014) Optimization of enzyme-assisted extraction and characterization of polysaccharides from *Hericium erinaceus*. *Carbohydr Polym* 101(1):606–613. <https://doi.org/10.1016/j.carbpol.2013.09.099>
13. Dobbelaere T et al (2019) Nanoscale advances. 4166–4172. <https://doi.org/10.1039/c9na00391f>
14. Zheng Y, Fu Z, Li D, Wu M (2018) Effects of ball milling processes on the microstructure and rheological properties of microcrystalline cellulose as a sustainable polymer additive. *Materials (Basel)* 11(7):1–13. <https://doi.org/10.3390/ma11071057>

15. Khan AS et al (2016) Impact of ball-milling pretreatment on pyrolysis behavior and kinetics of crystalline cellulose. *Waste and Biomass Valorization* 7(3):571–581. <https://doi.org/10.1007/s12649-015-9460-6>
16. Zhang L, Tsuzuki T, Wang X (2010) Preparation and characterization on cellulose nanofiber film. *Mater Sci Forum* vol. 654–656:1760–1763. <https://doi.org/10.4028/www.scientific.net/MSF.654-656.1760>
17. Zhang L et al (2018) Multiple factor analysis on preparation of cellulose nanofiber by ball milling from softwood pulp. *BioResources* 13(2):2397–2410. <https://doi.org/10.15376/biores.13.2.2397-2410>
18. Hidenó A (2016) Comparison of the thermal degradation properties of crystalline and amorphous cellulose, as well as treated lignocellulosic biomass. *BioResources* 11(3):6309–6319. <https://doi.org/10.15376/biores.11.3.6309-6319>
19. Park S, Kim JG (2019) Mechanochemical synthesis of poly(trimethylene carbonate)s: an example of rate acceleration. *Beilstein J Org Chem* 15:963–970. <https://doi.org/10.3762/bjoc.15.93>
20. Miyamoto H, Yamane C, Seguchi M, Okajima K (2009) Structure and properties of cellulose-starch blend films regenerated from aqueous sodium hydroxide solution. *Food Sci Technol Res* 15(4):403–412. <https://doi.org/10.3136/fstr.15.403>
21. Rajaonarivony K, Rouau X, Lampoh K, Delenne J, Mayer-laigle C (2019) Fine comminution of pine bark : how does mechanical loading influence particles properties and milling efficiency ?
22. Thang NV, Van Dijk NH, Brück E (2015) Effects of milling conditions on nano-scale MnFe (P, Si) particles by surfactant-assisted high-energy ball milling. *ng*. 75:1104–1111. <https://doi.org/10.1016/j.phpro.2015.12.183>
23. Ammonium Q, Solvent D, Jiang Z, Miao J, Yu Y, Zhang L (2016) Effective preparation of bamboo cellulose fibers. *ng*. 11(2):4536–4549
24. Abbasi R, Baheti V (2018) Preparation of nanocellulose from jute fiber waste. *J Text Eng Fash Technol* 4(1):101–104. <https://doi.org/10.15406/jteft.2018.04.00126>
25. Gallego R et al (2020) Green approach for the activation and functionalization of jute fibers through ball milling. *Cellulose* 27(2):643–656. <https://doi.org/10.1007/s10570-019-02831-0>
26. Ling Z et al (2019) Effects of ball milling on the structure of cotton cellulose. *Cellulose* 26(1):305–328. <https://doi.org/10.1007/s10570-018-02230-x>
27. Piras CC, Fernández-Prieto S, De Borggraeve WM (2019) Ball milling: a green technology for the preparation and functionalisation of nanocellulose derivatives. *Nanoscale Adv* 1(3):937–947. <https://doi.org/10.1039/c8na00238j>

Design and Synthesis

Brush Plating on Aluminum for High-Reliable Use



Vaishali Umrانيا , Vimal M. Shah, and Sharad Shukla 

Abstract Brush plating offers a high degree of flexibility to apply accurately controlled thickness of engineered deposits and coatings onto localized areas of metal components. Brush plating is done when tank electroplating is not an option. Requirement of soldering on feeder network for SAR component is one application which can be catered by brush silver plating. The paper describes plating sequences for pre-treatment, including cleaning, zincating, nickel plating, and silver plating by brush plating to produce solderable surface. Optimization of process parameters is carried out for required thickness with quality silver plating. The effect of various parameters on the deposited film is studied. The surface morphology and surface roughness of the silver deposited specimens are analyzed using confocal laser microscope. Samples are subjected to heat, bend adhesion, and solderability test to ensure high reliability plating.

Keywords Brush plating · Silver · Solderability · Aluminum

1 Introduction

Brush plating is portable method of plating which provides ease of plating on selective area. Brush plating includes specially formulated solutions, power supply, and specifically designed anode. Brush plating is considered to get controlled thickness on a localized area of a part when tank electroplating is not an option. It is also known as “spot plating,” allows to plate a specific part of that item, using a brush saturated with plating solution. This process is widely used in plating industry to repair worn parts. It offers greater portability than tank plating, minimal masking is required, and often requires less plating solution. Brush plating is a good choice for items that cannot be bath plated, including oversized items or components that cannot be disconnected for plating. Negative terminal of power supply is connected to job, and positive terminal is connected to anode which is covered by absorbent

V. Umrانيا (✉) · V. M. Shah · S. Shukla
Space Applications Centre (ISRO), Ahmedabad, Gujarat, India
e-mail: vaishali@sac.isro.gov.in

material to hold the solution. This anode is dipped in the solution and brushed on the surface of job. Plating occurs when anode touches the surface via absorbent material and completes the circuit. During this process, anode is kept in motion continuously to avoid burning of deposit.

Literature is referred regarding brush plating but work is done majorly on ferrous-based metals. Basic information regarding brush plating is given in “Brush plating” by Norris [1], and “An update on brush plating” by Vanek [2]. Kan-Lin Hsueh and I-Yuan Wei reviewed published literatures and patents on reel-to-reel selective plating processes [3]. Wang et al. deposited Zn–Ni alloy coatings on rolled copper foil via electro-brush plating with different micro-force [4]. Shaojun et al. carried out fabrication and characterization of electro-brush plated nickel graphene oxide nano-composite coatings on steel substrate [5]. Isern et al. studied the deposition of aluminum-incorporated nickel coatings on a substrate of low carbon steel by brush electroplating [6]. Hurrell et al. described selective brush plating for decorative applications [7]. Wei et al. prepared anti-corrosion super-hydrophobic coatings on commercial A3 steel plates by Fe-based micro/nano-composite electro-brush plating and blackening process [8]. Wang et al. studied Zn–Ni and Sn–Zn alloy coatings on the rolled copper foil surface by brush plating [9]. Wu et al. developed an automatic brush plating system to eliminate the disadvantages resulting from the operator in conventional brush plating [10]. Vaishnu et al. studied wear characteristics of nano CuO/Ni composite coating on cylindrical pin of aluminum A356 alloy by brush plating technique [11]. The author has given cleaning procedure but not provided information regarding plating of aluminum. However, literature regarding precious metal brush plating on aluminum alloy is not reported. Present work reports silver brush plating on aluminum alloy 6061 T6 with nickel undercoat for high-reliable use.

Requirement was generated for silver plating of feeder network for SAR component. Job dimension is about $1400 \times 450 \times 300$ mm. TNC connector needs to be soldered on single element patch antenna element and 1×3 full array patch antenna V polarization feeder. To obtain solder adhered to surface, silver plating is proposed, owing to best electrical conductivity and cost benefit vis a vis gold plating alternative. There are two options available: to silver plate whole job or to plate localized functional area using selective plating. Brush plating is considered when the part is too large for the tank plating. Brush plating is a proven process in plating industry that offers a high degree of flexibility to apply accurately controlled thickness of engineered deposits and coatings onto localized areas of metal components. But this process is not attempted on high reliability jobs at SAC. So, we are planning to establish brush plating on high-reliable jobs to cater the project requirement.

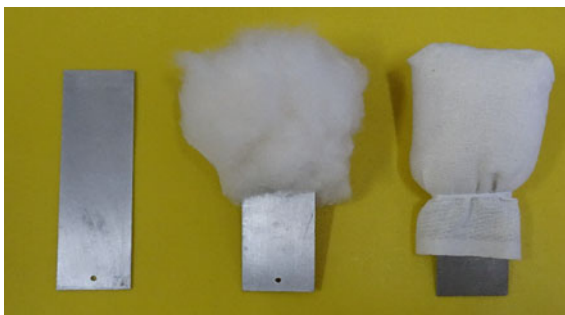
2 Experimental

2.1 Materials

Aluminum plating is multistep process. It is difficult to electroplate aluminum as it is having natural oxide film in its stable state. Aluminum brush plating was done using scheme of cleaning, activation, zincating, nickel plating, and silver plating. Cleaning was done using solvents like acetone and trichloroethylene. Activation done by nitric acid and ammonium bifluoride solution. Zincating, nickel, and silver plating were carried out in proprietary formulations purchased from M/s Grauer and Weil, Mumbai [12–14]. Solutions were prepared as per manufacturer datasheet. Gold flash plating was done using citric buffered bath to protect solderability of silver, which tends to tarnish. After initial experiments, specific type of anode was designed to do brush plating (Fig. 1). Stainless steel specimen was wrapped with cotton to get media for plating solution passage to job and prevent anode–cathode short circuit. Cotton was covered with lint free cloth material to prevent loss of fibers during process.

Before electroplating area was masked where plating was not required. Undercoat nickel was required to get optimum protection of base metal as well as good seed layer for top layer silver. For undercoat, two options were attempted: (1) Electroless nickel solution was poured on sample continuously for five minutes. Very thin nickel plating was achieved which was not suitable for further plating. (2) Nickel electroplating was done using nickel sulfate, boric acid, and nickel chloride-based bath. In this case, good adherent nickel deposits were plated by optimizing current density. For brush plating, initial experiments were done using 40 g/l nickel metal in nickel plating bath and parameters were monitored such as time, current density, and thickness. As per thickness requirement 2–3 μm nickel and 2–3 μm silver of brush plating procedure, higher concentration bath solutions were formulated to get desired thickness in limited time frame. Samples were prepared by varying nickel metal concentration from 40–100 g/l. Current parameters were also optimized to get desired thickness without defects. Nickel plating solution was heated to 70 °C by hot plate, and anode was dipped hot in solution, and current was applied and brushed on job to get plating. Silver plating was carried out at room temperature,

Fig. 1 Specific anode designed for brush plating



and silver concentration was maintained 32 g/l as per manufacturer recommendation. After every plating experiment, specimen thickness was measured using X-ray fluorescence spectrometer. Measured results are given in Table 1.

Sample number 7 parameters were selected for further testing. Nickel plating was optimized, refer Fig. 2. On top of nickel plating, silver brush plating was optimized to obtain 2 μm thickness refer Fig. 3. On silver plating gold flash coating was applied to prevent tarnishing of silver deposit. Gold flash was obtained using acidic gold cyanide plating solution. Plating time was 1 min with 100 mA current refer Fig. 4.

Table 1 Parameter optimization for brush plating parameters

Sample No	Nickel plating					Silver plating		
	Time min	Temp °C	Current mA	Ni conc. g/l	Thickness μm	Time min	Current mA	Thickness μm
1	3	35	300	40	1.08	5	100	2.00
2	3	70	300	40	1.50	5	100	2.00
3	5	70	300	60	1.80	5	100	2.50
4	5	70	300	60	1.90	5	100	2.60
5	5	70	300	80	3.00	5	100	2.00
6	7	70	300	80	3.30	5	100	2.00
7	5	70	300	90	2.01	5	100	1.99
8	3	70	300	90	1.27	5	100	1.79
9	5	70	400	90	1.33	5	100	1.78
10	5	70	500	90	1.40	5	100	1.98
11	5	70	600	90	1.55	5	100	2.00
12	5	70	300	90	1.25	5	100	2.01
13	5	70	300	100	1.43	5	100	1.98
14	5	70	300	100	1.13	5	100	2.02

Fig. 2 Nickel plated samples

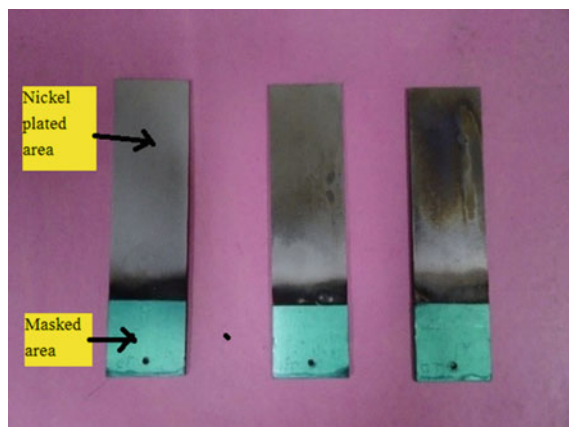
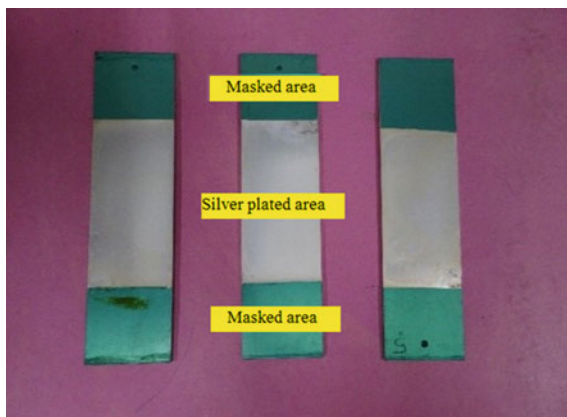
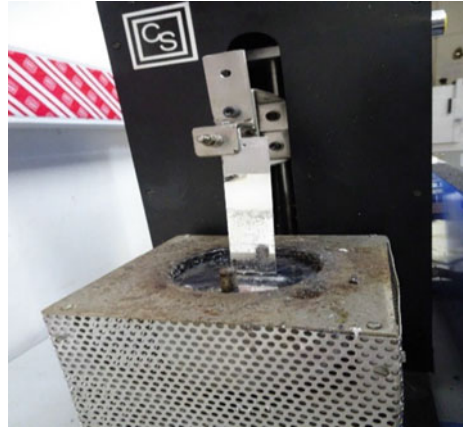


Fig. 3 Silver plated samples**Fig. 4** Gold flash sample

After brush plating, samples were subjected for heat test at 190 °C for 1 hour to check adhesion of successive deposits and occurrence of blister, if any. Samples were subjected to bend test to check adhesion in case of tensile and compressive forces. Solderability test was also performed to check adhesion of solder on brush plated deposits. Results are given in section 3.

Fig. 5 Solderability test setup and sample



2.2 Profile Surface Roughness Analysis and Morphology Study by Confocal Laser Microscope

For comparison of profile surface roughness before and after plating, bare aluminum and silver plated sample were analyzed using confocal laser microscope (CLM). (Make: Olympus). Results are given in Sect. 3.

2.3 Solderability Test

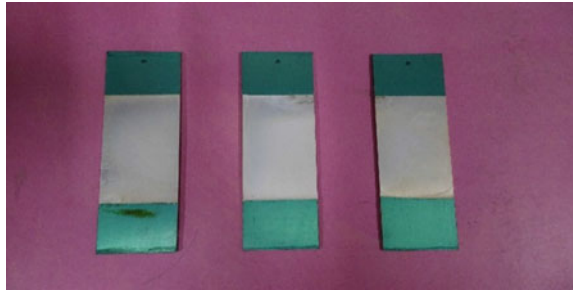
Plating was subjected to solder ability test in accordance with method 208 of MIL-STD-202 [15] and was carried out using solderability test setup is shown in Fig. 5.

Sample is dipped in hot solder at 250 °C and checked for solder adhesion. Solder ability test was carried out to evaluate the ability of plated surface to get soldered with the components.

3 Results and Discussion

It was observed that at room temperature nickel plating rate was almost 0.35 μm per minute. At higher temperature of 70 °C, deposition rate was increased to 0.5 μm per minute. Anode was dipped in plating solution after every 20 s to replenish electrolyte absorbed on it.

After successful brush plating, samples had passed heat test at 190 °C for 1 hour as per Fig. 6. Adhesion of successive deposits was good, and occurrence of blister was not observed.

Fig. 6 After heat test**Fig. 7** Bend test
(compressive side and tensile side)

During bend test on mandrel by 180° sample did not show any traces of peel off or delamination from base material. It was having excellent ductility so that it did not fail either in tensile and compressive forces region refer Fig. 7.

The ultimate aim of doing brush silver plating is to do solder on selective area of a big job. Solderability test was also successful on brush silver plated samples, and solder was found adherent and properly wetted, refer Fig. 8.

Brush silver plated aluminum is having better surface as compared to bare aluminum when analyzed using confocal laser microscope, its clearly evident in Figs. 9 and 10.

Measured profile roughness data for bare and silver plated aluminum is given in Table 2.

It is observed that average surface roughness of silver plated aluminum is less by 350–400 nm as compared to bare aluminum.

Surface morphology was studied by CLM at 200X (Fig. 11). It was observed that there were no pin holes, and silver plating was continuous without any unplated surface.

By using this process, one job was brush silver plated for SAR project as given in Fig. 12.



Fig. 8 Solderability test

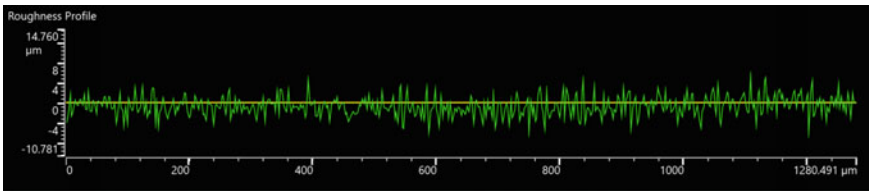


Fig. 9 Profile of bare aluminum

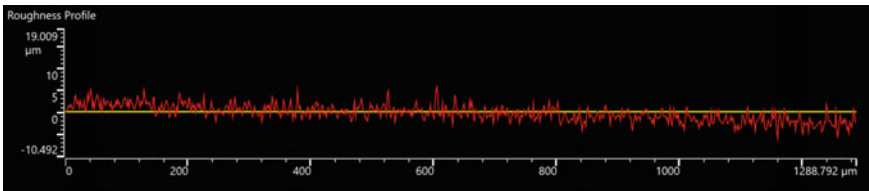


Fig. 10 Profile of silver plated aluminum

Table 2 Profile roughness data

Sr. No	Type of sample	Rp (μm) Maximum profile peak height	Rv (μm) Maximum profile valley depth	Rz (μm) Average maximum height of the profile	Rc (μm) Mean height of profile irregularities	Rt (μm) Maximum height of the profile	Ra (μm) Roughness average	Rq (μm) Root mean square (RMS) roughness	Rz (μm) Average maximum height of the profile
1	Bare Al	5.84	5.82	11.66	4.00	11.46	1.32	1.70	10.6
2	Silver plated Al	5.82	4.04	9.86	3.12	9.86	0.97	1.26	7.92

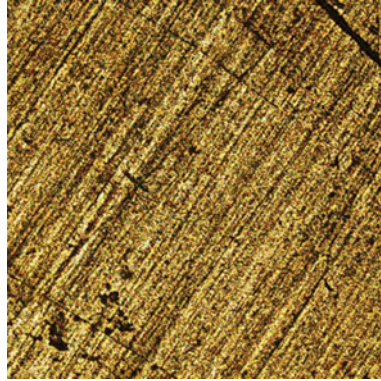


Fig. 11 Surface morphology of silver plated aluminum (Magnification: 200X)

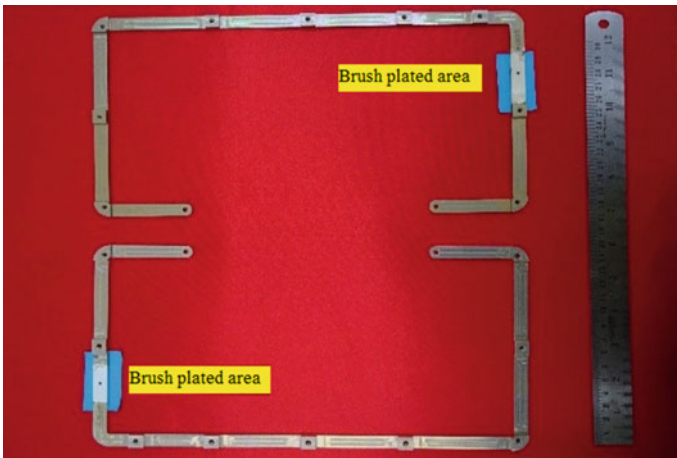


Fig. 12 Brush plating on job

4 Conclusion

Brush plating is a very handy tool for selective plating. Process of brush plating is successfully developed and demonstrated. Proper design and selection of anode are necessary to get best quality brush plating. Proposed undercoat electroplating nickel thickness is 2–3 μm , silver plating 2–3 μm and top layer gold flash submicron to prevent silver from tarnishing effects. Solder was found properly adhered to the sample which served required purpose. Brush plating by manual method is operator dependent method, it can be improved by automation of plating system using motorized brush movement and plating solution replenishment can be done by pump.

Acknowledgements The authors appreciate technical help received from STPD colleagues during the course of experiments reported in this paper. The authors gratefully acknowledge the inspiration received from Shri R S Sharma, Group Director, EFMG. SRA/PMQD-M team, for testing support and best regards to reviewers for spending their valuable time in the evaluation. Sincere thanks to Shri A. Bhattacharya, DD ESSA, and Director-SAC for their necessary guidance and facilitating us to do this experiment.

References

1. JCN (1995) Brush plating. *Metal Finishing* 93:349–361
2. Vanek DL (2002) An updating on brush plating. *Metal Finishing* 100:18–20
3. Kan-Lin H, I-Yuan W (2002) Reel-to-reel selective plating processes. *AESF SUR/FIN*, pp 486–492
4. Wang W, Liu X, Shi Z (2016) Mechanisms and influences of electro-brush plating micro-force on coatings performances. *J Mater Res* 31. <https://doi.org/10.1557/jmr.2016.191>
5. Qi S, Li X, Zhang Z (2017) Fabrication and characterisation of electro-brush plated nickel-graphene oxide nano-composite coatings. *Thin Solid Films* 644:106–114. <https://doi.org/10.1016/j.tsf.2017.06.064>
6. L I, S I, H A (2017) Structure zone diagram and particle incorporation of nickel brush plated composite coatings. *Sci Rep* 7. <https://doi.org/10.1038/srep44561>
7. Jeff H (1992) Selective brush plating for decorative applications. In: The proceedings of the 7 AESF annual technical conference. The American electroplaters and surface finishers society, Atlanta, Georgia, pp 1223–1232
8. Yan W, Liu H, Zhu W (2015) Preparation of anti-corrosion superhydrophobic coatings by Fe-based micro/nano composite electro-brush plating and blackening process. *RSC Adv*. <https://doi.org/10.1039/C5RA15640H>
9. Wenjing W, Xuefeng L (2015) Influences of brush plating solutions composition and technological parameters on the quality of rolled copper foil surface coatings. *J Mater Res* 30:3766–3775. <https://doi.org/10.1557/jmr.2015.369>
10. Bin W, Bin-shi X, Bin Z (2006) Automatic brush plating: an update on brush plating. *Mater Lett* 60:1673–1677
11. YP V, K BK, S R (2019) Parameter optimization and wear characteristics of nano CuO/Ni composite coating by brush plating technique. *Proc I MechE Part J: J Eng Tribol*. <https://doi.org/10.1177/1350650119864466>

12. M/s Grauer and Weil (2009) Technical datasheet for Alzincate D
13. M/s Grauer and Weil (1990) Technical datasheet for Ginplate electroless nickel 422
14. M/s Grauer and Weil (2003) Technical datasheet for Silvermix bright silver
15. MIL-STD-202 G electronic electrical component parts. http://everyspec.com/MIL-STD/MIL-STD-0100-0299/MIL-STD-202G_2397/. Accessed 7 May 2018

Numerical Synthesis of Bending Behaviour of Flexible Composite Tape Spring



Megha Thaker , Hemant Arora , Dhaval Patel , and Shashikant Joshi 

Abstract The tape spring is defined as a straight, thin-walled elastic strip with a curved cross section. It has inherent properties which allow for folding elastically, and when unfolded, it releases stored energy. In aerospace applications, these properties are used to deploy an antenna, solar panels, structural booms, and arrays. For many years, metallic tape springs have been in application, but the present trend is towards a tape spring made of carbon fibre-reinforced plastic (CFRP) due to its low mass, low coefficient of thermal expansion, and tailorable properties. The tape springs made of CFRP have wide applications for space deployable structures. This work comprises the exploration of numerical methods to find the moment-rotation relation of folding the CFRP tape spring. The moment-rotation relation is obtained for equal and opposite sense bending using numerical methods like the analytical approach and the finite element (FE) method. Detailed nonlinear structures simulations are carried out using the nonlinear explicit dynamic solver Altair Radioss. Material properties $[0^\circ, 90^\circ]_2$ lay-up style for laminates and boundary conditions are applied to the CFRP tape spring to analyse the effect of a moment with angular rotation. Conclusions were made with the results obtained by FE simulations in comparison with the results obtained by an analytical model. The FE simulation results deviate from the analytical model with a maximum bending moment for equal sense by 5.84% and the opposite sense bending by 1.01%. The results are in good agreement and presented with logical conclusions.

M. Thaker (✉) · D. Patel · S. Joshi
Nirma University, Ahmedabad, Gujarat 382481, India
e-mail: 19mmcc16@nirmauni.ac.in

D. Patel
e-mail: dhaval.patel@nirmauni.ac.in

S. Joshi
e-mail: s.j.joshi@nirmauni.ac.in

H. Arora
Space Applications Centre, Indian Space Research Organisation, Ahmedabad, Gujarat 380015, India
e-mail: hemant_arora@sac.isro.gov.in

Keywords Carbon fibre-reinforced plastic (CFRP) · Tape spring · Numerical synthesis · Nonlinear finite element analysis · Bending moment-rotation relation · Deployable structure

1 Introduction

In the current scenario, the aerospace industry trends are growing towards simple, cheap, and more reliable deployable structures. A deployable mechanism is being replaced by the traditional space structure in applications for transportation and launches. This facilitates the assembly of the large-scale structures of aerospace into a small enough space. During aerospace missions, it can be expanded into large structures. Many satellite systems now use deployable mechanisms, such as satellite antennas, synthetic aperture radar (SAR), booms, and solar arrays [1]. In the initial phases of space exploration, deployable structural members used thin cylindrical shells [2]. The carpenter tape spring is widely used in shell-type structures because of its beneficial engineering characteristics.

Tape springs have a low mass-to-stiffness ratio, no mechanical joints, high efficiency of enfoldment, and a low cost. One of the major reasons for its use in space applications is that it spontaneously deploys without external driving forces [3]. For several years, the tape spring was typically manufactured using metallic materials like beryllium copper (BeCu) or high-strength steel. But with a current trend, a tape spring is being explored to be manufactured with a carbon fibre-reinforced plastic (CFRP) composite material. It potentially offers tailorable performance, low mass, low coefficient of thermal expansion, and also integral construction with other parts.

The moment-rotation behaviour is very easy to evaluate for a metallic tape spring because it is made of isotropic material. The study of composite tape spring behaviour is slightly complex due to its orthotropic material properties. A tape spring can fold in an equal (same) sense or the opposite sense. For equal sense bending, the longitudinal and transverse curvatures are in the same sense, see Fig. 1a. For the equal sense bending case, the compressive stresses appear on the edges and deformation occurs. Moreover, for opposite sense bending, the longitudinal and transverse curvatures are in the opposite direction, see Fig. 1b. In this case, tensile stresses act on the edges.

The moment-rotation relationship of the tape spring is symmetric bending and nonlinear as a direction-dependent relationship. For example, in the opposite sense of bending, the tape spring suddenly buckles from the fold due to the transverse curvature in the opposite direction of bending. An equal sense of bending creates transverse curvature in the same direction, so the fold changes more gradually.

Significant characteristics of moment-rotation behaviour for equal and opposite sense bending of the tape spring are [4]: (1) both senses of bending have elastic folds that have a longitudinal radius of curvature, and that is independent of the end rotations when a force is applied on the ends; (2) the peak stress and strains of a folded tape spring are independent of the end rotations; (3) while unfolding a tape spring, it snaps back into a straight configuration that is most noticeable for the opposite sense

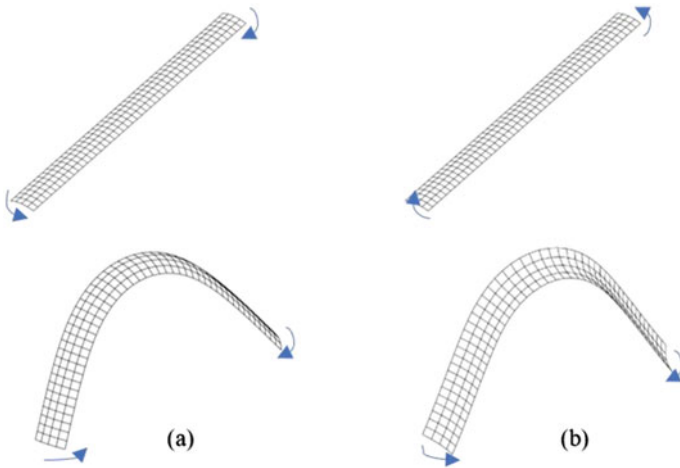


Fig. 1 Folding a tape spring: **a** equal sense bending and **b** opposite sense bending

of bending. This last characteristic is most useful for self-latching components in the deployable structure.

This paper is presented with a detailed study of numerical approaches explored for evaluating the bending behaviour by prediction of the moment-rotation relation of the CFRP tape spring in equal and opposite senses. Various analytical approaches are explored widely by many researchers for evaluating the bending behaviour of curved beams. An effort has been made in establishing an understanding of analytical expressions and applied to solve the moment-rotation relationship of curved beams made of orthotropic material like CFRP. To correlate the analogy, the laminate of the CFRP curved section beam is modelled with the finite element method and assigned to orthotropic lay-up sequence properties. A methodology for solving nonlinear structural simulation has been established using the explicit dynamic solver, Altair’s Radioss.

2 Analytical Method

Wuest [5] and Mansfield [6] introduced tape spring rotation angle and moment response. For the thin-walled hinges, Mobrem and Adams [7] studied the relationship between angle and bending moment of the deployment process. Seffen and Pellegrino [8] studied the deployment dynamics of a tape spring. Soykasap [9] experimented with the composite thin-walled tube hinge which has three tape springs and matched simulation results of the mechanical properties during the quasi-static deploying process with experimental results. Huina and Tibert [10] proposed lightweight fibre-reinforced tape spring composites for deployable space structures for nanosatellites. Liangwei et al. [11] analysed the bending characteristics of composite tape springs

using analytical and finite element models. Zuo et al. [12] studied the opposite sense bending process of the CFRP tape spring and derived its bending moment calculative formula. And also, those results are assessed by the FE analysis results. Yee et al. [4] derived the analytical expression for the bending moment of a general CFRP tape spring, and the accuracy of that expression is evaluated by FE analysis.

To the best of the author's knowledge, the majority of the research work has been carried out to evaluate the bending characteristics of the tape spring made of isotropic material. Moreover, the available studies focus on the steady moment rather than the maximum moment for bending of the tape spring. At present, the tape spring finds applications in the space domain for the deployment of payload structures. Therefore, it is required to investigate the bending behaviour of tape springs made of orthotropic material in both equal and opposite senses. Therefore, this paper is presented with a detailed study of bending behaviour by prediction of the moment-rotation relation of the CFRP tape spring in equal and opposite senses. The maximum and steady moment results are computed for equal and opposite sense bending. The tape spring is proposed to be constructed from a laminate of CFRP layers in the design direction and has orthotropic material properties.

2.1 Material Properties of the CFRP Tape Spring

The material properties of the CFRP tape spring are given in Table 1. In this paper, the CFRP tape spring adopts the asymmetric $[0^\circ, 90^\circ]_2$ lay-up style. It is estimated that the tape spring will generate large and small deformations in the longitudinal and transverse directions, respectively. Furthermore, the selection and lay-up direction of the CFRP material are estimated based on loading conditions. CFRP laminates are typically oriented in three major fibre directions: 0° , 45° and 90° . The 0° ply mainly carries the axial load, the $\pm 45^\circ$ carries the shear load which is negligible in bending of tape spring hence not considered, and the 90° ply mainly carries the transverse load.

2.2 Geometric Characteristics of the Tape Spring

The geometry of a CFRP tape spring is defined through its length L , thickness t , its subtended angle α , and transverse radius of curvature R . The tape spring structure is straight without any longitudinal curvature, as shown in Fig. 2. The geometric parameters of the tape spring which are considered for the study are explained in Table 2. The general coordinate system used in the analysis is also shown in Fig. 2. The Y -axis is defined vertically along the longitudinal direction of the tape spring, the Z -axis lies along the transverse direction, and the X -axis is normal to the centreline of the Y -axis.

Table 1 Material properties for CFRP tape spring

Property	Value
Longitudinal modulus, E_1 (GPa)	126
Transverse modulus, E_2 (GPa)	8
Poisson's ratio	0.33
In-plane shear modulus, G_{12}, G_{31} (GPa)	5.6
Out-of-plane shear modulus, G_{23} (GPa)	3.7
Density (kg/m^3)	1780
Longitudinal tensile strength, F_{1t} (GPa)	1.05
Transverse tensile strength, F_{2t} (GPa)	0.04
Longitudinal compressive strength, F_{1c} (GPa)	0.703
Transverse compressive strength, F_{2c} (GPa)	0.12
Out-of-plane shear strength, S_{12} (GPa)	0.07

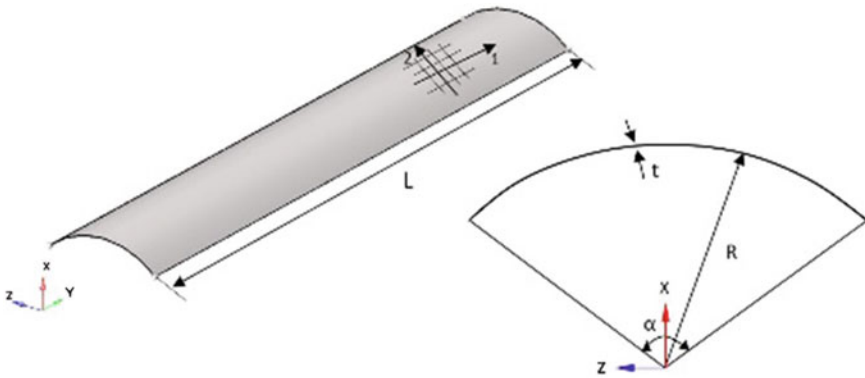


Fig. 2 Geometrical parameters of the CFRP tape spring

Table 2 Geometric parameters of the CFRP tape spring

Parameter	Value
Length, L	140 mm
Thickness, t	0.3 mm
Subtended angle, α	85°
Transverse radius of curvature, R	18 mm
Lay-up style	$[0^\circ, 90^\circ]_2$

2.3 Bending Behaviour of Tape Spring

A schematic diagram of the moment-rotation relation of opposite and equal sense bending of the tape spring is shown in Fig. 3. For the opposite sense of bending, the moment linearly changes with the bending angle for a small rotation and produces a

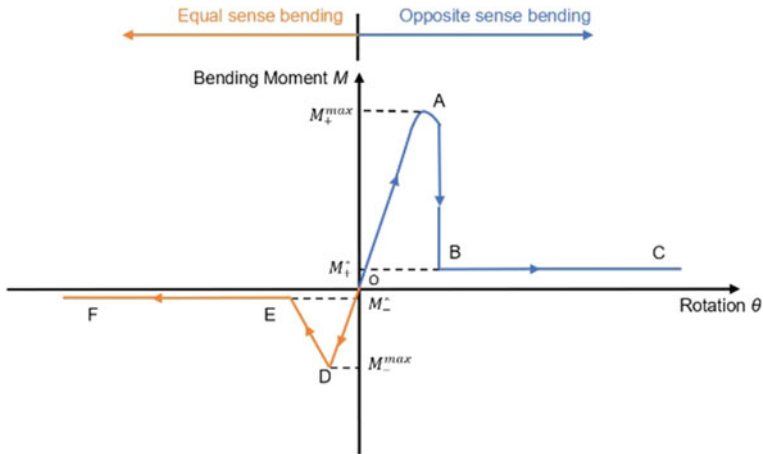


Fig. 3 Bending moment-rotation diagram for tape spring

smooth curve. For large rotations, the forces increase, and the cross section becomes flat, mainly in the middle area, until it reaches a maximum moment (A). When the value of a moment reaches its maximum, a fold forms in the middle and buckling occurs. At this maximum value of a moment, the longitudinal curvature becomes nonzero, and transverse curvature becomes zero. The bending moment is decreased suddenly (AB) with the buckling, as shown in Fig. 3. After that, the rotation increases (BC), and the bending moment remains constant, which is called a steady-state moment [5].

For the equal sense of bending and small rotation, the bending moment varies with the bending angle. First, the OD is the same as the slope of OA, but linear behaviour ends up quickly. While in the opposite sense, buckling occurs at point A, likewise, in the equal sense, buckling occurs at point D, $M_-^{max} < M_+^{max}$. In the same sense, the structure becomes stiffer. At extreme values, the tape increases the value of asymmetric torsional folds and moves towards the middle. And at the same time, the bending moment (DE) decreases. But when the tape spring folding reaches the middle, it produces symmetric values, the same as in the opposite sense. Then, for the folding (EF), the bending moment remains constant as M_-^* .

2.4 The Analytical Approach

An analytical expression for the tape spring’s moment–curvature relationship during its opposite sense of bending was first obtained by Wuest [5]. Wuest studied a tape spring loaded by end moments that created a longitudinal curvature. The CFRP tape spring is typically made from several fabrics that are laminated together to give it orthotropic material properties. Wuest’s moment–curvature relationship is suitable

for isotropic materials, and it does not apply to the orthotropic material CFRP tape spring. So, Wuest's relationship was extended to evaluating the bending behaviour of the orthotropic CFRP tape spring. As described in Sect. 2.3.1, M_+^* and M_-^* are the steady-state moments for the tape spring under opposite sense and equal sense bending, respectively. Soykasap et al. [4] have explained the evaluation of steady-state moments and fold radius of curved tape spring, which is also applicable to non-symmetric laminates.

The analytical expression for the fold region in a tape spring can be calculated by observing that it is approximately cylindrical, as the transverse radius of curvature is zero. The theoretical equations for a thin plate, in terms of stress and strain resultants [4], are

$$\begin{Bmatrix} N \\ \dots \\ M \end{Bmatrix} = \begin{bmatrix} A & \vdots & B \\ \dots & \dots & \\ B & \vdots & D \end{bmatrix} \begin{Bmatrix} \varepsilon^0 \\ \dots \\ k \end{Bmatrix} \quad (1)$$

where $N = [N_x N_y N_{xy}]^T$ represents mid-surface stress and $M = [M_x M_y M_{xy}]^T$ represents mid-surface bending moments. $\varepsilon^0 = [\varepsilon_x^0 \varepsilon_y^0 \varepsilon_{xy}^0]^T$ represents mid-surface strain. $K = [K_x K_y K_{xy}]^T$ represents mid-surface twist curvature. A is the stiffness coefficient related to internal force and ε^0 , called tensile stiffness. D is the stiffness coefficient of the internal moment related to K , called bending stiffness. B is a coupling relationship, called coupling stiffness. The value of B is equal to zero if the symmetric laminates are used because there is no coupling relation between stretching and tensile.

Equation 1 can be converted to the mixed form,

$$\begin{Bmatrix} \varepsilon^0 \\ \dots \\ M \end{Bmatrix} = \begin{bmatrix} A^* & \vdots & B^* \\ \dots & \dots & \\ C^* & \vdots & D^* \end{bmatrix} \begin{Bmatrix} N \\ \dots \\ k \end{Bmatrix} \quad (2)$$

where

$$[A^*] = [A]^{-1} \quad [C^*] = [B][A]^{-1}$$

$$[B^*] = -[A]^{-1}[B] \quad [D^*] = [B] - [B][A]^{-1}[B]$$

The results of in-plane stress are assumed to be negligible ($N = 0$). So, mid-plane strains (ε^0) and bending moments (M) are obtained. By folding tape, curvatures change in longitudinal and transverse directions ($\Delta k_x, \Delta k_y$). By this, the corresponding bending moments can be calculated (M_x, M_y). In the area of the fold tape

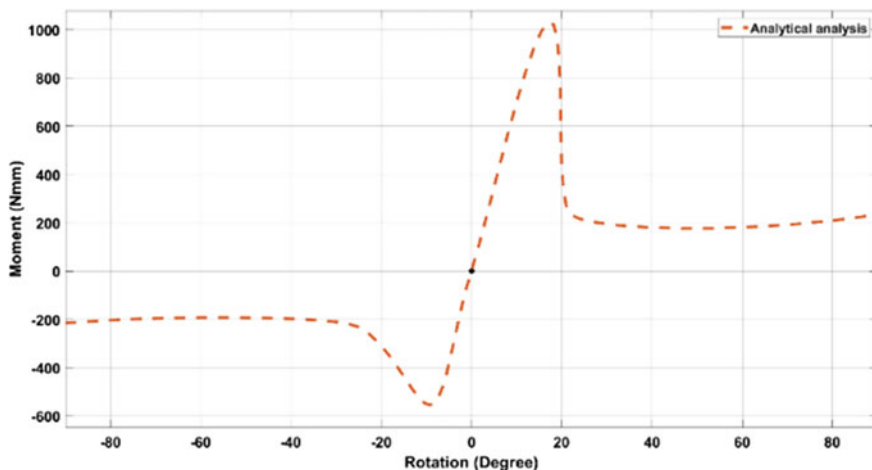


Fig. 4 Plot of moment-rotation relationship of the CFRP tape spring

region, the total bending strain energy (U) is obtained. The steady-state bending moments for equal and opposite sense bending of CFRP tape spring are calculated

$$M_+^* = \left(\sqrt{D_{11}D_{22}} + D_{12} \right) \alpha \quad (3)$$

$$M_-^* = \left(-\sqrt{D_{11}D_{22}} + D_{12} \right) \alpha \quad (4)$$

where D_{11} , D_{22} , and D_{12} are the bending stiffness and α is the subtended angle of tape spring. The subscripts + and – denote opposite sense and equal sense bending, respectively.

The CFRP tape spring's moment-rotation relation can be obtained by Eqs. (3, 4) through the MATLAB [13] software, see Fig. 4. Its maximum bending moment (M_+^{\max}) is 1030.7 Nmm, and steady-state moment (M_+^*) is 233.54 Nmm for opposite sense bending. And for equal sense 555.52 Nmm, and 215.78 Nmm is maximum (M_-^{\max}), and steady-state (M_-^*) bending moments, respectively.

3 Finite Element Method

The tape spring is modelled by thin shell elements using hypermesh simulation software and Radioss as a nonlinear dynamic solver. The stacking sequence direction of laminates is defined as $[0^\circ, 90^\circ]$ orientation. Orthotropic material properties are considered to be formulated as full laminates as described in Table 1. In Radioss, the property definition of laminate zone-based shell modelling, a ply defines the shape,

material, thickness, and fibre direction [14]. This data is useful for the automatic calculation of the composite laminate zones. As explained in earlier sections, the $[0^\circ, 90^\circ]_2$ lay-up style is considered to model the CFRP tape spring, shown in Fig. 5. The total thickness of the tape spring is 0.3 mm and each ply has 0.075 mm thickness.

A node-set (GNODE) is created in the middle of the tape spring, which is further connected to the tape spring ends by RBE2 rigid connections. The node-set consists of three nodes, viz. one node at the centre of the tape spring and the other two nodes connected to the ends of the tape springs. Boundary conditions are applied as described in Fig. 6. For pure bending of tape spring ends, rotational moments are applied to rigid elements and keep one node fixed at the centre. For bending, BCs have been given to both RBE2 elements as unconstrained in the Z-rotation direction. And another BCs to the central node, which translates in the X and Y direction, are shown in Fig. 6. The velocity is given to both RBE2 elements in the ZZ direction. The HyperView is used to investigate various parameters such as displacement, angular displacement, and stress. And HyperGraph is used to generate the moment-rotation plot.

Figure 7 shows the moment-rotation relationship of the CFRP tape spring by FEA. The maximum and steady bending moment is 1020.4 Nmm and 249.65 Nmm for opposite sense bending, respectively. And in an equal sense, the maximum bending moment attains 590 Nmm, and the steady moment is 230.42 Nmm.

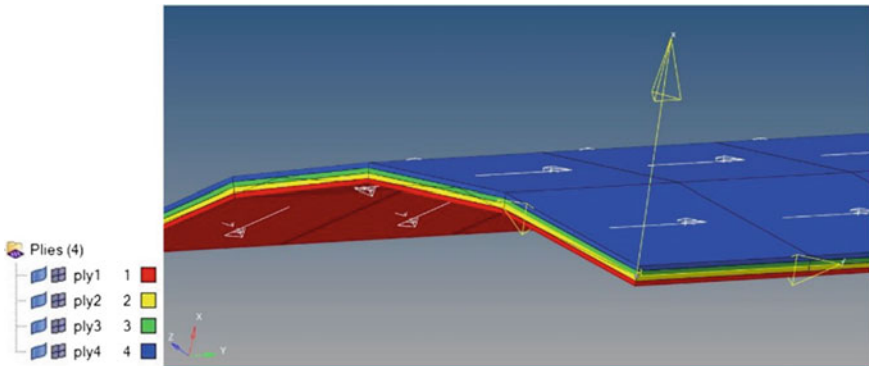


Fig. 5 Create piles

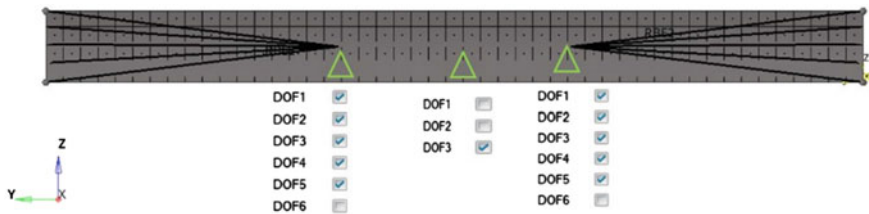


Fig. 6 BCs for the CFRP tape spring in the bending process

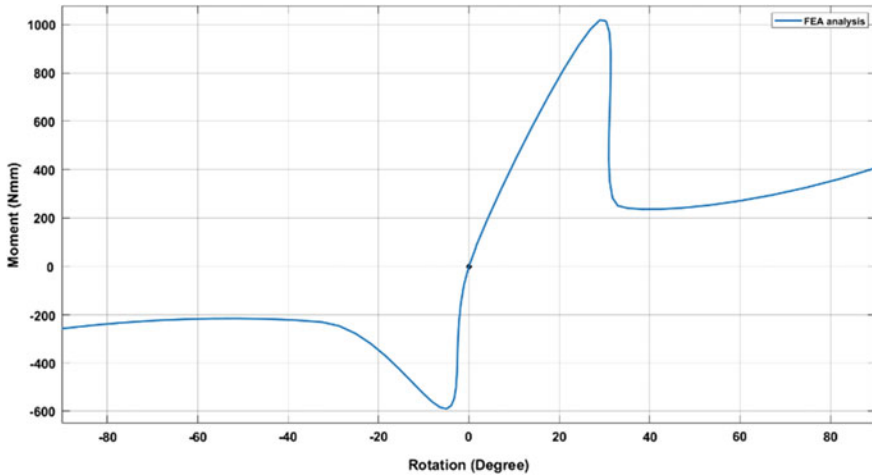


Fig. 7 Moment-rotation relationship of the CFRP tape spring by FEA

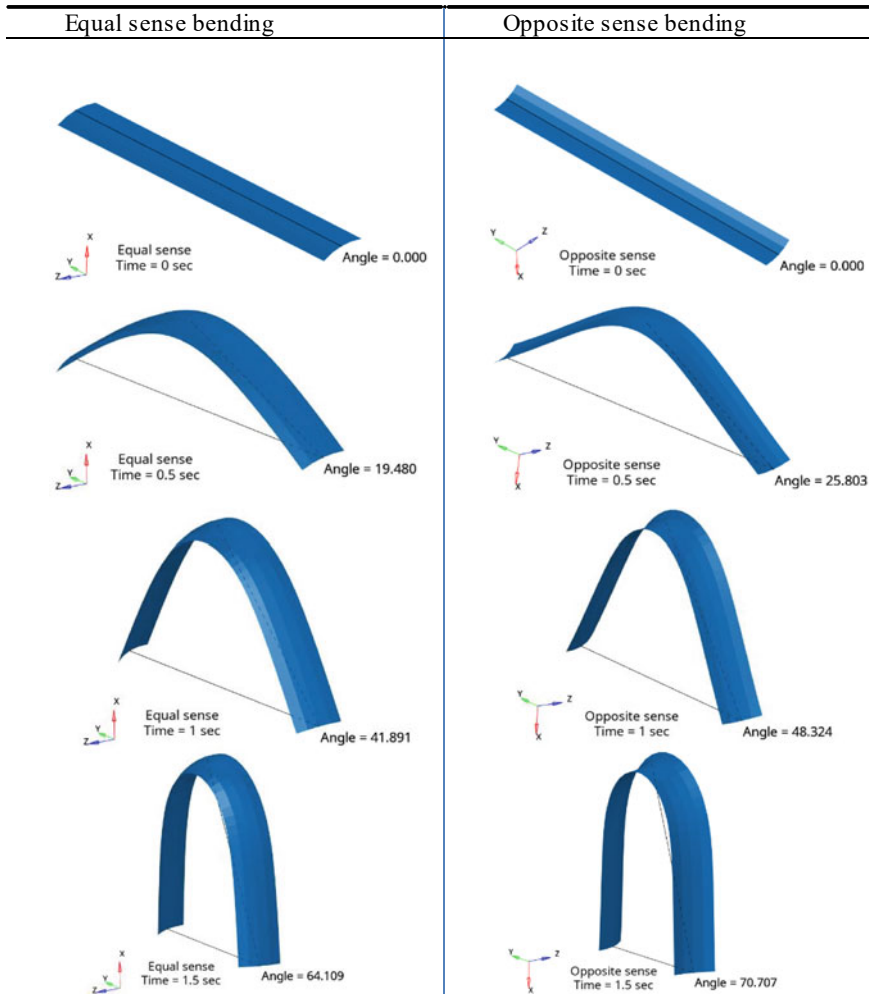
4 Results and Discussion

A detailed numerical synthesis of the moment-rotation induced by folding the CFRP tape spring with a $[0^\circ, 90^\circ]_2$ lay-up has been carried out by analytical and finite element methods for both equal and opposite sense bending. In both cases, localized folds of the tape spring are formed in a curved shape which has a uniform longitudinal radius of curvature and zero transverse curvature.

A series of snapshots of the folding sequence for equal and opposite sense bending of the CFRP tape spring is given in Table 3. The tape is subjected to angular deflections at the ends to create an equal and opposite sense of bending. It is observed that at the same time, the bending angle in the opposite sense is more than the equal sense bending which shows the stiffness behaviour of tape spring while bending in both cases (Fig. 8).

The difference in maximum bending moments for equal and opposite sense bending cases is predicted at 5.84 and 1.01% (see Table 4). It is necessary to discuss the probable causes of this difference: (1) For theoretical analysis, bending moment results are obtained under many assumptions, like that the bending and torsion coupling effects are neglected and pure bending is considered. Also, the tape spring is infinitely long and ignores its end effect. And the tape spring's curvature also changes from 0 to $1/r$ in its longitudinal direction and $1/r$ to 0 in the transverse direction. (2) For FE analysis, the tape spring is discretized into several finite elements. So, the finite element's quantity and quality will affect the accuracy of solving FEA. Also, in the FEM, the inaccurate assignment of the properties of parts and materials, loads, and BCs will govern the accuracy of solving the FEA.

Table 3 Bending sequence for equal and opposite sense bending of CFRP tape spring



5 Conclusion

This paper presented a detailed investigation of equal and opposite sense bending behaviour for the CFRP tape spring. The CFRP tape spring folding behaviour was studied through analytical and finite element methods. The folding process is highly nonlinear and also, by changing the direction of bending, the bending behaviour differs. The bending moments are solved analytically using expressions evolved by researchers. The finite element analysis is carried out by an explicit nonlinear solver Radioss using a detailed finite element model of a tape spring with the desired lay-up sequence and with orthotropic material properties. The whole folding sequence

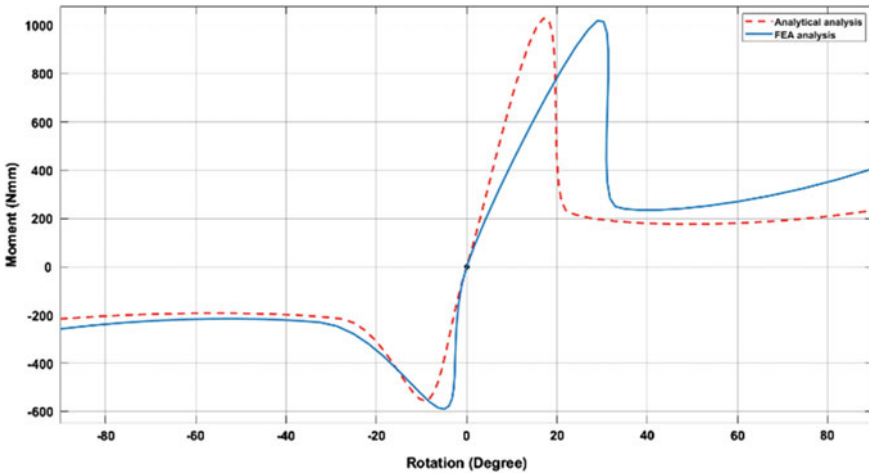


Fig. 8 Equal and opposite sense bending moment—angle diagram of CFRP tape spring

Table 4 Comparison of theoretical and FEA results for equal and opposite sense bending moments

Results	$M_*^*(Nmm)$	$M_-^{max}(Nmm)$	$M_+^{max}(Nmm)$	$M_*^+(Nmm)$
Theoretical	215.78	555.52	1030.7	233.54
FEA	230.42	590	1020.4	249.65
Difference (%)	6.35	5.84	1.01	6.45

is captured at multiple angular deformations for both equal and opposite sense bending cases. The results obtained by both methods are correlated and found to be a maximum difference of 6.4% with almost matching profile which is quite encouraging. Based on the comparison, it is observed that the opposite sense bending gives more angular displacement and bending moment than an equal sense of bending.

The key feature is that the bending moment of an asymmetric tape spring increases uniformly in equal and opposite directions. Therefore, this study will be helpful for future design and applications of CFRP tape spring. The present exercise has given the confidence to move further, as these CFRP-based tape springs have potential applications for flexible hinges in space deployable systems for futuristic Indian space missions.

Acknowledgements The authors would like to thank the team from DesignTech Systems Pvt. Ltd., Mumbai, for his kind support and valuable guidance in the Altairs Hyperworks and Radioss platforms. Authors extend gratitude towards Space Applications Center-ISRO for providing the opportunity towards working on space deployable systems.

References

1. Yang H, Liu R, Wang Y, Deng Z, Guo H (2015) Experiment and multi-objective optimization design of tape spring hinges. *Struct Multidiscip Optim* 51:1373–1384. <https://doi.org/10.1007/s00158-014-1205-9>
2. Bowden ML (1998) Space vehicle mechanisms: elements of successful design, Deployment devices. In: Conley PL (ed), pp 495–542
3. Seffen KA, You Z, Pellegrino S (2000) Folding and deployment of curved tape springs. *Int J Mech Sci* 42(10):2055–2073
4. Yee JCH, Soykasap O, Pellegrino S (2004) Carbon fibre reinforced plastic tape springs. American Institute of Aeronautics and Astronautics Paper, 2004–1819
5. Wuest W (1954) Einige anwendungen der theorie der zylinderschale. *J Appl Mathem Mech Zeitschrift Für Angewandte Mathematik Und Mechanik* 12:444–454. <https://doi.org/10.1002/zamm.19540341203>
6. Mansfield EH (1973) Large deflexion torsion and flexure of initially curved strips. *Proc R Soc Lond A* 334:279–298. <https://doi.org/10.1098/rspa.1973.0092>
7. Mobrem M, Adams D (2009) Deployment analysis of the lenticular jointed antennas onboard the mars express spacecraft. *J Spacecr Rocket* 46:394–402. <https://doi.org/10.2514/1.36890>
8. Seffen KA, Pellegrino S (1999) Deployment dynamics of tape springs. *Proc Royal Soc London A: Mathem Phys Eng Sci* 455(1983):1003–1048. <https://doi.org/10.1098/rspa.1999.0347>
9. Soykasap Ö (2009) Deployment analysis of a self-deployable composite boom. *Composite Struct* 3:374–381. <https://doi.org/10.1016/j.compstruct.2008.08.012>
10. Mao H, Tibert G (2017) Experiments and analytical modeling for designing tape spring composites. In: 21st international conference on composite materials
11. Su L, Sun B, Zhang Y (2019) Progressive damage analysis of deployable composite cylindrical thin-walled hinges. In: 10th international conference on mechanical and aerospace engineering, pp 338–342
12. Zuo Y-d, Jin G, Xie P (2018) Calculative and experimental study of the CFRP tape spring. *J Mech Sci Technol* 32(8):3603–3609
13. Borse GJ (1997) Numerical method with MATLAB: a resource for scientists and engineers. International Thomson Publishing, London, Britain
14. HyperWorks Introduction to practical aspects of composites ((2019)) Altair Engineering, Inc. 285. <https://www.altair.com/radioss>

A Review on Different Mechanisms Used in Power Generation Through Speed Bumps



Kunj Patel, Parth Patel, Tejas Ghodasara, and Sumit Tripathi

Abstract With the advancement of technology and change in human lifestyle, the use of motor vehicles has increased significantly over the last few decades. Increase in number of motor vehicles on road necessitates traffic calming measures for enhanced safety conditions and help reducing the accident rates. Speed bumps (or speed breakers) are widely used in several areas where a controlled movement of vehicle is required at reduced speeds such as signals, crossway, parking area, railway crossing, hospital area, roundabouts, markets, toll booths, and school areas. When a vehicle passes through a speed bump, a large amount of energy is exchanged between the vehicle and the road bump which depends on the type and weight of the vehicle and also on the height and material of the bump. Using appropriate mechanisms, the speed breakers can be converted to power generating units, and the produced electricity can be used for low power consuming devices like traffic signals, lights, hoardings, speed indicators, and emergency calling systems. In this work, we review four different mechanisms of power generation through a speed breaker: roller mechanism, rack and pinion mechanism, air piston mechanism, and crankshaft mechanism. We also briefly compare these mechanisms in terms of their design, maintenance, vibrations, and efficiency. It is noted that the ‘rack and pinion mechanism’ offers several advantages over other mechanisms in terms of mounting, frictional losses, and efficiency.

Keywords Electricity generation · Speed bumps · Alternative energy · Rack-pinion mechanism

1 Introduction

Around the world, the automotive industry has significantly contributed to the economic development of the society. To accommodate and manage the increase in number of vehicles, better road infrastructure and enhanced traffic management

K. Patel · P. Patel · T. Ghodasara · S. Tripathi (✉)

Department of Mechanical and Aero-Space Engineering, Institute of Infrastructure, Technology, Research and Management, Ahmedabad 380026, India
e-mail: sumittripathi@iitram.ac.in

© The Author(s), under exclusive license to Springer Nature Singapore Pte Ltd. 2023
B. Pramod P. et al. (eds.), *Advances in Material Science and Metallurgy*, Lecture Notes in Mechanical Engineering, https://doi.org/10.1007/978-981-19-4918-0_13

127

systems are required. Speed breakers are traffic calming measures that can help reducing accident rates by allowing controlled movement of vehicles in sensitive or crowded areas. Using suitable mechanisms, the speed breakers can be converted to small power generating units, and the produced energy can be used to power small devices for better road safety. The kinetic energy of moving vehicles can be transformed to mechanical energy by using various types of mechanisms, which can ultimately be converted to electrical energy through a generator. Such mechanisms can be easily placed under the speed breaker using a dome like structure. The produced electricity can be used for low power consuming devices such as traffic signals, streetlights, hoardings, and safety devices. The popular mechanisms used to produce electricity from speed breaker are—roller mechanism, rack and pinion mechanism, crankshaft mechanism, and air piston mechanism. Each of these mechanisms has their own advantages and limitations. In this work, we review these four mechanisms, and compare their performance in terms of maintenance, design, and efficiency.

2 Different Mechanisms for Power Generation Through Speed Bumps

2.1 *Roller Mechanism*

This mechanism consists of a roller placed between two sides of a speed breaker as shown in Fig. 1. The roller rotates whenever a vehicle passes over it (because of the grip on the surface of the roller), this rotates the generator shaft which is connected through a chain drive with roller [1]. Thus, the vehicle's kinetic energy is ultimately transformed into electrical energy. This energy is stored in batteries and can be used by low power consuming devices such as small streetlights and traffic signals.

Das et al. used a roller mechanism for power generation by passing vehicles over the speed breaker with a velocity of 39 kmph with two passengers [2]. When the vehicle is ahead of the speed breaker, there is no movement of the roller due to which there is no production of electricity. As the vehicle passes over the speed breaker, roller starts to rotate, and torque is induced in the roller resulting in generation of voltage and current. Once the vehicle crosses the speed breaker, roller rotation starts decreasing and gradually reaches to stop position, which results in decrease in terminal voltage and current to nearly zero [2]. Das et al. collected experimental data using a CNG auto rickshaw for different types of load (kg) [2]. The experimental data of variation in maximum generated voltage and mean power with respect to various loads is shown in Fig. 2.

Because of large variations in voltage and current, Das et al. calculated power for 12 observations and estimated the means power using [2]:

$$W = \sum W_j/n \quad (1)$$

Fig. 1 Sketch of roller mechanism (reconstructed from [2])

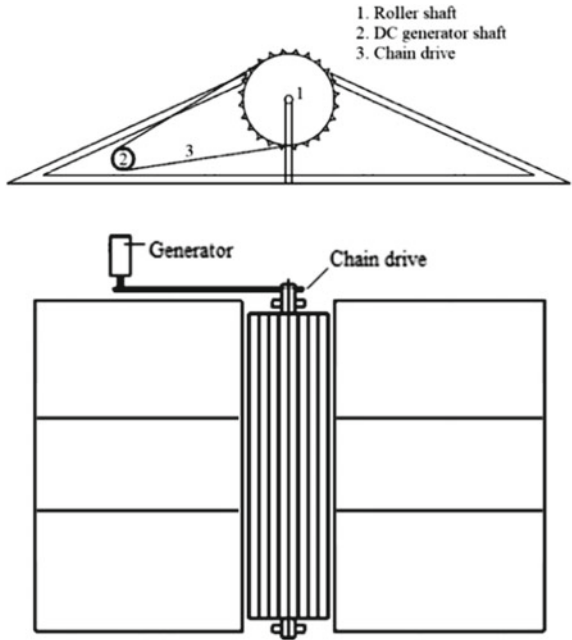
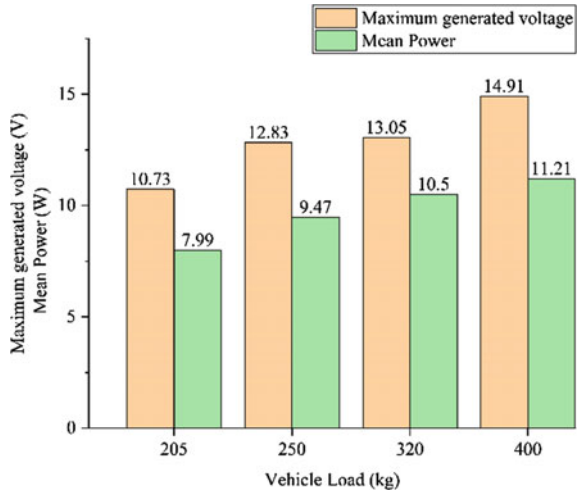


Fig. 2 Mean power and voltage versus vehicle load (data from [2])



where

W = Mean power

W_i = Power in i th observation ($i = 1$ to n)

n = Total observations.

The estimated mean power in their experiment was 9.47 W for vehicle load of 250 kg (CNG auto rickshaw with one passenger) [2].

2.2 Rack and Pinion Mechanism

Rack and pinion mechanism includes gear in circular shape called pinion, and a rack, which is a bar in linear shape having teeth. As rack and pinion are connected, the mechanism converts the rack's reciprocating motion into rotational motion of pinion [3]. In this mechanism, as the speed breaker shifts downwards due to a vehicle passing over it, the springs linked with it also get compressed. When the vehicle crosses the speed breaker, the spring brings it back to original position. As the rack is connected to the lower part of the speed breaker, it also moves up and down and rotates the pinion. Thus, reciprocating motion of the rack is converted to rotary motion of the pinion, and a generator can convert this mechanical rotational energy to electrical energy. Generation of energy by this mechanism depends on several factors including traffic density and vehicle load [3]. The arrangement of rack-pinion mechanism is shown in Fig. 3.

Ramadana et al. constructed a prototype for generating electricity using the rack and pinion mechanism and performed an experimental study to measure the amount of voltage, current, and angular speed for three different masses of 41 kg, 65 kg, and 80 kg, respectively [4]. From the experiment, they observed that electrical power of 6.5 W, 26.2 W, and 44.7 W was produced by masses of 41 kg, 65 kg, and 80 kg, respectively. Thus, produced power was 0.16 W/kg, 0.40 W/kg, and 0.56 W/kg, respectively [4]. Hossain et al. opined that power generation by rack and pinion mechanism is slightly cheaper than other available alternatives [3]. This observation was based on an experiment using 70 kg mass of the vehicle for both rack-pinion and roller mechanisms. The power developed in one hour by the rack-pinion mechanism and roller mechanisms were 23.76 kW and 7.29 kW, respectively [3]. A comparison of results using similar parameters showed that the rack and pinion mechanism produced

Fig. 3 Sketch of rack-pinion mechanism (reconstructed from [4])

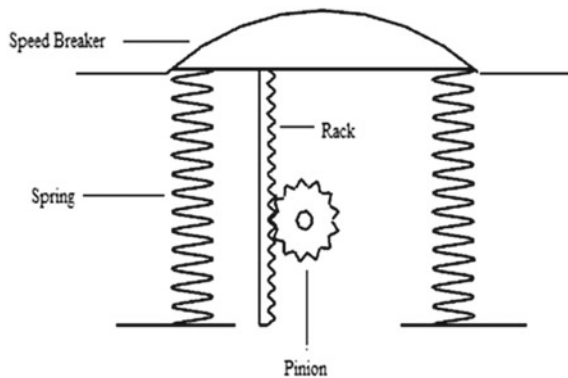
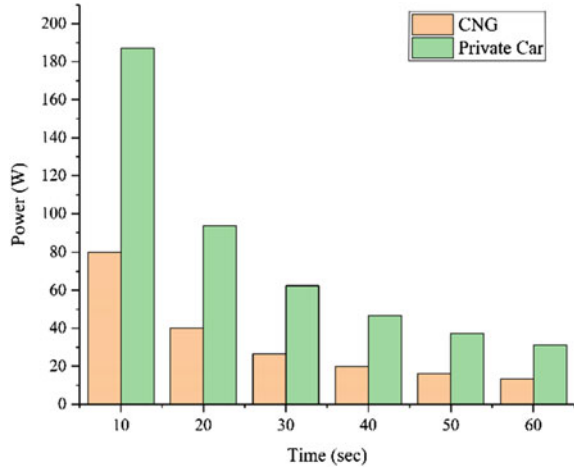


Fig. 4 Power versus time for CNG auto rickshaw and private car (data from [7])



almost three times the power as compared to roller mechanism [3]. Further, the rack and pinion mechanism consists of lesser number of parts that are easily available, and the assembly of this mechanism is also cheaper. Ahmadi et al. conducted an experiment using rack-pinion mechanism, where 500 kg vehicle moved over speed breaker with speed of 15 kmph. The width and height of the speed breaker were 20 cm and 10 cm, respectively. They reported that for 1000 cars having 500 kg weight, the generated electrical energy will be 2.6 MW considering 25% energy conversion efficiency [5]. Haris et al. performed an experimental study using the rack-pinion mechanism by applying a fixed amount of force to the speed breaker which was equivalent to 13 vehicles passing over it [6]. The continuous passing of vehicles caused an increase in rotational speed until 26 humps, beyond which the rotational speed did not increase because of its physical capability [6]. Voltage up to 10.903 V was generated using a power hump from the speed breaker [6]. Haider et al. used the rack-pinion mechanism and performed an experiment with a CNG auto rickshaw having 680 kg weight and private car weighing 1590 kg [7]. They presented that during smaller time duration, the power generated is high, and it is comparatively low in longer time duration, as shown in Fig. 4 [7]. Dara et al. studied and analyzed papers by several researchers who worked on rack and pinion mechanism in their studies [8]. The recorded output powers for a vehicle load of 400 kg over different heights of speed breaker dome are shown in Table 1 [8].

2.3 Crankshaft Mechanism

The main motive of the crankshaft mechanism is to convert linear movement into rotary movement and vice versa. In place of rack and pinion, crankshaft is used as the main mechanical component of this mechanism, however, the working principle

Table 1 Output power for different dome heights with vehicle load of 400 kg [8]

Height of dome (cm)	Power output (W)
10	392.4
15	588.6
5	178.2
8	313.9

is similar to the rack and pinion mechanism [9]. Due to compression of the speed breaker (while passing the vehicle), the crankshaft’s linear motion is converted to rotary motion, which is connected to a larger gear. Transmission of power takes place from larger gear to the smaller pinion; this rotates the pinion at a higher speed sufficient to generate power [9]. The crankshaft arrangement along with supporting mechanisms is shown in Fig. 5.

Sinha et al. used a slider crank mechanism for generating electricity through a speed breaker [11]. Kumar et al. studied a trisection with six routes for a time period of 8 h and considered passenger cars, two wheelers and three wheelers, with 10% increment of traffic every year since 2015 [12]. Considering that the crank will rotate two times for each passing car as it contains two axles [11], they calculated average power generated as follows:

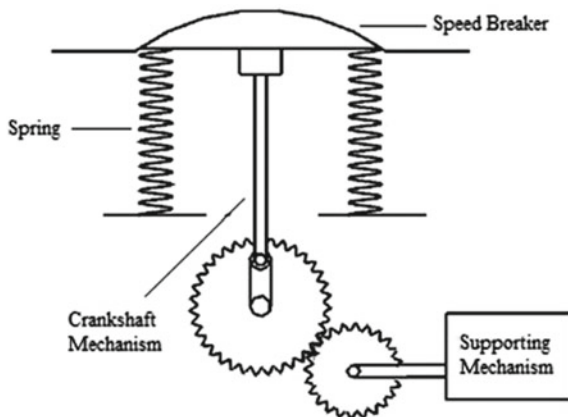
Average mass of a vehicle

$$M_{avg} = (P_1 \times m_1) + (P_2 \times m_2) + (P_3 \times m_3)$$

where

- P_1 is percentage of two wheelers,
- P_2 is percentage of three wheelers,
- P_3 is percentage of other vehicles,

Fig. 5 Sketch of crankshaft mechanism (reconstructed from [10])



- m_1 is mass of two wheelers,
- m_2 is mass of three wheelers,
- m_3 is the mass of other vehicles.

Average work done per vehicle $W_{avg} = M_{avg} \times g \times h$, where g is the gravitational acceleration and h is the height of the speed breaker. Therefore, average power generated is given as $P_{avg} = W_{avg} \times n/60$, where n is the number of passenger cars passing per minute. In their study, the mechanical efficiency and electrical efficiency were assumed to be 70% and 90%, respectively, for the whole system, and energy generated in one day was estimated to be 1.542 kWh [11].

2.4 Air Piston Mechanism

In the air piston mechanism also, the dome goes down when a load of vehicles is applied on it. Curved shaped dome is attached to the piston by a connecting rod which is supported by spring as shown in Fig. 6. Compression of air takes place in the compressor cylinder because of this downward movement of the piston. This compressed air gets out from the delivery valve, which is also called exhaust stroke, and then, it is conserved in the air storage tank [13, 14]. Whenever the vehicle crosses the speed breaker, the piston changing its position moves upwards due to which spring moves. This movement of spring lets the compressor to intake air which is similar to suction stroke. This whole process is repeated due to continuous passing of vehicles. This frequent reciprocating motion of the piston connected to the dome completes both strokes of the compressor resulting in shaft's rotation of the generator [13, 14].

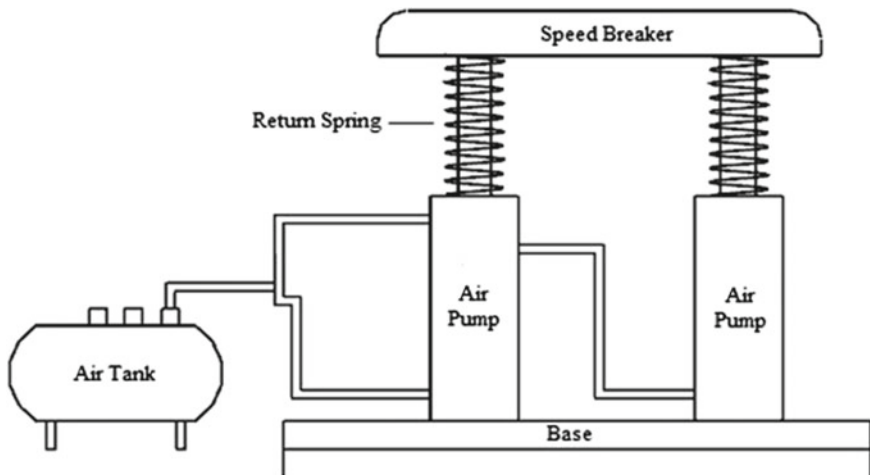


Fig. 6 Sketch of air piston mechanism (reconstructed from [15])

Table 2 Comparison of different mechanisms [7, 13]

Criteria	Types of mechanism			
	Roller	Rack and pinion	Air piston	Crank shaft
Setup	Simple	Difficult	Complicated	Difficult
Setup cost	Cheaper	Moderate	Costlier	Costlier
Design	Easy	Depends on weight capacity	Depends on compressing power	Depends on load applied
Maintenance required	Daily basis	Weekly basis	Daily basis	Daily basis
Efficiency	Poor (~50%)	Good (~70)	Better (~85)	Very poor (~40)

3 Comparison and Discussion

All the mechanisms have their own advantages as well as drawbacks. A major downside of roller mechanism is that the roller sometimes slips, which reduces mechanism efficiency, additionally, there are collision and maintenance issues [16]. Crankshaft mechanisms also have some disadvantages including mechanical vibrations which may cause damages to the bearing [16]. Due to usage of crankshaft, balancing problems also increase in the bearings. Further, the air piston mechanism has higher efficiency than any other mechanism because of fewer components, however, the setup cost is high, and maintenance is difficult. A mechanism which has fewer disadvantages and several advantages over other mechanisms is the rack and pinion mechanism. It gives good mounting, has minimum gear losses, and has higher efficiency, which makes it the most suitable mechanism. A comparison of all four mechanisms is shown in Table 2.

4 Conclusions

Different mechanisms of power generation through speed breaker are reviewed, and basic limitations of each mechanism is presented. It is noted that the rack and pinion mechanism is a relatively better option for generation of electricity through speed breaker because it has several advantages over other mechanisms. However, other mechanisms have their own merits, and the final choice of mechanism should be based on critical evaluation of all the parameters. Overall, speed breakers can be used for energy generation in controlled areas such as toll plaza, signals, and parking areas. A test facility in such areas can produce more electricity compared to the experimental and estimated results and give better estimate of its suitability in field applications.

References

1. Sarma BS, Jyothi V, Sudhir D (2014) Design of power generation unit using roller mechanism. *IOSR J Electr Electron Eng (IOSR-JEEE)* 9(3):55–60
2. Das CK, Hossain SM, Hossan MS (2013, May) Introducing speed breaker as a power generation unit for minor needs. In: 2013 international conference on informatics, electronics and vision (ICIEV). IEEE, pp 1–6
3. Hossain ME, Hasan MR, Ahmed KT, Shawon MNM (2017, September) Design and performance of power generation using speed breaker with the help of Rack and Pinion mechanism. In: 2017 4th international conference on advances in electrical engineering (ICAEE). IEEE, pp 7–11
4. Ramadan M, Khaled M, El Hage H (2015) Using speed bump for power generation—experimental study. *Energ Procedia* 75:867–872
5. Al Ahmadi AA, Alshehhi AS, Alnahdi HA, Albulooshi MM, Radaideh O, Voudouris KN (2018) Power generation through road speed breakers—an experimental approach. In: 2018 advances in science and engineering technology international conferences (ASET). IEEE, pp 1–6
6. Haris HM, Nor MM, Rahiman MF, Rahman NA (2016, December) Development of energy harvesting using speed breaker. In: 2016 IEEE conference on systems, process and control (ICSPC). IEEE, pp 53–57
7. Hossam-E-Haider M, Rokonzaman M (2015, February.) Design of a efficient energy generating system using speed breaker for Bangladesh. In: 2015 5th national symposium on information technology: towards new smart world (NSITNSW). IEEE, pp 1–5
8. Dara JE, Odazie CM, Okolie PC, Azaka AO (2020) Design and construction of a double actuated mechanical speed breaker electricity generator. *Heliyon* 6(9):e04802
9. Santhosh MR, Kumar BS, Yuvaraja T (2017, December) Energy harvesting using speed breaker mechanism. In: 2017 international conference on electrical, electronics, communication, computer, and optimization techniques (ICEECCOT). IEEE, pp 201–204
10. Ravivarma K, Divya B, Prajith CP, Sivamurugan A, Vengatesan K (2013) Power generation using hydraulic mechanism at speed bumper. *Int J Sci Eng Res* 4(6):258–266
11. Sinha A, Mittal S, Jakhmola A, Mishra SK (2021) Green energy generation from road traffic using speed breakers. *Mater Today Proc* 38:160–168
12. Kumar SV, Priyadharshini P, Dhanalakshmi B, Settu K (2018) Study of traffic flow at a three-legged busy intersection in Vellore, India. *IOP Conf Ser Mater Sci Eng* 396(1):012015. IOP Publishing
13. Kumar M, Rahul KNS, Narra M, Ranga Rao BP (2020) Efficient method on energy regeneration through speed breakers. *Int J Innov Technol Explor Eng (IJITEE)* 9(3S2). ISSN 2278-3075
14. Sharma AK, Trivedi O, Amberiya U, Sharma V (2012) Development of speed breaker device for generation of compressed air on highways in remote areas. *Int J Rec Res Rev* 1:11–15
15. Majgankar R, Agarwal Y, Jadhav G, Suryawanshi T, Jangale S (2019) Study on generation of electricity using speed breakers of different mechanisms. *Int J Innov Res Sci Eng Technol* 8(3)
16. Teja S, Reddy S, Kumar A, Raj V, Babu VP (2016) Power generation through speed breakers. *Int J Mag Eng Technol Manage Res* 314–320

The Behavior of Pyro-Carbon Matrix Synthesized Through Isothermal Chemical Vapor Infiltration (I-CVI) Process



Dipoo Kumar, N. Gomati, Deepak Kumar Agarwal, and B. Santhosh

Abstract Isothermal chemical vapor infiltration (I-CVI) process used for the manufacture of carbon fiber-reinforced carbon matrix (C/C) composite products is process parametric sensitive. In this work, the characteristics of the pyro-carbon (PyC) matrix deposited through the I-CVI process are investigated. The chemical kinetics of this process was simulated to study the change in microstructure of PyC with the variation of process parameter. The nature of the carbon deposited at various temperatures, pressure, residence time of gas, and the effect of the molar ratio of methane to nitrogen gas on the microstructure of the deposited (PyC) is examined. The effect of carbon fiber preform porous structure on the I-CVI process and its densification characteristics was further studied. It was observed that during the I-CVI process, pores are playing a major role in the densification characteristics. The results have revealed that the properties of I-CVI processed C/C products can be improved by proper selection and controlling of process parameters. Based on this study, process guidelines are proposed for densification of continuous carbon fiber preform to optimally develop C/C composite products.

Keywords I-CVI · Pyro-carbon texture · Residence time of gas · Thiele modulus

1 Introduction

Carbon–carbon composites exhibit lightweight and excellent mechanical properties at high temperatures, extreme thermal stabilities, and better erosion properties. These properties of C/C composite make it a synergistic material suitable for hot structures

D. Kumar (✉) · B. Santhosh
Vikram Sarabhai Space Centre, Thiruvananthapuram, India
e-mail: hellodipoo.kumar@gmail.com

D. K. Agarwal
IIST, Thiruvananthapuram, India

N. Gomati
Liquid Propulsion System Centre, Thiruvananthapuram, India

ISRO, Thiruvananthapuram, India

in re-entry systems including carbon–carbon nozzle divergent cones of upper stages of the rocket and C/C throats for rocket nozzles [1, 2]. C/C composite products are realized either by densification of carbon fiber preform with carbon matrix derived from an organic precursor-like resin (phenol formaldehyde, furfuryl alcohol, etc.), coal tar pitch, or through cracking of light hydrocarbon like methane or propane gas, which decomposes and produces carbon matrix through the process of chemical vapor infiltration (CVI). One of the most promising techniques, to manufacture C/C composite products is isothermal chemical vapor infiltration (I-CVI), considering the crystalline structure of PyC, uniform densification, and liberty to realize complex shape products in their near net shape without defect, this process technique is better than other conventional processes [3]. The main limitation of this process is very slow and sensitive toward the process parameter which will attribute high cost and material properties repeatability, respectively. The process has been thoroughly investigated by several researchers to reduce process duration as well as to improve the microstructure of PyC [4–7]. The I-CVI process for pyrolytic carbon deposition in the porous carbon fiber preform using methane as a precursor gas and nitrogen as a carrier gas is a complex process. In this process, the precursor gas undergoes homogeneous gas-phase reactions and forms various hydrocarbon species such as acetylene, benzene, naphthalene. These gaseous species are transported into the pores by diffusion and convection. Then, it undergoes heterogeneous reactions with the surface of the pores during which pyrolytic carbon is deposited on the wall of the pore. In this process, high texture PyC is formed directly as compared to the resin route process, where multiple processing cycles are required to obtain carbon matrix such as resin infusion, curing, carbonization, and graphitization. Furthermore, this carbon matrix in resin route is noncrystalline in nature and its properties are inferior.

Even though the I-CVI process has been studied extensively for C/C composites with methane and hydrogen gas process conditions but the densification mechanism of the methane and nitrogen gas process conditions is different [8]. Since this gas system is widely used in industry for the realization of C/C composite, this necessitates the investigation of the effect of process parameters for methane and nitrogen gas system and the quality of the PyC matrix deposited in C/C composites, which finds applications for strategic areas. Thus, one of the objectives of the present study is to analyze the kinetics of the I-CVI process and examine the transition of PyC texture with change in process conditions. The thermo-structural properties of C/C composites, which are essential attributes to design for various applications, depend on the nature of the carbon matrix deposited by the process. The nature of the PyC deposited at various process conditions through I-CVI, and the effect of process parameters on the microstructure of the deposited PyC is further analyzed. The characteristic of the PyC matrix has been examined to propose process conditions desirable for synthesizing a better type of PyC through I-CVI. The results of these studies are corroborated to adopt process methodologies for the realization of C/C composites.

2 Methods

CFD simulation has been carried out for the I-CVI process in order to know the effect of porosity of the preform, temperature, pressure, residence time of gas, and inlet molar mixture ratio of methane and nitrogen gas. The I-CVI process has been simulated for PyC deposition inside the capillary tube. The effect of porosity, the molecular mass of precursor gas, the reactivity of the hydrocarbon species, and the thickness of the carbon fiber preform are explained with a non-dimensional number, Thiele modulus. The effect of the residence time of the gas in this process is analyzed at temperature, pressure, and initial mole fractions of methane and nitrogen of 1373 K, 0.05 bar, and 0.5, respectively. From this analysis, the variations of mole fraction of reactant and various hydrocarbon products in I-CVI reactor are obtained with variations of the residence time of gas. Latter the ratio ' R ' (concentration ratio of acetylene and benzene) is also analyzed with the variations of the residence time of gas. Then, the residence time required for obtaining rough laminar PyC (RL-PyC) is obtained. To find the effect of temperature, pressure, and inlet mole fraction of precursor gas in the I-CVI process, homogeneous gas-phase reaction simulation is carried out by Gibb's free energy minimization method for a temperature range of 1073–1473 K where other process parameters such as pressure and inlet mole fractions of methane and nitrogen are kept constant. Mole fractions of methane and various hydrocarbons are evaluated with variations of temperature. Subsequently, the transition of PyC morphology with temperature variations is found and the right temperature range for I-CVI process is obtained. To know the effect of pressure, analysis has been carried out for a pressure range of 0.01–0.1 bar where other process parameters are kept constant such as temperature is 1373 K and inlet mole fraction of methane gas and nitrogen gas is 0.5. From this, the suitable vacuum pressure required for this process is obtained. The effect of the inlet mole fraction of methane gas is also simulated for this process. From this analysis, mole fraction of reactant and hydrocarbon product is analyzed with change in inlet mole fraction of methane gas. Subsequently, the transition of PyC texture is evaluated. In order to validate the results obtained from the analysis, C/C specimens have been processed through I-CVI in two different conditions. The morphology of PyC has been investigated with XRD, Raman, SEM. The densification growth in the C/C has been evaluated by the Archimedes principle.

2.1 Result and Discussion Effect of Porous Body Geometry in I-CVI Process

I-CVI process has been simulated for PyC deposition inside the capillary pore. It is found that the concentration of hydrocarbon species inside the pore is a function of a non-dimensional number known as Thiele modulus, which is a function of rate

constate of reaction (k), pore depth (L), the radius of the pore (R), and diffusion coefficient of hydrocarbon species (D). The hydrocarbon species concentration variations inside the pore depth are illustrated in Fig. 1, which shows that the concentration of hydrocarbon species decreases with an increase in the Thiele modulus.

$$\text{Thiele modulu} = \left(\sqrt{\frac{2 * k * L^2}{R * D}} \right)$$

From the analysis, it is found that Thiele modulus increases with an increase in the rate constant of hydrocarbon species or with an increase in pore depth of carbon fiber preform, which is not good for the I-CVI process. This reveals that the I-CVI process is not good for thicker C/C composite because the pore depth of the thicker C/C composite is large. Since Thiele modulus increases with an increase in the rate constant of the hydrocarbon species, it is also not good for the I-CVI process. Because high reactive species may not get sufficient time to infiltrate inside the pore. Thiele modulus decreases as the pore diameter is increased which is good for the I-CVI process. This reveals that the I-CVI process is more efficient initially when the porosity of carbon fiber preform is high. The I-CVI process efficiency is decreased as the porosity of the preform is decreased due to PyC deposition during the process. Therefore, in order to maintain the optimum infiltration of gas, it is required to change the process parameter after a certain duration (Table 1).

Similarly, the Thiele modulus value is decreased with an increase in diffusivity of the gaseous species. This reveals that low molecular weight hydrocarbon species are more suitable for the I-CVI process. Therefore, light molecular weight hydrocarbons

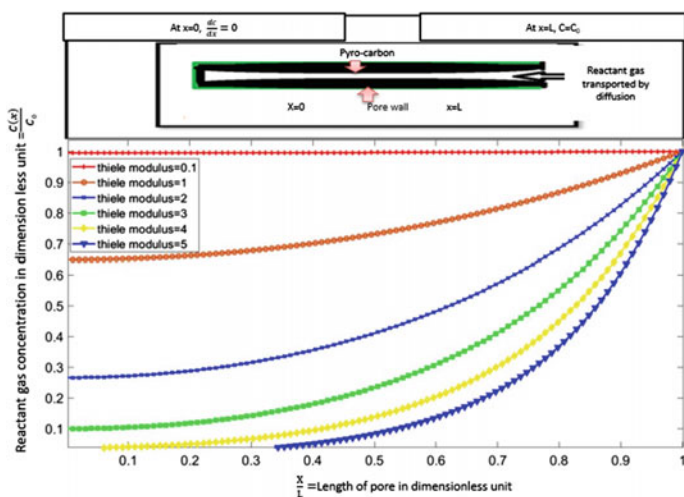


Fig. 1 Variation of hydrocarbon gas inside the pores of the preform

Table 1 Effect of process condition on Thiele modulus

Thiele modulus	When	Reason
Increasing	Process temperature increases	The rate constant of reaction increases
Increasing	Unstable hydrocarbon species is from	The rate constant of reaction increases
Increasing	The thickness of preform increases	Infiltration of gas inside the pore becomes difficult
Decreasing	Porosity of preform increases	Gas may easily be transported inside the pore
Decreasing	Light molecular weight Hydrocarbon species is used	Diffusivity of gas species is high

such as methane gas is more suitable for the I-CVI process. Based on the experiment, similar observation was obtained by Huttinger et al. [9].

2.2 *Effect of the Residence Time of Methane Gas in I-CVI Process*

The chemical kinetics of homogeneous gas-phase reactions is analyzed with the variation of the residence time of gas, and the mole fraction of major hydrocarbon species formed during the process is illustrated in Fig. 2. It is found that the mole fraction of methane gas decreases exponentially with an increase in the residence time of gas. This may happen because methane is a reactant gas. Further, it is found that for the optimum utilization of reactant gas, a minimum of ten seconds residence time of the gas is required. The mole fraction of acetylene, benzene increases with an increase in residence time of gas. This has happened because acetylene and benzene are comparatively more stable than other hydrocarbons at 1373 K. While the poly-aromatic hydrocarbon species such as naphthalene mole fraction is increased first then decreased. This revealed that gas-phase nucleation may happen as the residence time of gas increases and soot carbon will be formed. Delhaes et al. have also reported similar findings [10]. More fractions of hydrocarbon species C_2H_4 , C_2H_6 , C_4H_4 , and C_4H_6 are increased first then decreased. Because these are highly reactive species and are unstable at high temperatures. These species may form PyC when the residence time of the gas is low while at a high residence time of gas these hydrocarbon species may not play a big role in PyC formation.

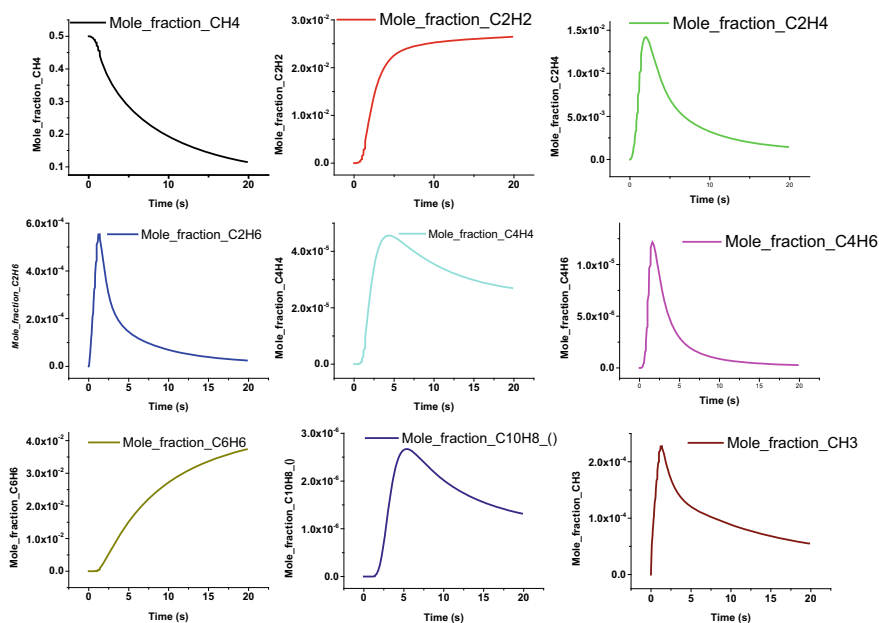


Fig. 2 Mole fraction of hydrocarbon with the residence time of gas

2.3 Effect of Process Temperature on I-CVI Process

The chemical kinetics of gas-phase reactions is simulated with the variation of process temperature from 1000 to 1500 K. The mole fraction of major hydrocarbon species formed during the I-CVI process is compared with temperature which is illustrated in Fig. 3. From this analysis, it is found that the mole fraction of methane gas is decreased with increases in process temperature. Because the rate constant for chemical reactions is increased exponentially with temperature. Most of the methane gas is dissociated in the temperature range 1350–1400 K which means this temperature range is appropriate for the optimum utilization of reactant gas in order to avoid wastage of reactant gas. Mole fraction of acetylene increases with an increase in temperature as the rate constant of reaction for acetylene gas formation is increased with temperature, and further, it is more stable at high temperature. Therefore, the value of R is increased. Mole fraction of hydrocarbon species like C_2H_4 is first increased then decreased due to the highly reactive C_2H_4 at high temperatures. Similarly, the mole fraction of C_2H_6 decreased with an increase in temperature because it is less stable at high temperatures. Mole fraction of aromatic and poly-aromatic compound is first increased with temperature then decreases with further increase in temperature. Because at high-temperature gas-phase nucleation may happen and aromatic hydrocarbon species are the main growth species for the soot carbon formation at high temperature. From Fig. 3, it is found that soot carbon formation may be started

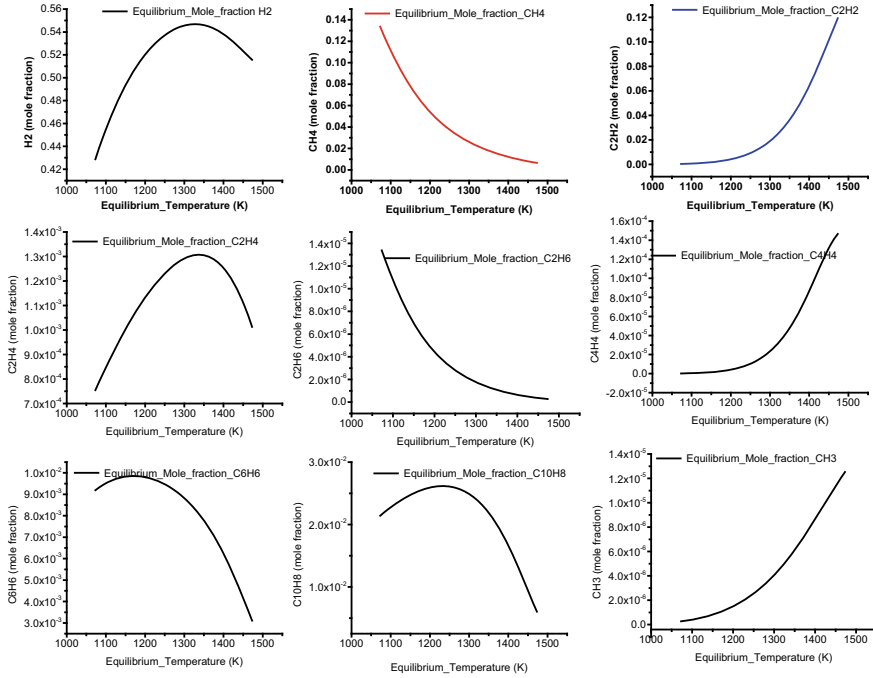


Fig. 3 Mole fraction of hydrocarbon gas with process temperature

at 1200 K but this soot carbon formation may be predominated above 1400 K. Therefore, I-CVI process temperature above 1400 K is not suitable. A similar observation was reported by Oberlin et al. [11].

2.4 Effect of Pressure on I-CVI Process

The chemical kinetics of the gas-phase reaction is simulated with the variation of process zone vacuum pressure (from 0.01 to 0.1 bar). The mole fraction of major hydrocarbon species formed during the process is illustrated in Fig. 4. From this analysis, it is found that the mole fraction of methane increases with an increase in pressure because not much variation in the rate constant of a reaction but the mole of the precursor gas is increased with an increase in pressure. Hence, more un-reacted gas comes out from the I-CVI reactor with an increase in pressure. Therefore, the wastage of reactant gas will be more at high pressure as a result of that production costs will be further high. Therefore, I-CVI process is carried out under optimum vacuum pressure. Mole fraction of acetylene gas is decreased with an increase in pressure because acetylene will form more aromatic and poly-aromatic hydrocarbon at high pressure. Since aromatic and poly-aromatic hydrocarbon formation increases

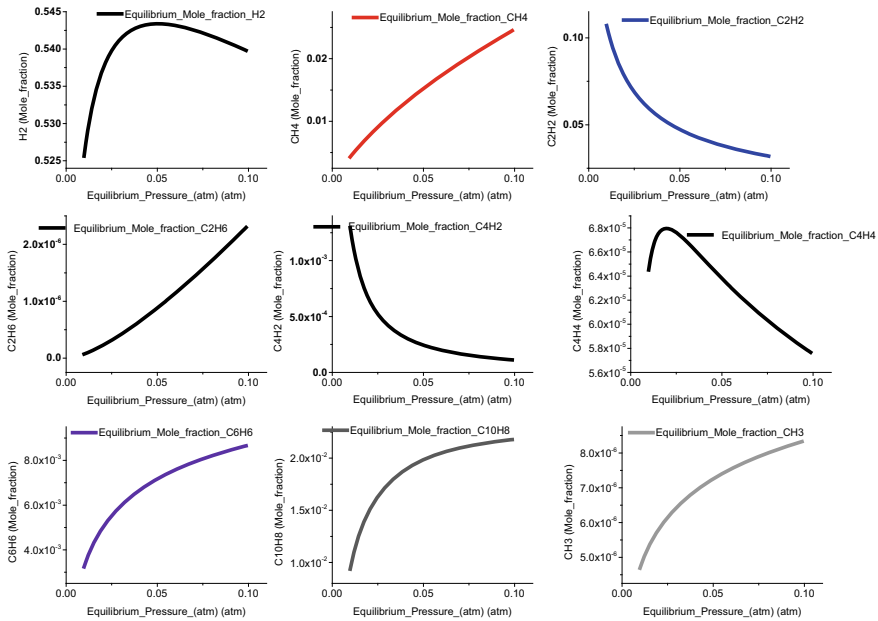


Fig. 4 Mole fraction of hydrocarbon with pressure

with pressure, therefore, gas-phase nucleation is increased because these species may condense and form soot carbon. Therefore, very high pressure is not suitable for the I-CVI process. Further, at high-pressure pore blockage may also happen because these soot carbons may be deposited on the pore mouth and block the pore and reduce the further infiltration of gas inside the pore.

2.5 Effect of Inlet Molar Ratio of Methane and Nitrogen Gas on I-CVI Process

The chemical kinetics for gas-phase reactions is simulated with the variation of methane and nitrogen gas ratio (from 1:9 to 10:0). The mole fraction of major hydrocarbon species with change in mole fraction of methane gas is shown in Fig. 5. From this analysis, it is found that the mole fraction of methane gas in the I-CVI reactor is increased with an increase in the inlet mole fraction of methane gas. This may happen because the mole fraction of reactant gas is increased. Similarly, all hydrocarbon species mole fractions are also increased because the nitrogen gas mole fraction is decreased which acts as inert gas during the I-CVI process.

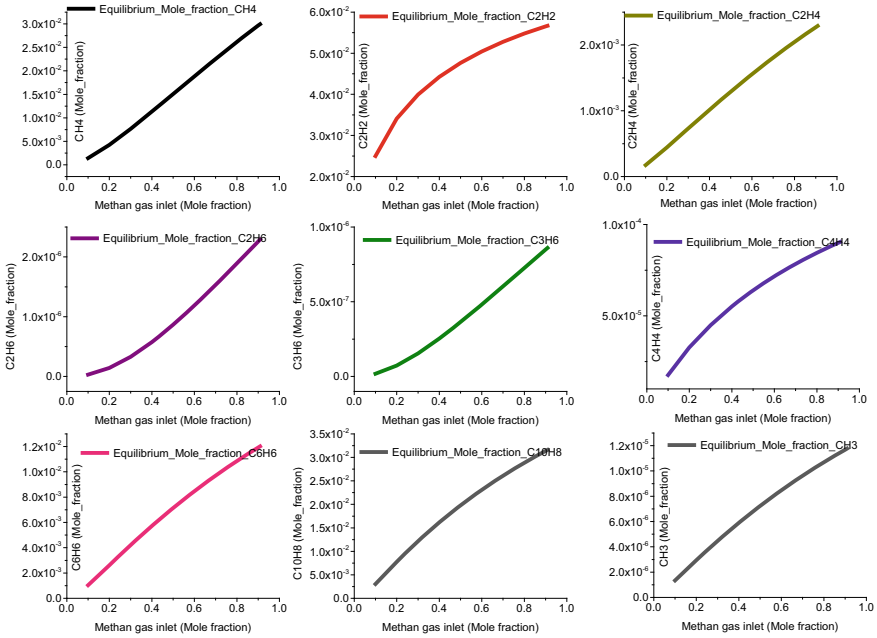


Fig. 5 Mole fraction of hydrocarbon with methane gas inlet mole fraction

2.6 Effect of Process Parameter on the PyC Texture

The variation of acetylene to benzene ratio (R) with the process parameter is shown in Fig. 6. From this simulation, it is found that the value of R is decreased with an increase in the residence time of gas. Hence, PyC texture transition has happened from ISO-PyC (Isotropic PyC) \rightarrow RL-PyC (Rough laminar PyC) \rightarrow SL-PyC (Smooth laminar PyC) with an increase in residence time of gas. RL-PyC will be formed when the residence time of the gas is in the range of 10–20 s.

Again, it is found that the value of ' R ' is increasing with an increase in temperature. ISO-PyC is formed at high temperatures (above 1430 K), and SL-PyC is formed at low temperatures (below 1350 K). The temperature range from 1350 to 1430 K is more suitable for the I-CVI process because RL-PyC is formed as a matrix. Further, it is found that the value of ' R ' is decreasing with an increase in pressure. SL-PyC is formed at high pressure (above 0.07 bar), and ISO-PyC is formed at low pressure (below 0.0158 bar). I-CVI process pressure between 0.0158 and 0.070 bar is optimum to obtain RL-PyC as a matrix. It is found that the value of R is decreasing when the inlet mole fraction of methane gas is increasing, which showed that ISO-PyC is formed as a matrix when highly diluted methane gas (<0.1) is fed in I-CVI reactor, while SL-PyC is formed as a matrix when highly concentrated methane gas (>0.6) is fed in the I-CVI reactor. The inlet mole fraction of methane gas between 0.1 and 0.6 is suitable for the I-CVI process because of RL-PyC is formed as a matrix.

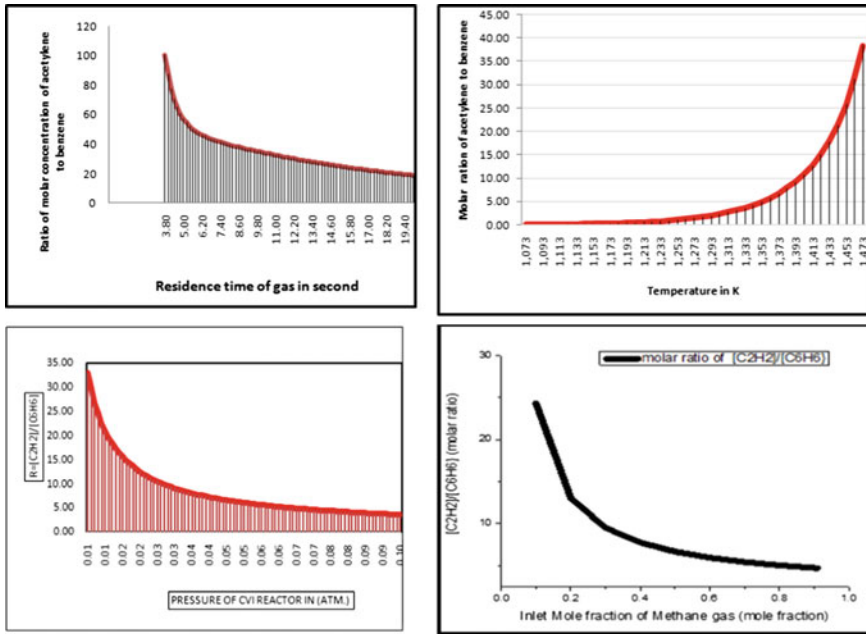


Fig. 6 Effect of process parameter on acetylene to benzene ratio (R)

3 Experimental Investigation of I-CVI for C/C Sample Processing

C/C samples are processed at two different process conditions as shown in Table 2. The density of C/C samples was checked at various stages. The density growth in C/C samples is shown in Fig. 7. From the plot, it is found that the rate of PyC deposition in Sample 1 is faster than the sample 2. Sample 1 is processed at 0.05 bar pressure, while sample 2 is processed at 0.01 bar pressure. This density plot revealed that high pressure is better for fast densification of the C/C sample. A similar finding was reported by Benzinger et al. [12].

Density growth in C/C sample

See Fig. 7.

Table 2 I-CVI process parameter

C/C sample	Temperature (K)	Pressure	Residence time (s)	(CH ₄ :N ₂)	Process duration (h)
Sample-1	1373	0.050 bar	20	1:1	420
Sample-2	1353	0.010 bar	40	1:1.5	700

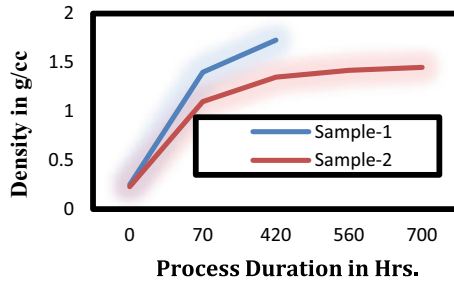


Fig. 7 Density growth in C/C sample

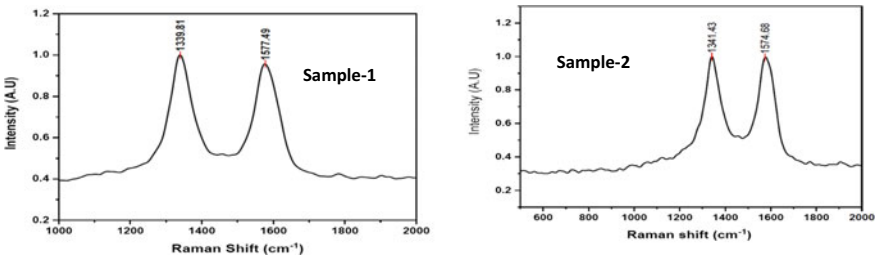


Fig. 8 Raman spectra of PyC in C/C specimen

Raman spectra of PyC in C/C specimen

Raman spectroscopy has been carried out for both sample and found that PyC in sample 1 is more crystalline than PyC obtain in sample 2. This reveals that the process parameter for sample 1 is better than process parameter 2 (Fig. 8).

XRD Result of C/C samples

Further, the XRD spectroscopy is also carried out for both samples and found that PyC obtain in sample one is more crystalline and the crystal size of this PyC is bigger than the sample-2. Savage et al. have reported that the rough laminar PyC crystal size is bigger than the SL-PyC and ISO-PyC [13]. From this, it is found that PyC obtain in sample 1 is more crystalline than sample 2. Therefore, it concluded that the process parameter for sample 1 is better than sample 2 (Fig. 9).

4 Conclusion

In this study, a combined theoretical, CFD simulation, and experimental investigation of C/C samples are employed to analyze the I-CVI process and the texture of the PyC matrix deposited through this process. It is found that the value of 'R' decreases with an increase of either the residence time of gas or vacuum pressure or inlet mole

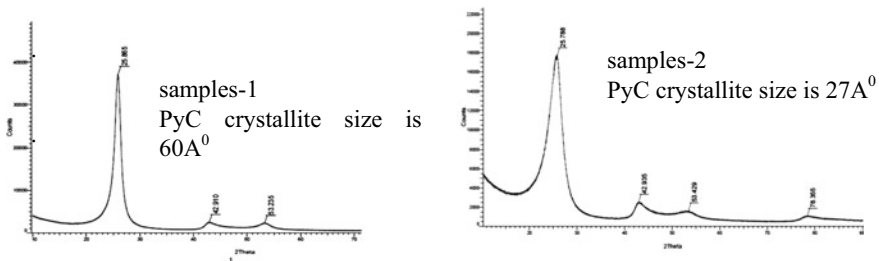


Fig. 9 XRD of C/C samples

fraction of methane gas. Hence, PyC texture transition has happened from ISO-PyC \rightarrow RL-PyC \rightarrow SL-PyC with an increase of the above parameter. The residence time of gas from 10 to 20 s, vacuum pressure 0.0158–0.07 bar, and inlet mole fraction of methane gas 0.1–0.6 is appropriate for the I-CVI process because RL-PyC is obtained. Again it is found that the value of R is increased exponentially with an increase in temperature hence, the PyC texture transition has happened from SL-PyC \rightarrow RL-PyC \rightarrow ISO-PyC. The temperature range from 1350 to 1430 K is suitable for this process. Through the experiment, it is concluded that the rate of PyC deposition increases with an increase in pressure from 0.010 to 0.050 bar. The crystallinity of the PyC matrix is also increased with an increase in pressure from 0.01 to 0.05 bar.

This study has revealed critical insights of the I-CVI process, specific to the texture of the PyC matrix deposited during the process and the effect of process parameters. Further, work is needed for rigorous analysis of this process considering the in-situ weight gain measurement during the process.

References

1. Hancox NL (1995) Essentials of carbon-carbon composites. In: Thomas CR (ed). Chapman and Hall, London (1993). ISBN 0-85186 804-5
2. Broquere B, Broquere B (1997) Carbon/carbon nozzle exit cones-SEP's experience and new developments. In: 33rd joint propulsion conference and exhibit, p 2674
3. Lazzeri A (2012) CVI processing of ceramic matrix composites. In: Ceramics and composites processing methods, pp 313–349
4. Zhang DS, Li KZ, Li HJ, Guo LJ, Lu JH (2011) The influence of deposition temperature on the microstructure of isotropic pyrocarbon obtained by hot-wall chemical vapor deposition. *J Mater Sci* 46(10):3632–3638
5. Zhang YF, Luo RY (2012) Influence of infiltration pressure on densification rate and microstructure of pyrocarbon during chemical vapor infiltration. *New Carbon Mater* 27(1):42–48
6. Benzinger W, Becker A, Hüttinger KJ (1996) Chemistry and kinetics of chemical vapour deposition of pyrocarbon: I. Fundamentals of kinetics and chemical reaction engineering. *Carbon* 34(8):957–966
7. Zhang WG, Hu ZJ, Hüttinger KJ (2002) Chemical vapor infiltration of carbon fiber felt: optimization of densification and carbon microstructure. *Carbon* 40(14):2529–2545
8. Kuguchin AE, Vnukov SP (1990) Effect of inert gases on the rate of pyrocarbon formation in the thermal decomposition of methane. *Kinet Catal* 31(3 pt 2):641–643

9. Benzinger W, Hüttinger KJ (1996) Chemical vapour infiltration of pyrocarbon: I Some kinetic considerations. *Carbon* 34(12):1465–1471
10. Delhaes P (2002) Chemical vapor deposition and infiltration processes of carbon materials. *Carbon* 40(5):641–657
11. Oberlin A (2002) Pyrocarbons. *Carbon* 40(1):7–24
12. Benzinger W, Hüttinger KJ (1998) Chemical vapor infiltration of pyrocarbon—II. The influence of increasing methane partial pressure at constant total pressure on infiltration rate and degree of pore filling. *Carbon* 36(7–8):1033–1042
13. Savage G, Savage GM, Savage E (1993) *Carbon-carbon composites*. Springer Science & Business Media
14. Benzinger W, Hüttinger KJ (1998) Chemicalvapor infiltration of pyrocarbon—II. The influence of increasing methane partial pressure at constant total pressure on infiltration rate and degree of pore filling. *Carbon* 36(7–8):1033–1042

Material Properties

Deformation Effect on Corrosion Resistance of 316 ASS—A Review



Sourabh Shukla, Abhay Kewati, Anshula Gaurkar, Tulika Bawankar, and Abhishek Gawai

Abstract The main application in sheet metal forming is austenitic stainless steel (ASS), which is utilised in a various applications, including plate heat exchangers. The martensitic transition can occur during plastic deformation. Temperature, stress and strain are all factors that influence martensite development. The main focus of this research is on the impact of the martensite transformation that occurs during cold working on the corrosion resistance of AISI 316. Corrosion investigation revealed that the martensitic transformation that happens during the cold forming process has a significant impact on the corrosion resistance of AISI 316 ASS plate heat exchangers. The capacity of molybdenum to generate insoluble chloride complexes at the base of pits has been attributed to its role in the creation of passive films. However, due to the cyclic working circumstances of plate heat exchangers, the protective film generated as a result of passivation or repassivation was continuously damaged due to continuous martensitic transformation. The passive layer was continually broken by martensite volume expansion, exposing fresh unprotected surfaces to chlorine-treated water (used in heat exchanger plate as a thermal agent). The martensite transition, which occurs as a result of cold plastic deformation, alters the steel structure as well as its physical and chemical properties. Stainless steel's magnetic characteristics are highly reliant on the components added to the alloy. Because they have differing corrosion potentials, it is simple for them to become the anode and cathode of a corrosion battery.

Keywords Corrosion resistance · Martensitic transformation · Cold work

S. Shukla (✉) · A. Kewati · A. Gaurkar · T. Bawankar · A. Gawai
Mechanical Engineering Department, G H Raisoni College of Engineering, Nagpur 440016, India
e-mail: sourabh.shukla@raisoni.net

© The Author(s), under exclusive license to Springer Nature Singapore Pte Ltd. 2023
B. Pramod P. et al. (eds.), *Advances in Material Science and Metallurgy*, Lecture Notes
in Mechanical Engineering, https://doi.org/10.1007/978-981-19-4918-0_15

1 Introduction

On the basis of the crystalline structure, the stainless steel is divided into five classes, viz. ferritic, martensitic, duplex, precipitation hardened and ASS with austenite (face-centred cube) as its primary crystalline structure having very good corrosion resistance [1–12]. It is used in various industries, because of its rich range of metallurgical properties like high ductility, good heat resistance, excellent corrosion resistance, etc. [2, 4, 8, 9]. As it has wide range of application, there is extensively study going on. The improvement of strength of ASS is done by using grain size refinement, precipitation hardening and cold deformation strengthening [5, 10, 11]. It has low yield strength to overcome, and this grain refinement is done because of this austenite to martensite transformation occurs which has impact on corrosion resistance of the ASS [12, 13]. With availability to form a thin chromium-rich passive surface film, stainless steel has good corrosion resistance. But even if they have good corrosion resistance, they are inclined to localized corrosion attack. Resistance to corrosion cracking due to stress is increased with addition of nickel and molybdenum, while the high level of chromium and molybdenum increases resistance to general corrosion, pitting and crevice corrosion [4]. Different parameters are there such as material chemistry, strain rate and stacking fault energy (SFE) which help to form the deformation-induced martensite (DIM) [1, 2, 4, 13–15]. Austenite has a SFE which is a function of temperature, and composition has a prominent effect on amount of martensite transformation during the deformation [12, 14, 15]. With increase in stacking fault energy, there is shift from ϵ -martensite formation to deformation twinning [14, 15]. The defect structure created due to plastic deformation of austenite acts as embryo for transformation. There is large number of shear band which is formed in biaxial tension than in uniaxial tension which increase the larger volume fraction of α' martensite. At low deformation (<10%), ϵ -martensite is formed, and with increase in strain levels, the ϵ -martensite is converted to α' martensite [14, 16].

2 Current Research in ASS 316

ASS 316 is second most utilized stainless steel after 304. In the recent years, much research is done to develop its properties and makes more use of it in various industries like automobiles, aircraft manufacturing, medical devices, etc. [7, 12]. Figure 1 shows the number of publications published in ASS in the recent years calculated from the Science direct. The graph shows there is an increase in publication every year. With such excellent set of properties, ASS has only one drawback low yield strength in process of overcoming that there is decrease in corrosion resistance, so in recent years, it is one of leading area of research so as to make ASS high yield strength material with not any effect on its corrosion resistance.

Figure 2 shows number of publications published in the recent ten years under the topic improvement in corrosion resistance of ASS. This graph shows that in

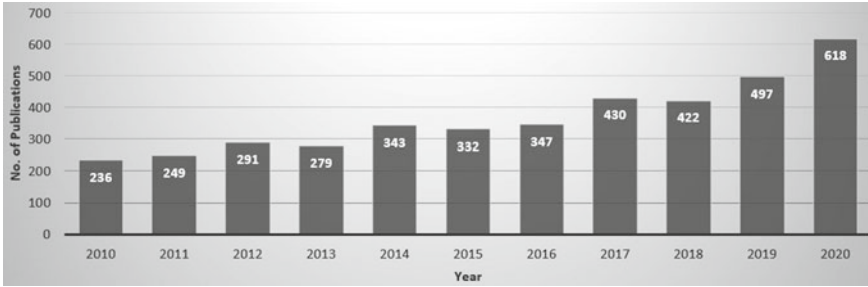


Fig. 1 Trends of research in ASS

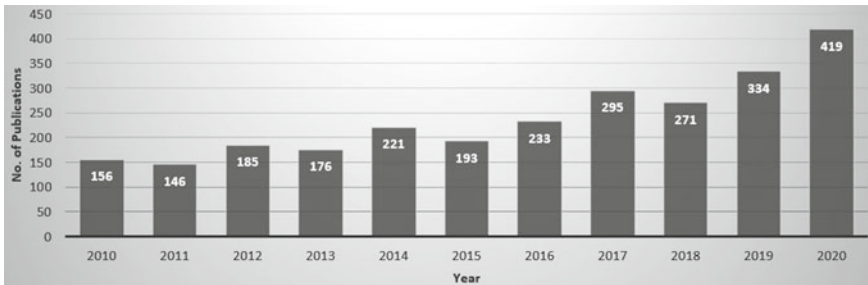


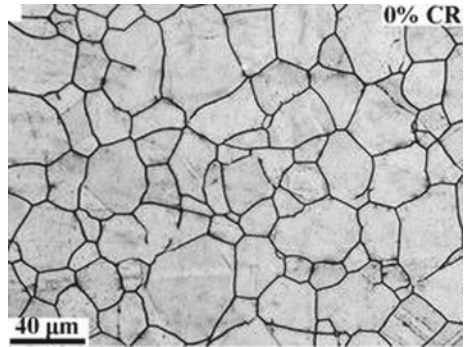
Fig. 2 Trends of ASS research based on corrosion resistance

the beginning era (2010–2013), there are less number of publication written but, thereafter, there is increase in publication.

3 Experimentation

Xu et al. [7] have done cold rolling on 316 ASS. They have observed it using optical microscope and micrographs at various level of cold rolling. Figure 3 shows the original structure of material, and it has coarse-grained austenite with many annealing twins, while Figs. 4, 5, 6, 7 and 8 show the evolution of martensite with increasing cold rolling. At 10c/o cold rolling, there were many shear band and mechanical twins discovered in austenite phase, also in austenite grains formation of grain, boundaries and small amount of strain-induced martensite take place. With increasing cold rolling, volume fraction of martensite and density of grain boundary increases. Dislocation starts gathering at twins boundaries and shear band as shown in Fig. 4. Figure 5 shows that at shear band, some strain-induced martensite is formed at 30c/o cold rolling, and the martensite boundary suppresses the dislocation movement, as a result, the dislocations are gathered around the martensite boundary. With this segmentation of the untransformed austenite, structure is done by dislocation boundaries. At

Fig. 3 Original [7]



50% cold rolling, elongation of untransformed austenite takes place in direction of rolling, and lath of martensite is formed (Fig. 6). With 70% cold rolling, the amount of martensite goes on increasing and also the martensite formed segment the untransformed austenite (Fig. 7). Still there is large block of untransformed austenite exist, the martensite till formed likely to be divided into fine martensite and mixed with austenite.

Fig.4 10% cold rolling [7]

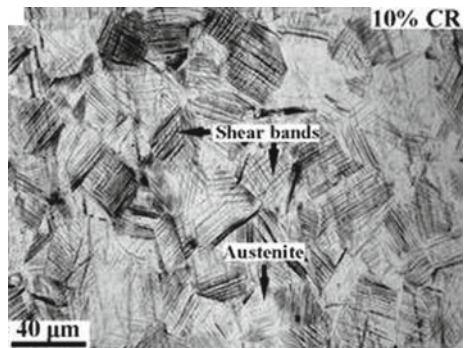


Fig. 5 30% cold rolling [7]

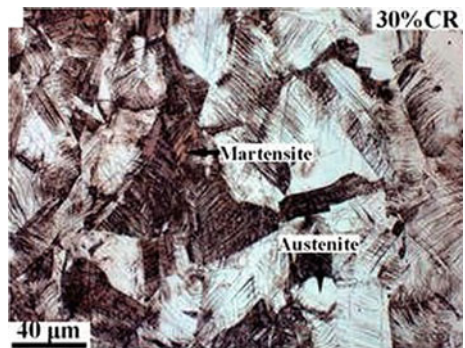


Fig. 6 50% cold rolling [7]

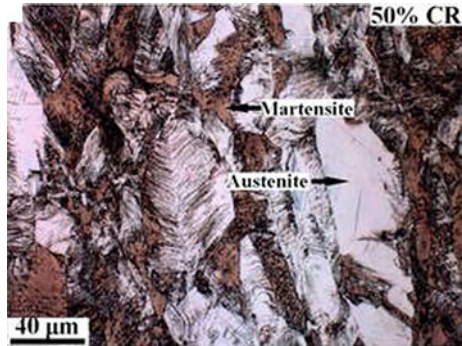


Fig. 7 70% cold rolling [7]

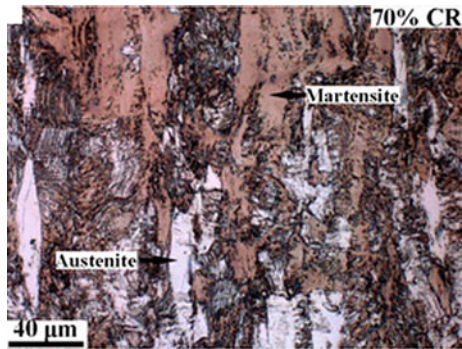
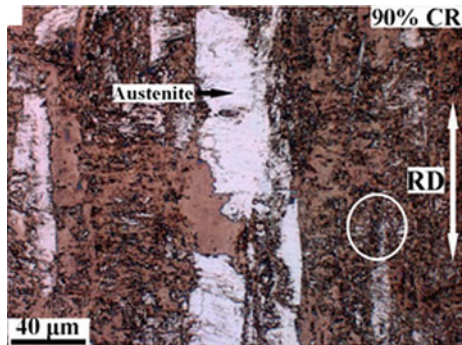


Fig. 8 90% cold rolling [7]



4 Grain Refinement Effect on Transformation of Martensite

Numerous investigations have indicated that refining the grain size of austenite improves its resistance to deformation-induced martensitic transformation [17–19].

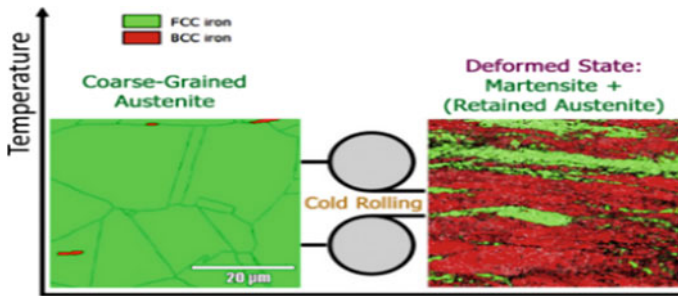


Fig. 9 Schematic of the martensite process applied to ASSs

The austenite grain size has influence on martensitic transformation, and microstructural evolutions are represented in Fig. 9. The amount of transformation is the product of the size of the transformed region and number of nuclei formed [20]. With increase in austenite grain size (AGS), the martensite start temperature also increases reason which is unclear till date. But, this might be because the AGS provides more nucleation sites which in turn promotes nucleation kinetics [21]. Moreover, the grain having size smaller than the equilibrium width of stacking fault creates the distraction against dissociation of dislocations [22, 23]. So, there is increase in apparent stacking fault energy value with refining the grain size of low stacking fault energy, which favours the activation of deformation twinning and suppresses the formation of deformation-induced martensite [24, 25]. However, yet the effect on mechanical stability of austenite of grain size is not clear. But according to the report on the effect of grain sizes larger than 50 μm on the mechanical stability of austenite phase [26], where with decreasing grain size the amount of deformation-induced martensite increased.

5 Martensite Transformation

Austenitic stainless steel is metastable stainless steel which is suspected to martensite transformation. There are so many theories that are associated with it. But the most accepted theory is Bain Theory which investigated that with cooperative movement of atoms, transformation of austenite (FCC) to α' -martensite (BCC) occurs [8, 27]. Cause for the start of martensitic transformation is the critical chemical driving force which is the difference of free energies between austenitic and martensite at temperature of martensite start temperature (M_s) [28]. T_0 is the temperature at which there exist the equilibrium in between martensite and austenite. When the stress is applied to austenite at T_1 (between M_s and T_0), the stress-assisted martensite transformation is triggered by chemical driving force whose shortage might be compensated by the mechanical driving force. [29, 30]. The required stress for the stress-assisted martensitic transformation increases linearly as the temperature increases up to M_s

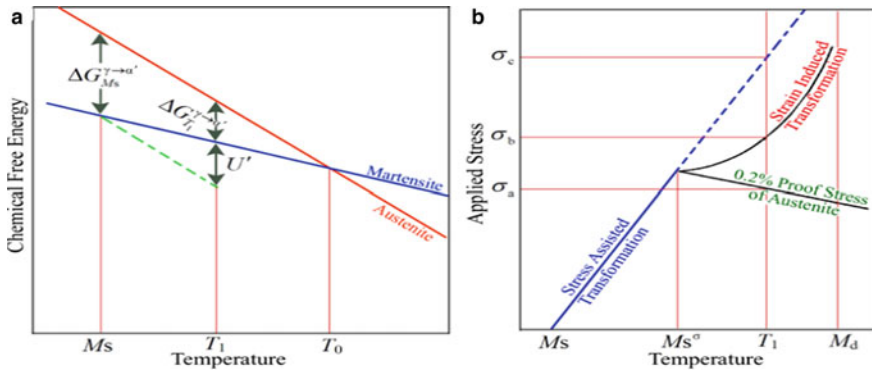


Fig. 10 a Graph showing chemical-free energy as temperature of martensite and austenite [28] b Graph showing critical stress as function of temperature for martensite formation [28]

σ as shown in Fig. 10 (1a). But as temperature increases more, before reaching the critical stress required for stress-assisted martensitic transformation, austenite phase starts to deform plastically [29, 31]. However, based on another mechanism, i.e. strain-induced martensitic transformation at lower stresses, the martensitic transformation is possible at these temperatures. The strain-induced martensitic transformation begins between M_s^σ and M_d , where the latter is the upper limit for the strain-induced transformation (at temperature of T_1) as shown in Fig. 10b at a austenite plastically deforms, hardened up to b . At the lower stress, occurrence of martensitic transformation can be attributed to the plastic deformation, which was effected by the formation nucleation sites which are energetically favourable, specially in chemical composition which lead to relatively low stacking fault energies [31–33]. At lower stacking fault energy, against the deformation-induced martensitic transformation, austenite has lower stability. The intersections of shear band are involved by the nucleation sites. [34]The strain-induced martensitic transformation occurs in two simple sequences of $\gamma \rightarrow \epsilon \rightarrow \alpha'$ and $\gamma \rightarrow \alpha$. In fact, with increase in degree of deformation, quantity of α' -martensite increases continuously, and ϵ -martensite amount reaches maximum and then lowers in the transformation sequence $\gamma \rightarrow \epsilon \rightarrow \alpha'$ [17, 35]. There are various method like X-ray diffraction (XRD), electron backscatter diffraction (EBSD) and metallography with the help of which we can detect and evaluate the formation of martensite [28].

6 Effect of Martensitic Transformation on Corrosion Resistance

Uniform Corrosion is most simplest but most destructive form of the corrosion. It attacks almost surface of the material uniformly. The material forms passive layers

on them to protect for this corrosion. But the martensite transformation occurred as a result of cold working repeatedly breaks that layer which decreases the corrosion resistance [36]. **Pitting Corrosion** Due to damage of protective passive film present on surface formation of microscopic holed cavities take place knows as pits [37, 38]. At higher levels, cold working leads the formation of DIM and some residual stresses which increases number of anodic sites and thereby decreasing the corrosion resistance of ASS [38, 39]. Also ASS has relatively less stacking fault energy, and in that cold work introduces deformation which includes dislocation. Depending upon the level of cold working, it defects the structure and also has a significant effect on diffusion kinetics of alloying elements. All these microstructural changes collectively increasing number of anodic sites in passive film and reduce the pitting corrosion resistance of ASS [40, 41]. Also cold working introduces the martensitic phase which does not change the pitting potential at lower levels but with higher level, number of pits also goes on increasing. Kamachi Muddle et al. [39] also studied that the effect of cold working on pitting corrosion resistance is dependent on content of nitrogen present (Figs. 11 and 12).

Crevice Corrosion is one of the most serious localized corrosion issues with stainless steel. Gaps and contact areas between parts, behind gaskets or seals, inside cracks and seams, deposits-filled crevices and sludge piles are all affected. Up to about 15% increase in cold working the crevice corrosion resistance decreases but any further increasing in cold working has very less effect on crevice corrosion resistance [42]. The amount of fault sites and the textural change caused by cold work has a significant impact on crevice corrosion behaviour [37, 42]. **Stress Corrosion cracking** is the failure of materials occurred due to crack propagation induced environmentally. Mainly, this take place in metals Or alloys which are protected from uniform corrosion

Fig. 11 Pitting resistance of cold worked nitrogen-containing alloys [37]

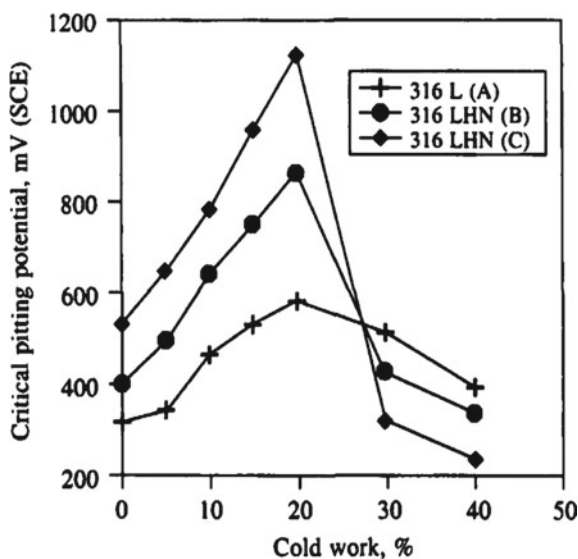
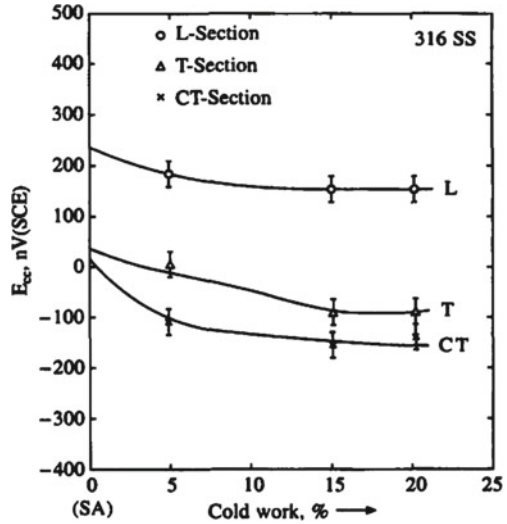


Fig. 12 Crevice resistance effected by cold work [42]



by passive layer formation [43–46]. Here, the attack in narrow region is accelerated due to localized breakdown of passive layer by stress (mechanical means) [37, 47]. There have been various studies which have stated that the cold work has influence on stress corrosion cracking of ASS. But unfortunately, direct comparison is not possible between various studies as there is variation in alloys, deformation method, etc. [44, 45]. Muraleedharan et al. [47] studied 316 ASS under constant load method at a constant initial stress. He got result as shown in Fig. 13. The graph shows the time to fracture vs pre-strain percentage of 316 ASS.

At applied stress 112Mpa, with increasing cold work, total time to fracture decreases and reaches minimum about 15% cold work. Then, for higher deformation levels, it increases. Figure 14 shows the 316 ASS initially has transgranular path of crack. As crack proceeds, it changes to intergranular mode and finally ends with ductile mode. On an average, with increase in degree of deformation, there is increase in ratio of intergranular to transgranular SCC area (Figs. 15, 16 and 17).

7 Conclusion

In this review, an overview of the martensitic transformation formed due to cold work and its effect on the corrosion resistance of the ASS 316 is given.

- According to various studies, it has been found that with cold working, martensitic transformation occurs. The amount of martensite formation depends upon various factors, viz. stacking fault energy, grain refinement, amount of cold work, etc.
- The martensite formed has an effect of the corrosion resistance towards the pitting, crevice and stress cracking corrosion of the ASS 316.

Fig. 13 Graph of time to fracture for type 316 stainless steel effected by cold work [47]

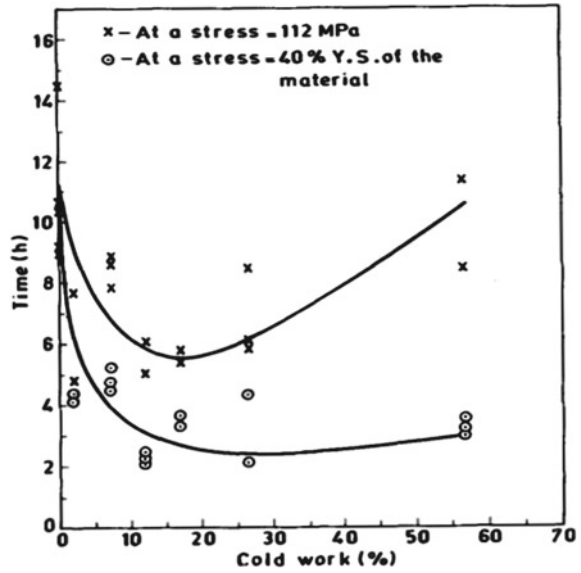


Fig. 14 Three alternative types of fracture in 316 stainless steel with 6.9% cold work, tested at 112 MPa, as shown by SEM [47]

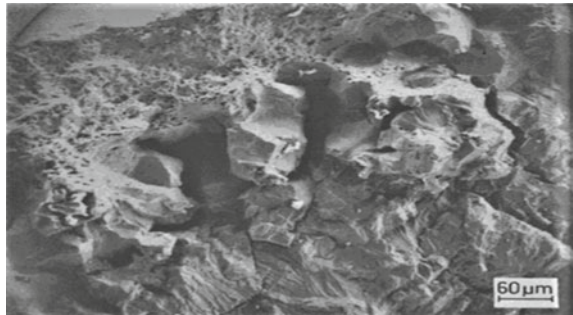


Fig. 15 Crevice corrosion [37]

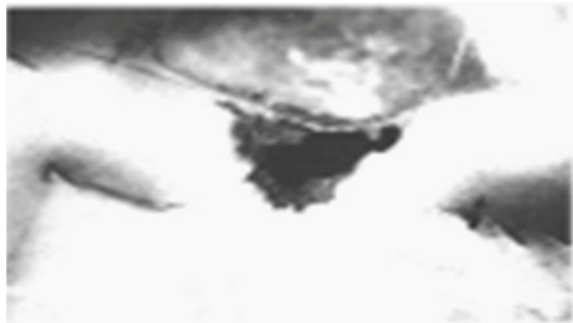


Fig. 16 Pitting corrosion [42]

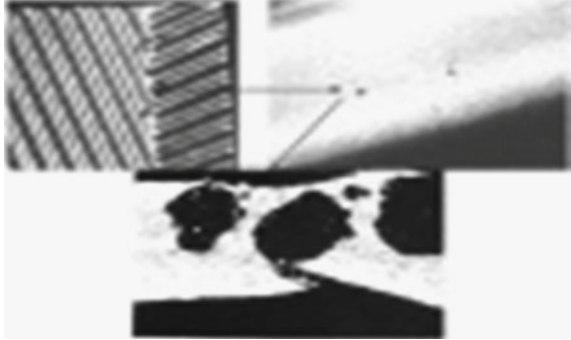
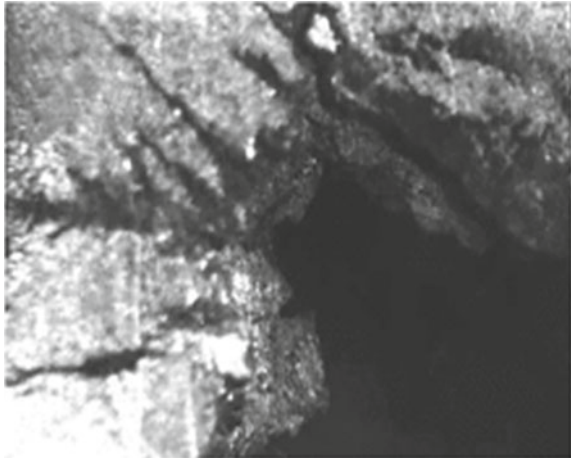


Fig. 17 Stress cracking corrosion [43]



- In future, research can be focused on decreasing the corrosion rate of given ASS through thermo-mechanical treatment by optimizing the thermal ageing and deformation rate.

References

1. Zeng W, Yuan H (2016) Mechanical behaviour and fatigue performance of ASS under consideration of martensitic phase transformation
2. Lo KH, Shek CH, Lai JKL (2009) Recent developments in stainless steels
3. Hedström P (2005) Deformation induced martensitic transformation of metastable stainless steel AISI 301
4. Solomon N, Solomon I (2017) Effect of deformation-induced phase transformation on AISI 316 stainless steel corrosion resistance. <https://doi.org/10.1016/j.engfailanal.2017.05.031>
5. Karjalainen LP, Taulavuori T, Sellman M, Kyrolainen A (2016) Some strengthening methods for ASSs. <https://doi.org/10.1002/srin.200806146>

6. Etefagh AH, Guo S, Raush J (2020) Corrosion performance of additively manufactured stainless steel parts: A review
7. Xu D, Wan X, Yu J, Xu G, Guangqiang (2018) Effect of cold deformation on microstructures and mechanical properties of ASS. <https://doi.org/10.3390/met807052-2>
8. Tiamiyu AA, Eduok U, Szpunar JA, Odeshi AG (2019) Corrosion behavior of metastable AISI 321 ASS: investigating the effect of grain size and prior plastic deformation on its degradation pattern in saline media. <https://doi.org/10.1038/s41598-019-48594-3>
9. Tiamiyu AA, Eduok U, Odeshi AG, Szpunar JA (2019) Effect of prior plastic deformation and deformation rate on the corrosion resistance of AISI 321 ASS
10. Kisko A, Misra RDK, Talonen J, Karjalainen LP (2013) The influence of grain size on the strain induced martensite formation in tensile straining of an austenitic 15Cr-9Mn-Ni-Cu stainless steel
11. Naraghi R (2009) Martensitic transformation in ASSs
12. Handoko W, Pahlevani F, Hossain R, Sahajwalla V (2019) Stress-induced phase transformation and its correlation with corrosion properties of dual-phase high carbon steel
13. Mirzadeh* H, Najafzadeh A (2008) ANN modeling of strain-induced martensite and its applications in metastable ASSs
14. Ghosh SK, Mallick P, Chattopadhyay PP (2012) Effect of cold deformation on phase evolution and mechanical properties in an ASS for structural and safety applications (Department of Metallurgy and Materials Engineering, Bengal Engineering and Science University, Shibpur, Howrah 711 103, India)
15. Choi J-Y, Jin W (1977) Strain induced martensite formation and its effect on strain hardening behavior in the cold drawn 304 ASSS
16. High-energy synchrotron x-ray study of deformation-induced martensitic transformation in a neutron-irradiated Type 316 stainless steel (2020)
17. Suzuki T, Kojima H, Suzuki K, Hashimoto T, Ichihara M (1977) An experimental study of the martensite nucleation and growth in 18/8 stainless steel
18. Mirzadeh H, Najafzadeh A (2008) Correlation between processing parameters and strain-induced martensitic transformation in cold worked AISI 301 stainless steel
19. Lee CY, Yoo CS, Kermanpur A, Lee YK (2014) The effects of multicyclic thermo-mechanical treatment on the grain refinement and tensile properties of a metastable austenitic steel
20. Fisher JC, Hollomon JH, Turnbull D (1949) Kinetics of the austenite to martensite transformation
21. Lee S-J, Lee Y-K (2005) Effect of austenite grain size on martensitic transformation of a low alloy steel
22. Jung YS, Lee YK, Matlock DK, Mataya MC (2011) Effect of grain size on strain-induced martensitic transformation start temperature in an ultrafine grained metastable austenitic steel
23. Varma SK, Kalyanam J, Murr LE, Srinivas V (1994) Effect of grain size on deformation-induced martensite formation in 304 and 316 stainless steels during room temperature tensile testing
24. Saeed-Akbari A, Imlau J, Prah U, Bleck W (2009) Derivation and variation in composition-dependent stacking fault energy maps based on subregular solution model in high-manganese steels
25. Somani MC, Karjalainen LP (2015) Interplay between grain structure, deformation mechanisms and austenite stability in phase-reversion induced nanograined/ultrafine-grained austenitic ferrous alloy
26. Shrinivas V, Varma SK, Murr LE (1995) Deformation-induced martensitic characteristics in 304 and 316 stainless steels during room temperature rolling
27. Therrien, Stevanovi V (2020) Minimization of atomic displacements as a guiding principle of the martensitic phase transformation Felix
28. Mohammad, Sohrabi J, Naghizadeh M, Mirzadeh H (2020) Deformation-induced martensite in ASSs: a review
29. Tamura I (1982) Deformation-induced martensitic transformation and transformation-induced plasticity in steels. *Metal Sci*

30. Patel JR, Cohen M (1953) Criterion for the action of applied stress in the martensitic transformation
31. Bolling GF, Richman RH (1970) The plastic deformation-transformation of paramagnetic fcc Fe–Ni–C alloys
32. Olson GB, Cohen M (1972) A mechanism for the strain-induced nucleation of martensitic transformations
33. Das A, Sivaprasad S, Ghosh M, Chakraborti PC, Tarafder S (2008) Morphologies and characteristics of deformation induced martensite during tensile deformation of 304 LN stainless steel
34. Venables JA (1970) The martensite transformation in stainless steel
35. De AK, Speer JG, Matlock DK, Murdock DC, Mataya MC, Comstock RJ (2006) Deformation-induced phase transformation and strain hardening in type 304 ASS
36. Ningshen S, Kamachi Mudali U (2002) Uniform corrosion of ASSs
37. Talha M, Ma Y, Lin* Y, Pan Y, Kong X, Sinha OP, Behera CK (2019) Corrosion performance of cold deformed ASSs for biomedical applications
38. Influence of Cold Working on the Pitting Corrosion Resistance of Stainless Steels (2006)
39. Kamachi Mudali U, Pujar MG (2015) Pitting corrosion of ASSs and their weldments
40. Elayaperumal K, De PK, Balachandra J (2013) Passivity of type 304 stainless steel effect of plastic deformation
41. Kamachi Mudali U, Ningshen S, Tyagi AK, Dayal, Dayal RK (2021) Influence of metallurgical and chemical variables on the pitting corrosion behaviour of nitrogen-bearing ASSs
42. Dayal RK (1984) Crevice corrosion of stainless steel
43. Muraleedharan P (2002) Metallurgical influences on stress corrosion cracking
44. Hänninen HE (1979) Influence of metallurgical variables on environment-sensitive cracking of austenitic alloys
45. Parvathavarthini N (2002) Sensitization and testing for intergranular corrosion
46. Zheng JH, Bogaert WF (1993) Effects of cold work on stress corrosion cracking of type 316L stainless steel in hot lithium hydroxide solution
47. Muraleedharan P, Khatak HS, Gnanamoorthy JB, Rodriguez P (1985) Effect of cold work on stress corrosion cracking behavior of types 304 and 316 stainless steels

Experimental and Numerical Analysis of Diametric Compression Test of FRP Rings



T. K. Nagaraja , K. B. Yogesha , and M. Mruthunjaya 

Abstract The diametrical compression test remains as a mechanical testing method crossing various technical fields, since concrete to ceramics, to metal composites to fiber reinforced polymer (FRP) materials used in dentistry, and other medical applications. The trial prompts a limited tensile stress in the crosswise path of the practical compressive stress. It permits for the practice of simple sample geometry such as disk and ring to know the limit energy necessary to cause failure, and is used in the approximation of tensile strength in the transverse direction. Review of open literature suggests that diametrical compression test on FRP ring specimens for finding the transverse Young's Modulus are scarcely reported. The main aim of the investigation was to estimate the equivalent Young's Modulus in the transverse track of FRP ring specimens of internal diameter 398 mm, external diameter 462 mm, and width 30 mm which are part of the underwater vehicle structures by diametrical compression test and FE analysis of the test to predict transverse material properties.

Keywords FRP ring · Diametrical compression · FE analysis

1 Introduction

Cylinder-shaped shells have abundant uses in aerospace, industrial structures, such as in launch vehicle fuel tanks and fuselages. It is capability to maintain the great stages of compression loadings along the axial direction, where most of the structure is submitted to membrane loads, and its efficiency is resulting from the absence of stress gradients [1]. The tensile and compression test was done domestically conducted experiments [2]. It is used as a mechanical testing technique spanning many technological fields, from concrete to ceramics, to metal composites to materials used in dentistry, to materials used in the handling of medicinal quantity forms. The mechanical test prompts a native tensile stress in the cross wise path of the

T. K. Nagaraja (✉) · K. B. Yogesha · M. Mruthunjaya
Department of Mechanical Engineering, JSS Academy of Technical Education,
Bengaluru 560060, India
e-mail: nagarajatk@jssateb.ac.in

practical compressive stress. The diametrical compressive test permits for the practice of modest sample geometry like ring to measure a boundary force essential to cause failure, which is used in the approximation of tensile strength in the transverse direction [3]. Glass composite cylindrical structures are frequently used in defense, aerospace, and flying owing to their great strength to weight fraction. Among the composite developed procedures, filament winding (FW) opinions due to excessive accuracy in fiber arranging, great fiber gratified, noble mechanization competency and small void satisfied, presence the most regular development for industrial revolution and axisymmetric components, underwater vehicle assemblies and fuel tanks [4].

2 Literature Review

The consequence of interaction flattening and material properties arranged the rupture stress design for the diametrical compression trial was used to estimate compact strength which was studied complete FE simulations [3]. The sequence of biaxial stationary trials of e-glass/epoxy samples $[+/-45]^2$, exposed to collective torsion and tension/compression remained performed to excite compound stress states met in a wind turbine rotor blade [5]. Effects on pressure containers, created by looping glass fiber with vinyl ester resin above a polyethylene lining, remained mathematically and experimentally examined [6]. Pressure containers mounted experimentally verified in low velocity impact loads. Diverse positions and instance energies were verified in order to estimate the prompted damage and the competency of the established mathematical model [7]. A analytical method was established to plan and forecast the behavior of fiber reinforced composite pressure containers [8]. The traditional lamination concept and universal plane strain model are used in the preparation of the spring problem. Internal pressure, axial force and body force owing to revolution in totalling to temperature and moist difference during the body are deliberated [4]. Now, this both experimental and analytical investigation was performed under external hydrostatic pressure [9]. The hypothetical examinations were approved out by means of a simple result for isotropic materials, using 'von Mises' formula. The trial investigations exhibited that the composite samples performed likewise to isotropic materials before verified [10]. This paper presented a common purpose software for finite element analysis to calculate the fiber volume fraction in various practice environments [11]. Numerical results were related by the investigational information for authentication. In direction to forecast distribution the fiber size portion inside a wet looped tube, three exclusive consumer-defined subroutines stood integrated into the commercial FE code [12]. These comparisons confirmed that the, FEM method can able to forecast fiber volume portion over a variety of twisting situations [13].

3 Experimental Procedure

3.1 *Materials and Its Properties*

The materials of glass/epoxy polymer with the ratio of 80:20 wt % were used for fabrication of various FRP rings, namely, ring 1, ring 2, ring 3, and ring 4. The fabrication of FRP rings (part of UUV structures) were done by filament winding method for inner diameter of 400 mm, outer diameter of 460 mm, and fabrication of diametric compression test fixture using MS material (cutting and welding) [14].

3.2 *Diametric Compression Test*

Ring specimens of required dimensions were cut out from the open end hollow cylinder [15]. Underwater structures are mainly subjected to hydrostatic compressive loads. Hydrostatic tests of these structures are complex and cost inhibitive [16]. It is not feasible to subject all of these designs to experimental tests. Hence, analysis of these designs using numerical methods is vital to assess the change in performance of changed design [17]. The numerical analysis of these designs requires the material properties of the tubes [18]. Results of the analysis entirely depend on the accuracy of these properties. For this purpose, it is necessary to evaluate mechanical properties of the tube in two directions (X and Y). Properties along the X-direction are evaluated through available literature and relevant formulae. Properties along the Y-direction (transverse direction) are evaluated by conducting diametric compression tests [19]. The diametric test was carried in a universal testing machine (UTM). A special test fixture was selected to carry out the compressive test on the test specimen. Four rings are used, and diametric compression test is conducted for both specimens. The dimensions of the specimen are shown in Table 1. The conduction of diametric compression test in universal testing machine (10 ton capacity) by using custom made test fixtures and computation of equivalent Young's Modulus by as per Roark's Formula. Finite element analysis of diametric compression of FRP Rings using ANSYS 15.0. Finally, validation of FEA results with experimental results of deflection.

3.3 *Experimental Procedure*

The lower plate of the test fixture is placed on the base of the universal testing machine (UTM). The ring specimen is then placed between the two guide plates of the lower dish. The top plate is now located on the top of the ring specimen so as to arrest it in between the two guide plates of the top plate. The head of the UTM is then lowered until it makes contact with the top plate. Screws and bolts are used to

Table 1 Dimensions of FRP ring specimens in mm

Measured dimensions of FRP rings used for diametric compression test				
Parameter	Ring 1	Ring 2	Ring 3	Ring 4
Outer diameter	462	463	462	462
Inner diameter	398	398	398	398
Thickness	32	32.5	32	32
Width/length	30.5	24.5	25	30
Mean radius	215	215.25	215	215
Thickness/inner radius (h/R)	0.0804 > 0.033	0.0816 > 0.033	0.0804 > 0.033	0.0804 > 0.033
Classification (thick/thin)	Thick shell	Thick shell	Thick shell	Thick shell

fasten the top and bottom plates to UTM to prevent any relative motion between the UTM and the test fixture plates. The UTM head is lowered until the ring specimen is tightly held between the top and bottom plates. Superior care must be taken to check the alignment of the ring specimen. It should be held vertically straight otherwise as shear forces could affect the test results. Once, the ring specimen has been placed in the compression test fixture, the compression test is configured on the computer.

The compression test loading was carried out gradually, and readings were noted until one of the layers of the GFRP ring specimen begins to delaminate [20]. The delaminating of the GFRP ring specimen is the point of its failure [21]. If any load is further applied, the specimen fails instantly. The load and deflection readings are taken until this point. The ring specimen is then unloaded and carefully removed from the compression test fixture. The point of delamination is marked using a permanent marker. The top and bottom plates are also removed from the UTM machine. Figure 1 shows the FRP ring 1 positioned between fixtures in UTM machine. Figure 2 shows the delaminated FRP ring 1.

Fig. 1 FRP ring 1 positioned between fixtures in UTM machine

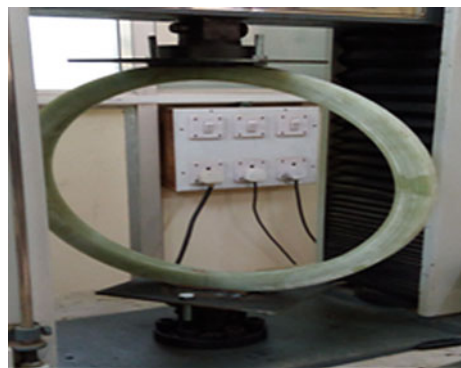




Fig. 2 Delaminated FRP ring 1

4 Results and Discussion

In this process, composite layers are continuously wound on a rotating mandrel. This technique offers a high speed and precise method for placing many composite layers. Among these winding methods, wet winding is more commonly used for manufacturing fiber reinforced thermosetting matrix composite cylinders [22]. Compared with prepreg winding, wet winding has several advantages: low material cost, short winding time, and the resin formulation can be easily varied to meet specific requirements.

FRP ring four specimens are fabricated with ID 400 mm OD 460 mm glass epoxy in the ratio of 80:20 by weight. Test fixture fabricated with MS material which is required for the diametric compression test. Experiments of diametric compression were conducted in UTM by using custom made test fixture.

4.1 Stress–Strain Curve for Various Ring

Figures 3, 4, 5 and 6 shows the stress–strain curve for ring 1, ring 2, ring 3, and ring 4, respectively. The experimental results found in Fig. 6 at higher load, the maximum stress is induced in the ring 4 due to less amount of delamination occurred and there is a decrease in deflection along the Y-direction as compared to other rings at different directions.

Fig. 3 Stress versus strain graph for ring 1

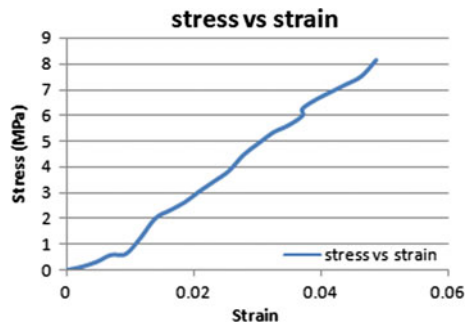


Fig. 4 Stress versus strain graph for ring 2

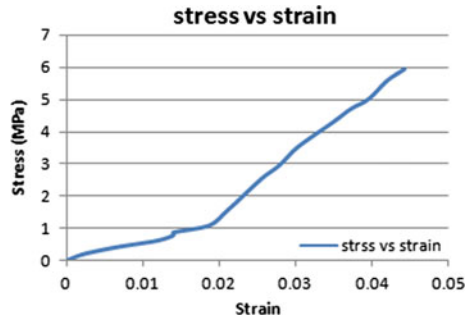


Fig. 5 Stress versus strain graph for ring 3

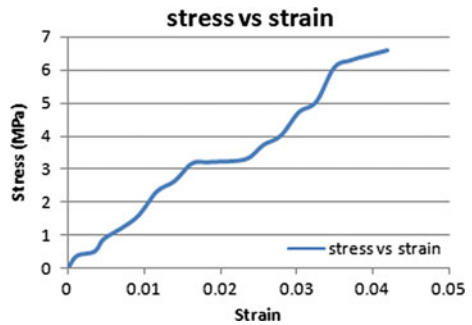
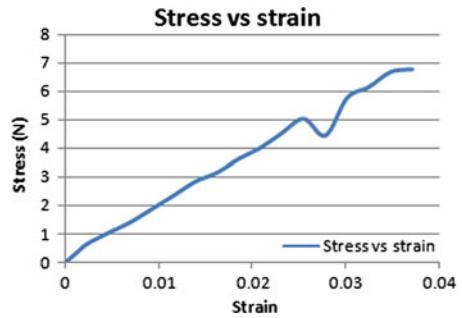


Fig. 6 Stress versus strain graph for ring 4



4.2 Load Versus Deflection Curve for Various Ring

Figures 7, 8, 9 and 10 shows the load versus deflection curve for ring 1, ring 2, ring 3, and ring 4, respectively.

Fig. 7 Load versus deflection graph of ring 1

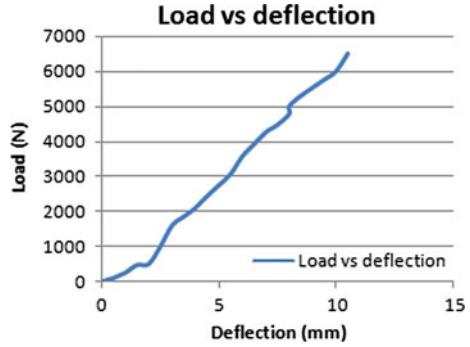


Fig. 8 Load versus deflection graph of ring 2

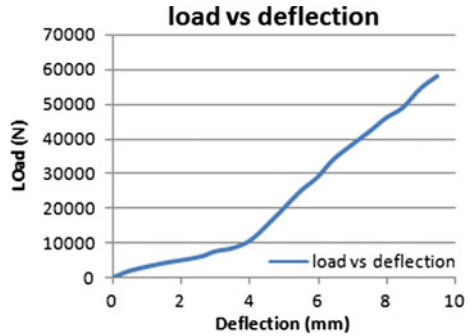
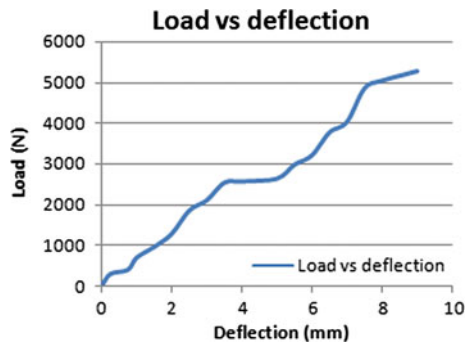


Fig. 9 Load versus deflection graph of ring 3

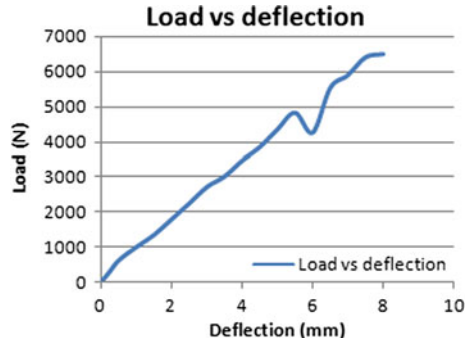


4.3 Analytical Method (Roark’s Formula)

Apply a vertical force (some load in elastic region), W in N and diametric deflection in mm (total diametric deflection, $D1/2$). With this data and the formula of Warren [23], tensile modulus of the ring in the Y-direction is calculated [2].

$$Dv = -(WR^3/EI)(\pi k1/4 - 2k22/\pi)$$

Fig. 10 Load versus deflection graph of ring 4



where

$A = t \times L = \text{thickness} \times \text{length of ring, mm}^2$

$Dv = \text{deflection of the ring due to the applied force (D1/2)}$

$Ey = \text{Equivalent Young's modulus in y-direction;}$

$F = \text{form factor} = 1 \text{ (assumed)}$

$G12 = \text{in-plane shear modulus in x-y plane (Material data)}$

$I = \text{second moment of area of rectangle; } I = L t^3/12, \text{ mm}^4$

$K1 = 1 - \alpha + \beta = 1, K2 = 1 - \alpha = 1$

$R = \text{mean radius of the ring, mm (mean of inner radius and outer radius)}$

Hoop (circumferential) stress deformation factor, $\alpha = I/(AR^2)$

Transverse shear deformation factor, $\beta = (FEI)/GAR^2$

$$Ey = (2R^3/I)(\pi/8 - 1/\pi)(W/Dv) \tag{1}$$

By applying a vertical load W in N, experimental diametric deformation Dv as shown above, substituting for R (mean radius), second moment of inertia $I = Lt^3$, Ey can be estimated. The calculated Ey for both the rings using Warren formula is given in Table 3.

Calculation of Ey using Roark's formula for Ring 1:

$$Ey = (2R^3/I)(\pi/8 - 1/\pi)(W/Dv)$$

$$I = (l * t^3)/12$$

$$R = (463 + 398)/4 = 215.25 \text{ mm}$$

$$t = 32.5 \text{ mm, } L = 24.5 \text{ mm, } W = 5530 \text{ N, } Dv = 9 \text{ mm, } Ey = 13.7 \text{ GPa}$$

Calculation of Ey using Roark's formula for Ring 2:

$$Ey = (2R^3/I)(\pi/8 - 1/\pi)(W/Dv)$$

$$I = (l * t^3)/12$$

$$R = (462 + 398)/4 = 215 \text{ mm}$$

Table 2 Mechanical properties of various rings

FRP rings	Ex (GPa)	Ey (GPa)	Ez (GPa)	G12 (Gpa)	G23 (GPa)	G31 (GPa)	μ_{12}	μ_{23}	μ_{31}
Ring 1	25.48	9.9	9.18	4.64	2.5	1.5	0.28	0.28	0.28
Ring 2	23.48	13.7	9.18	4.64	2.5	1.5	0.28	0.28	0.28
Ring 3	23.48	12.65	9.18	4.64	2.5	1.5	0.28	0.28	0.28
Ring 4	23.48	14.62	9.18	4.64	2.5	1.5	0.28	0.28	0.28

Table 3 Deflection obtained for various rings in mm

	Ring 1	Ring 2	Ring 3	Ring 4
Load (N)	5530	4200	5258	6480
Experimental (mm)	9.5	10.5	9	8
Numerical (mm)	9.59	11.39	9.99	8.95

$$t = 32 \text{ mm}, L = 30.5 \text{ mm}, W = 4200 \text{ N}, Dv = 7.5 \text{ mm}, Ey = 9.8 \text{ GPa}$$

Calculation of Ey using Roark’s formula for Ring 3:

$$Ey = (2R3/I)(\pi/8 - 1/\pi)(W/Dv)$$

$$I = (l * t^3)/12$$

$$R = (462 + 398)/4 = 215 \text{ mm}$$

$$t = 32 \text{ mm}, L = 25 \text{ mm}, W = 5258 \text{ N}, Dv = 9 \text{ mm}, Ey = 12.65 \text{ GPa}$$

Calculation of Ey using Roark’s formula for Ring 4:

$$Ey = (2R3/I)(\pi/8 - 1/\pi)(W/Dv)$$

$$I = (l * t^3)/12$$

$$R = (462 + 398)/4 = 215 \text{ mm}$$

$$t = 32 \text{ mm}, L = 30 \text{ mm}, W = 6480 \text{ N}, Dv = 8 \text{ mm}, Ey = 14.62 \text{ GPa}$$

The results are tabulated for various rings of FRP using empirical formula along x, y, and z direction as shown in Table 2.

4.4 Numerical Method (FE Analysis)

Based on the results obtained by the experimental studies, FE analysis is performed (Figs. 11, 12, 13 and 14).

Fig. 11 FEA analysis on ring 1

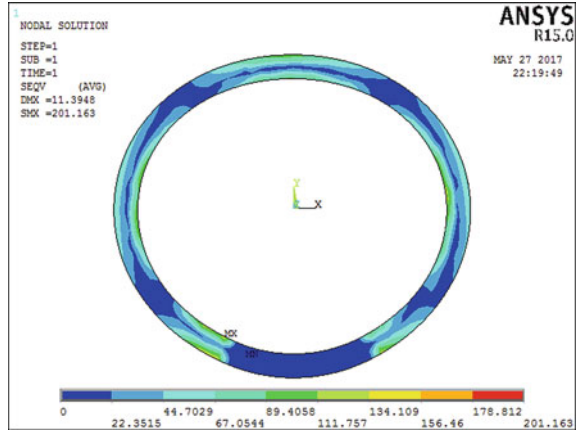


Fig. 12 FEA analysis of ring 2

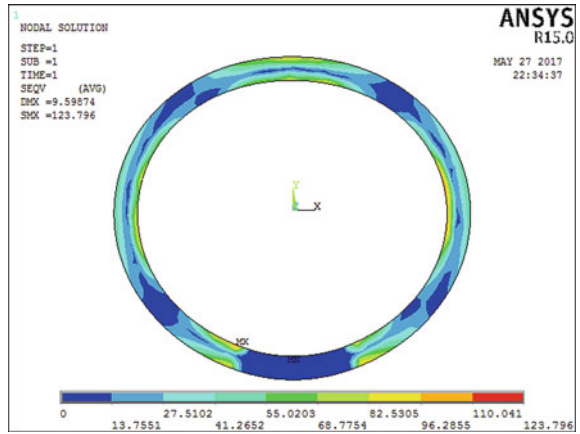


Fig. 13 FEA analysis of ring 3

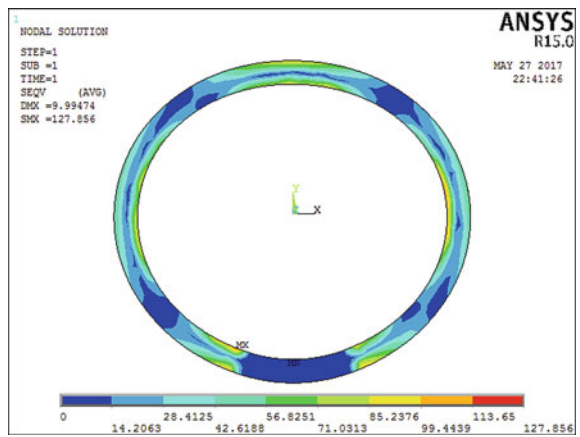
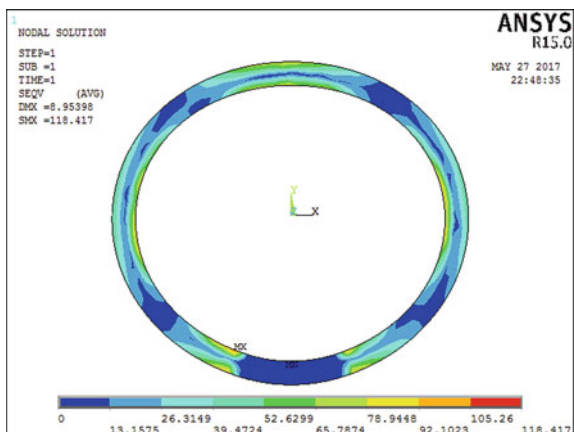


Fig. 14 FEA analysis of ring 4



The results are tabulated comparing the ring 1 to 4 with load (N) in experimental and numerical method in Table 3 as shown. FRP ring four specimens are fabricated with ID 400 mm OD 460 mm glass epoxy in the ratio of 80:20 by weight. Test fixture fabricated with MS material which is required for diametric compression test. Experiments of diametric compression were conducted in UTM by using custom made test fixture. Mechanical properties of all four FRP rings were calculated and tabulated. Experimental results found that the ring 4 has highest value in E_y that is 14.62 GPa. Therefore, from the numerical method we found the similar trend of result for ring 4. Hence, we can conclude that the diametric compression load taken in E_y direction is maximum in ring 4. The delamination of FRP ring due to compression test is very minimal in ring 4. Due to this, the deflection of the ring 4 is less and also load taken from this specimen is maximum 6480 N. Any FRP ring specimen having the load carrying capacity in y-direction during diametric compression test will withstand maximum load.

5 Conclusion

Following conclusions are made based on experimental studies and numerical analysis:

- The concept design to enable the diametric compression of the ring specimen was fabricated. Diametric compression test was successfully performed using the fabricated fixture.
- The GFRP filament wound tube was successfully manufactured according to the required dimensions (462 mm outer diameter, 398 inner diameters, and 32 thickness, $\pm 55^\circ$) [24].
- The diametric compression test was performed successfully on the GFRP ring specimen. The bend of the ring specimen owing to the applied load was obtained

and this was used to obtain the corresponding Young's modulus in the Y-direction. The Young's modulus was calculated to be 13.7 GPa, 9.8 GPa, 12.65 GPa, and 14.62 GPa for ring 1, ring 2, ring 3, ring 4 correspondingly and the deflections obtained are 9.5 mm, 10.5 mm, 9 mm, and 8 mm for ring 1, ring 2, ring 3, and ring 4 correspondingly.

- The deflection of the rings was determined by using ansys. The deflections obtained are 9.59 mm, 11.39 mm, 9.99 mm, and 8.95 mm for ring 1, ring 2, ring 3, and Ring 4.

References

1. Almeida Jr JHS et al (2017) Damage modeling for carbon fiber/epoxy filament wound composite tubes under radial compression. *Compos Struct* 160:204–210
2. Mates SP (2008) Tensile strength measurements of frangible bullets using the diametral compression test. *Int J Impact Eng* 35:511–520
3. Procopio AT et al (2003) Analysis of the diametrical compression test and the applicability to plastically deforming materials. *J Mater Sci* 38:3629–3639
4. Ross TF et al (2009) Buckling of carbon/glass composite tubes under uniform external hydrostatic pressure. *Int J Exp Mech*
5. Antoniou AE et al (2009) Mechanical behavior glass/epoxy tubes under combined static loading. *Compos Sci Technol* 60:2241–2247
6. Wichmann (2006) Glass-fibre-reinforced composites with enhanced mechanical and electrical properties—benefits and limitations of a nanoparticle modified matrix. *Eng Fract Mech* 74:2346–2359
7. Perillo G et al (2015) Numerical/experimental impact events on filament wound composite pressure vessel. *Compos Part B* 69:406–417
8. Parnas L (2002) Design of fiber-reinforced composite pressure vessels under various loading conditions. *Compos Struct* 58:83–95
9. Hu H (2015) Structural design and experimental investigation on filament wound toroidal pressure vessel. *Compos Struct* 121(2.15):114–120
10. Parnas L et al (2002) Design of fiber-reinforced composite pressure vessels under various loading conditions. *Compos Struct* 58:83–95
11. Gunasegaran V (2013) Experimental investigation and finite element analysis of filament wound GRP pipes for underground applications. In: *International conference on design and manufacturing, IConDM 2013*, vol 64. Elsevier, Procedia Engineering, pp 1293–1301
12. Hwang TK (2003) Size effect on the fibre strength of composite pressure vessel. *Compos Struct* 59:489–498
13. Zhao L et al (2001) Finite element modeling of the filament winding process. *Compos Struct* 52:499–510
14. Xia M et al (2008) Analysis of multi-layered filament-wound composite pipes under internal pressure. *Compos Struct* 53:483–491
15. Ross CTF (2009) Buckling of near-perfect thick-walled circular cylinders under uniform external hydrostatic pressure. *J Ocean Technol* 4(2)
16. Shen FC (1995) A filament wound structure technology overview. *Mater Chem Phys* 42:96–100
17. Wild PM, Vickers GW (2002) Analysis of filament wound composite structures considering the change of wind angles through the thickness direction. *Compos Struct* 55:63–71
18. Arikan H (2010) Failure analysis of filament wound composites pipes, composite structures. *Eng Geol* 92:182–187

19. Mellor M, Hawkes I (1971) Measurement of tensile strength by diametral compression of discs and annuli. *Eng Geol* 5:173–225
20. Kitching R, Soden PD (1993) Experimental failure stresses for 55 degree filament wound glass fibre reinforced plastic tubes under biaxial loads. *Compos Struct* 46:363–378
21. Rafiee R et al (2013) Experimental and theoretical investigations on the failure of filament wound GRP pipes. *Compos Part B* 45:257–267
22. Mertiny P, Ellyin F, Hothan A (2004) An experimental investigation on the effect of multi angle filament winding on the strength of tubular composite structures. *Compos Sci Technol* 64:1–9
23. Warren CY (1989) Roark's formulas for stress and strain, 6th edn. McGraw-Hill Book Co., Singapore
24. Tarakcioglu N (2005) Fatigue failure behavior of glass/epoxy +/-55 filament wound pipes under internal pressure. *Compos Sci Technol* 65:703–708

Modelling and Simulation

Alternate Bicycle Freewheel Mechanisms: Design and Finite Element Analysis Under Different Loading Conditions



Mohammad Ahmed Basri , Talvinder Singh , and Anoop Aggarwal

Abstract Freewheel mechanisms are predominantly used in several industries for obtaining uni-directional transfer of rotary motion, such as conveyer belts. In the current study, innovative freewheel mechanisms having the potential for being implemented in bicycle production as mountable parts are designed keeping specific parameters in consideration. Computer-aided design models of multiple bicycle freewheel assemblies are developed, and analytical calculations are incorporated to obtain the design parameters. Numerical techniques are utilized for the assessment of different loading conditions on the mechanical response of the designs. The effects of combined loading as experienced by the freewheel during standard bicycle riding conditions were examined and contrasted for the different designs. The results evaluated include maximum equivalent (von-Mises) stress, total deformation, and factor of safety. These results depict that each of the designs' behavior is different and that each is capable of withstanding the standard loading conditions. The results obtained from this study now form the basis for experimental testing and subsequent employment in the production of bicycles.

Keywords Freewheel · Bicycles · Finite element analysis · Combined loading · Pawl-ratchet · Von-Mises stress · Computer-aided design

1 Introduction

Freewheel mechanisms are widely used in applications such as bicycle and conveyor belts. To estimate the loading conditions on a bicycle freewheel, it is imperative to study the dynamics of the bicycle and its relationship with the freewheel. Many

M. A. Basri (✉)

Department of Mechanical Engineering, Indian Institute of Technology Delhi, Delhi, India
e-mail: mohammadahmedbasri@gmail.com

T. Singh

Department of Mechanical Engineering, Delhi Technological University, Delhi, India

A. Aggarwal

Spark Engineering Pvt Ltd., Ghaziabad, Uttar Pradesh, India

scholars have attempted to investigate the bicycle rider dynamics. One of the initial publications on bicycle dynamics includes the work done by Soden et al., where they estimated the forces that the rider is expected to apply on a bicycle under various cycling situations such as starting the cycle and speeding cycle [1]. Bini et al. presented a more comprehensive analysis of the pedal forces by dividing the force into components like anterior–posterior force and normal force [2]. Mathematical approaches were also utilized to study the effect of pedaling technique on the pedal force. Scholars have studied and conducted experiments on kinematic parameters of BMX bikes as well as the impact of human physiology on these parameters [3–6]. The beginning of a BMX cycle race is the gate start, followed by a kink, and holds importance in winning the race. Scholars also studied rider kinematics concerning the gate start action [3, 7]. Rylands et al. analyzed the rider's peak power, power to weight ratio, fatigue index, and cycling revolutions per minute with the help of a Schoberer Rad Messtechnik (SRM) BMX power meter [8]. Rylands et al. also discussed that cyclists' pumping technique comprises 44% of the total time in a BMX race and hence is an essential factor influencing other cycling parameters [9]. Rylands et al. studied the effect of the upper body on performance during BMX cycling [9]. It concluded that during standing sprints, the force applied on the bicycle is 32% higher than seated sprints. Mateo et al. divided the track into categories based on difficulty level, and their research confirms a direct relationship between the power and difficulty level [10]. The dynamics involved with an ergometer are somewhat comparable to the on-road cycling conditions. Hoes et al. studied the variation of pedal force and the power with crank rotation on an ergometer for different loads and speeds [11]. Vandewalle et al. conducted experiments to find force–velocity relationships on a Monark ergometer [12].

While talking about the kinematic parameters involved during cycling, it should be mentioned that the freewheel or the freehub forms an integral part of the cycle. The freewheel allows forward motion when desired and free movement without pedaling. The freewheel has many applications other than being used in bicycles. The freewheels are used in conveyor belts, where they act as a safety device and prevent “backstops”. A similar device like the freewheel is an overrunning clutch which is a crucial component in the dynamic transmission system of vehicles [13]. Depending upon the relative velocity of the drive shaft for the driven shaft, the clutch automatically engages and disengages. Overrunning clutches may be roller type [14], spring type, sprag type, or pawl-ratchet type [15]. Some have also developed and studied compliant overrunning clutches with compliant mechanisms being investigated as substitutes for conventional mechanisms [15, 16].

The pawl-ratchet mechanism is most prominently used in the freewheel mechanism of cycles. The study presented focuses on the freewheel of bicycle that helps in having a positive drive while pedaling and unrestricted motion in the absence of pedaling even though the cycle is still in motion. Design aspects of novel freewheel mechanisms are developed, and stress analysis is also done under various loading conditions to assess the safety of the design. The stress analysis is determined by finite element analysis using ANSYS mechanical. The freewheel mechanisms covered in this discussion are Freewheel A, B, C, and D and are explained in detail later. While

Table 1 Mechanical properties of heat treated are alloy steel 16MnCr5

Test parameter	Observed result	Test method
Ultimate tensile strength	797.4 MPa	IS 1608-2005
Yield stress	711.0 MPa	
Elongation [GL-50]	8.4%	

other freehubs are available in the market in which the freewheel mechanism is integrated within the rear wheel’s hub, the study concentrates only on freewheels that can be mounted as isolated parts on standard bicycle wheel hubs and thus are time-saving and cost-efficient.

2 Methodology

2.1 Material Testing

The primary material used to fabricate various parts of a freewheel is alloy steel 16MnCr5, except the steel balls for ball bearing and the ring spring. Steel balls that form an integral role in the freewheel mechanism and help in providing a smooth motion are fabricated using EN 31 material, while the ring spring, which is used to shift from one mode to another, is made up of spring steel. The mechanical properties of a raw material and heat-treated material differ; thus, incorporating the properties of the raw material is not advised as it would underestimate the material’s ultimate strength. The freewheel parts are individually undergone heat treatment which increases their strength. Mechanical testing of heat-treated freewheel material using standard ASTM Tests is cumbersome due to difficulty obtaining a standard specimen, and hence, a different approach is utilized. The raw material is cut into a standard UTM specimen, and this specimen was exposed to the same heat treatment processes as the freewheel parts, i.e., hardening at 890 °C for 60 min and quenching in oil at 60–70 °C. The heat-treated specimen is then tested on an Instron UTM machine using the IS 1608-2005 method to find out the material’s mechanical properties to be later used for finite element analysis (FEA). The properties thus obtained are mentioned along with the standard in Table 1.

2.2 Design Description of Freewheels

Freewheel-based pawl-ratchet mechanism is one wherein rotary motion is allowed in one direction and inhibited in the opposite direction with the help of pawls and teeth. The pawl is generally in the form of a tooth that engages and disengages with the linear/rotatory ratchet teeth allowing and restricting motion, respectively.

Pertaining to freewheels in bicycles, there are two modes of operation; in the first mode, the pawl engages with one of the teeth on the ratchet, which is generally a part of the hub of the bicycle's rear wheel due to which the torque applied to the pedal is transmitted to the rear wheel through chain, thus resulting in the positive drive. In the second mode, the pawl glides over the teeth of the ratchet and does not mesh with it; therefore, the pedal remains stationary relative to the rear wheel. In this mode, the hub is freewheeling, which suggests the origin of the mechanism's nomenclature.

Design of Freewheel-A

Figure 1 shows “Freewheel-A” which is the most common type of freewheel mechanism and has the following elements: middle part, outer sprocket, pawl, ring spring, side-cone, steel balls, and shim-washer. The CAD model of the Freewheel-A is developed by reverse-engineering the commercially available freewheel. In contrast, the rest freewheels are modified using CAD modeling software, SolidWorks. The current Freewheel-A under consideration is a standard 14T freewheel with a diameter of the inner hub equal to 34.8 mm. There are 30 inner teeth on the outer sprocket which means there is 12° engagement, i.e., after every 12° of rotation, a click sound would be heard in mode 2. The middle part consists of the pawl seat, which is where the pawl is placed. There is threading on the outer surface for 1/3rd the length for the side-cone and threading on the inner surface for securing the middle part onto the hub of the rear wheel of the bicycle. The outer sprocket has regular involute profile teeth cut out on the outer rim and splines cut out on the inner face. The outer teeth mesh with the roller chain and the internal splines accomplishes the function of a ratchet by interacting with the pawl. It also has two grooves called race for the placement of steel balls. The ring spring has a non-intuitive design, wherein a wire is bent into circular shape with ends untouched. The wire, due to its elasticity, acts as a spring.

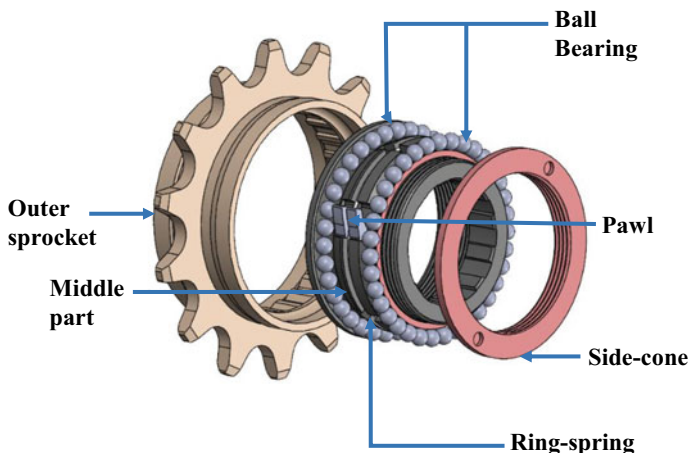


Fig. 1 Freewheel-A—exploded view of CAD model

When the freewheel is in mode 1, the ring spring is in tension, forcing the pawls to mesh with the splines on the inner face of the sprocket. During mode 2, when the middle part and the pawl rotate freely and the pawl glides over the inner splines, the spring is alternatively forced into compression and tension. Pawls are small teeth-like elements that have a groove between them for the placement of the ring spring. When the pawl meshes with the inner splines on the sprocket, the rear wheel rotates along with the rear wheel, i.e., mode 1, and during mode 2, the pawl slides over the inner sprocket wheels. The number of pawls may vary between 2 and 5. The current freewheel under consideration has 3 pawls placed 120° to each other. Side-cone is a basic element secured onto the middle part to house the steel balls, pawl, and ring spring. Steel balls placed in the race machined on the outer sprocket, fulfill the function of reducing friction, and also act as bearing. Shim-wash fulfills the purpose of keeping the steel balls in the race provided on the inside of the outer sprocket and some shock absorption.

Design of Freewheel-B

The Freewheel-B has a similar design to the “Freewheel-A” with a major difference of pawl seat on the inside of the sprocket as shown in Fig. 2, to utilize the Web thickness of the sprocket and maintain inner diameter of the middle part same as the hub of the wheel. The outer sprocket is modified to contain the pawl seat and groove for the placement of ring spring. Splined teeth is provided on the outside surface of the middle part, instead of the inner face of sprocket. The pawl was modified to have a slit on the opposite side in order to accommodate the changes developed in the outer sprocket and the middle part.

Design of Freewheel-C

The proposed mechanism has middle, outer sprocket, pawl, side-cone, steel balls, and shim-washer, same as “Freewheel-A”. Instead of the ring spring, each pawl is supported by a flat spring as shown in Fig. 3 which provides the restoring force for the pawls. Three pawls are made to have a surface contact with the teeth and thus

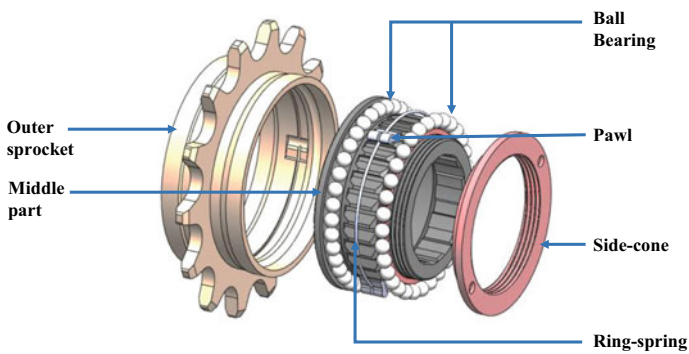


Fig. 2 Freewheel-B—exploded view of CAD model

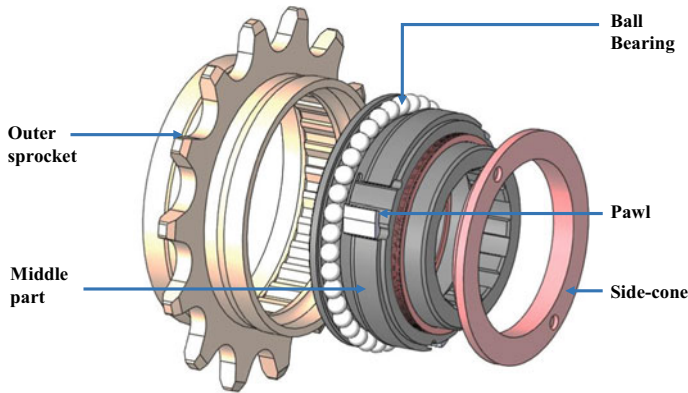


Fig. 3 Freewheel-C—exploded view of CAD model

result in low wear due to lower stress values, which FEA will further prove. The pawls are modified, and the slit for the ring spring, which is obsolete, is removed. The number of pawls is kept same as previous freewheel designs for the sake of comparison. The number of pawls and hence pawl-teeth contact is generally decided based on manufacturing cost—the more the number of connections, the lesser the delay before ratcheting starts.

Flat Spring Design

The flat spring is a wide and flat piece of material that is bent and pivoted on the middle part to act as a spring due to its own elasticity. The spring is modeled as a cantilever beam under transverse bending loading, and its deflection is calculated using the Castigliano's theorem. The Castigliano's first theorem may be stated as the first partial derivative of the strain energy of the structure with respect to any particular force gives the displacement of the point of application of that force in the direction of its line of action [17].

The strain energy stored in the system due to bending is as follows:

$$U = \int_0^L \frac{M^2}{2EI} dx \quad (1)$$

Moment at any section at a distance x away from the free end is given by

$$M = -Px \quad (2)$$

Substituting the moment in the strain energy relation and integrating from 0 to L , we get

$$U = \frac{P^2 L^3}{6EI} \quad (3)$$

where I is the moment of area of the cross-section of the beam. The deflection from Castigliano's theorem is thus given by partially differentiating U with respect to the load P :

Therefore, deflection in the direction of force,

$$\delta = \frac{PL^3}{3EI} \quad (4)$$

and stiffness,

$$k = \frac{P}{\delta} = \frac{3EI}{L^3} \quad (5)$$

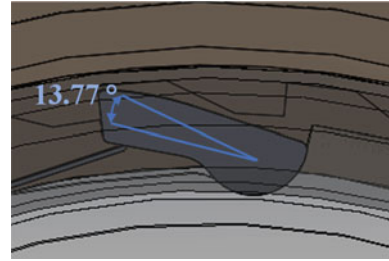
And therefore, by knowing the appropriate stiffness values or a combination of force and deflection desired, one can easily calculate the dimensions of the spring required.

The design criteria for the flat spring of "Freewheel-C" are developed based on the worst-case scenario of the BMX bikes. The limiting factor was the BMX bike's highest speed in normal operation. Mateo et al. [10] have conducted experiments to find out the relation of velocity of bicycle with the level of difficulty. The velocities are measured for three scenarios: not pedaling, gate start pedaling, and full pedaling. A comprehensive analysis of the variation of velocity with time is done, and the peak velocity, mean velocity, and the time to peak velocity are also noted. It is imperative to note that the velocity in the non-pedaling scenario is not of use in case of freewheel analysis since, in the non-pedaling case, the freewheel is in its mode 2, and there is no force being exerted on the pawls. Therefore, the peak full pedaling velocity for high-difficulty track is taken as the design input for the flat spring. The speed of bicycle determines the least amount of time available for the pawl to come back to its original position due to the restoring force of the spring. This is to ensure that the pawl is available for ratcheting as soon as the tooth leaves contact from the pawl, and there is a minimum delay before the ratcheting starts. Using this value of time interval, we can calculate the required angular acceleration of the pawl and further use the following relation to find out the torque.

$$T = I_m \alpha \quad (6)$$

where " I_m " is the mass moment of inertia of the pawl about its axis of rotation, which is modeled as the moment of inertia of a rectangular plate having dimensions: Width, $w = 1.11$ mm and depth, $d = 3.57$ mm with the axis of rotation at the end of the plate. Therefore, the moment of inertia of the pawl about its axis of rotation is given by

Fig. 4 Angle covered by the rotation of the pawl



$$I_m = \frac{m}{12}(w^2 + 4d^2) \quad (7)$$

After substitution, we get $I_m = 11.7 \times 10^{-10} \text{ kg m}^2$. The angular acceleration is calculated by using the time available for motion, and the angle (φ) by which the pawl has to rotate in that time, and thus from rotational mechanics, we have

$$\theta_2 = \theta_1 + \frac{1}{2}(\alpha t^2) \quad (8)$$

where t = time available, α = angular acceleration, θ_1 = initial angular position, θ_2 = final angular position.

Taking $\theta_2 - \theta_1 = \varphi$ = angular displacement (radians).

We get

$$\alpha = \frac{2\varphi}{t^2} \quad (9)$$

The angle $\varphi = 13.770$ is the angle covered by the rotation of the pawl and is shown in the CAD model of “Freewheel-C” (Fig. 4).

The time “ t ” was determined by first finding out the angle subtended by the space between the ratchet teeth at the center of the freewheel and then determining the time required for the freewheel to rotate by that angle when the bicycle is moving at 17.88 m/s. The speed in RPM was calculated as follows:

$$V = \frac{\pi DN}{60} \quad (10)$$

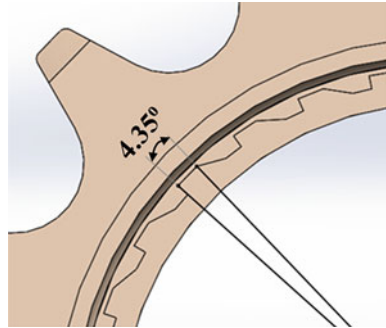
For a 20” BMX wheel, the speed in RPM was calculated to be 672.5 RPM. Therefore, the time required for one complete revolution is 0.0892 s, and thus, the time available between ratcheting, i.e., for 4.350 as shown in Fig. 5 is 0.00107 s.

Thus, using the value of “ φ ” and “ t ”, the angular acceleration required for the pawl was calculated using Eq. (9) to be $\alpha = 419.2 \times 10^3 \text{ rad/s}^2$.

Therefore, $T = 4.9 \times 10^{-4} \text{ N m}$.

The restoring force required was then calculated by using the length of the point of contact of the pawl and spring from the axis of rotation of pawl, which is 2.92 mm,

Fig. 5 Angle subtended by one tooth at center



and thus, the force is 0.167 N. For a maximum deflection of the spring equal to 0.74 mm in the direction of the force, the stiffness:

$$k = 0.167/0.00074 = 225.2 \text{ N/m} \tag{11}$$

The width and depth are limited to the pawl and the space available. The only unknown left is the length of the spring which can be obtained by knowing the values of “*I*” and “*E*” and using Eq. (5).

Depending on usage application, this calculation can be repeated for other maximum speeds and wheel and pawl sizes.

Design of Freewheel-D

This design as shown in Fig. 6 employs two concentric ratcheting rings that mesh with each other. The ratcheting teeth are along the common axis of rotation of the discs. One disc is integral with the inner hub of the freewheel, which is driven by the pedals. The other disc is keyed to the outer sprocket of the freewheel using splines. At the back of the second disc, a helical spring is placed in the space between the faces of the disc and the sprocket. This spring ensures that the second disc remains in its equilibrium position. Each ratcheting tooth of the ratcheting ring occupies an arc of 10°. When the drive is supplied to the inner hub in the clockwise direction + and the teeth of both ratcheting rings mesh together, motion is provided to the sprocket, and motion of the bicycle is initiated. In the opposite case, when the drive is supplied in the anticlockwise direction, the teeth of the ratcheting ring slide over the splines due to their relative angles with the ratcheting ring on the middle part. It is observed that this causes the second ratchet to move axially inwards into the sprocket. Subsequently, the spring is compressed. Immediately after the tips of the teeth are in contact, the secondary disc slides back into its original axial position. Table 2 shows the disengaged and engaged modes of the four freewheels under consideration, and Table 3 depicts the section view of the freewheels showing that each one of them has a different design, but each has two races for ball bearings.

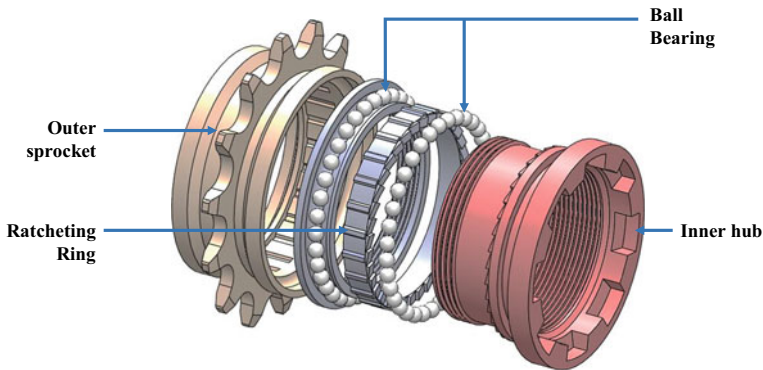


Fig. 6 Freewheel-D—exploded view of CAD model

3 Finite Element Analysis of Freewheels

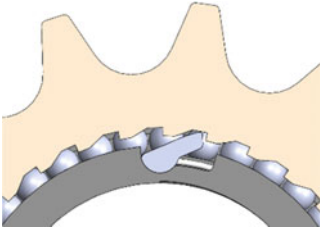
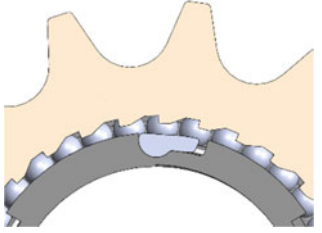
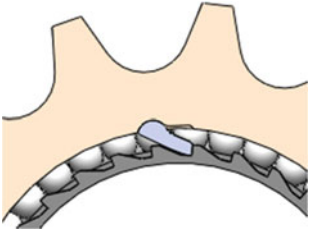
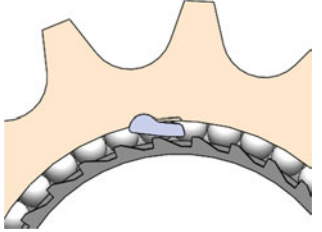
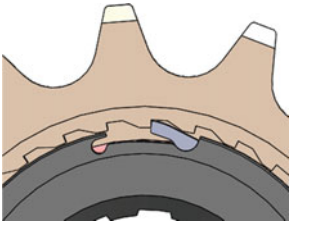
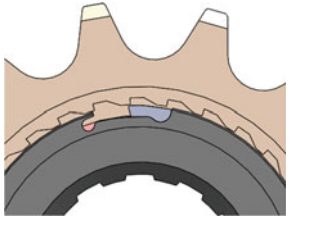
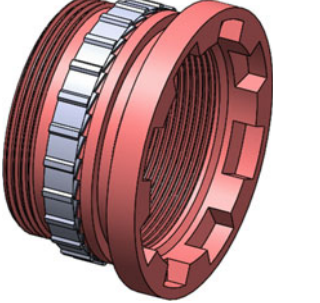
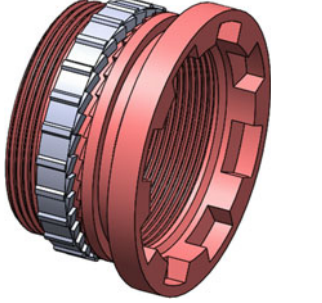
Finite element analysis simulations were performed on each one of the freewheels in order to obtain statistics on load-bearing capacity and safety factor. The simulations were performed with the use of ANSYS mechanical, and a specific set of loading conditions were applied. This section described these conditions and subsequent results obtained in detail.

The individual freewheel was subjected to a number of loading conditions. Firstly, ramped loading analysis of the outer sprocket was performed for ensuring safe functioning, especially in the region of the teeth, which may be subjected to stress concentration. Secondly, impact loading condition was applied to the freewheel's outer sprocket since it is clear that when the cyclist pedals to start the bicycle, force is transmitted to the freewheel which lasts for a short while. The pedal force applied on the pedal during a crank rotation varies with the crank angle. The maximum effective force on the pedal turns out to be 450 N during the crank rotation [18]. A factor of safety of 1.5 is considered, giving a pedal force of 675 N. The force transmitted to the pawls is calculated by transferring the force from the pedal through the chain to the freewheel, as shown in Fig. 7. The analysis is carried out for the pawl and the teeth with which it interacts. Finally, bearing loads and moments were simulated for the middle section of the freewheel. An additional moment loading of the ratcheting ring was performed to investigate the stress distribution exclusively for "Freewheel-D". The loading of the side-cone is sufficiently negligible and was hence not performed.

3.1 Ramped Loading of the Outer Sprocket

In the initial analysis of gradual loading, a specific testing apparatus (named as roller apparatus) was designed that operates similarly to a roller chain as shown in Fig. 8.

Table 2 Engaged and disengaged modes of freewheels

Mode	Engaged (Mode-1)	Engaged (Mode-2)
Freewheel-A		
Freewheel-B		
Freewheel-C		
Freewheel-D		

Since the purpose of the analysis was to ensure maximum load distribution within the sprocket and not on the other components such as the chain, this equivalent modeling was suitable. Simulations were conducted with the use of a chain which, however, did not provide a clear portrayal of the load distribution on the sprocket itself due to the complications in modeling the meshing followed by its meshing.

Table 3 Section views of freewheel assemblies

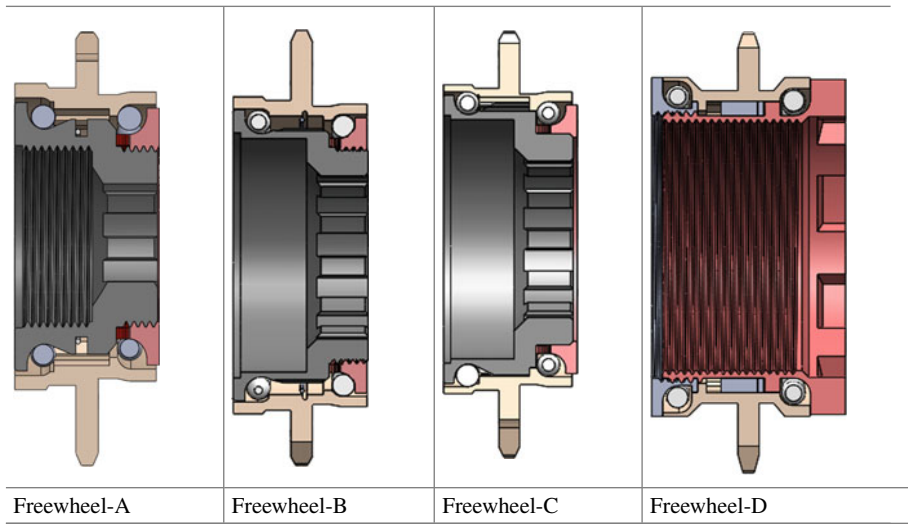


Fig. 7 Schematic diagram of force transmission from pedal to freewheel

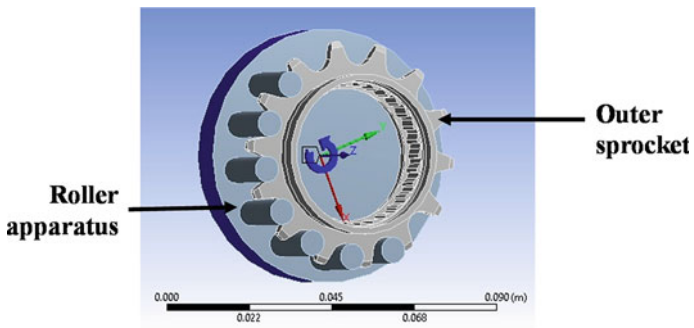
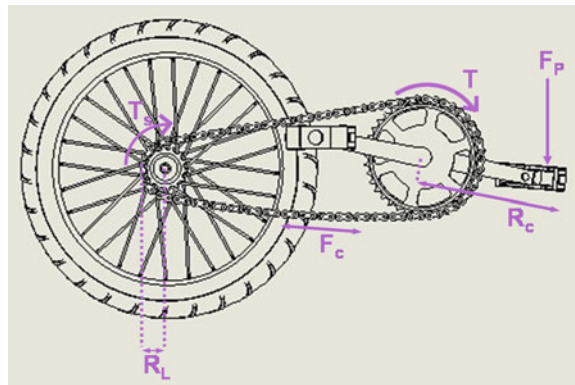


Fig. 8 Roller apparatus and outer sprocket

$$\text{Torque initiated by crank } (T) = F \times R_c \quad (12)$$

where F_p = pedal force = 675 N, R_c = radius of crank = 170 mm

$$\begin{aligned} T &= 675 \times 0.170 \\ T &= 114.75 \text{ N m} \end{aligned} \quad (13)$$

$$\text{Tension in chain } (F_c) = \frac{T}{R_L} \quad (14)$$

where R_L = radius of chain wheel (42 teeth) = 86 mm

$$\begin{aligned} F_c &= \frac{114.75}{0.086} \\ F_c &= 1334 \text{ N} \end{aligned}$$

$$\text{Torque about the sprocket of freewheel } (T_s) = F_c \times R_s \quad (15)$$

where R_s = radius of sprocket (14 teeth) = 28 mm

$$\begin{aligned} \text{Torque about the sprocket of freewheel } (T_s) &= 1334 \times 0.028 \\ T_s &= 37.45 \text{ N m} \\ T_s &= 3.75 \text{ kg m} \end{aligned}$$

Furthermore, incorporation of the chain was computationally expensive and was hence not considered. The middle part was taken as a fixed geometry, and for a pedal force of 675 N, a torque of **3.75** kg-m or **37.5** N-m was applied to the testing apparatus under ramped condition for span of 1 s as calculated.

3.2 Impact Loading of the Outer Sprocket

The analysis involved a systematic approach applying a parabolic impact load on the sprocket. Other boundary conditions remain same as the former analysis, and only the loading condition is modified. The cylindrical faces of the sprocket were taken as fixed supports, and the testing apparatus was mounted on a cylindrical joint. The teeth of the sprocket meshed with the testing apparatus, akin to a roller chain. Contacts between the faces of the apparatus and the sprocket were taken to be frictional with a dynamic friction coefficient of **0.74** [19, 20]. “Formulation” is one of the advanced settings in ANSYS structural used to define the behavior of

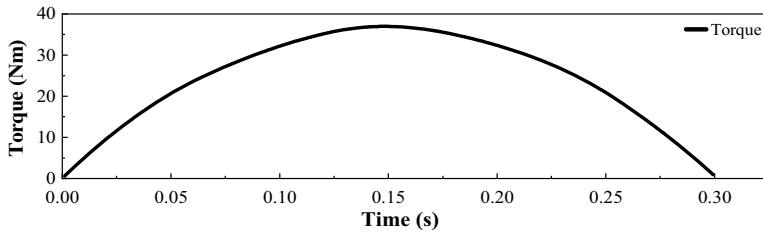


Fig. 9 Parabolic curve of torque versus time for impact loading

the contacts that are specified. There are multiple algorithms that are employed to specify the type of contact pair computation. The augmented Lagrangian formulation method was selected for this problem which is a penalty-based method. It uses the same equation for solving that is used in pure penalty but has an extra augmentation constant, λ . As there is an extra term in the equation, the contact force becomes less sensitive to the stiffness [21]. Therefore, there is lesser penetration at the contacts which will lead to more accurate results. Hence, this formulation is preferred.

$$F_{\text{Normal}} = K_{\text{Normal}} \times X_{\text{Penetration}} + \lambda \quad (16)$$

If penetration is significant, the solver will require additional iterations to converge. Contact penetration is allowed in this formulation, but it is more controlled than in the pure penalty method. The mesh was formulated with a majority of tetrahedral elements. The maximum size of mesh elements was taken as 1.8 mm, which was decided by a brief mesh convergence study. The testing apparatus uses coarse mesh since the stresses in the apparatus are not of primary concern. Following the standardized testing conditions, a load of **37.5 N-m** was applied to the testing apparatus. The torque was applied over a span of 0.3 s with a parabolic shape as shown in Fig. 9. Due to this, the torque initially increases to the desired value and then drops. All this happens in 0.3 s, and therefore, it imitates the condition of impact loading.

3.3 Loading on the Pawl of Freewheels

Analysis for Freewheel A, B, and C

Load transfer from the outer sprocket to the internal middle section of the freewheel occurs through the pawl component. It is a tiny element responsible for the majority of the torque transfer in the freewheel. The stress concentration on the pawl is quite significant for the safety of the design and must be considered for FEA analysis.

The following procedure calculates load which is to be applied on the pawl:

$$\text{Maximum torque} = 37.5 \text{ N-m (Rounded Off)}$$

The radius of the outer part at which chain force is applied is $r = 28 \text{ mm} = 0.028 \text{ m}$.

Since,

$$\text{Torque}(T) = \text{Force}(F) * \text{Radius}$$

Hence, force (F),

$$\begin{aligned} F &= \frac{37.5}{0.028} = 1339.28 \\ &= 1340(\text{Approx.}) \end{aligned} \quad (17)$$

As the number of pawls (n) = 3, therefore,

$$\text{Force on each pawl} = \frac{1340}{3} = 446 \text{ N} \quad (18)$$

The mesh for the pawl was formulated with a majority of tetrahedral elements, and the maximum size of mesh elements was taken as **0.34** mm. This time, the size of the mesh is smaller than the former analysis of outer sprocket since pawls are more prone to failure. The force of 2800 N is applied at the front face of the pawl, and the face at which pawl rests on the pawl seat is taken as fixed geometry.

Analysis for Freewheel-D

Since the freewheel mechanism is entirely different in Freewheel-D due to the elimination of the pawls, the analysis is modified. The teeth of the ratcheting ring, which is in contact with the teeth on the middle part, are taken as fixed geometry. The moment is given to the extruded portion of the ratcheting ring, which has splines on it meshing with the splines on the outer sprocket. The setup is done to depict the conditions when the freewheel is in engaged mode, and the torque applied to the larger sprocket through the pedal is transmitted to the outer sprocket of the rear wheel.

4 Results and Discussion

4.1 Ramped Loading of the Outer Sprocket FEA Results

The results of static structural analysis with ramped loading of the outer sprocket are discussed in this section. In case of ramped loading, the load, in this case, the torque gradually increases from zero to the desired torque of 37.5 N m. The von-Mises stress or equivalent stress contours for the ramped loading of outer sprocket is shown in Fig. 10. Freewheels A and C have the same outer sprocket and thus are

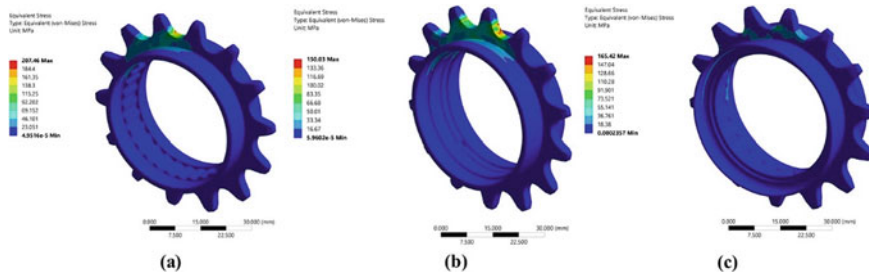


Fig. 10 Equivalent (von-Mises stress) for ramped loading on outer sprocket of **a** Freewheel-A and Freewheel-C, **b** Freewheel-B, **c** Freewheel-D

represented by one plot. The von-Mises for freewheels A and C is 207 MPa, which is the maximum among other values. In case freewheel B, the stress is reduced to 150 MPa, and for Freewheel-D, the max stress is 162 MPa. On comparing the outer sprocket of freewheels A and C with that of Freewheel-B, we see that the outer sprockets are non-uniform in thickness. For freewheels A and C, there are teeth cut on the inside surface, due to which it has highest von-Mises stress. In Freewheel-B, also the outer sprocket has less thickness, however, it is only at three points where the pawl seat is cut out, therefore the stress is less than other cases. The stress in the sprocket of the Freewheel-D is because its outer sprocket has splines cut out on the inside to accommodate the movement of the ratcheting ring.

4.2 Impact Loading of the Outer Sprocket FEA Results

The results for the impact loading of the freewheel in which the torque acts for a short duration are shown in Fig. 11. The impact loading is crucial to understand the dynamics of the cycle in the actual scenario, as the freewheel experiences high-initial torque when the cyclist initially applies the force on the pedal. As shown in Fig. 11, for every case, the max von-Mises stress is greater in impact loading as compared to in ramped loading. Impact loading is a high-strain rate phenomenon, and thus, the dynamic effects result in higher stress in the parts. If we compare the freewheels with one another, similar trend is observed as in the case of ramped loading. The max von-Mises stress for sprocket of freewheels A and C is 276 MPa, while that of freewheels B and D are 243 MPa and 256 MPa, respectively. Figure 12 shows the comparison between the maximum von-Mises stress in ramped and impact loading of the sprocket of freewheels.

We see that in both the cases of loading, the max stress is much less than the yield strength of the constituent material (Table 1), therefore the factor of safety in every case is greater than 1, hence ensuring the safety of the design.

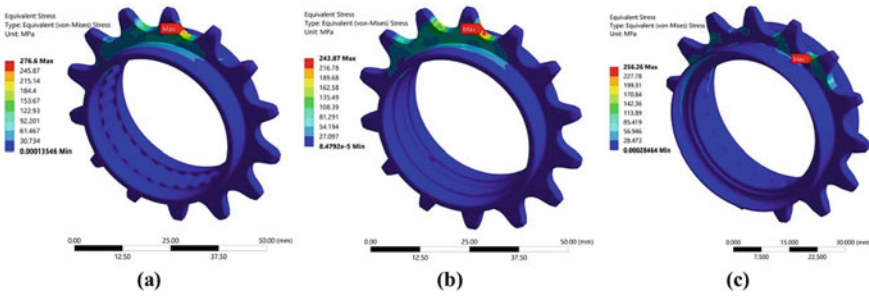
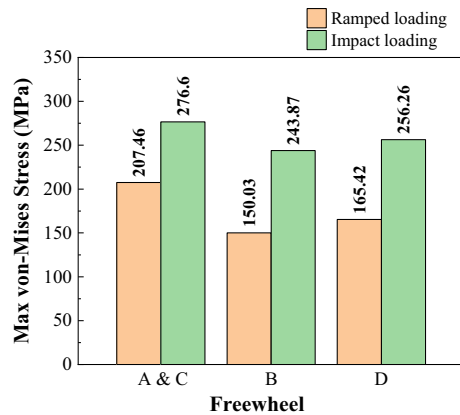


Fig. 11 Equivalent (von-Mises stress) for impact loading on outer sprocket of **a** Freewheel-A and Freewheel-C, **b** Freewheel-B, **c** Freewheel-D

Fig. 12 Max equivalent (von-Mises stress) for all freewheels in case of ramped and impact loading on outer sprocket



4.3 Loading on the Pawl FEA Results

Pawls of the four freewheel mechanisms differ in their design and thus exhibit different maximum equivalent stress values as shown in Fig. 13. Max von-Mises stress in pawl for Freewheel-A has stress of 102 MPa, while pawl of Freewheel-C has satisfactory value of 116.5 MPa. Freewheel-B’s pawl has the maximum stress concentration at 128.8 MPa, which is due to sharp corners where the ring spring is located. Lastly, ratcheting ring does not fail and has maximum stress of 84.1 MPa. The high values of maximum stress are not uniform over entire ring but only exists at points where there is stress concentration. It can also be observed that for the pawls of freewheels A, B, and C, 80% of the part (referred by green-yellow portion) has stress which is around 85% the value of the max stress. Whereas in case of the ratchet ring of Freewheel-D, the entire part is blue except at the location of teeth where the stress is high. In this case also, the max stress is much below the strength of the material, and hence, no failure of the design will occur. Figure 14 shows the deformation pattern of the pawls and the star ratchet, and it can be concluded that the

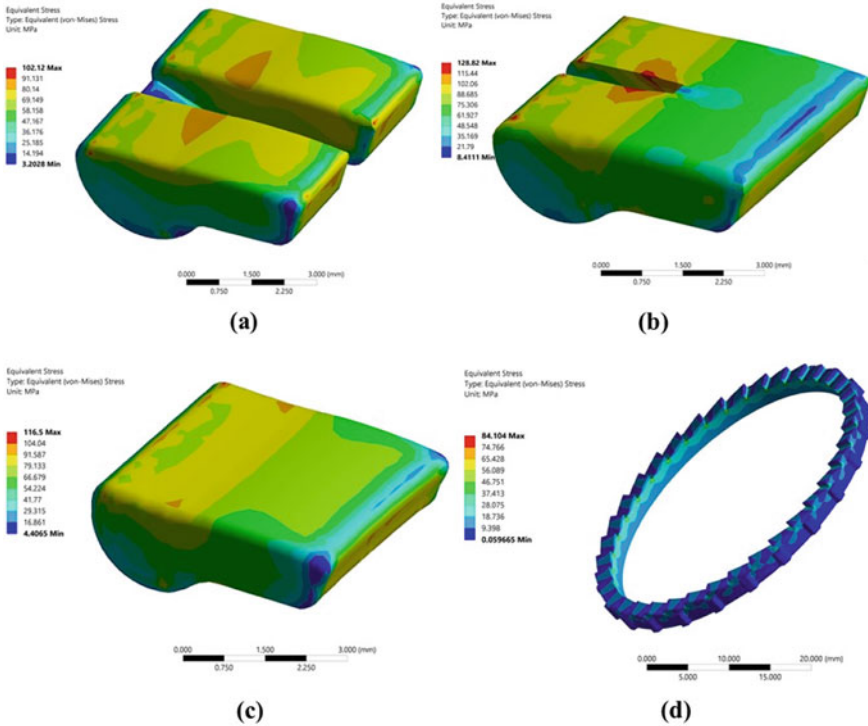


Fig. 13 Equivalent (von-Mises stress) for loading on pawl of **a** Freewheel-A, **b** Freewheel-B, **c** Freewheel-C, and **d** star ratchet of Freewheel-D

max deformation is around 0.002 mm, which is negligible and hence can be ignored. The seat of the pawl has zero deformation (shown in blue), whereas the end part of the pawl which comes in contact with the teeth on the sprocket undergoes slight deformation.

While “Freewheel-A” is one of the most generic freewheel mechanisms being used in the bicycle industry, other freewheels are new developments to satisfy some of the customer’s needs. Parts of “Freewheel-A” occupy much of the radial space available and leaves less space for the middle part whose internal diameter matches with the outside diameter of the hub of the rear wheel. Due to this fact, they cannot be used for larger diameter hubs. Freewheel-C solves this issue by utilizing the Web thickness of the outer sprocket while Freewheel-B incorporates the use of flat springs for space optimization. Freewheels A and C have pawls making a line contact with the teeth, while Freewheel-B administers a surface contact, leading to better grip and torque transmitting capability. “Freewheel-A” poses two main challenges: One is that the pawl wears out over a long duration of usage, and the second is that the spring snaps or fails during the course of the usage. Both of these can prove to be catastrophic for the freewheel. “Freewheel-D” mechanism can effectively overcome both of these challenges while simultaneously minimizing the space consumed by

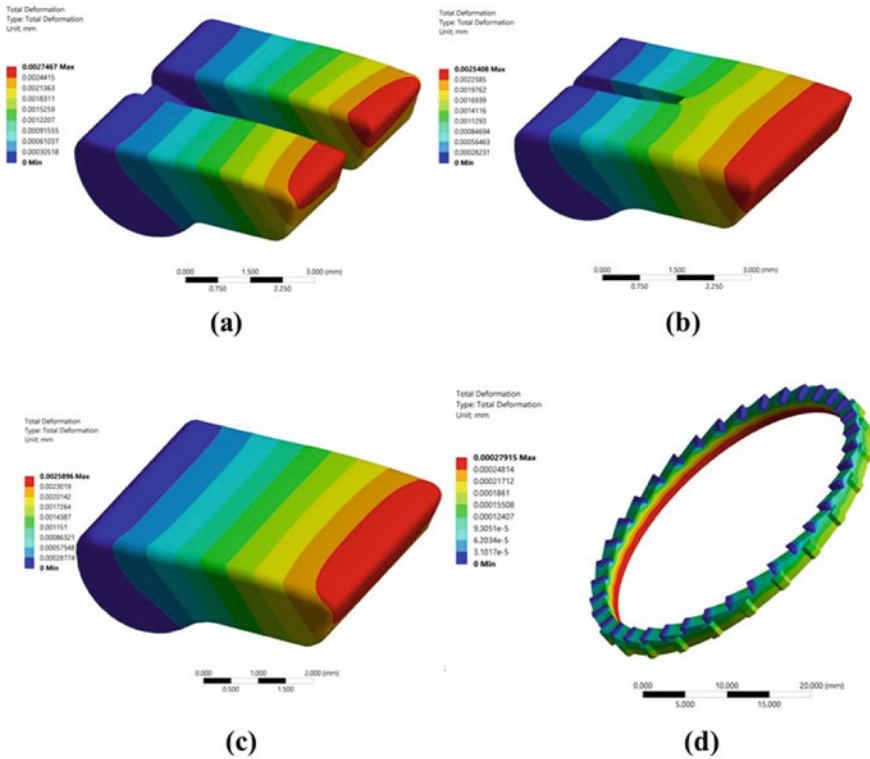


Fig. 14 Total deformation for loading on pawl of **a** Freewheel-A, **b** Freewheel-B, **c** Freewheel-C, and **d** star ratchet of Freewheel-D

the mechanism. The large surface area of contact between the teeth of the ratcheting ring ensures minimal wear over time, while the use of a standard helical spring gives it a distinct advantage over standard ring springs and flat springs. Another major advantage of “Freewheel-D” is that there are more than 3 contact points and all transferring torque simultaneously, which maximizes mechanical advantage. And since, there are multiple contact points, the load gets distributed, and hence, there are fewer chances of failure of the ratcheting ring.

Manufacturability is the most important process in the development of a new product. An attempt is made to give insight into the manufacturing techniques that can be used for the different freewheels. As already mentioned, Freewheel-A is the most generic freewheel and hence easily fabricated through CNC and cold forging techniques. Freewheel-C is mostly similar to Freewheel-A but having an extra groove in the middle part for the flat springs which can be fabricated using cold forging. The major concern arises in case Freewheel-B and Freewheel-D. As Freewheel-B has an opposite arrangement, the teeth can be cut out on the outer part by broaching process, and the grooves for pawl seat on the inside of outer sprocket can be made

by groove milling operation. For Freewheel-D, all components can be easily manufactured except tangential teeth on the ratcheting ring and the middle part. These tangential teeth can be processed using innovative methods like Revacycle method, face-hobbing process, generation method, and generic CNC machining. Future work involves fabricating the freewheel using the different manufacturing process with aid from freewheel manufacturing companies. Also, testing of these freewheels on actual bicycles would be done to assess the validity of the designs.

5 Conclusions

The study investigates the design of freewheel mechanisms used in bicycles using finite element analysis. The freewheels designed and analyzed in the study have the potential for being implemented in bicycle production as mountable parts on the hubs of bicycle wheels. Computer-aided design models of multiple bicycle freewheel assemblies were developed, followed by analytical calculations and FEA used to assess the viability of design under different loading conditions. Particularly, ramped and impact loading cases were considered. For the FE analysis, the model of chain was replaced by a dummy apparatus that replicates the function of chain in a cycle. A novel impact loading technique is used in which the torque vs time input is given as a parabolic curve. These results show that the performance of each design differs and that each is able to endure the typical loading conditions. The results reveal that all designs of the freewheels are safe as their safety factor is greater than 1. In the case of impact loading, the max stress is less than the max stress in the case of ramped loading of sprockets of all freewheels. The findings of this study will now serve as the foundation for experimental testing and eventual use in the manufacture of bicycles.

Declaration of Conflicting Interests The author(s) declared no potential conflicts of interest with respect to the research, authorship, and/or publication of this article.

Author Contributions **Mohammad Ahmed Basri:** Conceptualization, methodology, software, formal analysis, investigation, data curation, writing-original draft and editing, visualization. **Talvinder Singh:** Methodology, formal analysis, data curation, writing-original draft, and editing **Anoop Aggarwal:** Project Administration, funding acquisition.

Acknowledgements The authors would also like to thank Mr. Ujjwal Suri and Mr. Abhinash Bharat of the Mechanical Engineering Department, Delhi Technological University and Mr. Baljinder Singh of the Mechanical Engineering Department, IIT Delhi for their valuable suggestions.

References

1. Soden P, Adeyefa B (1979) Forces applied to a bicycle during normal cycling. *J Biomech* 12(7):527–541

2. Bini RR, Rossato M (2014) Kinetics and pedaling technique. In: Biomechanics of cycling. Springer, Berlin, pp 43–53
3. Gianikellis K, Skiadopoulou S, Bote A (2011) 3D Kinematics applied to the study of individual BMX gate start technique. In: ISBS-Conference proceedings archive
4. Grigg J, Haakonssen E, Orr R, Keogh JW (2017) Literature review: kinematics of the BMX SX gate start. *J Sci Cycl* 6(1):3–10
5. Kalichová M, Hřebíčková S, Labounková R, Hedbávný P, Bago G et al (2013) Biomechanics analysis of bicross start. *Int J Med Health Pharm Biomed Eng* 7(10):361–369
6. Duc S, Bertucci W, Pemin J, Grappe F (2008) Muscular activity during uphill cycling: effect of slope, posture, hand grip position and constrained bicycle lateral sways. *J Electromyogr Kinesiol* 18(1):116–127
7. Cowell JF, McGuigan M, Cronin J (2012) Strength training considerations for the bicycle motocross athlete. *Strength Conditioning J* 34(1):1–7
8. Rylands L, Roberts SJ, Cheatham M, Baker A (2013) Velocity production in elite BMX riders: a field-based study using a SRM power meter. *J Exerc Physiol Online* 16(3):40–50
9. Rylands LP, Roberts SJ, Hurst HT (2017) Effect of gear ratio on peak power and time to peak power in BMX cyclists. *Eur J Sport Sci* 17(2):127–131
10. Mateo M, Blasco-Lafarga C, Zabala M (2011) Pedaling power and speed production vs. technical factors and track difficulty in bicycle motocross cycling. *J Strength Conditioning Res* 25(12):3248–3256
11. Hoes M, Binkhorst R, Smeekes-Kuyt A, Vissers A (1968) Measurement of forces exerted on pedal and crank during work on a bicycle ergometer at different loads. *Int Z Angew Physiol Einschließlich Arbeitsphysiol* 26(1):33–42
12. Vandewalle H, Peres G, Heller J, Panel J, Monod H (1987) Force-velocity relationship and maximal power on a cycle ergometer. *Eur J Appl Physiol Occup Physiol* 56(6):650–656
13. Zhong L, Zhang S, Xie C, Yao J (2018) Design and simulation analysis of an energy-saving type of overrunning clutch life testing device. In: 2018 International conference on mathematics, modelling, simulation and algorithms (MMSA 2018). Atlantis Press, pp 22–26
14. Chen Y-C, Chen L-W (2006) Effects of design parameters on the slipping torque of an overrunning clutch. *Proc Inst Mech Eng Part D J Automobile Eng* 220(5):563–570
15. Roach GM (2003) An investigation of compliant over-running ratchet and pawl clutches. Brigham Young University
16. Crane NB (2003) Compliant centrifugal clutches: design, analysis, and testing. Brigham Young University
17. Timoshenko SP (1955) Strength of materials. Part 1. Elementary Theory *Probl* 1955:165–310
18. Gregor JR, Broker JP, Ryan MM (1991) Biomechanics of cycling
19. Fuller DD (1963) 2D coefficients of friction. In: American Institute of physics handbook, vol 1. Columbia, New York, p 42
20. Stefancu A-I, Melenciuc S-C, Budescu M (2011) Penalty based algorithms for frictional contact problems. *Buletinul Institutului Politehnic din Iasi. Sectia Constructii, Arhitectura* 57(3):119
21. Fluent AN (2009) Ansys Fluent 12.0 theory guide. ANSYS Inc., Canonsburg, PA

Design and Analysis of Composite Spur Gear



Aniket Oswal, Deepesh Bhalodia, Akshay Sunctankar,
and Lokavarapu Bhaskara Rao

Abstract The present paper deals with the detailed and comprehensive methodology for FEA analysis of composite spur gears. Gears are an essential component in a mechanical power transmission system and rotary mechanical system. Predominantly, gears have been used as a potent means of transmitting power in mechanisms due to their high degree of dependability and compactness. The continuously changing and innovative industries like heavy industries, automobile manufacturing, and mechanical automation systems will demand novel application of gear technology. Presently, with regards to advancements in material sciences, composites are developed for various applications in aerospace, automotive, and biomechanical domains. Aluminum composites and alloys have been extensively produced and researched upon due to the mechanical properties of aluminum composites. In this work, modeling and FEA analysis of a selected spur gear is done by comparing the traditional cast steel spur gear with metal matrix composite (MMC's) materials like aluminum titanium (Al-Ti), aluminum boron carbide (Al-B₄C), and aluminum beryllium (AlBeMet) metal matrix composite. Here, a detailed comparison is performed between the conventional material and the composite material. The weight reduction advantages have been observed and recorded. Specific uses of the MMC's have been proposed in accordance with the observed results.

Keywords Composites · Spur gear · FEA analysis · Metal matrix composites · Torque

A. Oswal · D. Bhalodia · A. Sunctankar · L. Bhaskara Rao (✉)
School of Mechanical Engineering, Vellore Institute of Technology, Chennai,
Vandalur-Kelambakkam Road, Chennai, Tamil Nadu 600127, India
e-mail: bhaskarbabu_20@yahoo.com

A. Oswal
e-mail: aniketsanjay.oswal2018@vitstudent.ac.in

D. Bhalodia
e-mail: deepesh.bhalodia2018@vitstudent.ac.in

A. Sunctankar
e-mail: Dattarajakshay.mahesh2018@vitstudent.ac.in

1 Introduction

Spur gear is the most elementary and common class of gear manufactured that are cylindrical-shaped components utilized for transmission of rotational motion between two or more parallel shafts. Spur gears are the primary option among the gears unless the maximum speed, loads, and proportions are commanding to look for other options. Different types of gears maybe preferred which provide low vibration performance. Generally, spur gears are designed to sustain a pitch line velocity of 25 m/s and have a contact ratio ranging from 1:1 to 1:6. The efficiency of a spur gear is 98–99% [1]. The spur gear are easily produced and less costly. They possess very high-performance efficiency and exceptional accuracy. They are employed in rapid processes and high-loading condition in every single type of trains, buses and have gamut of velocity ratio. Therefore, these spur gears have varied applications from watches, industrial appliances, cycles, cars, and railways to airplanes. The price of replacing spur gear is expensive and gear failure causes breakdown of gear system., e.g., motor vehicle. It is therefore very important to increase the power of the gear to avoid failure. Composites deliver relatively good mechanical properties for instance great strength/weight ratio, better material hardness, and in turn reduce chances of mechanical failure. Hence, the objective of replacing conventional gear with gear made of composite material like Al–Ti, Al–B₄C, and AlBeMet is to have better performance of machine [2, 3].

Mohammed Safiullah et al. [4] suggested that in this paper, authors have suggested that Aluminum Titanium MMC can be well suited for the manufacturing of spur gear. A proposed material-Al (90%)–Ti (10%) was analyzed mathematically and experimentally. The results show that conventional material properties can be replaced by the above composite. Pawar and Abhay [5] mentioned that Al–SiC composites can be produced by either of the manufacturing process like powder metallurgy and also stir casting. It possesses properties like better stiffness and tensile strength with increased weight reduction. Here, the analysis for contact stress has been performed between gears at different contact points during dynamic condition. Based on the analysis, the conclusion was drawn that the strength-to-weight ratio for composite materials is about three times that of mild steel and it is twice less in weight than aluminum of the same dimension. Rajeshkumar and Manoharan [6] presented in this paper that the CAD design is made and analytical calculations of composite spur gears are performed theoretically. The gear tooth contact analysis is carried out using FEA method by varying the speeds. The spur gear is manufactured using three different materials. It was concluded that composite materials are better alternative to steel and plastic counterparts. Prasad et al. [7] performed design and analysis of spur gear and also mentioned about the convectional gears used in sugarcane juice machine replacing them with polymer gears to decrease the weight and vibrations. The primary objective was to examine different types of polymer gears like nylon, polycarbonate and their feasibility against the metallic gears like cast iron. They used FEA method to come to a conclusion that if composite gears are well designed and analyzed it will help the reduction in properties like cost, sound, vibrations and

will give show execution very similar to convectional gears. Mahendran et al. [8] mentioned that the impact analysis of spur gear is done using torque loading for conventional cast steel and other composites. At the end, they have compared and analyzed the existing spur gear made of cast steel with that of composite materials' spur gear. The material used here includes carbon fiber epoxy composite with high strength to weight ratio. Rao and Padmanabhan [9] fabricated aluminum matrix composite with boron carbide with verifying weight fraction like 2.5, 5, and 7.5%. In order to manufacture the composite through liquid metallurgy and observed the microstructure through scanning electron microscope and its material properties like hardness and compression were studied. Hardness and compressive strength were improved with increase in weight percentage of boron carbide reinforcement in the composite.

The objective of this project is to analyze the total deformation, stresses, and weight reduction of spur gear obtained by replacing cast steel spur gear with composites materials. ANSYS 19.2 tool is used for the computational analysis of the spur gear and a detailed methodology is executed. The analysis is carried out for different torque loading, with multiple materials and the results are observed. According to the results, proposal for use of metal matrix composites in spur gear is drawn.

2 Design of Spur Gear

2.1 Design Goal

The existing spur gear made of cast steel is compared with that of composite materials' spur gear. For this purpose, Ansys 19.2 is used for FEA simulations. The analysis of gears is performed by applying varied torque loading. Induced stresses are calculated for cast steel and composite materials. The end results obtained experimentally are compared with the conventional material, i.e., cast steel. From the above FEA, there has to be a reduction in stress, weight, and deformation of composite material spur gear to that of conventional gear.

2.2 Design Calculations

After finalizing the torque and the power to be transmitted, tangential load is calculated using Lewis equation and also pitch circle diameter is to be calculated from the calculated force. From the PSG design data book [10], ultimate stresses are taken for composite and metal. From the ultimate stresses, the allowable stresses are calculated to check if the design is safe or not.

The Torque applied (T) = 13.8 kg-m at rate of 2500 rpm (N)

$$T = 13.8 \times 10 \text{ N-m} = 138 \text{ N-m}$$

$$\begin{aligned} \text{Power Transferred } P &= \frac{2\pi NT}{60} \\ P &= \frac{2 \times 3.148 \times 2500 \times 138}{60} \\ P &= 36,128 \text{ W} \end{aligned} \quad (1)$$

Now, Power (P) = 36.128 kW

$$\text{And Torque } T = F \frac{d}{2} \quad (2)$$

where F is load applied, d is the pitch circle diameter ($zm - 180$) of the spur gear.

$$\begin{aligned} T &= F \frac{d}{2} \\ F &= \frac{T}{\frac{d}{2}} \text{ N} \\ F &= \frac{138,000 \text{ N-mm}}{90 \text{ mm}} \end{aligned} \quad (3)$$

Applied Load (F in N) = 1533.33 N

From Lewis equation for tangential load condition,

$$\begin{aligned} F &= \text{by } Pc\sigma b \\ Pc &= 3.14 \times \text{Module} \\ Pc &= 31.4 \text{ mm} \\ y &= \text{Lewis Form Factor} = 0.134 \text{ mm} \\ b &= \text{face width} = 54 \text{ mm} \end{aligned} \quad (4)$$

The maximum allowable stress = 8.7413 N/mm²

Ultimate Tensile Stress (UTS) of Cast Steel = 540 MPa

$$\begin{aligned} \text{Allowable Stress for cast steel} &= \frac{\text{UTS}}{3} \\ &= \frac{540 \text{ MPa}}{3} \\ &= 180 \text{ N/mm}^2 > 8.7413 \text{ N/mm}^2 \end{aligned} \quad (5)$$

Therefore, the design is safe to use.

2.3 Gear Calculation

Number of teeth (z) = 18

Module (m) = 10 mm

$$\begin{aligned} \text{Pitch circle diameter(PCD)} &= zm \\ &= 18 \times 10 = 180 \text{ mm} \end{aligned} \quad (6)$$

Pressure angle (\emptyset) = 20°

$$\begin{aligned} \text{Base circle diameter} &= \text{PCD} \times \cos \emptyset \\ &= 180 \times \cos 20^\circ = 169.144 \text{ mm} \end{aligned} \quad (7)$$

$$\begin{aligned} \text{Diameter of Outside circle} &= (z + 2)m \\ &= (18 + 2) \times 10 = 200 \text{ mm} \end{aligned} \quad (8)$$

$$\begin{aligned} \text{Clearance} &= \frac{m}{20} \\ &= \frac{3.14 \times 10}{20} = 1.57 \text{ mm} \end{aligned} \quad (9)$$

$$\begin{aligned} \text{Addendum(in mm)} &= m \\ &= 10 \text{ mm} \end{aligned} \quad (10)$$

$$\begin{aligned} \text{Dedendum(in mm)} &= D = \text{Addendum(mm)} + \text{Clearance(mm)} \\ &= 10 + 1.57 = 11.57 \text{ mm} \end{aligned} \quad (11)$$

$$\begin{aligned} \text{Diameter of Dedendum circle} &= \text{PCD} - 2D \\ &= 180 - 2(11.57) = 156.86 \text{ mm} \end{aligned} \quad (12)$$

$$\begin{aligned} \text{Radius of the fillet circle} &= \frac{m}{8} \\ &= \frac{3.14 \times 10}{8} = 3.9 \text{ mm} \end{aligned} \quad (13)$$

$$\begin{aligned} \text{Depth of the hole} &= 2.25 \times m \\ &= 2.25 \times 10 = 22.5 \text{ mm} \end{aligned} \quad (14)$$

$$\text{Thickness of teeth} = \text{Clearance} \times m$$

$$= 1.57 \times 10 = 15.71 \text{ mm} \quad (15)$$

$$\begin{aligned} \text{Face width}(b) &= 0.3 \times 180 \\ &= 54 \text{ mm} \end{aligned} \quad (16)$$

Center distance between two gears = 180 mm

$$\begin{aligned} \text{Diametric pitch} &= \frac{z}{\text{PCD}} \\ &= \frac{18}{180} = 0.1 \text{ mm} \end{aligned} \quad (17)$$

Torque (T) = 200 N-m = 200,000 N-mm at 2500 rpm

$$\begin{aligned} \text{Power} &= \frac{2\pi NT}{60} \\ &= \frac{2 \times 3.14 \times 2500 \times 200}{60} = 52,333.33 \text{ W} = 52.33 \text{ kW} \end{aligned} \quad (18)$$

$$\begin{aligned} \text{Load}(F) &= \frac{2T}{\text{PCD}} \\ &= \frac{2 \times 200,000}{180} = 2222.22 \text{ N} \end{aligned} \quad (19)$$

3 Methodology

A 3D model of the spur gear was made in solidworks 2020. Later, it was imported into Ansys workbench for further detailed FEA analysis. Moreover, in order to validate the results, mesh convergency was carried out. After obtaining the results, a detailed comparison was performed on various factors like von-Mises stress, total deformation, strain energy, and shear stress against the composite materials. The methodology is presented in Fig. 1.

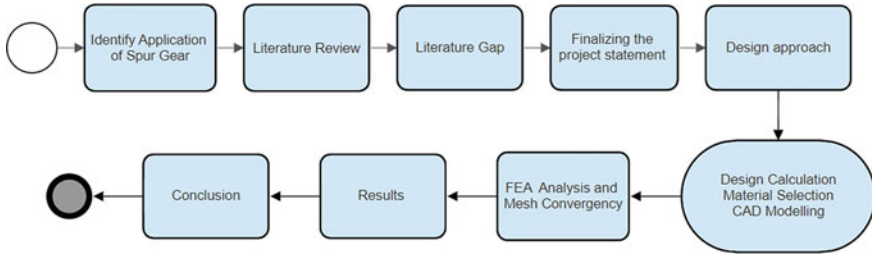


Fig. 1 Methodology of the design and analysis of spur gear

Table 1 Properties of cast steel

Density	7870 kg/m ³
Modulus of elasticity	200 GPa
Poisson’s ratio (μ)	0.29
Tensile strength	518 MPa
UTS	540 MPa
YTS	415 MPa
Bulk modulus of elasticity	140 GPa

4 Material Selection

4.1 Cast Steel

Steel is obtained by adding carbon in small percentages to iron for improving strength and fracture resistance compared to other forms of iron. Cast steel belongs to a class of carbon steel having carbon content around 0.1–0.5%. It is known for its impact resistance properties and can face sudden impact conditions without any deformation or bending. It is also known as crucible steel due to its origin when huntsmen made it by heating metal up to 2900 °F (1600 °C). Cast steel has a rough surface finish due to gas bubbling during the heating process, but the resulting metal has tensile strength, four times that of cast iron. Table 1 contains the mechanical properties of cast steel [11].

4.2 Selection of Composite Materials

Aluminum Titanium (Al–Ti)

The titanium aluminides, Al–Ti, are considered to be a perfect reinforcement material [12, 13] because of its excellent mechanical properties (Table 2) and low-density factor, principally at high temperatures. The main purpose of introducing this material was low-density and to produce aluminum and titanium with good wear resistance.

Table 2 Properties of Al–Ti

Density	3.141 g/cm ³
Modulus of elasticity	72,800 MPa
Poisson's ratio (μ)	0.3

Table 3 Properties of Al–B₄C

Density	2.63 g/cm ³
Modulus of elasticity	72.6 GPa
Poisson's ratio (μ)	0.3097
UTS	259 MPa

Table 4 Properties of AM-162

Density	2.10 g/cm ³
Modulus of elasticity	193 GPa
Poisson's ratio (μ)	0.17

Aluminum Boron Carbide (Al–B₄C)

Aluminum alloy AA6061 is used as a matrix in this case. Boron carbide is used as a reinforcement because of its exceptional characteristics like high strength, low density (around 2.52 g/cm³) [14, 15], good hardness, and better wear resistance. The density of the composite is less than the aluminum base metal. The hardness and compressive strength can be far increased by this reinforcement. The poison's ratio is also reduced than the base metal which reduces contact stress and increases the life of gears (Table 3). The chemical composition of LM6Al is used as a matrix material [16].

Aluminum Beryllium AM-162

Aluminum and beryllium are the primary constituents of the AlBeMet composite. Varying the ratio of both the metals gives different physical, thermal, and mechanical properties. This composite provides the high strength and low-density properties of beryllium with the fabrication in combination with the mechanical properties of aluminum (Table 4). AlBeMet (AM162) is comprises of 62% by weight of pure beryllium and 38% by weight of pure aluminum.

5 Modeling and Finite Element Analysis

In this study, spur gears are modeled in SOLIDWORKS 2020 [17] with different specifications like module and pressure angle [18] conducted modeling of spur gear using solidworks for FEA analysis of carbon fiber reinforced spur gear. After modeling spur gear pairs in solidworks according to the above specifications, those designs were converted into IGS format and were incorporated in the Ansys workbench [19]

to calculate various parameters like von Mises stress and deformities. Static structural analysis was performed in the Ansys work bench. Material characteristics such as the Young’s modulus of compounds are tested by tensile testing, and the poison’s ratio is determined by the law of mixtures. The physical features of the cast steel are taken from the design data book. Fixed support and frictionless support were used as boundary conditions to evaluate stresses.

5.1 Boundary Conditions

On the inner surface of the lower gear fixed support has been applied (Fig. 2), and the frictionless support has been applied on the inner surface of rim for the gear (left side in Fig. 3) to restrict radial translation and to allow tangential rotation. Moment of 140, 170, and 200 N-m has been applied on the inner surface of the gear in dextral direction as the applied torque [20] explored the technique for the FEA simulation (ref. Fig. 4).

Fig. 2 Fixed support

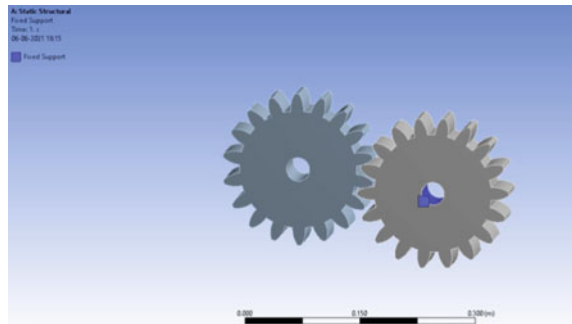


Fig. 3 Frictionless support

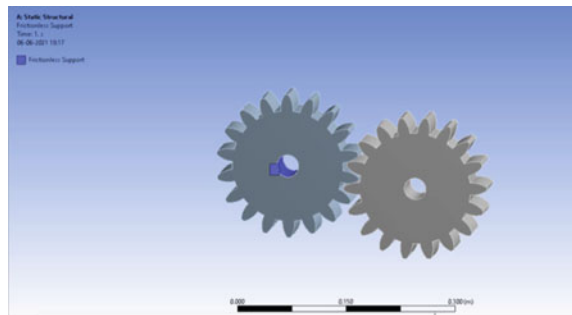


Fig. 4 Moment

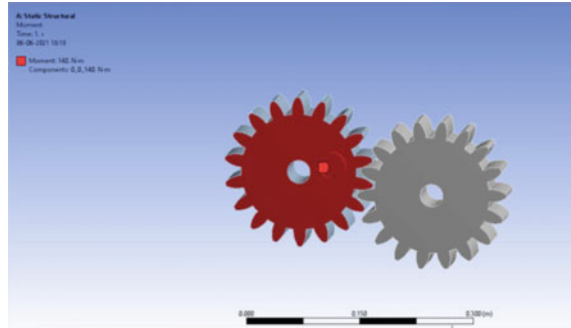
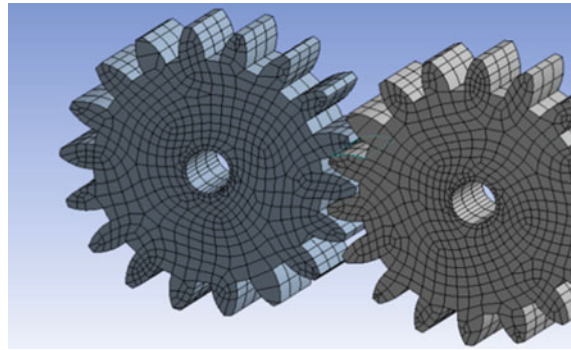


Fig. 5 Meshing



5.2 Meshing

Meshing is done using hexagonal mesh with number of elements of 3696 and number of nodes of 20,526 as shown in Fig. 5. The element size is set to default as per ANSYS 19.2. Hexagonal meshes are economic with the number of elements because the same degrees of freedom for one hexagon corresponds to six tetrahedra which means the computational time is less in case of hexagonal mesh. Moreover, since the geometry is not complex, hexagonal meshing is the suitable choice with very little distortion.

5.3 Static Structural

The von Mises stress, total deformations, shear stress, and strain energy were determined using a FEA-based analysis tool in this project, to examine and understand the behavior of the composite material under the provided boundary conditions, as shown in Figs. 6, 7, 8, and 9, respectively. If the stress value obtained in the analysis crosses the allowable limit, the gear will fail. To avert such a failure, static structural analysis is performed.

Fig. 6 Cast steel—von-Mises stress

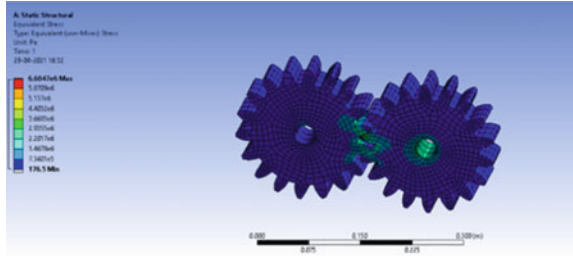


Fig. 7 Cast steel—total deformation

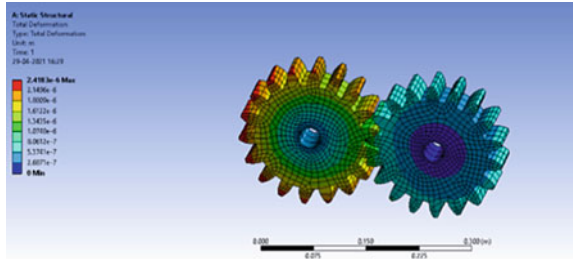


Fig. 8 Cast steel—shear stress

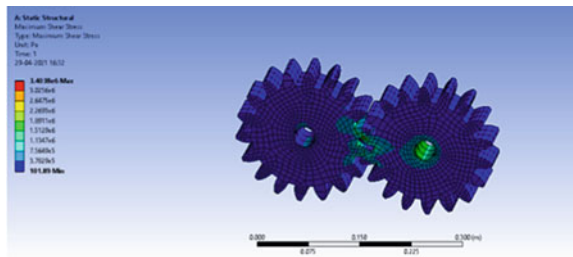
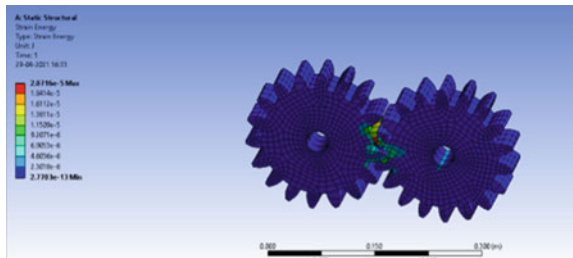


Fig. 9 Cast steel—strain energy



6 Mesh Convergency

The mesh convergency is the study of how small the element size should be so that the results obtained by the FEA analysis will not differ regardless of the mesh size.

Table 5 Mesh convergence

Sr. No.	Total deformation (m)	Change (%)	Nodes	Elements
1	2.4183e-006	–	20,526	3696
2	2.4147e-006	-0.15002	34,329	18,080
3	2.5754e-006	6.4391	132,221	83,713
4	2.6506e-006	2.8799	291,862	198,455
5	2.7333e-006	3.0719	613,421	426,540
6	2.7944e-006	2.2107	1,009,770	713,448

Mesh convergency and is crucial for the validation of the FEA results is consistent for the particular geometry [21]. Iterative solution is carried for by increasing the number of nodes and number of elements in the mesh. Greater the mesh density, smaller the element size. Table 5 shows the mesh convergency.

7 Results and Discussion

From the finite element analysis results as shown in Table 6, we observe that the stress and total deformation values for cast steel and aluminum beryllium (AM162) are comparable. The results of Al-Ti and Al-B₄C composites show higher total deformation value compared to cast steel as shown in Fig. 10. The FEA analysis was carried out to obtain the von-Mises stress, shear stress, strain energy and the total deformation at different torque loadings for the selected materials.

Table 6 FEA analysis results for given boundary conditions

Material	Torque (N-m)	von-Mises stress (Pa)	Shear stress (Pa)	Strain energy (J)	Total deformation (m)
Cast steel	140	6.6047e+6	3.4038e+6	2.0716e-5	2.4183e-6
	170	8.0200e+6	4.1332e+6	3.0546e-5	2.9366e-6
	200	9.4353e+6	4.8262e+6	4.2278e-5	3.4548e-6
Al-Ti	140	6.5792e+6	3.3836e+6	5.6892e-5	6.6560e-6
	170	7.9891e+6	4.1087e+6	8.3886e-5	8.0823e-6
	200	9.3989e+6	4.8337e+6	11.611e-5	9.5084e-6
Al-B ₄ C	140	6.5536e+6	3.3638e+6	5.7015e-5	6.6858e-6
	170	7.9580e+6	4.0846e+6	8.4068e-5	8.1185e-6
	200	9.3623e+6	4.8055e+6	11.636e-5	9.5511e-6
AlBeMet	140	6.8507e+6	3.6183e+6	2.1188e-5	2.4372e-6
	170	8.3187e+6	4.3987e+6	3.1242e-5	2.9595e-6
	200	9.7867e+6	5.1691e+6	4.3242e-5	3.4817e-6

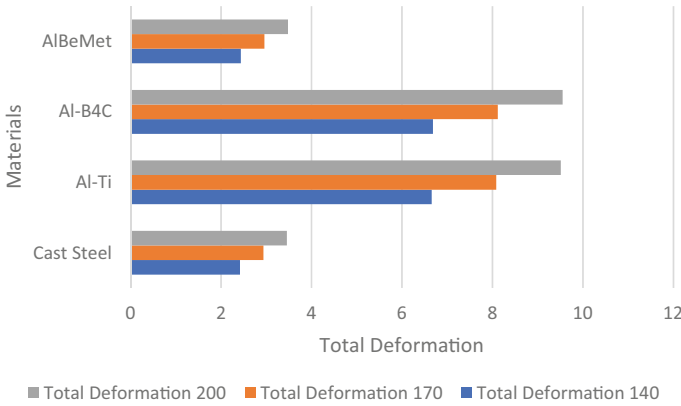


Fig. 10 Comparison of total deformation for various torque and composite materials

Table 7 Weight reduction in spur gear compared to cast steel

Material	Weight reduction (%)
Al-Ti	60.09
Al-B ₄ C	66.59
AlBeMet	73.316

Percentage Reduction in Weight Compared to Cast Steel

The weight reduction of sour gear compared to cast steel is presented in Table 7.

$$\text{Weight reduction}(\%) = \left(\frac{W_{\text{cast Steel}} - W_{\text{Al-Ti}}}{W_{\text{cast Steel}}} \right) \times 100$$

8 Conclusion

This paper uses Ansys Workbench to show the design and analysis of a novel composite spur gear under static loading conditions. The main goal of the current work is to determine a suitable composite material for spur gear as compared to conventional gear. In order to determine this, the analytical and finite element methods are applied for finding the total deformation, shear stress, von-Mises stress, and strain energy. The result which is obtained from FEA calculations can be compared with that of theoretical calculation. From the static structure analysis, we inferred that AlBeMet has slightly more deformation as compared to cast steel. But, while calculating the weight reduction in composite spur gear, we came to know that AlBeMet accounts for approximately 73.316% reduction in weight when compared with cast steel gear as shown in Table 7. Also, adding its wear resistance properties and higher




von misses stress, it is suitable for the application. So, to conclude, cast steel spur gear can be replaced with aluminum beryllium composite (AlBeMet) due to its improved strength/weight ratio and improved stiffness.

References

1. Diez-Ibarbia A, Fernandez del Rincon A, Iglesias M, De-Juan A, Garcia P, Viadero F (2016) Efficiency analysis of spur gears with a shifting profile. *Meccanica* 51(3):707–723
2. Bhandari VB (2020) Design of machine elements. Tata McGraw-Hill Education
3. Uvaraja VC, Natarajan N (2012) Comparison on Al6061 and Al7075 alloy with sic and B4C reinforcement hybrid metal matrix composites. *J Miner Mater Charact Eng* 11:757–768
4. Mohammed Safiullah SD, Nair Ajit V, Mohan Raj C, Rakesh S (2019) Design and analysis of composite spur gear using Al-Ti materials. *Int J Eng Res Technol* 8(3):182–186
5. Pawar PB, Utpat AA (2014) Development of aluminium based silicon carbide particulate metal matrix composite for spur gear. *Procedia Mater Sci* 6:1150–1156
6. Rajeshkumar S, Manoharan R (2017) Design and analysis of composite spur gears using finite element method. *IOP Conf Ser Mater Sci Eng* 263(6):062048
7. Prasad VS, Hussain SA, Pandurangadu V, Palani Kumar K (2012) Modeling and analysis of spur gear for sugarcane juice machine under static load condition by using FEA. *Int J Mod Eng Res* 2(4):2862–2866
8. Mahendran S, Eazhil KM, Senthil Kumar L (2014) Design and analysis of composite spur gear. *Int J Res Sci Innov* 1(6):42–53
9. Rao SR, Padmanabhan G (2012) Fabrication and mechanical properties of aluminium-boron carbide composites. *Int J Mater Biomater Appl* 2(3):15–18
10. (1966) PSG design data book. PSG College of Technology Coimbatore, pp 8.1–8.64
11. Patil NU, Chaphalkar SP, Chaudhari GL (2017) Stress analysis of spur gear by using different materials a review. *Int Conf Ideas Impact Innov Mech Eng* 5(6):355–363
12. Mukherjee A, Sharma R (2019) Design and analysis of composite spur gear using Al-Ti materials. *J Electr Eng Comput Sci* 01(1):19–27
13. Saikrupa Ch, Chandra Mohan Reddy G, Venkatesh S (2021) Aluminium metal matrix composites and effect of reinforcements—a review. *IOP Conf Ser Mater Sci Eng* 1057(1):012098
14. Nie C-Z, Gu J-J, Liu J-L, Zhang D (2007) Production of boron carbide reinforced 2024 aluminum matrix composites by mechanical alloying. *Mater Trans* 48(5):990–995
15. Rao KV (2016) Mechanical properties in MMC of aluminum alloy (A356/LM25) matrix and boron carbide (B4C) reinforcement. *Int J Eng Res* 5(2):683–689
16. Gowtham AVS, Lakshmana Kishore T, Komaleswara Rao M (2017) Analysis of spur gear using boron carbide particulate reinforced Lm6 aluminium metal matrix composite. *IJEDR* 1704102
Int J Eng Dev Res 5(4):2321–9939
17. Plancharth D (2019) SOLIDWORKS 2020 tutorial. SDC Publications
18. Devi SM (2017) Finite element analysis of composite spur gear. *J Mech Civ Eng* 3(1):13–16
19. Ansys A (2019) Workbench user manual
20. Karaveer V, Mogrekar A, Preman Reynold Joseph T (2013) Modeling and finite element analysis of spur gear. *Int J Curr Eng Technol* 3(5):2104–2107
21. Liu Y, Glass G (2013) Effects of mesh density on finite element analysis 2013-01-1375

Structural and Thermal Analysis of Modified Ventilated Paperboard Using Finite Element Analysis



Sagar Yanda , Jagadish , N. V. Swamy Naidu ,
Sathish Kumar Adapa , and Sivasankara Raju 

Abstract In today's world, edible polymers employed in biomedicines, cosmetics, drug delivery, tissue engineering, and food processing and packaging industries. In this work aims to modeling (CATIA V5) of a modified of ventilated paper board (VPB) followed by finite element analysis (ANSYS). In this study, the processing parameters such as line pressure, force, and temperature are considered for the static and thermal analysis. The results found that, the most deformation happened at the corners of the vent, while the greatest equivalent stress produced at the corners of the boxes in the case of static analysis. Also, the least heat flow formed along the edges of the boxes in the case of thermal analysis. The results from the static analysis shows the total deformation and equivalent stress is obtained from 120FL material are 0.0026 m and 1.866 MPa compared with other two materials. Similarly, the results from the thermal analysis shows that the temperature and heat flux is obtained from 125FL material are 29 °C and 942.76 W/m °C compared with other two materials.

Keywords Ventilated paperboard packing (VPP) · Computer aided design · ANSYS · Finite element analysis (FEA)

1 Introduction

Ventilated paper board packing play important key role in modern industries. Nowadays, a ventilated paper board is used in different applications because of their preferable properties such as low cost and less weight. The ventilated paperboard packing are used in transporting the material from one place to another place, that is, packing of food, drinks, consumer electronics, medicines, and personnel care. Mostly, India

S. Yanda (✉) · Jagadish · N. V. Swamy Naidu · S. K. Adapa
Department of Mechanical Engineering, National Institute of Technology (NIT), Raipur 492010, India
e-mail: sagaryanda@gmail.com

S. Yanda · S. K. Adapa · Sivasankara Raju
Department of Mechanical Engineering, Aditya Institute of Technology and Management, Tekkali, India

is the second place for transporting food and vegetable from one place to another place compared to other countries.

Fadiji et al. [1] used solid works for the design and ANSYS for analysis of ventilated paperboard. The authors are focused on compression load ventilated paperboard experimentally and numerically. It was noted stress concentration was more at the top of the packages and vent holes, corners at the side of the packages. Ambaw et al. [2] have analyzed the static behavior of the ventilated paperboard packages. The ventilated paperboard is achieved by finite element analysis was good agreement with experimental data. Pankaj et al. [3] explored the compression strength of ventilated paper board design used in citrus industries. Rodrigues et al. [4] investigated failure mode of the ventilated paperboard including tensile or compression and buckling loads. Han et al. [5] investigated the optimum parameters of the ventilated hole and hand holes in the ventilated paper board using finite element analysis. Talbi et al. [6] used a finite element numerical approach for evaluating the analytical homogenization of a corrugated board. Kostner et al. [7] studied that the creep behavior of the corrugated ventilated paperboard. Park et al. [8] investigated the mechanical behavior of the ventilated corrugated paperboard. To analyze the equivalent mechanical behavior of the ventilated paperboard using finite element modeling.

The literature review reveals that many of the authors have worked on design and analysis of ventilated paperboard using finite element analysis. However, the authors are not considered the aspects of design features of the structural and thermal of ventilated paperboard. After design changes, the static and thermal analysis of a ventilated paperboard was not carried out. Hence, this paper aims to design modification of ventilated paperboard packing followed by static and thermal analysis using finite element analysis. The results found that the maximum total deformation. Maximum stress and heat flows are obtained. Finally, the ventilated paperboard design considerations were compared with actual design considerations of the ventilated paperboard and verify the finite element analysis simulations.

2 Materials and Methods

2.1 *Ventilated Paper Board Materials*

In this study, three paperboard materials are used and their materials are 125 fluting liner (FL), 165 semi chemical paper board (SC), and 175 fully recycled board (T_1), respectively. In this study, the parameters like temperature and relative humidity is considered according to the standards of ASTM 4332 according to the study done by Fadiji et al. [2]. The different thickness of different paperboard materials is considered and same is tabulated in Table 1.

Table 1 Thickness of the paperboard grades

Paper grade	Thickness in mm
125FL	0.1992 ± 0.05
165SC	0.2174 ± 0.001
175T1	0.2604 ± 0.004

2.2 *Ventilated Paper Board Modeling*

In this section, modeling of a ventilated paperboard as shown in Fig. 1a is carried out. Modeling a ventilated paperboard is on in CATIA V5 software. The ventilated paperboard packing dimensions of 400 mm length (L), 300 mm width (W), and 270 mm height (H) and carries a capacity of 20 kg. In the design, there are five features added in this modified ventilated paperboard modeling. These features are four circular vent holes on each side at the top of the side, half circular hole at the bottom of the side, two circular vent holes on front side, two vent holes on the left side, and one slot at the top of the side. These features are added to decrease the deformation, heat flow and to increase the equivalent stress developed in the ventilated paperboard. The modified design with rear view is shown Fig. 1b designed in CATIA V5.

2.3 *Static and Thermal Analysis*

In this section, the static and thermal analysis procedure are been explained. The static analysis is carried out using ANSYS 15.0 software. During the static analysis, the first step is importing the model using.stp file, then the ventilated paperboard model is meshed with 1 mm mesh in automatic mode to the entire part. The second step is applying the boundary conditions that are force and pressure according to the condition, and then the third step is the simulation results are calculated. In thermal analysis of a ventilated paper board is carried out at 29 °C temperature is applied on the body.

Finally, the simulations results are carried out heat flow and temperatures are calculated. The ventilated paper board parts were meshed with 1 mm mesh in automatic mode to uniformly mesh the entire part as shown in Fig. 2. The force was applied uniformly distributed load of 0.9 N was applied at the top of the ventilated paper board. The line pressure was applied to the vent holes of the ventilated paper board depending on its position of the assembly. The temperature is applied to the entire part of the ventilated paper board.

Fig. 1 **a** Modified design of a ventilated paper board packing. **b** Represents the modified design of a ventilated paper board packing rear view

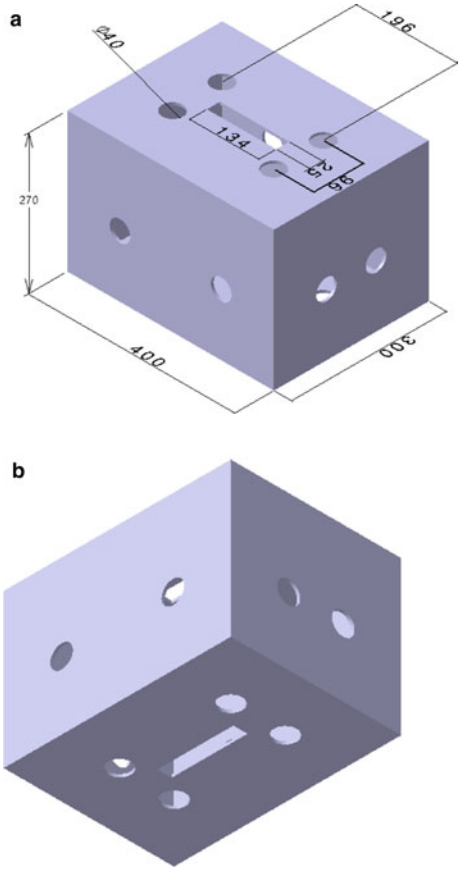
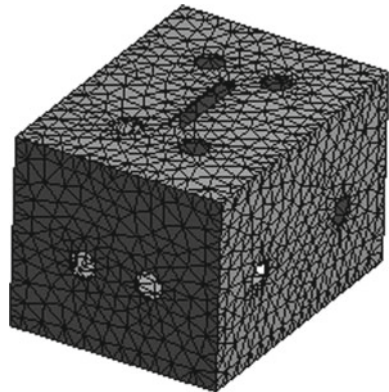


Fig. 2 FE model for the modified design of a ventilated paper board packing



3 Results and Discussions

After results are obtained from the analysis, 125FL, 165SC, and 175T₁ have close resemblances in their respective results. The results show that 125FL, 165SC, and 175T₁ material will be suitable for the ventilated paperboard. But, 125FL and 165SC will be preferred over 175T₁ it is much lighter and is providing us with similar results in both cases. The simulation of static and thermal analysis is carried out ventilated paper board in different materials 125FL, 165SC, and 175T₁ has been carried out.

The results of the static analysis are shown in the Figs. 3, 4, 5 and Table 2 that for different material of ventilated paperboard the maximum stress is obtained for 125FL material is 1.8633 MPa, 165SC material is 1.8644 MPa, and 175T₁ material is 1.8633 MPa. Similarly, the deformation is obtained 125FL material is 0.000206 m, 165SC material is 0.0001532 m, and 175T₁ material is 0.000122 m. obtained, respectively. It can be observed the static analysis the equivalent stress in case of 120FL are relevant to obtained similarly lesser deformation is obtained in case of ventilated paper board model.

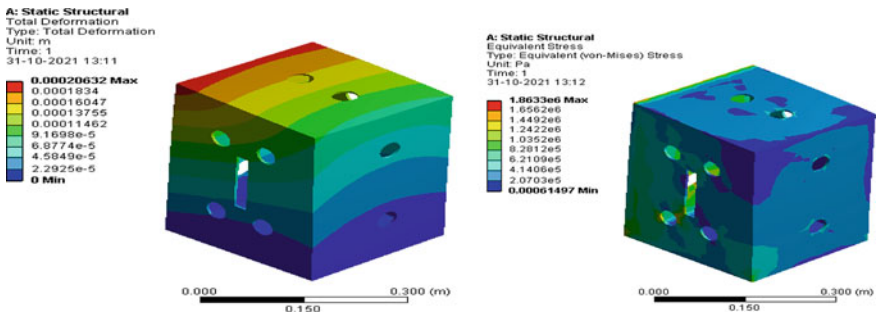


Fig. 3 Deformation and equivalent stress of ventilated paper board for 125FL

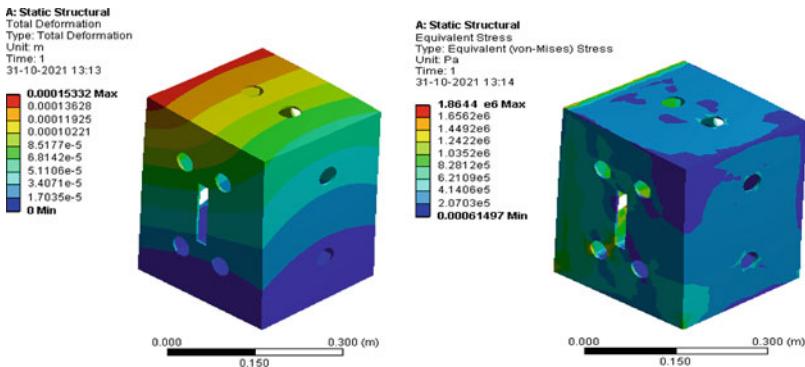


Fig. 4 Deformation and equivalent stress of ventilated paper board for 165SC

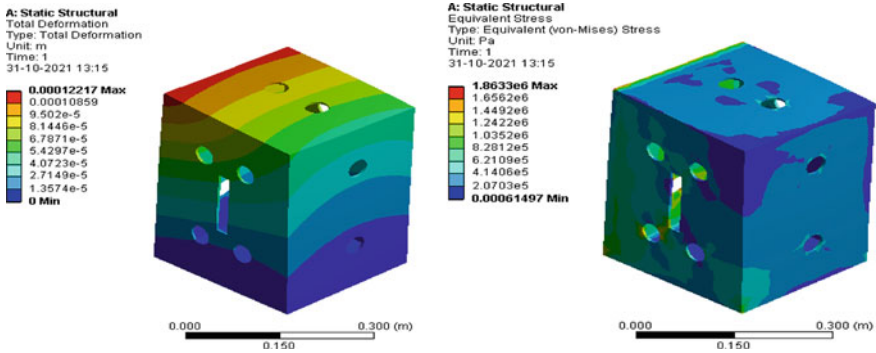


Fig. 5 Deformation and equivalent stress of ventilated paper board for 175T₁

Table 2 Represents the static analysis values of 125FL, 165SC, 175T₁

Terms of static analysis	Materials of ventilated paper board		
	125FL	165SC	175T ₁
Deformation (m)	0.000206	0.000152	0.000122
Stress (MPa)	1.8	1.864	1.8633

The results of the static analysis as shown in Fig. 3 represent the deformation, and equivalent stress of a ventilated paperboard made of 125FL material are 0.000206 m and 1.8633 MPa, respectively.

The results of the static analysis as shown in Fig. 4 represents the deformation and equivalent stress of a ventilated paper board made of 165SC material are 0.0001532 m and 1.8644 MPa, respectively.

The results of the static analysis as shown in Fig. 5 represents the deformation and equivalent stress of a ventilated paper board made of 175T₁ material are 0.000122 m and 1.8633 MPa, respectively.

The results of the thermal analysis show in Figs. 6, 7, 8 and Table 3 that three different material of ventilated paper board, the heat flow is obtained for 125FL material is 942.76 W/m °C, 165SC material is 938.08 W/m °C, 175T₁ material is 941.37 W/m °C obtained, respectively. It can be observed the thermal analysis, the heat flow and temperature are obtained lesser heat flow, and lesser temperature is obtained in the case of 165SC ventilated paper board compared to other two materials.

4 Conclusion

In this paper has the attempt can be made to change the existing design on a ventilated paper board using followed by static and thermal analysis. The features mainly five features of a ventilated paperboard has been changed, then the different materials is considered. The results of the static analysis shows the total deformation and the

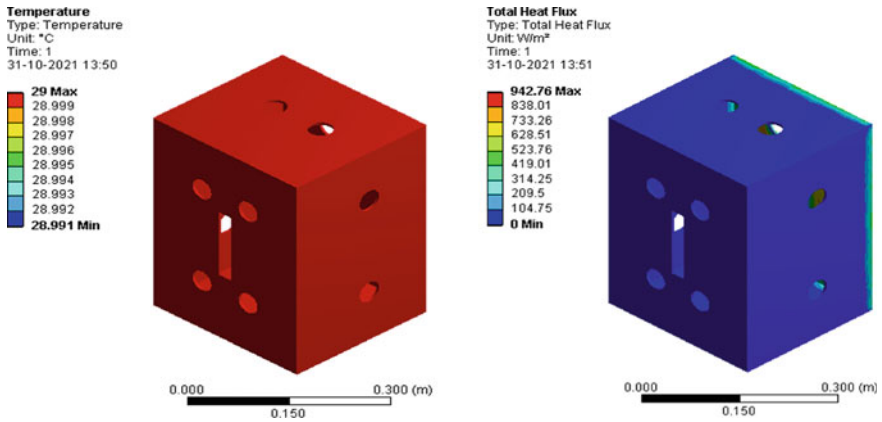


Fig. 6 Temperature and heat flow of ventilated paper board for 125FL

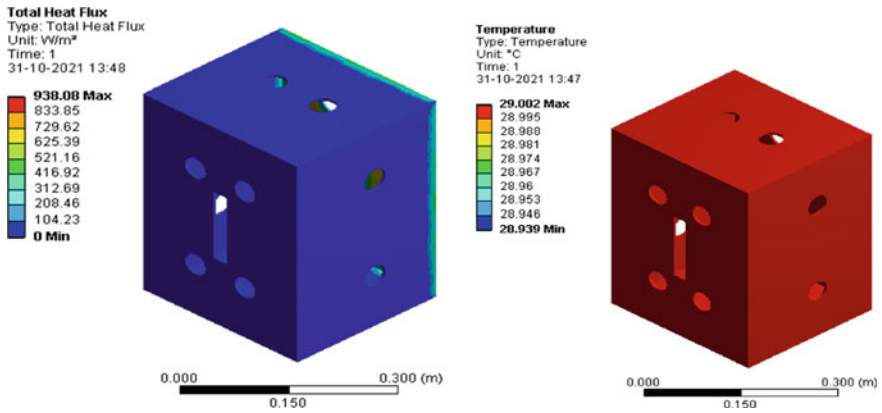


Fig. 7 Heat flow and temperature of ventilated paper board for 165SC

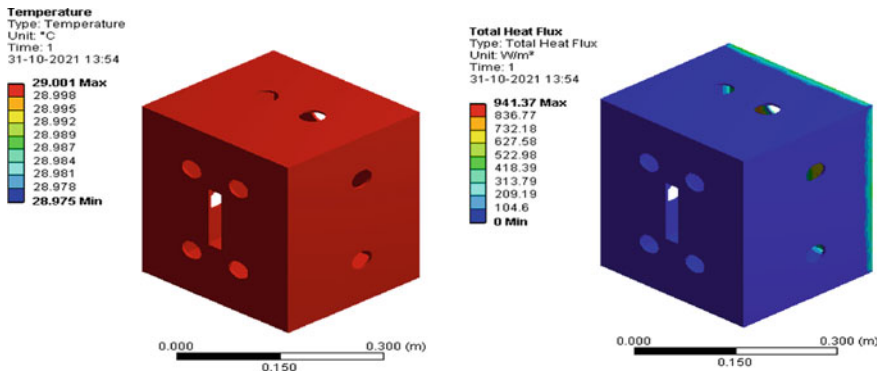


Fig. 8 Represents the temperature and heat flow of ventilated paperboard for 175T₁

Table 3 Represents the thermal analysis values of 125FL, 165SC, and 175T₁

Thermal analysis	Materials of ventilated paperboard		
	125FL	165SC	175T ₁
Temperature (°C)	29	29.002	29.001
Heat flux (W/m °C)	942.76	938.08	941.37

minimum equivalent stress is obtained in the material of 125FL ventilated paperboard compared with 165SC and 175T₁. In the thermal analysis, the heat flow and temperature are obtained lesser heat flow, and lesser temperature is obtained in the case of 165SC ventilated paperboard compared with other two materials. Therefore, the modified ventilated paperboard has giving greater results in compared with the existing design. Therefore, this design can be utilize further purpose.

References

1. Fadiji T, Ambaw A, Coetzee CJ, Berry TM, Opara UL (2018) Application of finite element analysis to predict the mechanical strength of ventilated corrugated paperboard packaging for handling fresh produce. *Bio Syst Eng* 174:260–281
2. Fadiji T, Berry TM, Ambaw A, Coetzee C, Opara UL (2018) Finite element modelling of the structural performance of ventilated paperboard packaging. *Int Soc Horticultur Sci* 1201:237–244
3. Pathare PB, Berry TM, Opara UL (2018) Experimental investigation of compression strength of ventilated corrugated citrus packaging. *Packag Res* 2:22–27
4. Rodrigues DF, Pereira JC (2018) Experimental tests and numerical simulations for failure investigation on corrugated boxes used on household appliance packaging. *J Appl Pack* 10:56–69
5. Han J, Park JM (2007) Finite element analysis of vent/hand hole designs for corrugated fibreboard boxes. *Packag Technol Sci Techno* 20:39–47
6. Talbi N, Batti A, Ayad R, Guo YQ (2009) An analytical homogenization model for finite element modelling of corrugated cardboard. *Compos Struct* 88:280–289
7. Köstner V, Ressel J, Sadlowsky B, Böröcz P (2018) Measuring the creep behaviour of corrugated board by cascade and individual test rig. *J Appl Pack Res* 4(1):46–61
8. Park J, Chang S, Jung HM (2020) Numerical prediction of equivalent mechanical properties of corrugated paperboard by 3D finite element analysis. *J Appl Sci* 10:1–16

Dynamic Analysis of Helical Planetary Gearbox Using Simulation Software



Sumit Singh Rajput, Shreya A. Tripathi, C. Subiksha,
and Lokavarapu Bhaskara Rao

Abstract In this paper, a 1.5 MW wind turbine gearbox design is proposed along with the static and dynamic analysis being carried out for different materials. A turbine gearbox with an epicyclic gear and two parallel helical gears is designed, and the total deformation, equivalent stresses, and strains are analysed. The parameters of the turbine box are varied and compared with two different materials to verify the analysed result. The design calculations were carried out using an iterative process in order to obtain the optimum dimensions of the gears. The modelling was done using Fusion 360, and the analysis was carried out in ANSYS. From the results, which are listed in the final analysis, it is proved that steel is better than grey cast iron.

Keywords Epicyclic gear · Dynamic analysis · Helical gear

1 Introduction

There is a tremendous increase in the amount of electricity produced annually. The average increase between 1980 and 2010 was estimated to be 407 billion kWh. In view of increased CO₂ emissions, enhanced greenhouse effect and issues regarding disposal of waste products, there has been an extremely rapid development of especially wind and solar power production. Wind energy is one of the most rapidly developed renewable energy resources, and as a result, it is gaining increasing global attention. [1, 2]. Simultaneously, wind turbines, which convert wind energy into electricity, have advanced rapidly in recent years [3–6]. Due to the large volume and weight of wind turbines, particularly MW-type turbines, it is difficult for the wind to

S. S. Rajput · S. A. Tripathi · C. Subiksha · L. B. Rao (✉)
School of Mechanical Engineering, Vellore Institute of Technology Chennai,
Vandalur-Kelambakkam Road, Chennai, Tamil Nadu 600127, India
e-mail: bhaskarbabu_20@yahoo.com

S. S. Rajput
e-mail: sumitsingh.rajput2018@vitstudent.ac.in

S. A. Tripathi
e-mail: shreyaa.tripathi2018@vitstudent.ac.in

drive turbine blades to rotate fast. The average wind turbine blade rotational speed is approximately 10–30 r/min, whereas the generator in the cabin requires an input rotational speed of approximately 1500 r/min [7, 8]. As a result, in addition to other direct-drive generators, most wind turbines require a speed-increasing gearbox with a high transmission ratio. Because of the good transmission performance, gearboxes with sun and planetary gears are a common choice in the design of wind turbines [9]. Instead of employing compound gear trains, high transmission ratios can be attained by using a planetary gearbox with very compact gear arrangements [10]. Gears are frequently required to work at high speeds and torques while being competitively cheap and dependable. The strength and condition of service are two elements that influence the gear material used in manufacturing [11]. In comparison with straight teeth, helical teeth may be a suitable alternative for high torque load applications [12]. One of the most important requirements in today's world is to achieve goals with maximum efficiency at the lowest possible cost [13]. It is crucial to understand the materials and qualities of the gear system while designing an efficient system [14]. The ability to design and build a range of equipment in a short period of time and with excellent quality is a major concern for transmission systems [15].

2 Methodology

Firstly, the design calculations were done for the epicyclic and two parallel helical gears. The design procedure for the gears was carried out using the PSG design data book [17]. The blades of traditional wind turbines rotate a shaft that is connected to the generator through a gearbox. For a large, one-megawatt turbine, the gearbox converts the blades' turning speed of 15–20 rotations per minute into the faster 1800 rotations per minute required by the generator to generate electricity.

We have assumed input to the turbine as 16 rpm which is given to the carrier and the desired output of the turbine as 1600 rpm.

- The total transmission ratio is 100:1.
- The gearbox contains one epicyclic gear and two helical gears connected in parallel.

Gear Calculations: Calculations were done with the help of PSG design data book [17]

1. Epicyclic Gear

Gear ratio: 6 (input rpm = 16 rpm and output rpm = 96 rpm).

Ultimate strength, $\sigma_e = 84$ MPa.

Young's modulus for pinion and gear, $E = 150$ GPa.

Surface endurance limit, $\sigma_{es} = 630$ MPa.

20° full depth involute gear.

Let the module of the epicyclic gear be $m = 25$ mm.

Let the face width of the gear be $b = 750$ mm.

Helix angle, $\alpha = 20^\circ$.

Pressure angle, $\phi = 20^\circ$.

Let the number of the teeth on the sun gear be $Z_s = 29$.

Hence, diameter of the sun is $D_s = 725$ mm.

Here, sun acts as the pinion.

$$\text{Pitch line velocity, } V = \frac{\pi D_p N_p}{60} = \frac{3.14 \times 725 \times 10^{-3} \times 96}{60} = 3.6424 \text{ m/s} \quad (1)$$

$$\text{Equivalent number of teeth, } Z_E = \frac{Z_p}{\cos^3 20} = 36 \quad (2)$$

Lewis's equation

$$F_t = \frac{\sigma_w P_c \cos \alpha y b}{C_w} \quad (3)$$

$$\sigma_w = \sigma_o C_v, \text{ where } \sigma_w = \text{Permissible working stress, } \sigma_o = \text{Allowable stress} \quad (4)$$

$$\text{Velocity factor, } C_v = \frac{4.5}{4.5 + V} \text{ (For } V \text{ upto } 5 \text{ m/s)} \quad (5)$$

Substituting the value of V in Eq. (5)

$$C_v = 0.55266 \quad (6)$$

Substituting the values in Eq. (4)

$$\sigma_w = 63.23068 \text{ MPa} \quad (7)$$

$$\text{Circular pitch, } P_c = \pi m = 3.14 \times 25 = 78.5 \text{ mm} \quad (8)$$

$$\text{Form Factor, } y = 0.154 - \frac{0.912}{Z_E} = 0.12867 \quad (9)$$

Now, finally substituting all values in Eq. (3)

$$F_t = 360090.6766 \text{ N} \quad (10)$$

Beam Strength

$$F_s = \sigma_c \times b \times y \times P_c = 84 \times 750 \times 0.12867 \times 78.5 = 636337.485 \text{ N} \quad (11)$$

Dynamic Load

$$F_d = F_t + \frac{21V(bC \cos^2 \alpha + F_t) \cos \alpha}{21V + \sqrt{bC \cos^2 \alpha + F_t}} \quad (12)$$

$$C = 5930e \text{ where } e = 0.022$$

$$C = 130.46 \quad (13)$$

Substituting the values in Eq. (12)

$$F_d = 403185.9126 \text{ N} \quad (14)$$

$$\text{For shock loads, } F_s > 1.5F_d \quad (15)$$

The beam strength must be 1.5 times greater than the dynamic load in order to have a safe gear.

The above condition is satisfied. Hence, the gear is safe under dynamic load.

Wear Load

$$F_w = \frac{D_p b Q K}{\cos^2 \alpha} \quad (16)$$

$$\text{where ratio factor, } Q = \frac{2i}{i+1} = \frac{2 \times 6}{6+1} = 1.71429 \quad (17)$$

$$\text{Load stress factor, } K = \frac{(\sigma_{es})^2 \sin \vartheta_n}{1.4} \left[\frac{1}{E_p} + \frac{1}{E_g} \right] = 1.22327 \quad (18)$$

$$\text{where } \tan \vartheta_n = \tan \vartheta \cos \alpha, \vartheta_n = 18.88172^\circ \text{ (Normal pressure angle)} \quad (19)$$

Substituting the values in Eq. (16)

$$F_w = 1291321.119 \text{ N} \quad (20)$$

In order to have a safe gear: $F_w > F_d$. The required condition is satisfied. Hence, the gear is safe under wear load.

2. Gear 2: Parallel Helical Gear

With gear ratio: 4. (input rpm = 96 rpm and output rpm = 384 rpm).

Ultimate strength, $\sigma_e = 84 \text{ MPa}$.

Young's modulus for pinion and gear, $E = 150 \text{ GPa}$.

Surface endurance limit, $\sigma_{es} = 630 \text{ MPa}$.

20° full depth involute gear.

Let the module of the epicyclic gear be $m = 16$ mm.

Let the face width of the gear be $b = 500$ mm.

Helix angle, $\alpha = 10^\circ$.

Pressure angle, $\phi = 20^\circ$.

Let the number of the teeth on the pinion be $Z_p = 27$.

Hence, diameter of the pinion is $D_p = 432$ mm.

Pinion is the weaker element. Hence, the design is based on pinion (same material).

The velocity is calculated using Eq. (1)

$$V = 8.68147 \text{ m/s} \quad (21)$$

Equivalent number of teeth is calculated using Eq. (2)

$$Z_e = 20 \quad (22)$$

$C_v = \frac{6}{6+v}$ (for velocity from 5 to 10 m/s)

$$C_v = 0.40868 \quad (23)$$

$$\text{Tangential Load } F_t = 114374.9037 \text{ N} \quad (24)$$

Beam Strength

$$F_s = 260805.888 \text{ N} \quad (25)$$

Dynamic Load

$$F_d = 167197.4859 \text{ N} \quad (26)$$

For shock loads, Eq. (15) must be satisfied, that is, $F_s > 1.5F_d$.

The beam strength must be 1.5 times greater than the dynamic load in order to have a safe gear.

The above condition is satisfied. Hence, the gear is safe under dynamic load.

Wear Load

$$F_w = 454500.383 \text{ N} \quad (27)$$

In order to have a safe gear: $F_w > F_d$. The required condition is satisfied. Hence, the gear is safe under wear load.

3. Gear 3: Parallel Helical Gear

With gear ratio: 4. (input rpm = 384 rpm and output rpm = 1536 rpm).

Ultimate strength, $\sigma_e = 84$ MPa.

Young's modulus for pinion and gear, $E = 150$ GPa.

Surface endurance limit, $\sigma_{es} = 630$ MPa.

20° full depth involute gear.

Let the module of the epicyclic gear be $m = 12$ mm.

Let the face width of gear be $b = 400$ mm.

Helix angle, $\alpha = 12^\circ$.

Pressure angle, $\phi = 20^\circ$.

Let the number of the teeth on the pinion be $Z_p = 25$.

Hence, diameter of the pinion is $D_p = 300$ mm.

Pinion is the weaker element. Hence, the design is based on pinion (same material).

The velocity is calculated using Eq. (1)

$$V = 24.1152 \text{ m/s} \quad (28)$$

Equivalent number of teeth is calculated using Eq. (2)

$$Z_e = 28 \quad (29)$$

$$C_v = \frac{5.5}{5.5 + \sqrt{V}} \text{ (For velocity greater than 20m/s)}$$

$$C_v = 0.52830 \quad (30)$$

$$\text{Tangential Load } F_t = 47610.1952 \text{ N} \quad (31)$$

Beam Strength

$$F_s = 153736.2086 \text{ N} \quad (32)$$

Dynamic Load

$$F_d = 95734.75127 \text{ N} \quad (33)$$

For shock loads, Eq. (15) must be satisfied, that is, $F_s > 1.5F_d$.

The beam strength must be 1.5 times greater than the dynamic load in order to have a safe gear.

The above condition is satisfied. Hence, the gear is safe under dynamic load.

Wear Load

$$F_w = 254333.0016 \text{ N} \quad (34)$$

Table 1 Load values for grey cast iron and steel

Gear type	Load	Grey cast iron (N)	Steel (N)
Gear 1(Epicyclic)	F_t	360090.6766	440625.972
	F_d	403185.9126	487832.6306
	F_w	129132.119	925925.1797
	F_s	636337.485	3181687.425
Gear 2 (Epicyclic)	F_t	114374.9037	139955.8229
	F_d	167197.4859	197585.9622
	F_w	454500.383	325,891.8662
	F_s	260805.888	1304029.440
Gear 3 (Epicyclic)	F_t	47610.1952	114374.9037
	F_d	95734.75127	167197.4859
	F_w	254333.0016	454500.383
	F_s	153736.2086	260805.888

In order to have a safe gear: $F_w > F_d$. The required condition is satisfied. Hence, the gear is safe under wear load.

The calculated load values for cast iron and steel are presented in Table 1, and the final specifications of the gearbox are given in Table 2.

Using the above dimensions, all the three gears were designed in Fusion 360 software [18]. The epicyclic gear is shown in Fig. 1, and the parallel helical gear is shown in Fig. 2.

The meshing was carried out in ANSYS Fluent 19.2 version software [19]. A general meshing was generated for both the epicyclic and the parallel helical gears with each having an element size of 50 mm as displayed in Figs. 3 and 4. The total number of nodes for the epicyclic gear was 408071, and the total number of elements

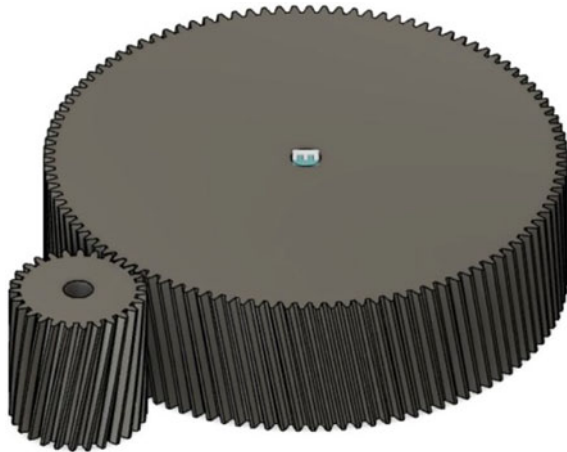
Table 2 Final dimensions

Parameters	Gear 1 (Epicyclic)	Gear 2(Parallel)	Gear 3 (Paralle)
Input (rpm)	16	96	384
Output (rpm)	96	384	1536
Module-m (mm)	25	16	12
Helix angle- α (°)	20	10	12
Width-b (mm)	750	500	400
Number of teeth- Z_p (pinion)	SUN: 29	27	25
Number of teeth- Z_g (Gear)	PLANET: 58, RING: 145	108	100
Diameter- d_p (pinion) (mm)	SUN:725	432	300
Diameter- d_g (gear) (mm)	PLANET:1450, RING:3625	1728	1200
Gear ratio	6	4	4
Pressure angle φ (°)	20	20	20

Fig. 1 Epicyclic gear
(isometric view)



Fig. 2 Parallel helical gear
(isometric view)



was 206244. As for the parallel helical gears, the total number of nodes was 112483 and the total number of elements was 29995.

Fig. 3 Meshed epicyclic gear

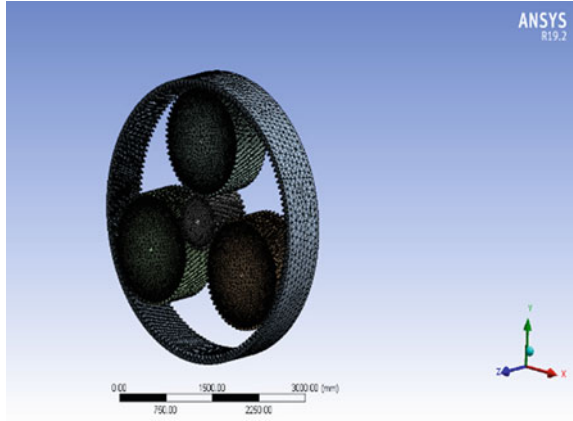
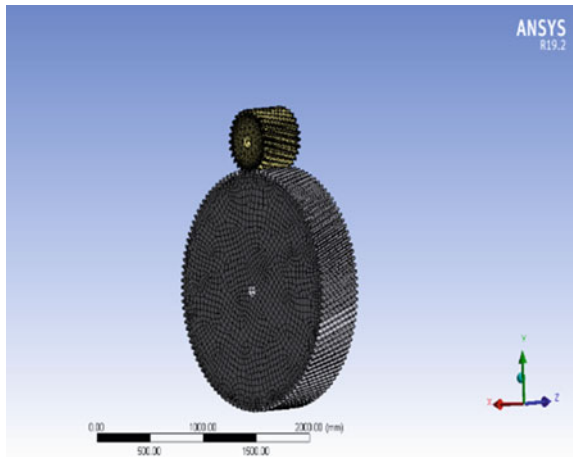


Fig. 4 Meshed parallel gear



3 Result

Dynamic Analysis

The CAD models were simulated using ANSYS Workbench. The explicit dynamics was selected in ANSYS. The results for all the three gears using grey cast iron material are shown in Figs. 5, 6, 7, 8, 9, 10, 11, 12, and 13. Additionally, for steel, the results are shown in Figs. 14, 15, 16, 17, 18, 19, 20, 21, and 22.

Material 1: Grey Cast Iron

1. Gear 1: Epicyclic Gear
2. Gear 2: Parallel Helical Gear

Fig. 5 Total deformation of epicyclic gear with grey cast iron

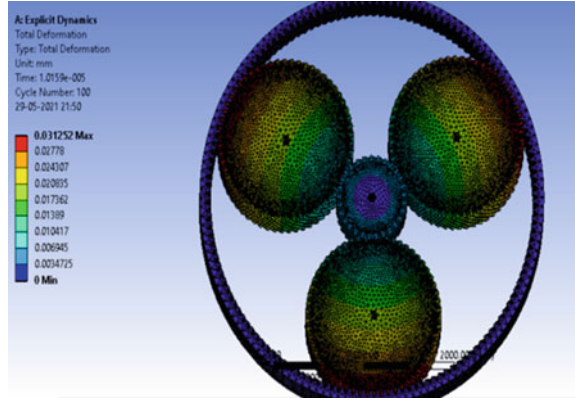


Fig. 6 Equivalent stress of epicyclic gear with grey cast iron

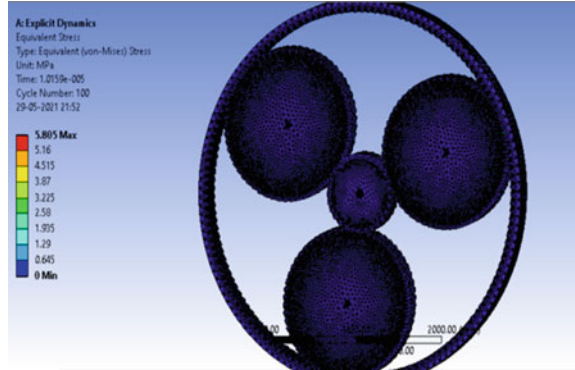
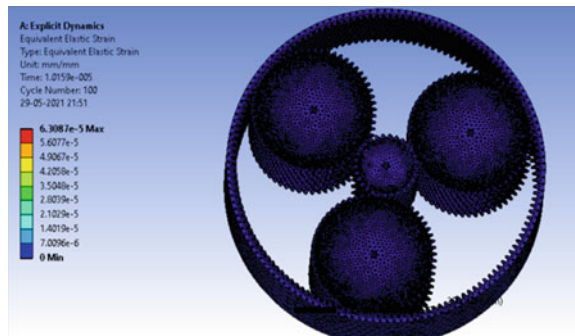


Fig. 7 Equivalent strain of epicyclic gear with grey cast iron



3. Gear 3: Parallel Helical Gear

Material 2: Steel

Gear 1: Epicyclic Gear

Fig. 8 Total deformation of parallel helical gear-1 with grey cast iron

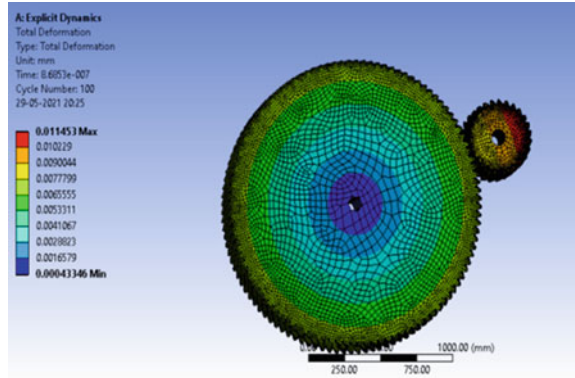


Fig. 9 Equivalent strain of parallel helical gear-1 with grey cast iron

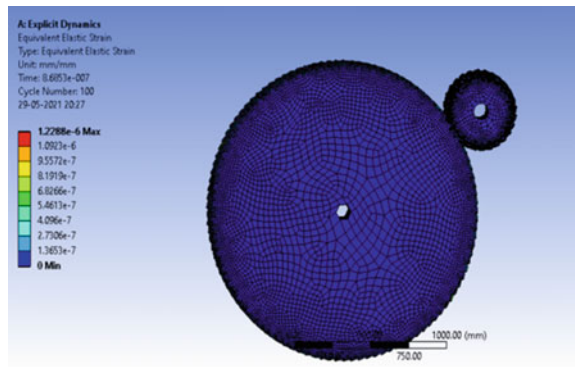
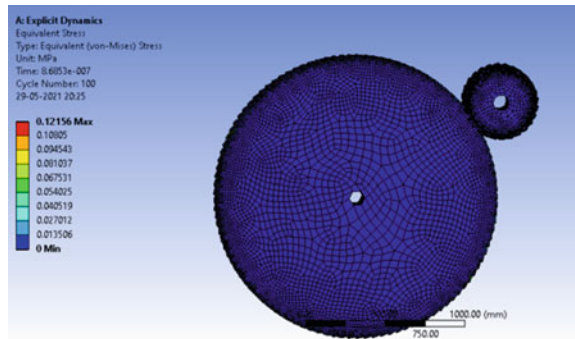


Fig. 10 Equivalent stress of parallel helical gear-1 with grey cast iron



Gear 2: Parallel Helical Gear

Gear 3: Parallel Helical Gear

In the first case of carrying out the dynamic analysis, considering the material as grey cast iron, the maximum total deformation obtained for the epicyclic gear was

Fig. 11 Total deformation of parallel helical gear-2 with grey cast iron

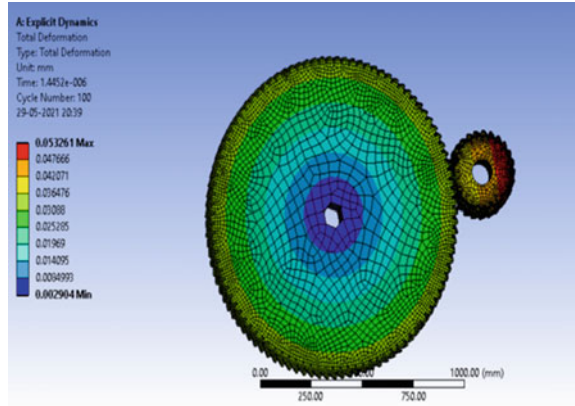


Fig. 12 Equivalent strain of parallel helical gear-2 with grey cast iron

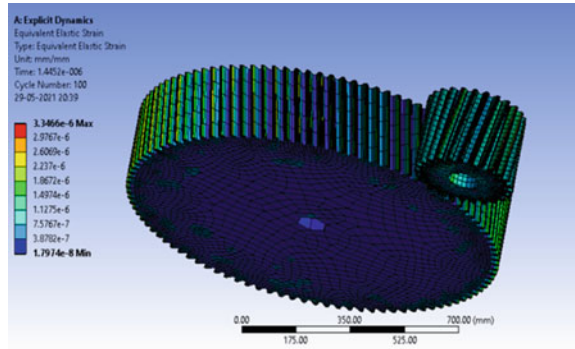
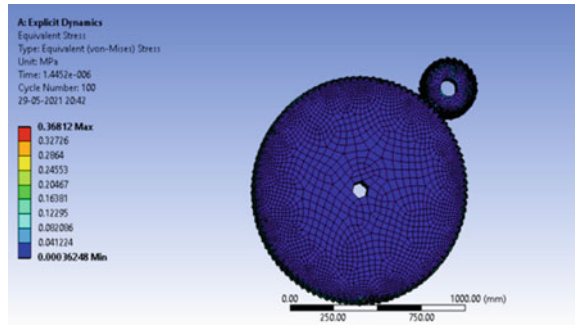


Fig. 13 Equivalent stress of parallel helical gear-2 with grey cast iron



0.031252 mm, while the equivalent strain and stress were found to be 6.3087×10^{-5} and 5.805 N/mm^2 , respectively which is evident from Figs. 5, 6, and 7. Moreover, for gears 2 and 3, which are the parallel helical gears, the total deformation was recorded to be 0.011453 and 0.053261 mm correspondingly as shown in contours of Figs. 8 and 11; also, Figs. 9 and 12 display the equivalent strain that was of the order of

Fig. 14 Total deformation of epicyclic gear with steel

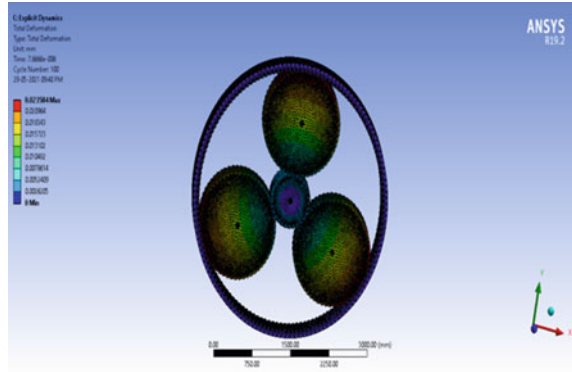


Fig. 15 Equivalent strain of epicyclic gear with steel

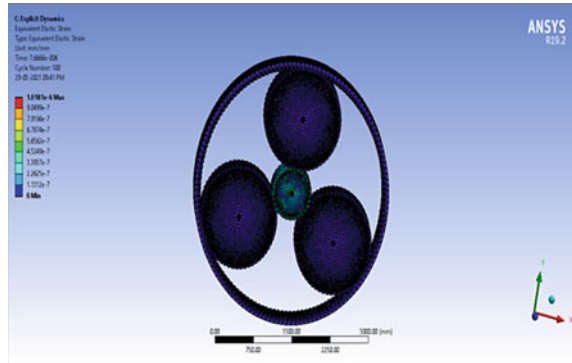
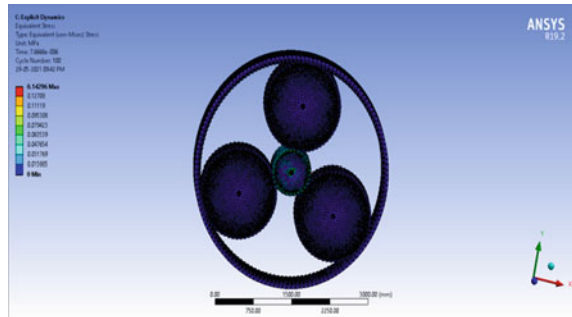


Fig. 16 Equivalent stress of epicyclic gear with steel



10^{-6} having values 1.2288×10^{-6} and 3.466×10^{-6} accordingly. Finally, Figs. 10 and 13 are contours based on the equivalent stress with values 0.12156 N/mm^2 and 0.36812 N/mm^2 , respectively.

Furthermore, for the next case, the material was selected as steel, and results were procured using the same procedure. Figure 14 depicts the total deformation distribution of the epicyclic gear with a maximum value of 0.023584 mm ; similarly,

Fig. 17 Total deformation of parallel helical gear-1 with steel

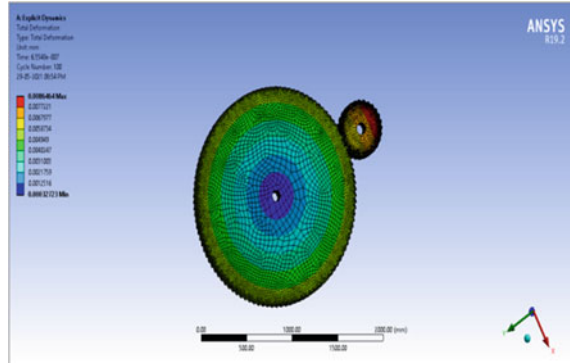


Fig. 18 Equivalent strain of parallel helical gear-1 with steel

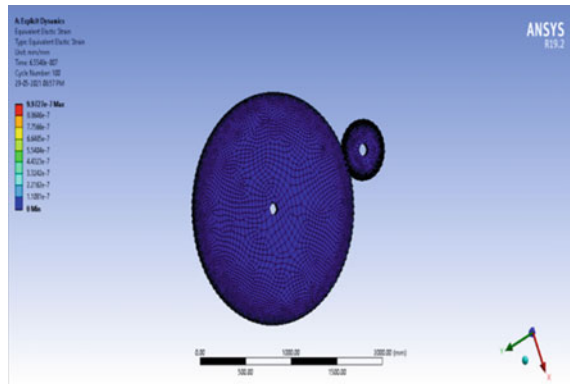
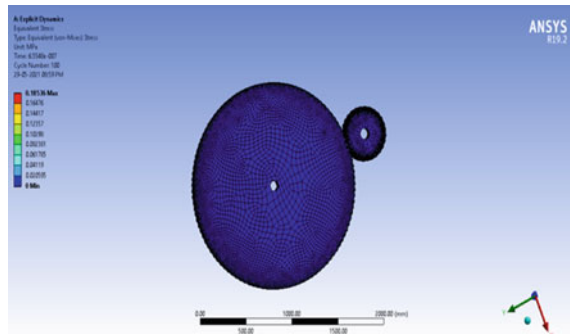


Fig. 19 Equivalent stress of parallel helical gear-1 with steel



Figs. 17 and 20 illustrate the same for the two parallel helical gears having the highest values of 0.0086464 mm and 0.040011 each. Additionally, as for the equivalent strain, Figs. 15, 18, and 21 exhibit the distributions for all three models with each having values of 1.0181×10^{-6} , 9.9727×10^{-7} , and 2.6267×10^{-6} . Lastly, the equivalent stress for them from Figs. 16, 19, and 22 was noted to be 0.14296, 0.18536, and

Fig. 20 Total deformation of parallel helical gear-2 with steel

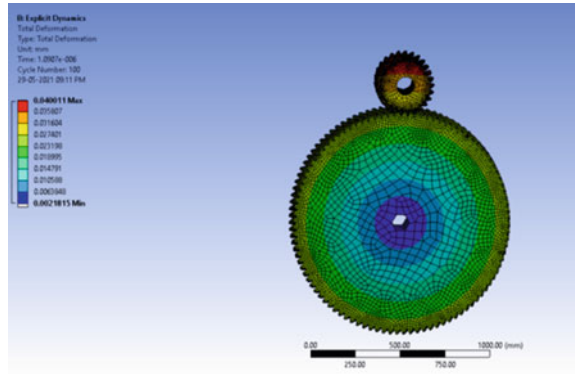


Fig. 21 Equivalent strain of parallel helical gear-2 with steel

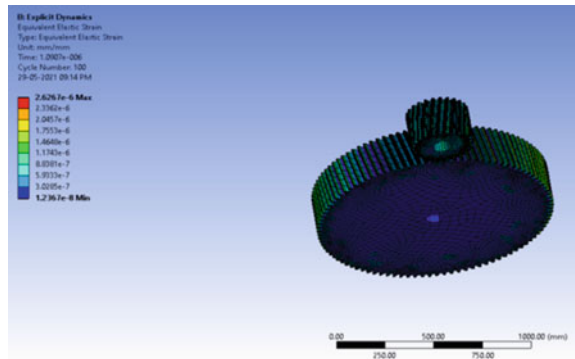
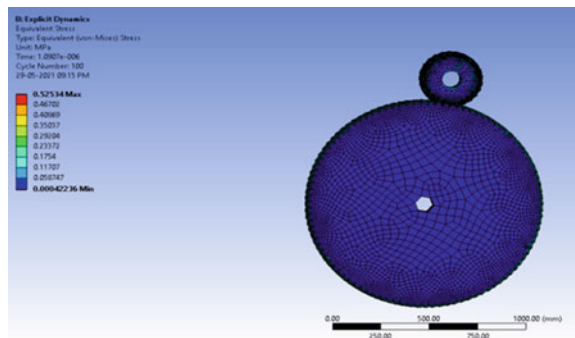


Fig. 22 Equivalent stress of parallel helical gear-2 with steel



0.52534 N/mm² correspondingly. Comparing the values obtained from the analysed deformation contours, it is clear that steel has less deformation than cast iron, and generally, it is observed that steel has more strength as compared to cast iron.

All the results obtained after conducting dynamic analysis of both materials for all models are presented in Table 3.

Table 3 Values obtained from dynamic analysis

Model	Cast iron			Steel		
	Total deformation (mm)	Equivalent strain	Equivalent stress (N/mm ²)	Total deformation (mm)	Equivalent strain	Equivalent stress (N/mm ²)
Epicyclic gear	0.031252	6.3087e-5	5.805	0.023584	1.0181e-6	0.14296
Gear 2	0.011453	1.2288e-6	0.12156	0.0086464	9.9727e-7	0.18536
Gear 3	0.053261	3.466e-6	0.36812	0.040011	2.6267e-6	0.52534

Table 4 Mesh convergence

Mesh element size (mm)	Normal stress minimum (MPa)	Time (s)	Time (min)
500	25.1439	336	5.6
450	24.4567	753.6	12.56
400	22.6021	915.48	15.258
350	21.9965	1531.2	25.52
300	21.1557	2097.6	34.96
250	20.5123	2611.2	43.52
200	20.4322	2974.8	49.58
150	20.4296	3338.4	55.64
100	20.4227	3741	62.35
50	20.4219	3867	64.45

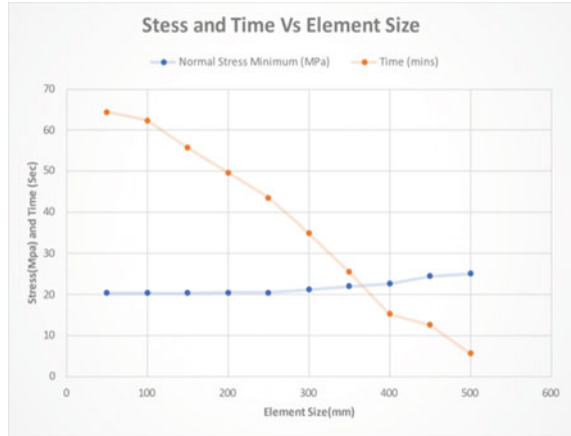
Mesh Convergence

Mesh convergence establishes how many elements are required in a model to ensure that altering the mesh size has no effect on the analysis results. With decreasing element size, the system response (stress, deformation) will converge to a repeatable solution, these are shown in Table 4 and Plot. 1. After decreasing the element size from 200 to 50 mm, the output becomes stable.

4 Conclusion

The explicit dynamic analysis of the helical planetary gearbox used in the wind turbines was done using the ANSYS 19.2 version software to determine the total deformation; maximum induced stress and strain of grey cast iron and carbon steel and the modelling was done using Fusion 360 software. Now, according to the results obtained from the simulations, the large power and torque can be delivered with steel for a long time. Cast iron has poor tensile stress/strength compared to steel, and cast iron parts are section sensitive. But, cast iron is cheaper compared to steel. So,

Plot. 1 Stress and time versus element size



a designer can choose the material based on the lifecycle of the gearbox and the expenses needed to manufacture the gearbox of the horizontal axis wind turbines.

References

1. Liu WY, Tang BP, Han JG (2015) The structure healthy condition monitoring and fault diagnosis methods in wind turbines: a review. *Renew Sustain Energy Rev* 44(C):466–472
2. Patrik P (2015) Damage equivalent wind–wave correlations on basis of damage contour lines for the fatigue design of offshore wind turbines. *Renew Energy* 81(9):723–736
3. Liu WY (2013) The vibration analysis of wind turbine blade–cabin–tower coupling system. *Eng Struct* 56(C):954–957
4. Capuzzi M, Pirrera A, Weaver PM (2015) Structural design of a novel aero elastically tailored wind turbine blade. *Thin-Walled Struct* 95(10):7–15
5. Barnes RH, Morozov EV, Shankar K (2015) Improved methodology for design of low wind speed specific wind turbine blades. *Compos Struct* 119(1):677–684
6. Liu WY, Han JG, Lu XN (2014) Experiment and performance analysis of the Northwind 100 wind turbine in CASE. *Energy Build* 68(PA):471–475
7. Roth-Johnson P, Wirz RE, Lin E (2014) Structural design of spars for 100-m biplane wind turbine blades. *Renew Energy* 71(11):133–155
8. Hu Y, Baniotopoulos C, Yang J (2014) Effect of internal stiffening rings and wall thickness on the structural response of steel wind turbine towers. *Eng Struct* 81(12):148–161
9. Liu WY, Gao QW, Ye G (2015) A novel wind turbine bearing fault diagnosis method based on integral extension LMD. *Measurement* 74(10):70–77
10. Patel T, Dubey A, Rao LB (2019) Design and analysis of an epicyclic gearbox for an electric drivetrain. *Int J Recent Technol Eng* 8(3):6834–6842
11. Cherian S, Azam AB, Rao LB (2020) Analysis of various cooling mechanisms for plastic gears using decision tree algorithms. In: *Recent trends in mechanical engineering, Lecture notes in mechanical engineering*, pp 407–418
12. Anand S, Srikeshav AD, Sharran B, Rao LB (2020) Design and analysis of helical teeth harmonic drive. In: *Recent trends in mechanical engineering, Lecture notes in mechanical engineering*, pp 507–519

13. Bardiya N, Karthik T, Rao LB (2014) Analysis and simulation of gearless transmission mechanism. *Int J Core Eng Manag* 1(6):136–143
14. Gupta A, Yashvanth VP, Rao LB (2020) Design of gears using aluminium 6061-T6 alloy for formula SAE steering system. In: *Recent trends in mechanical engineering, Lecture notes in mechanical engineering*, pp 489–505
15. Gujaba KP, Parashar S, Rao LB (2020) Design and analysis of permanent magnetic gears. In: *Recent trends in mechanical engineering, Lecture notes in mechanical engineering*, pp 521–530
16. Bhandari VB (2010) *Design of machine elements*. Tata McGraw Hills Education Pvt. Ltd., New Delhi, India
17. *Design data: data book of engineers* by PSG College-Kalaikathir Achachagam—Coimbatore
18. Autodesk FUSION 360 user manual
19. Ansys user's guide for Ansys 19.2

Electromechanical Instability Modeling of Particle-Reinforced Dielectric Elastomeric Actuators



Sankalp Gour , Deepak Kumar, and Vinod Yadav

Abstract This work presents the modeling and analysis of an electromechanical instability phenomenon of a particle-reinforced dielectric elastomeric (DE) material-based plate actuator. An analytical model is developed here to predict the critical charge-controlled actuation response of the actuator by spraying the charges on the two in-plane compliant electrodes via an external circuit. The model is formulated following the first law of thermodynamics-based continuum mechanics approach. In addition, the filler-dependent dielectric permittivity effect on the actuation response of the actuator is also investigated. In general, the developed model will be helpful to the researchers in designing the different DE material-based plate actuators for various soft robotic applications.

Keywords Dielectric elastomers · Electromechanical instability · Continuum mechanics · Particle-reinforcement · Actuators

1 Introduction

Dielectric elastomers (DE) are innovative and non-conducting soft electroactive polymers consisting of cross-linked molecular chain networks that exhibit high elastic energy density, high efficiency, and large deformation [1, 2]. When a voltage is applied to its compliant electrodes, DE deforms hyperelastically, reducing in thickness while expanding in area to maintain its incompressibility constraint. Such electrically governed actuation phenomenon of DE is known as electrostriction [3, 4]. DE-based actuators have vast usage in medical science, robotics, aerospace engineering, and bionics [5, 6]. Some practical applications are artificial muscles, manipulators, optical devices, energy harvesters, and braille displays, etc. [3, 7]. At the same time, a typical DE performance is restricted to date due to the electromechanical instabilities, which leads to the electrical breakdown [8, 9] of the DE material. To improve

S. Gour (✉) · D. Kumar · V. Yadav

Department of Mechanical Engineering, Maulana Azad National Institute of Technology, Bhopal, Madhya Pradesh 462003, India

e-mail: sankalpgour@gmail.com

the performance of DE actuators, we must first understand the mechanism of large deformation and the electromechanical behavior of such materials.

Recent research and experiments [10–16] suggested that the pre-stretching may result in suppression or elimination of electromechanical instability and enhance actuation performance. The other potential solutions also exist to overcome such instabilities such as nonlinear polarization [10, 17] spraying the charges on surface of DE [18, 19]. Several researchers [20, 21] have studied the effect of dielectric permittivity on instabilities leading to electrical breakdown. Furthermore, fillers are critical in transforming the material characteristics of smart polymers and lowering the total cost of the resulting composites. Goshkoderia et al. [22] studied the tunable permittivity for DE composites under finite strains. They [22] examined the finitely strained dielectric composite behavior with periodic and random distributions of inclusions. Further, Todd et al. [23] established a unique model for a physical understanding of the complex permittivity for composite systems. Later, Poikelispaa et al. [24] experimented with an acrylic elastomer matrix by adding the carbon black and barium titanate fillers. A significant increase in the permittivity was observed with an overall improvement in the actuation performance of the DE composite. In recent, a lot of research work [25, 26] has been carried out to examine the impact of deformation-dependent dielectric permittivity. Moreover, various experimental studies [25, 27, 28] have confirmed that under large deformation, the permittivity of some DEs ratifies significant deformation-dependent behavior. Finally, many works have been devoted to modeling the deformation-dependent permittivity-based electromechanical instability (EMI) phenomenon of DEs. However, to the best of our knowledge, no study on the filler-dependent permittivity-based EMI of DEs has been published.

The current work aims to study the deformation and filler-dependent permittivity-based EMI phenomenon of a DE actuator. The actuation response of the DE actuator is focused on different volume fractions of filler particles. In addition, a pre-stretching effect on EMI for DE is also considered. An analytical model is developed following the first law of thermodynamics-based continuum mechanics approach as an output. The developed model has reported the actuation response and examined the EMI conditions for DE undergoing large deformations.

2 Modeling

In this section, an analytical model for the EMI phenomenon of a particle-reinforced DE actuator is developed. The continuum mechanics approach based on the first law of thermodynamics is used. The critical charge-controlled actuation response of the DE actuator is predicted for an applied electromechanical load for different cases of (a) constant permittivity, (b) deformation-dependent permittivity, (c) permittivity dependent on the volume fraction of fillers filled in the parent material.

2.1 Free Energy and Equations of State

A schematic representation of filler particle-reinforced DE is shown in Fig. 1. The undeformed, pre-stretched, and finally, deformed configurations are drawn here to manifest all the deformation states of a DE plate actuator. We assumed the material of dielectric actuator membrane as homogeneous, incompressible and isotropic. The DE membrane is placed between two carbon grease-based compliant electrodes. In undeformed state, the actuator has the geometric specifications $(L'_1 \times L'_2 \times L'_3)$. Then, an intermediate state $(L_1 \times L_2 \times L_3)$, as shown in Fig. 1(b), is obtained by the pre-stretching of the DE from the undeformed state applying in-plane bi-axial mechanical forces P_1 and P_2 . By connecting the electrodes to a voltage supply ϕ , the DE is later exposed to an electric field. Charge polarization $\pm Q$ occurs on compliant surfaces as the charge travels through the conducting wire. The effective electromechanical loading condition deforms the DE from the reference configuration to the current configuration $(l_1 \times l_2 \times l_3)$ as shown in Fig. 1c.

When subjected to electromechanical forces, the DE actuator membrane enlarges of surface area and thickness reduction during the process of deformation. The free energy of the particle-reinforced DE actuator membrane transforms by δF when the

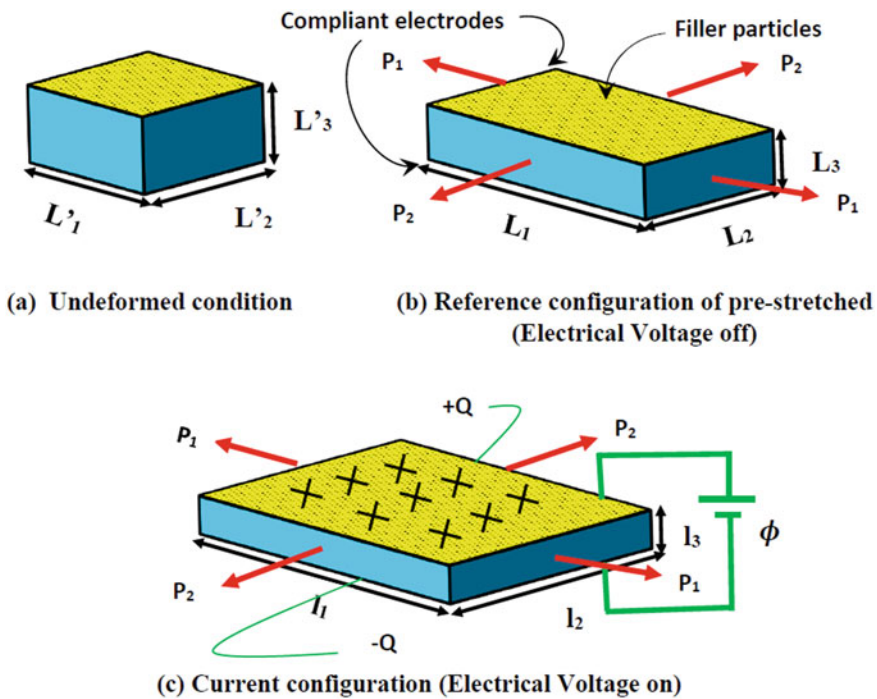


Fig. 1 Schematic diagram of a filler particle-reinforced DE plate in, **a** undeformed configuration, **b** reference configuration, and **c** current configuration

size of the DE actuator membrane deforms and an infinitesimal quantity of charge flows across the system. In a condition of equilibrium, an increase in the system's free energy is represented by the total work done as a result of all applied forces and the charge as

$$\delta F = P_1 \delta l_1 + P_2 \delta l_2 + Q \delta \phi. \quad (1)$$

The principal stretches of the nominal state and the deformed state are defined as

$$\lambda_1 = \frac{l_1}{L_1}, \lambda_2 = \frac{l_2}{L_2}, \lambda_3 = \frac{l_3}{L_3}, \quad (2)$$

The pre-stretches for the variation in size from the undeformed to a pre-stretched state are calculated as follows:

$$\lambda_{1p} = \frac{L'_1}{L_1}, \lambda_{2p} = \frac{L'_2}{L_2}, \lambda_{3p} = \frac{L'_3}{L_3}. \quad (3)$$

The corresponding electric field intensity E , the electrical displacement D , and true stresses s_1 and s_2 can be written as

$$E = \frac{\phi}{l_3}, D = \frac{Q}{l_2 l_3}, s_1 = \frac{P_1}{l_2 l_3}, s_2 = \frac{P_2}{l_3 l_1}. \quad (4)$$

The infinitesimal change in the electrical voltage is given by

$$\delta \phi = \delta(E l_3) = E \delta l_3 + l_3 \delta E. \quad (5)$$

The volume of the DE actuator membrane is assumed to be constant for the entire process of deformation (i.e., $\lambda_1 \lambda_2 \lambda_3 = 1$) according to the incompressibility condition for the given material is expressed as

$$\delta \lambda_3 = -\lambda_1^{-2} \lambda_2^{-1} \delta \lambda_1 - \lambda_1^{-1} \lambda_2^{-2} \delta \lambda_2. \quad (6)$$

On dividing Eq. (1) by volume of the reference configuration of the DE plate actuator ($L_1 \times L_2 \times L_3$) and connecting the Eqs. (4), (5), and (6), We obtain the formula for the free energy density δW , which is represented by

$$\delta W = (s_1 - DE) \lambda_1^{-1} \delta \lambda_1 + (s_2 - DE) \lambda_2^{-1} \delta \lambda_2 + D \delta E. \quad (7)$$

In equilibrium, Eq. (6) is transformed into the following constitutive equations of state for a given free energy density $W(\lambda_1, \lambda_2, E)$ as for a given free energy density $W(\lambda_1, \lambda_2, E)$, Eq. (6) transforms into the corresponding constitutive equations of state in equilibrium as

$$\begin{aligned} s_1 &= \lambda_1 \frac{\partial W(\lambda_1, \lambda_2, E)}{\partial \lambda_1} + DE, s_2 = \lambda_2 \frac{\partial W(\lambda_1, \lambda_2, E)}{\partial \lambda_2} + DE, \\ D &= \frac{\partial W(\lambda_1, \lambda_2, E)}{\partial E}. \end{aligned} \quad (8)$$

A special kind of elastic energy density inline with augmented Gent type [29, 30] is used in coordination with electrical energy density superposition similar to [31] may be utilized here to anticipate the impact of molecular chain extensibility limit as

$$W(\lambda_1, \lambda_2, E) = - \underbrace{(1 - v_f)(1 + 3.5v_f + 30v_f^2)}_{\alpha} C_1 \ln\left(\frac{I_m - I_1}{I_m - 3}\right) + C_2 \sqrt{I_2} + \frac{1}{2} \bar{\epsilon} E^2, \tag{9}$$

where C_1 and C_2 are material constants, I_m denotes chain extensibility parameter at a maximum value of stretch, v_f is the volume fraction of filler particles, and $\bar{\epsilon}$ denotes the material permittivity. In addition, I_1 and I_2 represent here the first and second invariants of the deformation tensor given by $I_1 = 2\lambda^2 + \lambda^{-4}$ and $I_2 = 2\lambda^{-2} + \lambda^4$ for a given equi-bi-axial deformation case ($\lambda_1 = \lambda_2$). Next, the material parameters $C_1 = 10.5$ MPa, $C_2 = 0.09$ MPa, and $I_m = 84$ are obtained from the literature [32] by fitting the above augmented Gent material model (9) for a given polymeric material.

2.2 Electromechanical Instability Model

For the development of an EMI model, we considered an equi-bi-axial in-plane deformation condition ($\lambda_1 = \lambda_2 = \lambda$) of the filler particle-reinforced DE plate actuator is considered. Using Eq. (4) for the parallel plate capacitor system of a dielectric actuator membrane, we have

$$D = \frac{Q}{l_1 l_2} = \left(\frac{Q}{L_1 L_2}\right) \lambda^{-2}, \quad E = \frac{D}{\bar{\epsilon}} = \frac{1}{\bar{\epsilon}} \left(\frac{Q}{L_1 L_2}\right) \lambda^{-2}. \tag{10}$$

Further, the normalized charge $\frac{Q}{L_1 L_2 \sqrt{C_1 \epsilon_0}}$ and normalized voltage $\frac{\phi}{L_3 \sqrt{\frac{C_1}{\epsilon_0}}}$ are computed for the following three different cases of DE permittivity.

(a) **Constant Permittivity Case**

The material permittivity $\bar{\epsilon}$ is defined as a function of permittivity of the free space ϵ_0 and the relative permittivity ϵ_r as

$$\bar{\epsilon} = \epsilon_0 \epsilon_r. \tag{11}$$

Using Eqs. (8), (9), (10), and (11), the normalized charge as well as voltage expressions for a given constant DE permittivity ϵ_0 are obtained as

$$\frac{Q}{L_1 L_2 \sqrt{C_1 \epsilon_0}} = \sqrt{\left(\alpha \left[\frac{4(\lambda^2 - \lambda^{-4})}{I_m - 2\lambda^2 - \lambda^{-4}} \right] + \frac{C_2}{C_1} \left[\frac{2(\lambda^4 - \lambda^{-2})}{\sqrt{2\lambda^{-2} + \lambda^4}} \right] - S_p\right) \lambda^4}, \tag{12}$$

where S_p denotes the cauchy stress obtained from the theory of hyperelasticity for bi-axial deformation of rubber plate for evaluation of pre-stretching effect.

$$\frac{\phi}{L_3\sqrt{\frac{C_1}{\epsilon_0}}} = \sqrt{\left(\alpha \left[\frac{4(\lambda^2 - \lambda^{-4})}{I_m - 2\lambda^2 - \lambda^{-4}} \right] + \frac{C_2}{C_1} \left[\frac{2(\lambda^4 - \lambda^{-2})}{\sqrt{2\lambda^{-2} + \lambda^4}} \right] - S_p\right) \lambda^{-4}}. \quad (13)$$

(b) Deformation-dependent Permittivity Case

In view of the deformation-dependent permittivity model, Mistral et al. [33] experimented VHB 4910 type of dielectric elastomer material and derived the relative permittivity as a function of the stretch can be expressed as

$$\epsilon_r(\lambda) = p\lambda^2 + q, \quad (14)$$

where the constants p and q indicate the electrostrictive coefficients at infinitesimal stretches. Fitting Mistral et al. [28, 33] experimental data for a VHB 4910 type of DE material at fixed room temperature yielded the parameters $p = -0.056$ and $q = 5.54$. Using Eqs. (8), (9), and (10), the normalized charge, as well as voltage expressions for a given deformation-dependent permittivity model (14) are obtained as

$$\frac{Q}{L_1 L_2 \sqrt{C_1 \epsilon_0}} = \sqrt{\left(\alpha \left[\frac{4(\lambda^2 - \lambda^{-4})}{I_m - 2\lambda^2 - \lambda^{-4}} \right] + \frac{C_2}{C_1} \left[\frac{2(\lambda^4 - \lambda^{-2})}{\sqrt{2\lambda^{-2} + \lambda^4}} \right] - S_p\right) \left[\frac{(p\lambda^2 + q)^2}{2p\lambda^{-2} + q\lambda^4} \right]}, \quad (15)$$

$$\frac{\phi}{L_3\sqrt{\frac{C_1}{\epsilon_0}}} = \sqrt{\left(\alpha \left[\frac{4(\lambda^2 - \lambda^{-4})}{I_m - 2\lambda^2 - \lambda^{-4}} \right] + \frac{C_2}{C_1} \left[\frac{2(\lambda^4 - \lambda^{-2})}{\sqrt{2\lambda^{-2} + \lambda^4}} \right] - S_p\right) \left[\frac{1}{2p\lambda^6 + q\lambda^4} \right]}. \quad (16)$$

(c) Filler-dependent Permittivity Case

In the context of a filler-dependent permittivity model, the Maxwell Garnett model [24] applicable for the volume fraction of filler particles up to 10% is given by

$$\epsilon_r(v_f) = \epsilon_m \left[1 + \frac{3v_f(\epsilon_f - \epsilon_m)}{(1 - v_f)(\epsilon_f - \epsilon_m) + 3\epsilon_m} \right], \quad (17)$$

where ϵ_m and ϵ_f represent permittivity of the parent material and filler, respectively. For this purpose, we have considered $\epsilon_f = 2$ and $\epsilon_m = 4.5$. Using again Eqs. (8), (9), and (10), the normalized charge and voltage expressions for a given filler-dependent permittivity model (17) are obtained as

$$\frac{Q}{L_1 L_2 \sqrt{C_1 \epsilon_0}} = \sqrt{\left(\alpha \left[\frac{4(\lambda^2 - \lambda^{-4})}{I_m - 2\lambda^2 - \lambda^{-4}} \right] + \frac{C_2}{C_1} \left[\frac{2(\lambda^4 - \lambda^{-2})}{\sqrt{2\lambda^{-2} + \lambda^4}} \right] - S_p\right) \epsilon_r \lambda^4} \quad (18)$$

$$\frac{\phi}{L_3\sqrt{\frac{C_1}{\epsilon_0}}} = \sqrt{\left(\alpha \left[\frac{4(\lambda^2 - \lambda^{-4})}{I_m - 2\lambda^2 - \lambda^{-4}} \right] + \frac{C_2}{C_1} \left[\frac{2(\lambda^4 - \lambda^{-2})}{\sqrt{2\lambda^{-2} + \lambda^4}} \right] - S_p\right) \frac{\lambda^{-4}}{\epsilon_r}} \quad (19)$$

Finally, the above-derived relations (12–13), (15–16), and (18–19) represent a physics-based instability model for an EMI phenomenon of a DE material-based plate actuator for the different cases as mentioned above, respectively.

3 Results and Discussion

This section utilizes the instability model for an EMI phenomenon of a DE actuator presented in Sect. 2 to illustrate and analyze the normalized charge and normalized voltage for the different permittivity cases by varying several input parameters.

Figure 2 plots the normalized charge (12) and (15) against stretch at constant and deformation-dependent permittivity cases for the different volume fractions of filler particles in DE material with and without pre-stretch. We herein observe that the curves are strictly increasing. At the same time, the curve steepness in the deformation-dependent permittivity case with and without pre-stretch is more than the constant permittivity case. Also, the curves are relatively gradual in the case of constant permittivity. This physically implies that the actuator charge saturation limit reduces in a constant permittivity case in comparison to the deformation-dependent permittivity. Further, with an increase in the volume fraction of the filler particles in the DE material, the corresponding normalized charge peaks for the given value of stretch. Therefore, it may be concluded that to restrict the deformation for a given stretch value, the deformation-dependent permittivity case may be utilized. Simultaneously, the pre-stretching also suppresses the deformation of the actuator to a significant amount.

In general, a dielectric elastomer is capable of giant electromechanical actuation but fails at breakdown due to pull-in instability under certain conditions with a small deformation. Such instability in the system is controlled by applying a mechanical pre-stretch to obtain a stabilized large actuation. The effect of pre-stretch enhances the stretchability of the polymer chains that suppress the electromechanical deformation of the dielectric elastomer.

Figure 3 plots normalized voltage (13) and (16) against stretch at constant and deformation-dependent permittivity cases for the different volume fractions of filler particles in DE material with and without pre-stretch. In these plots, when we evaluate the EMI peak without pre-stretch for both of the cases, a significant drop in the normalized voltage around 56% is noted in each plot. Simultaneously, scrutinizing the pre-stretching effect for both cases, we witness an effective suppression in electromechanical instability due to removing the instability peak in the curves. While examining the influence of pre-stretching in both cases, we noticed a drop of approximately 46% in electromechanical instability. On intensifying the volume fraction of filler particles in DE material, the normalized voltage gradually escalates for the same values of stretch. This physically implies that at a lower voltage supply without considering the effect of pre-stretch, the dielectric elastomeric (DE) actuator electrically breakdowns rapidly in case of deformation-dependent permittivity as comparison to the constant permittivity case. Additionally, a rise in the volume

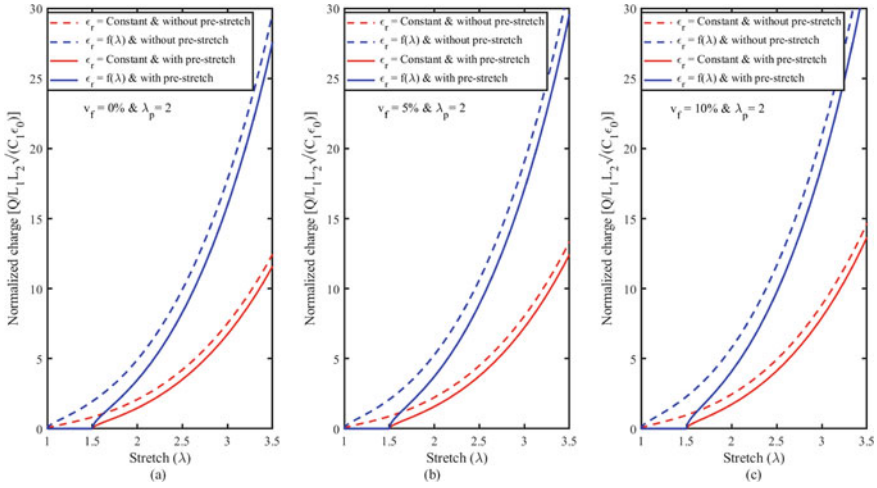


Fig. 2 Normalized charge versus stretch plots at different volume fractions of filler particles, **a** 0%, **b** 5%, and **c** 10% for constant and deformation-dependent permittivity cases with $\lambda_p = 2$ and without pre-stretch

fraction of the filler particles in the DE material quasi-statically enhances this breakdown limit, which implies that the reinforcement mechanism helps in increasing the strength of material towards failure due to EMI.

Figure 4 plots the normalized charge (12) and (18) against stretch at constant and filler-dependent permittivity cases for the different volume fractions of filler particles

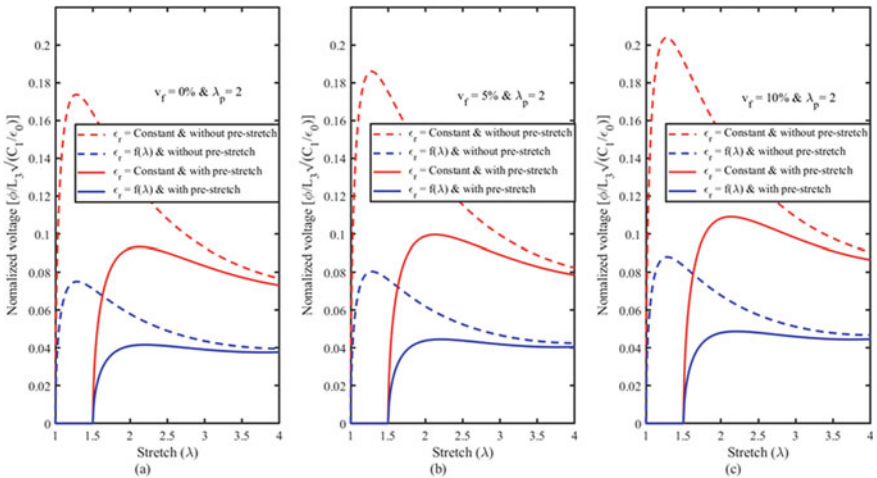


Fig. 3 Normalized voltage versus stretch plots at different volume fractions of filler particles, **a** 0%, **b** 5%, and **c** 10% for constant and deformation-dependent permittivity cases with $\lambda_p = 2$ and without pre-stretch

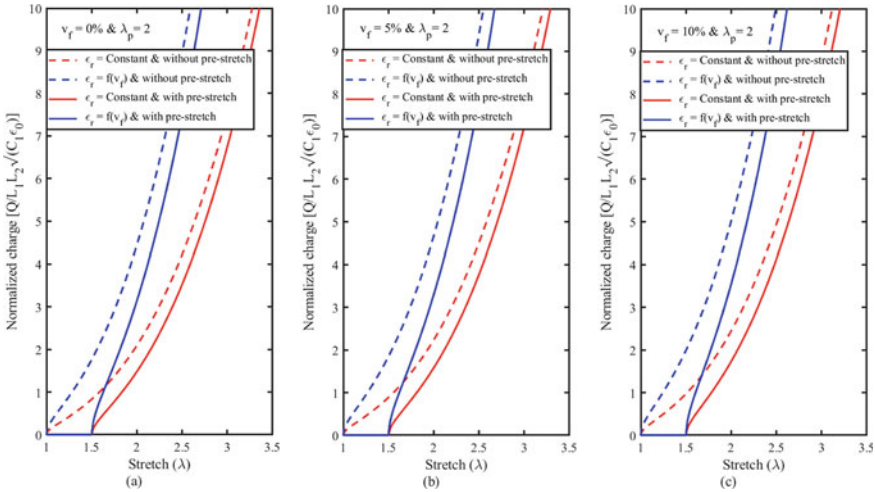


Fig. 4 Normalized charge versus stretch plots at different volume fractions of filler particles, **a** 0%, **b** 5%, and **c** 10% for constant and filler-dependent permittivity cases with $\lambda_p = 2$ and without pre-stretch

in DE material with and without pre-stretch. We recognized here that the curves strictly increased, and the curves’ steepness in both cases is comparable. This implies that the deformation of the actuator is also quite close in both of the cases. Also, the corresponding normalized charge curve moves upwards for the predefined stretch value by introducing the fillers in the DE material. Therefore, the filler-dependent permittivity case may be utilized to restrict the deformation up to a certain extent for a given stretch value. At the same time, the effect of pre-stretch acts as a resistance in deformation of the actuator to a considerable amount.

Figure 5 plots the normalized voltage (13) and (19) against stretch at constant and filler-dependent permittivity cases for the different volume fractions of filler particles in DE material with and without pre-stretch. In these plots, when we evaluate the EMI peak without considering the pre-stretching effect for both of the cases, a significant drop in the normalized voltage around 52% is shown in Fig. 5a–b and 51% shown in Fig. 5c are marked. Simultaneously identifying the pre-stretching effect for both cases, we observe a remarkable suppression in EMI due to the absence of the instability points in the curves. While correlating the influence of pre-stretching for filler-dependent permittivity cases with and without pre-stretch, approximately 46% drop in EMI is noticed. Similar findings are observed for a constant permittivity case as well. In addition, the normalized voltage gradually increases for stretch values by amplifying the volume fraction of filler particles in DE material.

At last, as illustrated in Figs. 2 and 4, one may note that the pull-in instability does not occur in the charge-controlled deformation compared to the voltage-controlled deformation illustrated in Figs. 3 and 4. In addition, we can obtain the saturation

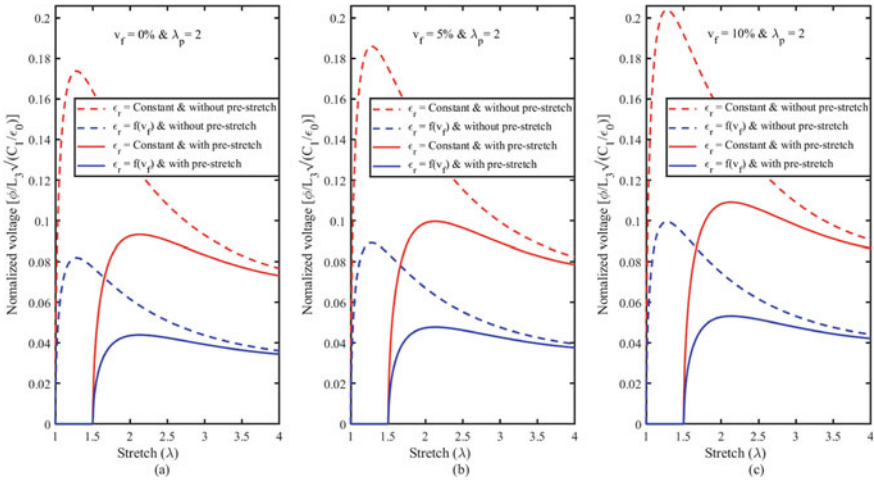


Fig. 5 Normalized voltage versus stretch plots at different volume fractions of filler particles, **a** 0%, **b** 5%, and **c** 10% for constant and filler-dependent permittivity cases with $\lambda_p = 2$ and without pre-stretch

charge limit for the dielectric actuator from normalized charge curves from Figs. 2 and 4 at the critical deformation state noted in Figs. 3 and 4.

4 Conclusion

In summary, we presented a continuum physics-based analytical model to study the deformation and filler-dependent permittivity-based electromechanical instability (EMI) phenomenon of a DE actuator. The charges are sprayed on both compliant electrodes via an external circuit in this technique. We also obtained critical stretch from the normalized voltage plots to indicate the saturation limit for the supplied charge in the DE-based actuator. Further, we noticed that particle-reinforcement in DE materials also significantly suppressed EMI in DE-based actuators similar to pre-stretch implementation. Such findings related to particle-reinforcement in DE materials will be useful to researchers and material scientists in further research and development of the dielectric elastomeric actuators undergoing large deformations.

References

1. Pelrine R, Kornbluh R, Pei Q, Joseph J (2000) High-speed electrically actuated elastomers with strain greater than 100%. *Science* 287(5454):836–839
2. Behera SK, Kumar D, Sarangi S (2021) Modeling of electro-viscoelastic dielectric elastomer:

- a continuum mechanics approach. *Eur J Mech-A/Solids* 90:104369
3. Brochu P, Li H, Niu X, Pei Q (2010) Factors influencing the performance of dielectric elastomer energy harvesters. In: *Electroactive polymer actuators and devices (EAPAD) 2010*, vol 7642. International Society for Optics and Photonics, Apr 2010, p 76422J
 4. Kumar D, Sarangi S (2019) Electro-magnetostriction under large deformation: modeling with experimental validation. *Mech Mater* 128:1–10
 5. Kumar D, Ghosh S, Roy S, Santapuri S (2021) Modeling and analysis of an electro-pneumatic braided muscle actuator. *J Intell Mater Syst Struct* 32(4):399–409
 6. Kumar D, Sarangi S (2021) A novel class of universal relation for incompressible isotropic electro-viscoelastic materials. *Mech Res Commun* 103784
 7. McKay TG, O'Brien BM, Calius EP, Anderson IA (2011) Soft generators using dielectric elastomers. *Appl Phys Lett* 98(14):142903
 8. Plante JS, Dubowsky S (2006) Large-scale failure modes of dielectric elastomer actuators. *Int J Solids Struct* 43(25–26):7727–7751
 9. Koh SJA, Zhao X, Suo Z (2009) Maximal energy that can be converted by a dielectric elastomer generator. *Appl Phys Lett* 94(26):262902
 10. Qiang J, Chen H, Li B (2012) Experimental study on the dielectric properties of polyacrylate dielectric elastomer. *Smart Mater Struct* 21(2):025006
 11. Zakaria S, Yu L, Kofod G, Skov AL (2015) The influence of static pre-stretching on the mechanical ageing of filled silicone rubbers for dielectric elastomer applications. *Mater Today Commun* 4:204–213
 12. Koh SJA, Li T, Zhou J, Zhao X, Hong W, Zhu J, Suo Z (2011) Mechanisms of large actuation strain in dielectric elastomers. *J Polym Sci Part B Polym Phys* 49(7):504–515
 13. Kumar D, Sarangi S (2018) Instability analysis of an electro-magneto-elastic actuator: a continuum mechanics approach. *AIP Adv* 8(11):115314
 14. Kumar D, Arya K, Sarangi S (2019) Modeling of a pre-stretched dielectric elastomer: a second law of thermodynamics-based approach. *J Phys Conf Ser* 1276(1):012047
 15. Kumar D, Sarangi S (2019) Pre-stretch and frequency variation effect on the dielectric permittivity of a dielectric elastomer: an amended permittivity model. *Sādhanā* 44(8):1–4
 16. Kumar D, Sarangi S (2020) Pre-stretching effect modeling of a dielectric elastomer under the electrical loading condition. *Mater Today Proc* 24:290–297
 17. Li B, Chen H, Zhou J, Zhu Z, Wang Y (2011) Polarization-modified instability and actuation transition of deformable dielectric. *EPL (Europhys Lett)* 95(3):37006
 18. Li B, Zhou J, Chen H (2011) Electromechanical stability in charge-controlled dielectric elastomer actuation. *Appl Phys Lett* 99(24):244101
 19. Broderick HC, Righi M, Destrade M, Ogden RW (2020) Stability analysis of charge-controlled soft dielectric plates. *Int J Eng Sci* 151:103280
 20. Huang J, Shian S, Diebold RM, Suo Z, Clarke DR (2012) The thickness and stretch dependence of the electrical breakdown strength of an acrylic dielectric elastomer. *Appl Phys Lett* 101(12):122905
 21. Tröls A, Kogler A, Baumgartner R, Kaltseis R, Keplinger C, Schwödauer R, Graz I, Bauer S (2013) Stretch dependence of the electrical breakdown strength and dielectric constant of dielectric elastomers. *Smart Mater Struct* 22(10):104012
 22. Goshkoderia A, Arora N, Slesarenko V, Li J, Chen V, Juhl A, Buskohl P, Rudykh S (2020) Tunable permittivity in dielectric elastomer composites under finite strains: periodicity, randomness, and instabilities. *Int J Mech Sci* 186:105880
 23. Todd MG, Shi FG (2005) Complex permittivity of composite systems: a comprehensive interphase approach. *IEEE Trans Dielectr Electr Insul* 12(3):601–611
 24. Poikelispiää M, Shakun A, Das A, Vuorinen J (2016) Improvement of actuation performance of dielectric elastomers by barium titanate and carbon black fillers. *J Appl Polym Sci* 133(42)
 25. Zeng C, Gao X (2019) Effect of the deformation dependent permittivity on the actuation of a pre-stretched circular dielectric actuator. *Mech Res Commun* 101:103420
 26. Kumar A, Patra K (2021) Proposal of a generic constitutive model for deformation-dependent dielectric elastomers of dielectric elastomers. *Eng Sci Technol Int J*

27. Li H, Chen L, Zhao C, Yang S (2021) Evoking or suppressing electromechanical instabilities in soft dielectrics with deformation-dependent dielectric permittivity. *Int J Mech Sci* 202:106507
28. Gour S, Kumar D, Yadav V (2021) Charge-controlled electromechanical instability modeling of a dielectric plate actuator. In: 2021 IEEE Madras section conference (MASCOS). IEEE. Aug 2021, pp 1–4
29. Carroll MM (2011) A strain energy function for vulcanized rubbers. *J Elast* 103(2):173–187
30. Khurana A, Kumar D, Sharma AK, Joglekar MM (2021) Nonlinear oscillations of particle-reinforced electro-magneto-viscoelastomer actuators. *J Appl Mech* 88(12)
31. Kumar D, Sarangi S (2019) Electro-mechanical instability modelling in elastomeric actuators: a second law of thermodynamics-based approach. *Soft Mater* 17(3):308–320
32. Treloar LRG (1944) Stress-strain data for vulcanized rubber under various types of deformation. *Rubber Chem Technol* 17(4):813–825
33. Jean-Mistral C, Sylvestre A, Basrour S, Chaillout JJ (2010) Dielectric properties of polyacrylate thick films used in sensors and actuators. *Smart Mater Struct* 19(7):075019

An Advance Optimal Torque Control MPPT Technique for Variable-Speed WECS



Shailendra Kumar Gupta, Motilal Rinawa, Kishor Thakre, Neeraj Garg, Ashwani Sharma, Harish Sharma, and Haris Arquam

Abstract The maximum power point technique (MPPT) of operating a wind energy conversion system (WECS) is one of the most emerging topics owing to its higher efficiency and ability to operate at variable wind speed. The optimal torque control (OTC) is one of the most popular sensorless MPPT techniques used in WECS. However, the rotor inertia delays the rotor speed response time. A modified OTC technique proposed by Xia et al. offers a solution to the existing problem. However, the technique needs real-time wind turbine-torque information, which increases the cost of the system. Therefore, this paper proposes an advance OTC technique that does not need any turbine-torque information. Here, the proposed technique is compared with the OTC and tip-speed ratio MPPT techniques. The proposed WECS had been modeled in MATLAB SIMULINK software, and the simulation results have been used for the verification of the same.

Keywords Wind energy conversion system · MPPT · PMSG · Variable-speed WECS · Renewable energy

1 Introduction

In the recent times, the world has seen exponential growth in wind energy conversion systems (WECS) installations due to the increase in demand for a clean energy

S. K. Gupta (✉)

Chandigarh University, Mohali, Punjab 140413, India

e-mail: shailendra.e12031@cumail.in

M. Rinawa · N. Garg · A. Sharma

Engineering College, Jhalawar, Rajasthan 326519, India

K. Thakre

Rabindranath Tagore University, Bhopal, MP 462045, India

H. Sharma

Rajasthan Technical University, Kota, Rajasthan 324022, India

H. Arquam

Nirwan University, Jaipur, Rajasthan 303301, India

source. In WECS, the variation in wind speed has always been a concern for system engineers. Due to high wind speed variation, the electrical power output also varies. In a weak-grid system where wind energy shares a significant fraction of grid power, the electrical power generated by the wind generator is regulated as per load [1–3]. However, when WECS is connected to a standard interconnected grid, the maximum power from the input wind power may be extracted and fed into the grid. The technique is called maximum power point technique (MPPT). An MPPT uses a variable-speed wind generator. In a variable-speed wind generator, the generator rotor speed coupled to the turbine rotor speed is varied, such as to extract maximum power from wind energy. In literature, all the MPPT techniques of wind turbine are broadly categorized among three techniques, namely tip-speed ratio (TSR), Perturb and Observe (PO), and optimal torque control (OTC) [4].

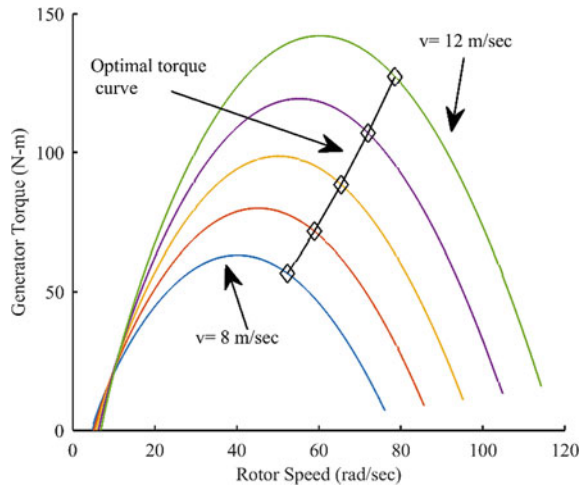
In the TSR control technique, the wind turbine blade tip-speed to wind-velocity ratio is maintained constant at the optimal point to extract maximum power at all the wind speed. The control technique is simple but tough to implement due to the need of an anemometer to sense the wind speed. The sensor increases the system's cost and deteriorates the control technique's reliability due to its inaccuracy and possible failure [5]. Therefore, in the recent past, researchers have proposed techniques using anemometer-free MPPT control techniques such as PO [6–13] and OTC control [14].

In the PO control technique, the control variable is perturbed by a small value, and the resultant change in the dependent system variable is observed. If the control variable's perturbation and change in system variable are of the same sign, the control variable is again perturbed in the same direction in the next cycle; otherwise, in the reverse direction. PO is a sensorless control technique and is effective in slow-changing wind conditions and systems with low inertia. The PO's performance deteriorates at fast-changing wind conditions as the controller cannot conclude the cause of the change. The cause of change in the system variable may be due to the control variable's perturbation or the wind speed change, and therefore, the controller may lead to the wrong perturbation command in the next cycle [5]. Also, in high inertia system, the effect of perturbation is delayed, and therefore, the time taken for convergence is high.

In the OTC control technique, the wind generator's electromagnetic torque is controlled at the wind turbine's optimal torque curve [14] as shown in Fig. 1. The optimal torque curve is experimentally evaluated before the installation of the wind turbine. The difference in the turbine-torque and the regulated wind generator's electromagnetic torque, i.e., the system's net driving torque, accelerates/decelerates the rotor to its optimal point where the turbine-torque is equal to generator torque [14]. The OTC technique is more reliable than TSR due to the absence of the wind speed sensor [4]. However, OTC is slower owing to the speed response delay due to the rotor inertia. The delay is significantly higher for the high inertia system. Therefore, the efficiency of OTC is lower than that of TSR [5]. The technique is also ineffective at low wind speed due to the lower net driving torque in the system [15].

Therefore, an adaptive OTC technique has been proposed in by Xia et al. [15]. The generator torque is regulated at the optimal torque plus torque proportional to the system's net driving torque in the adaptive OTC technique. Thus, a higher net

Fig. 1 Wind turbine-torque speed characteristic at different wind speed



driving torque is supplied to a high inertia system. However, the controller needs real-time turbine-torque information from a torque sensor/estimator to implement the technique. The extra sensors/estimators are needed that decrease the reliability of the system.

This paper proposes an advance OTC MPPT technique that does not require turbine-torque information and maintains the conventional OTC control technique’s simplicity with the TSR control technique’s effectiveness. Here, the torque proportional to the system’s net driving torque is determined by sensing the rotor speed time rate of change. In this proposed work, nature-inspired algorithms, namely Artificial Bee Colony (ABC), Particle Swarm Optimization (PSO), and Grey Wolf Optimization, have been used to determine the optimal torque proportionality constant and verify the convergence of the algorithm.

In this paper, the proposed advance OTC MPPT technique had been compared with conventional OTC and TSR control techniques. The comparison had been conducted through simulation studies on MATLAB SIMULINK software.

2 Wind Energy Conversion System Model

Figure 2 shows the block diagram of a popular configuration of a variable-speed WECS. The system includes a wind turbine, a surface-mounted permanent magnet synchronous generator (SM PMSG), a front-end fully controlled rectifier with necessary filters, and a DC load [16–19]. A three-phase inverter may replace the DC load, and the power could be injected into the grid. The system has been designed in the MATLAB SIMULINK. The gate signals to the switches in the front-end rectifier are generated by the PMSG drive, as explained in the following section.

Equations (1), (2), and (3), models wind turbine power characteristic.

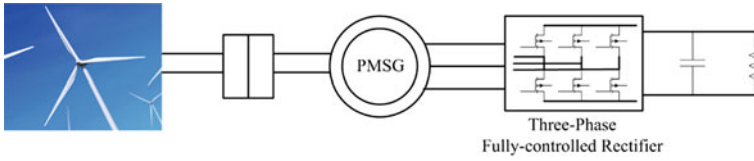


Fig. 2 Block diagram of WECS [16]

$$P_t = \frac{1}{2} \rho \pi r^2 C_p(\lambda) v^3 \tag{1}$$

$$C_p(\lambda) = a_0 + a_1 \lambda + a_2 \lambda^2 + a_3 \lambda^3 + a_4 \lambda^4 \tag{2}$$

$$\lambda = \frac{\omega r}{v} \tag{3}$$

Here, P_t is the turbine power, ρ is the air density, r is the radius of the turbine blades, $C_p(\lambda)$ is the wind turbine power coefficient, λ is the wind turbine tip-speed ratio, v is the wind speed in m/s, and a_0 – a_4 are constants that depend on the wind turbine construction, and ω is the turbine generator rotor speed. Figure 1 shows the turbine characteristic for different wind speeds. Table 1 presents the parameters of the turbine and generator.

Table 1 Turbine and generator parameters

Parameter	Specification
Generator rated power	10 kW
Rated rotor speed	750 rpm
Rated line current (rms)	14.43 A
Stator per phase resistance	0.005 Ω
Rotor inertia (Turbine + Generator)	0.017 kg m ²
Rotor friction coefficient	0.049 N sec/rad
Turbine rated power	10 kW
Rated wind speed	12 m/sec
Turbine optimal tip-speed ratio (λ)	8.25
$C_p(\lambda)$	0.1822
a_0	–0.0024
a_1	–0.0027
a_2	0.0089
a_3	-7.269×10^{-4}
a_4	2.0309×10^{-6}

3 Principal of Operation

As per Fig. 2, the PMSG drive has been simulated in MATLAB SIMULINK. Figure 3 depicts the signal flow of the drive. The operating principle of the proposed MPPT technique is based on the interaction of turbine-torque and the generator torque in real time. Mathematically, the governing equation is given by Eq. (4)

$$T_t - T_g = J \frac{d\omega}{dt} + B\omega \tag{4}$$

here, T_t is the turbine-torque, T_g is the generator torque, J is the turbine and generator's combined rotor inertia, B is the friction coefficient, and ω is rotor speed. Equation (5) models T_t , mathematically.

$$T_t = \frac{P_t}{\omega} \tag{5}$$

The generator torque, T_g , is determined by the optimal torque curve, as shown in Fig. 3, minus the torque proportional to the rotor speed's time rate of change. Equation (6) models T_g mathematically.

$$T_g = k_t \omega^2 - k \frac{d\omega}{dt} \tag{6}$$

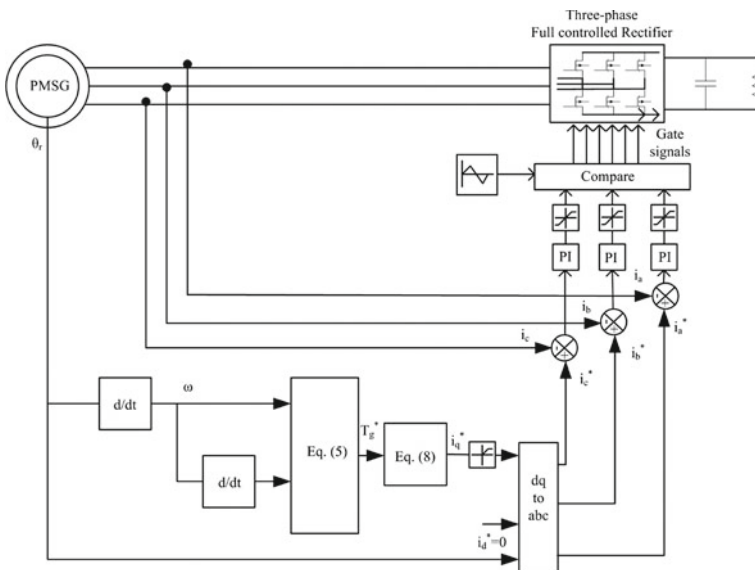


Fig. 3 PMSG drive for advance OTC MPPT control in the rotor reference frame

here, k_t is the constant of the optimal torque curve, and k is a constant. From Eqs. (6) and (4), we get

$$\frac{d\omega}{dt} = \frac{T_t - k_t\omega^2 - B\omega}{J - k} \quad (7)$$

The rate of change of the turbine generator rotor speed is governed by Eq. (7). As per Eq. (7), we can control the acceleration and deceleration of the rotor by controlling constant, k . In following section, the ‘constant k ’ has been optimized to give faster tracking of the MPPT.

As per the proposed technique’s operating principle discussed above, the generator torque needs to be controlled with respect to the turbine-torque in real time. As per the SM PMSG d - q model theory [20], where the d - q axis is fixed at the rotor reference speed, the q -axis current, I_q , regulates the generator torque. Mathematically, the generator torque, T_g , is given by Eq. (8)

$$T_g = \frac{3}{2}p\psi I_q \quad (8)$$

where ψ is stator flux linkage and p is the number of pole pairs of the generator. In the PMSG drive, the d -axis current, I_d , is maintained at zero. In the drive, the reference current, I_q^* , is generated using Eqs. (6) and (8). The I_q^* can be derived as in Eq. (9).

$$I_q^* = \frac{k_t\omega^2 - k\frac{d\omega}{dt}}{\frac{3}{2}p\psi} \quad (9)$$

4 Nature-Inspired Optimization Technique

Recent developments in artificial intelligence infer that nature-inspired algorithms are best suited for solving constrained complex problems such as PID controller parameters tuning in a nonlinear system [21–25]. In a WECS, the wind turbine and the wind generator both have nonlinear characteristics. Moreover, as shown in Fig. 3, the proposed system consists of three PI current controllers to be tuned, making the system complex. Further, the inclusion of the ‘constant k ’ increases the order of complexity of the present system.

Therefore, in the present work, the tuning of the PI controller and the ‘constant k ’ has been carried out using different nature-inspired algorithms such as ABC, PSO, and GWO. Different algorithms have been used to compare the convergence of all algorithms and verify the tuned constant values. The fitness function, population, search region, and termination condition are the same for all algorithms for properly comparing the algorithms.

4.1 Problem Definition

Equations (10) and (11) give the fitness function, F , to calculate the fitness value of a solution in tuning constant k value.

$$F = \frac{1}{\text{Err}} \quad (10)$$

$$\text{Err} = |\text{Err}_\omega| + |\text{Err}_{I_a}| + |\text{Err}_{I_b}| + |\text{Err}_{I_c}| \quad (11)$$

where, Err is the control variable error, and the subscript is the control variable. The problem has been defined to minimize the generator three-phase current error plus the speed error. Here, the absolute values of the errors are considered the index to judge the overall performance of the advance OTC MPPT technique. The logic behind this is to have a faster MPPT performance at variable wind speed and load. Here, PI controllers, as shown in Fig. 3, PID speed controller used in TSR MPPT technique, and the 'constant k ' of advance OTC MPPT technique are optimized to minimize the accumulative error of the phase currents and rotor speed.

4.2 Algorithms

In any nature-inspired optimization technique, there are three important phases: initialization/exploration, exploitation, and termination on the convergence of the problem. This section discusses the same for all the algorithms considered in the present work.

4.3 Initialization Phase

An initial random set of probable solutions, called population, is initiated in the search region in all the algorithms. All the algorithms have the inherent characteristic of learning from their current set of solutions and updating the solutions in a stochastic manner based on the quality of the solution. The quality of a solution is accessed by its fitness value. Here, each element's fitness value in the population is calculated through Eqs. (10) and (11). Thus, as per Eqs. (10) and (11), the lower is the speed and phase current error of the MPPT technique, better the solution is.

4.4 Exploitation Phase

Different algorithms have different methods of exploiting or searching for the optimal solution in the neighborhood of a probable solution. In ABC, the solution updates based on the position difference with a random solution in the population [21–23]. In PSO, the solution updates based on the difference between the current position and its own best position, and the difference between the current position and the global best position. [24]. In GWO, the solution is updated based on the position of the global best, first degree local best, and second degree local best solutions [25].

In all the algorithms, the new solution is compared with the old solution. If the new solution's fitness value is higher than the old solution, it is updated; otherwise, it is retained. All the solutions in the population, including the global best solution, are updated in every iteration.

4.5 Termination Condition

In all the algorithms, the program is assumed to have converged if the global best solution does not update its value for continuously 50 iterations. Subsequently, the program is terminated, and the final global best solution is considered our final solution. The maximum iterations for each algorithm are 1000.

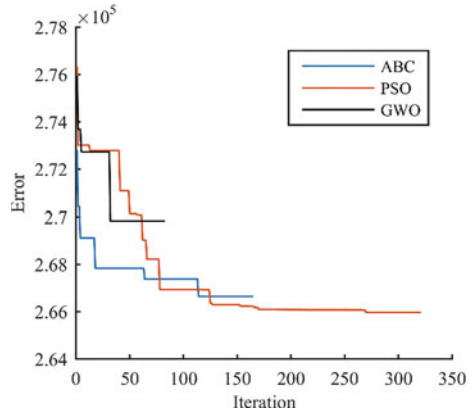
4.6 Convergence Plot

Table 2 compares the different algorithms parameters and the tuned 'constant k ' value for each. Figure 4 shows the plot of the convergence versus no. of iteration for each algorithm. It is observed that PSO and ABC are far better than GWO in minimizing the error. In the ABC technique, it has been found that the algorithm gets stuck at local minima. The PSO algorithm has been found best for the current optimization problem.

Table 2 Comparison between different algorithms used for tuning of 'constant k '

Parameter	ABC	PSO	GWO
Population	10 employed bee 10 onlooker bee	20	20
Tuned variable	Constant k	Constant k	Constant k
Search region	[0, 0.0171]	[0, 0.0171]	[0, 0.0171]
No. of iteration	164	320	82
Minimized error	268874.47	266637.73	270782.52
Optimized ' k '	0.01699054	0.01698975	0.01698730

Fig. 4 Convergence plot of all the three nature-inspired algorithms



5 Result and Discussion

The principle of operation of this paper has been supported by simulation studies on a WECS model in MATLAB SIMULINK. The WECS model is based on Fig. 3. Three MPPT techniques have been implemented in the simulation model, namely TSR, conventional OTC, and the proposed advance OTC. The proposed technique has been verified and compared to the TSR and the conventional OTC MPPT technique.

The first step to implement the MPPT technique in the WECS model is to tune all the controllers. However, due to a higher number of controllers in the system, the optimization technique’s dimension increases, which results in slow convergence. Therefore, the controllers have been tuned in steps. The following is the steps taken to tune all the controllers. Table 3 shows the parameters of the current and speed controllers.

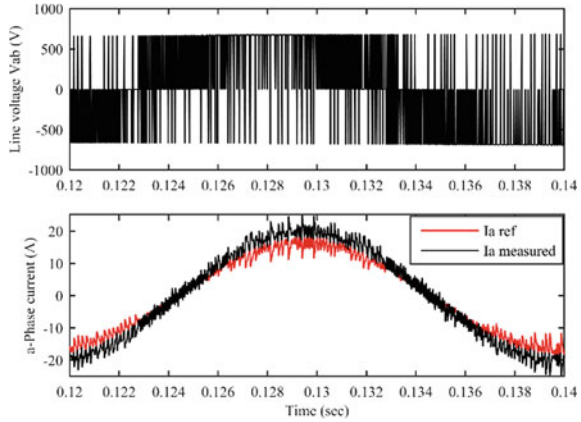
1. The d-q axis and inner current controllers of the PMSG drive have been tuned to implement the OTC control technique [14].
2. The outer PID speed controller of the PMSG drive to implement the TSR control technique has been tuned with the pre-tuned inner phase current controllers.
3. Finally, the ‘constant *k*’ of the advance OTC technique has been tuned.

Figure 5 shows the line-voltage waveform and the phase current controller performance. The reference current has been generated to have unity power factor operation.

Table 3 Current and speed controller parameters

Controller	k_p	k_i	k_d
Phase current controller	66.4243	255.3255	–
<i>d</i> -axis current controller	0.0168	524.8726	–
<i>q</i> -axis current controller	1.0325	209.7803	–
Speed controller	9.3090	744.9565	0.0278

Fig. 5 Generator line-voltage and line-current waveforms



To test the MPPT in toughest conditions, the wind speed has been changed in step from 11 m/s to 12 m/s at $t = 0.1$ s. Figures 6 and 7 show the d -axis and q -axis current controller responses at step wind speed change. At $t = 0.1$ s, the q -axis current's reference value increases to generate a torque signal with respect to higher wind speed.

As is seen by the rotor speed dynamics in Fig. 8, the speed response in advance OTC control has been found to be faster than conventional OTC control technique and matches to that of TSR control technique. The advance OTC control is a clear winner owing to its wind sensorless technique.

Figure 9 shows the wind turbine's power coefficient plot for all the three MPPT techniques. The advanced OTC and TSR reach their maximum operating condition earlier than the conventional OTC technique, increasing power output and efficiency. Figure 10 shows the power generated at the load end by the SM PMSG generator. A higher amount of output power has been generated by advance OTC control when compared to the OTC MPPT control technique. However, the response of the TSR MPPT technique is still the fastest due to directly sensing the wind speed and thus

Fig. 6 d -axis current control at step wind speed change

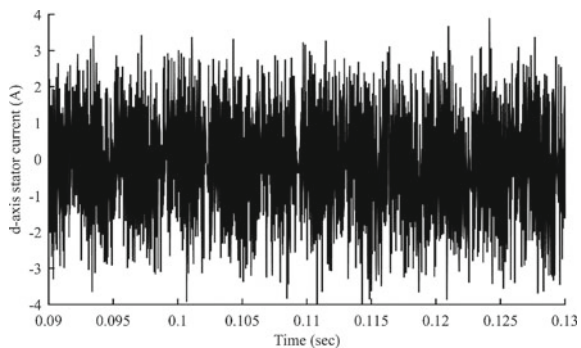
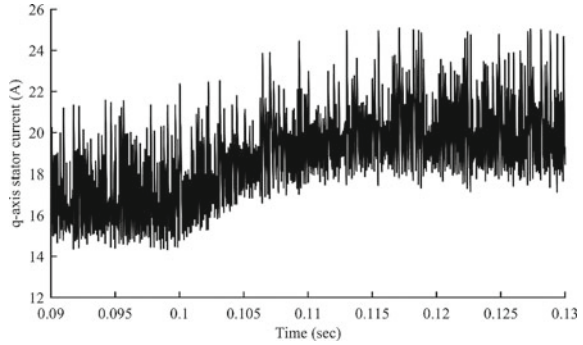


Fig. 7 q -axis current control at step wind speed change



saving the delay present in OTC MPPT based techniques. Overall, the sensorless technique used in advance OTC gives it an edge over the TSR MPPT technique.

Fig. 8 Rotor speed dynamics of the turbine generator system for the TSR, OTC and advance OTC MPPT techniques

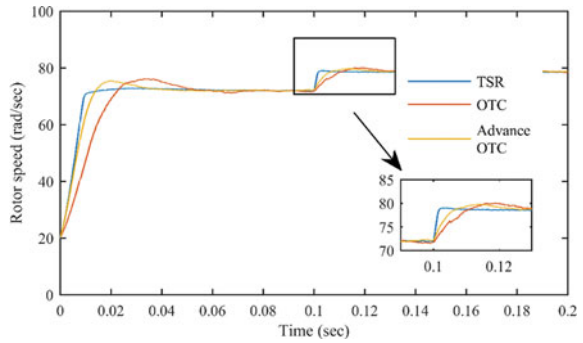


Fig. 9 Wind turbine's power coefficient waveform for the three MPPT techniques

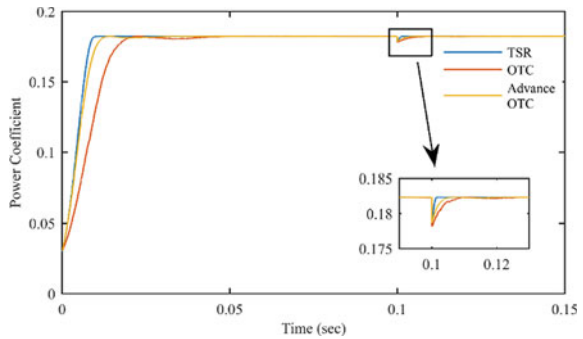
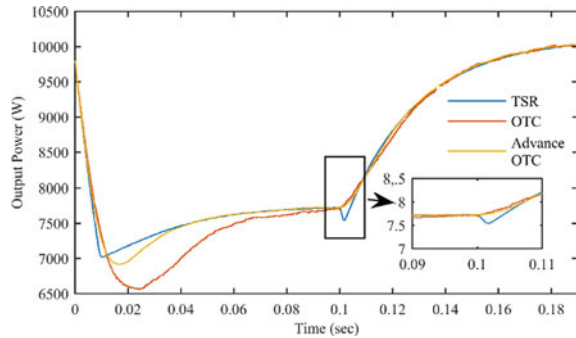


Fig. 10 Power output at DC-link for the three MPPT techniques



6 Conclusion

Optimal torque control (OTC) is one of the popular MPPT methods in variable-speed WECS due to its sensorless technology. However, the technique suffers from the rotor speed response delay to wind speed change due to the system's rotor inertia. This paper discusses an advanced OTC MPPT technique to solve the response delay issue. The proposed technique does not require any turbine-torque sensor/estimator as required in an adaptive OTC control technique. The simulation results verify the efficacy of advanced OTC control technique. The advanced OTC control technique's speed response is nearly as effective as the classic tip-speed ratio MPPT technique.

References

- Gupta SK, Srivastava RK (2018) DC-Link voltage regulation of full-power converter for WECS in weak-grid using a variable-flux dual-stator PMSG. In: Proceedings: IEEE international conference on power electronics, drives and energy systems, Chennai, India, pp 1-6
- Gupta SK, Srivastava RK (2018) Roof-top wind energy conversion system. *J Inst Eng India Ser B* 99:1-10
- Gupta SK, Srivastava RK (2020) A novel hybrid solar-wind energy conversion system for remote area electrification. *Recent Adv Electr Electron Eng* 13(6):906-917
- Abdullah MA, Yatim AHM, Tan CW, Saidur R (2012) A review of maximum power point tracking algorithms for wind energy systems. *Renew Sustain Energy Rev* 16(5):3220-3227
- Kazmi SMR, Goto H, Guo H, Ichinokura O (2010) Review and critical analysis of the research papers published till date on maximum power point tracking in wind energy conversion system. In: Proceedings: IEEE energy conversion congress and exposition, Atlanta, GA, pp 4075-4082
- Quincy W, Chang L (2004) An intelligent maximum power extraction algorithm for inverter-based variable speed wind turbine systems. *IEEE Trans Power Electron* 19(5):1242-1249
- Patsios C, Chaniotis A, Rotas M, Kladas AG (2009) A comparison of maximum-power-point tracking control techniques for low-power variable-speed wind generators. In: Proceedings: 8th IEEE international symposium on advanced electromechanical motion systems & electric drives joint symposium, Lille, pp 1-6
- Hua C, Chen W, Fang Y (2013) Design and implementation of digital power converter for wind energy conversion system. In: Proceedings: 1st IEEE international future energy electronics conference, Taiwan, pp 181-186

9. Koutroulis E, Kalaitzakis K (2006) Design of a maximum power tracking system for wind-energy-conversion applications. *IEEE Trans Industr Electron* 53(2):486–494
10. Soetedjo A, Lomi A, Mulayanto WP (2011) Modeling of wind energy system with MPPT control. In: Proceedings: Syaichu-Rohman A (eds) IEEE international conference on electrical engineering and informatics 2011, vol 1–2. Bandung, pp 1–6
11. Tiang TL, Dahaman I (2011) Novel MPPT control in permanent magnet synchronous generator system for battery energy storage. *Appl Mech Mater* 110–116:5179–5183
12. Neammanee B, Sirisumranukul S, Chatratana S (2006) Control Performance analysis of feed forward and maximum peak power tracking for small-and medium-sized fixed pitch wind turbines. In: Proceedings: 9th IEEE international conference on control, automation, robotics, and vision, Singapore, pp 1–7
13. Kesraoui M, Korichi N, Belkadi A (2011) Maximum power point tracker of wind energy conversion system. *Renew Energy* 36(10):2655–2662
14. Morimoto S, Nakayama H, Sanada M, Takeda Y (2005) Sensorless output maximization control for variable-speed wind generation system using IPMSG. *IEEE Trans Ind Appl* 41(1):60–67
15. Xia Y, Ahmed KH, Williams BW (2011) A new maximum power point tracking technique for permanent magnet synchronous generator based wind energy conversion system. *IEEE Trans Power Electron* 26(12):3609–3620
16. Gupta SK (2020) Design and implementation of an off-grid roof-top wind energy conversion system. Dissertation, Department of Electrical Engineering, IIT BHU, Varanasi, India
17. Gupta SK, Srivastava RK, Mahendra SN (2015) Voltage regulation of dual stator permanent magnet synchronous generator. In: Proceedings: IEEE international transportation electrification conference, Chennai, India, pp 1–6
18. Gupta SK, Srivastava RK (2016) Experimental evaluation of VF controlled off-grid generating system. In: Proceedings: IEEE international conference on power electronics, drives and energy systems, Trivandrum, India, pp 1–5
19. Gupta SK, Srivastava RK (2020) Performance comparison of AFDS PMSG during voltage regulation by mechanical field-weakening in extended-speed-range. *Recent Pat Eng* 14(4):643–654
20. Peter V (1998) Sensorless vector and direct torque control. Oxford Science Publication
21. Karaboga D, Basturk B (2007) Artificial Bee Colony (ABC) optimization algorithm for solving constrained optimization problems. In: Proceedings: Melin P, Castillo O, Aguilar LT, Kacprzyk J, Pedrycz W (eds) Foundations of fuzzy logic and soft computing 2007, LNAI, vol 4529. Springer, Berlin, Heidelberg, pp 789–798
22. Gaowei Y, Chuangqin LI (2011) An effective refinement artificial bee colony optimization algorithm based on chaotic search and application for PID control tuning. *J Comput Inf Syst* 7(9):3309–3316
23. Mishra AK, Tiwari VK, Kumar R, Verma T (2013) Speed control of DC motor using artificial bee colony optimization technique. In: Proceeding: IEEE international conference on control, automation, robotics and embedded systems, Jabalpur, India, pp 1–6
24. Solihin MI, Tack LF, Kean ML (2011) Tuning of PID controller using particle swarm optimization (PSO). *Int J Adv Sci Eng Inf Technol* 1:458–461
25. Sen MA, Kalyoncu M (2018) Optimal tuning of PID controller using grey wolf optimizer algorithm for quadruped robot. *Balkan J Electr Comput Eng* 6(1):29–35

Mechanical Characterization and Numerical Modeling of Moso Bamboo for a Collapsible Stretcher Cum Chair



Mohammad Ahmed Basri , Vijay Gautam , Mukul Rai ,
and Nikhil Rajput 

Abstract Bamboo is a natural composite material that competes with the conventional structural materials in terms of strength-to-weight ratio. The present work focuses on characterizing Moso bamboo to understand its mechanical behavior and use it as a structural material for a cost-effective collapsible stretcher cum chair. Tensile and bending tests of Moso bamboo were done in a graded manner with subsized samples taken at different radial depths. Their stress vs strain response was obtained and used to develop graded numerical model for finite element analysis. The tensile tests revealed that the tensile strength of Moso bamboo increases with increasing grain density from the inside to the outside of the wall in a bamboo specimen, indicating a clear gradation in its strength in the radial direction. The outermost layer has the highest density and the highest elastic limit of 260 MPa, compared to the least dense innermost layer with 150 MPa elastic limit. To test the structural application of Moso bamboo, a collapsible stretcher is designed and fabricated to full scale. The stretcher has a standing height of 835 mm and can collapse to the ground (185 mm) using a novel elevated collapsing mechanism. 95th percentile anthropometric data is used to calculate the lengths of all the essential parts and then creates a conceptual design of the stretcher which is modified to obtain the realistic design. The design is followed by an iterative finite element analysis (FEA) encompassing possible loading and operating conditions to deliver a safe design with factor of safety greater than 2.

Keywords Anthropometry · Biodegradable · Collapsible stretcher · Composites · Factor of safety · Finite element analysis · Mechanical properties · Modeling · Moso bamboo · Strength · Tensile properties

M. A. Basri (✉) · V. Gautam · M. Rai · N. Rajput
Department of Mechanical Engineering, Delhi Technological University, Delhi, India
e-mail: mohammadahmedbasri@gmail.com

1 Introduction

Bamboo, a member of the grass family, is a conventional structural material used globally and preferred for building temporary houses [1]. Although bamboo presents excellent potential as an engineering material, the use of bamboo is limited to rural areas due to a lack of engineering standards and material properties. Bamboo came into focus as a prospective engineering material through the works of Jules Janssen, considered a pioneer in the field of bamboo in the 1970s when he was awarded the world's first doctorate in the specialization of bamboo [2]. The bamboo culms grow longitudinally much faster in their natural habitat than in the radial directions, with a specific hollow tubular section subjected to wind loads causing bending. The fibrous structure and hollow section of bamboo offer high tension and compression strength coupled with high stiffness-to-weight ratio. This hollow structure, strong in bending and torsion due to high moment of inertia, also renders the bamboo, a classical material suitable for various engineering applications, including composites, temporary scaffoldings, bridges, structural frames of furniture, carts, and bicycles. [3].

Recently, many researchers have shown interest in a vision to empower and promote the use of bamboo as a composite and natural eco-friendly material. Bhalla et al. [4, 5] investigated a typical bamboo-based shed under various wind loads and self-weight. The shed's roof is supported by bamboo-tied arches and proposed using bamboo as a better and more robust material than other conventional materials. Tan et al. [3] conducted experimental and numerical studies on the mechanical properties of Moso culm functionally graded bamboo structures. Mixed-mode interfacial crack growth was observed with cellulose bridging at the outside and inside crack orientations. The effect of crack orientation and its growth on structures is discussed in detail using finite element analysis.

Dixon et al. [6] characterized the mechanical properties of Moso bamboo and observed significant variation in mechanical properties in specimens taken from different positions radially and axially in the culm. The Young's modulus of the solid cell wall (39.8 GPa) is 167% greater than the mean modulus value, indicating higher density and higher modulus toward the periphery of the bamboo pole. It is also stressed that Moso bamboo is more like a functionally graded fiber-reinforced composite resulting in high density and strength of the material. Sharma et al. [7] carried out experimental studies on the effect of processing on bamboo composites by bleaching and semi-caramelizing laminated bamboo specimens. It is observed that with thermal treatment, there is an increase of bending modulus (20%) compressive and shear strengths parallel to the grain increases. Additionally, a 16% increase in stiffness was observed for caramelized specimens over the bleached and semi-caramelized. Reynolds et al. [8] studied the fracture behavior of dowelled connections in Sitka spruce and laminated bamboo. The 5th percentile strength of Sitka spruce, bleached bamboo, and caramelized bamboo was found to be 11.4, 19.5, and 17.6 kN, respectively. Xiao et al. [9] investigated the design, construction, and testing of the modern bamboo bridge in which laminated bamboo girders are developed to full scale for mechanical testing. They concluded that bamboo laminated structures

have = appropriate stiffness and load-carrying capacity. They found that for the same type of loading, shear strengths for the bamboo fiber ratios 100, 80, and 50% are 10.9, 14.74, and 14.99 MPa, respectively. Penellum et al. [10] investigated the application of laminated bamboo in structures by modeling material as a fiber-reinforced composite using volume fraction method. It is concluded that the fiber volume fraction method is an effective tool for the nondestructive evaluation of the stiffness of the bamboo beam. Azwa et al. [11] studied the effect of moisture on the physical and mechanical properties of bamboo fiber/polyester composite based on the percentage of swelling thickness and expansion. They concluded a 13.6% reduction in strength at 80 °C. Godina et al. [12] experimentally and numerically developed a composite material model for exploring the behavior of stress and strain distribution across the culm to be adopted for structural design. They also compared the effect of moisture content for entire column and small coupon specimens and observed a 4% reduction in modulus of elasticity at 12% moisture content. Bansal et al. [13] stressed and discussed the need for favorable policy and technological initiatives to encourage bamboo as a popular engineering material with excellent research and development support from entrepreneurs and industries. Bamboo has the highest tensile strength along the longitudinal axis because its fibers run axially. It can be combined with other construction materials, like reinforcing materials for making foundations. It is considered a cost-effective and easy-to-use material and thus is generally termed the “Material of the future” [13, 14].

Wegst et al. [15] concluded in their study that bamboo has a gradient structure, and the distribution of vascular bundle decreases from the outer layer to the inner layer of bamboo. A few researchers have studied the density and strength gradation in the radial direction of bamboo [6, 15]. However, there is still a lack of study on the graded nature of bamboo, and the numerical modeling incorporating the gradation in mechanical properties of bamboo.

In the present work, Moso bamboo is characterized for its mechanical properties by tensile and bending experiments of samples taken from different depths in the radial direction of wall thickness. For assessing the structural application of Moso bamboo, a simple, easy-to-use, light in weight, and cost-effective stretcher is designed using a graded material model in finite element analysis. Bamboo is used for structural applications like furniture and bridges, however, its application to develop a stretcher has not been done in the past. High-end stretchers are expensive because of the materials and mechanisms used, thus there is a demand for lightweight, cost-effective stretchers that can provide prompt health care in remote areas, where health care is not easily accessible. Quality function deployment (QFD) chart and anthropometric data of weight and length distribution of human body were used for the design of the collapsible stretcher. A robust numerical model was formulated to include the graded properties of bamboo. Mechanisms were specially developed considering the cylindrical shape of the Moso bamboo poles. Moso bamboo poles were processed and used to fabricate the stretcher into a full-scale model to depict the manufacturability of the design.

2 Materials and Methodology

2.1 Mechanical Tests of Moso Bamboo

Bamboo is among some of the fastest-growing plants globally, a wild grass that grows in diverse natural conditions. There are over 90 genera of bamboo with about 1200 species globally, and the size of bamboo ranges from a small diameter (a few inches) to a large diameter of around a few feet. It is an excellent eco-friendly raw material for structural applications due to its enhanced mechanical properties comparable with other conventional materials like steel, concrete, and wood [16, 17]. The strength of bamboo varies mainly from one species to another, the part of the stem, the age of bamboo, as well as the moisture content [18–20]. For the design of the collapsible stretcher, Moso bamboo is taken as the structural material. Moso bamboo, which goes by the scientific name “*Phyllostachys edulis*,” is cultivated in India and has edible shoots. Its physical and mechanical properties are promising and are suitable for structures. These bamboo have diameters ranging from 20 to 150 mm and reach heights up to 28 m. Table 1 compares the density and strength of Moso bamboo with other conventional materials. The strength-to-weight ratio or the strength-to-density ratio of Moso bamboo is 79% more than stainless steel (SS-304) and 62% more than aluminum alloy (AL-6061-T6). This particular property of bamboo attracts engineers to use bamboo for structural applications. Moso bamboo is chosen for the current study since it outperforms other bamboo species in terms of mechanical properties, regeneration capabilities, annual yield, and carbon footprint [21]. Furthermore, the hardness of Moso is about twice as high as the hardness of *Guadua* bamboo [22].

Bamboo poles, with a light brown color of outer diameter 32 mm (approximately) with a minimum wall thickness of 11 mm and a central hole diameter of about 10 mm, were procured to characterize mechanical properties and fabrication. Since the density of the grains varies significantly in the radial direction, the tensile samples of thickness 1.5 mm are taken from different depths in the radial direction to evaluate the strength gradation in the thickness direction. As shown in Fig. 1a, all the subsized tensile specimens are prepared by a special purpose wood milling machine as per ASTM E8 standard. These tensile specimens are tested in uniaxial direction on a 50 kN capacity UTM (Tenius Olsen make) with a 2.5 mm/min cross head speed as shown in Fig. 1b. A dedicated HORIZON software is used to acquire the load and

Table 1 Comparison of the strength–density ratio of Moso bamboo with conventional materials

Material	Density (kg/m ³)	Ultimate strength (MPa)	Strength-density ratio
Moso bamboo	710	220	0.310
Stainless steel SS-304 [23]	7900	515	0.065
Aluminum alloy AL-6061-T6 [24]	2700	310	0.115

elongation data. These data points are further used to draw the stress–strain plots for the tested specimens.

To evaluate the bending strength using a three-point bend test, the bending specimens with a cross section size of 10×10 mm and 100 mm in length are prepared carefully using a special purpose machine. The test samples are simply supported on a three-point bend test setup in such a way that the support length is 80 mm rested on the pin supports on the two vertical arms of the UTM, and the punch touches the specimen precisely in the center as shown in Fig. 1c. The punch is moved down at a 10 mm/min crosshead speed until the specimen fractures in bending, and the punch stops its advancement automatically. To observe the gradation in bending strength, the bending specimens are placed in two different ways: In the first case, the specimen with the higher density of grains faces toward the punch and in the other case, the specimen with the lower density of grains. The different density of grains is shown in the microstructure of bamboo pole taken by a trinocular microscope at 10

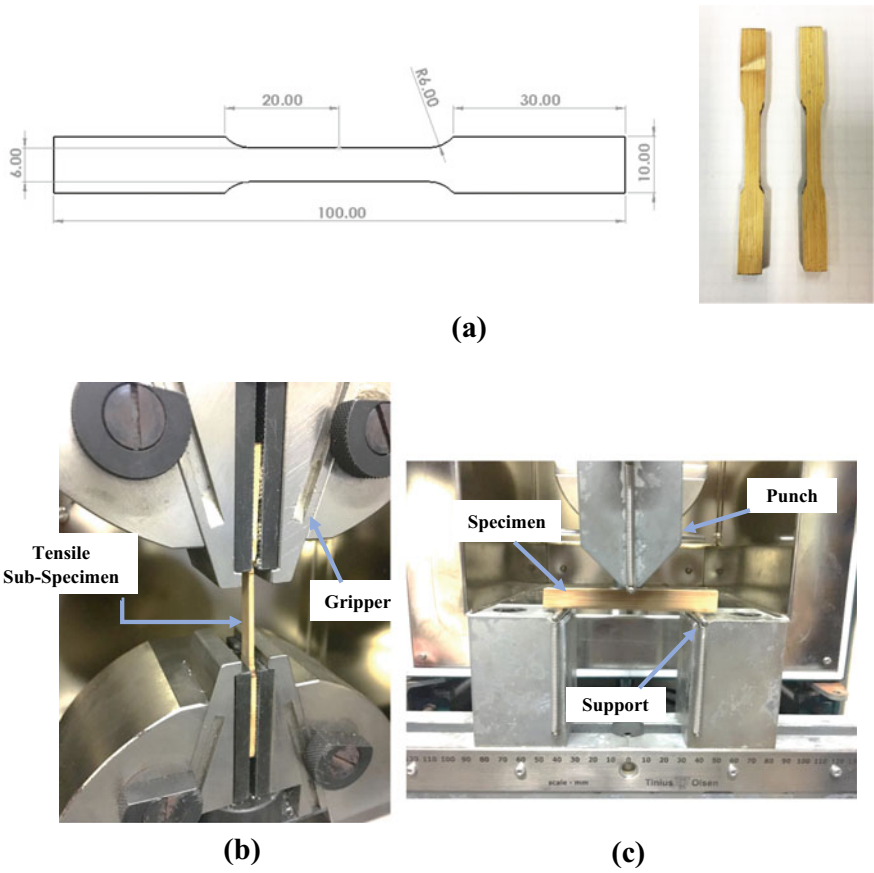


Fig. 1 a Tensile test specimen. b Tensile testing. c Three-point bend test of specimens

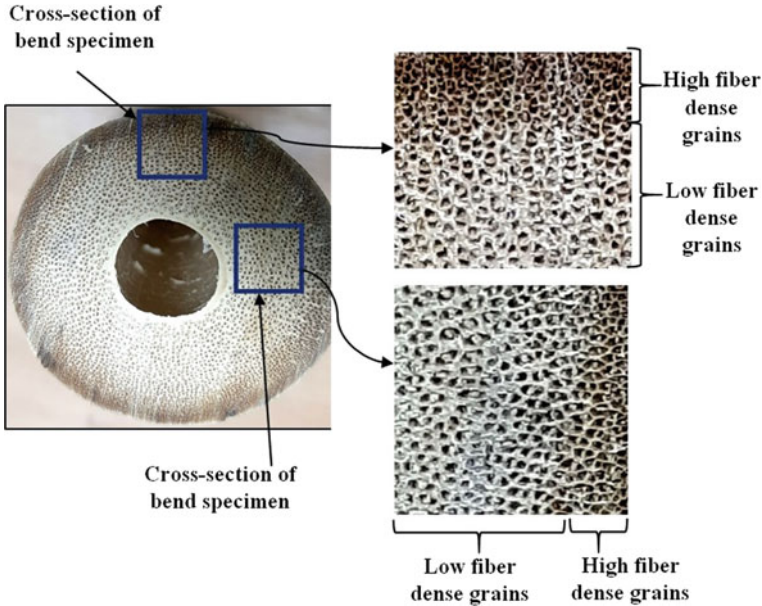


Fig. 2 Cross section of bamboo culms showing microstructural details

× zoom (shown in Fig. 2). It can be seen that high fiber density is at the periphery of the bamboo, which is also exhibited by a dark color. While toward the center of the bamboo, fiber density is less and thus is light in color. This gradation, however, is not uniform along the whole transversal plane.

2.2 Design of Collapsible Stretcher Cum Chair

Stretchers are primarily used in acute out-of-hospital care situations by emergency medical services, military, and search and rescue personnel [25]. This section discusses the design of a collapsible stretcher cum chair using Moso bamboo. The design of the stretcher was preceded by the quality function deployment (QFD) chart (shown in Fig. 3), which identifies a structured way to voice the customer requirements in terms of engineering targets. In the QFD, three relations are defined, each with a score to calculate the priority ranking of the parameters. ‘S’ stands for ‘Strong’ with a score of 5, ‘M’ stands for ‘Medium’ with a score of 3, and ‘W’ stands for ‘Weak’ with a score of 1. A matrix of customer requirements and engineering parameters was drawn, and their priority was ranked to identify the design parameter with the highest priority. It was identified from the QFD that safety, capacity to collapse to the ground, validation by engineering principles, and the use of lightweight material are the top priority parameters for the stretcher’s design.

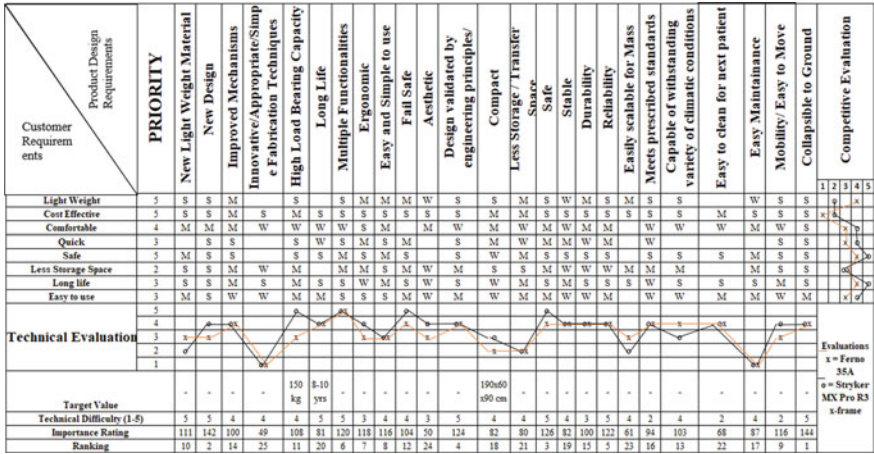


Fig. 3 Quality function deployment chart for the collapsible stretcher cum chair

First, a conceptual design is formulated, keeping in mind the ranking of the requirements obtained from the QFD. The conceptual design is then transformed into the final design through an iterative process involving the application of engineering principles of strength of materials and kinematics of machines along with the use of validated FEA frameworks to obtain a stretcher design that is realistic and easy to fabricate. To keep the stretcher lightweight, the primary material used for the stretcher is Moso bamboo which is characterized and tested to obtain the properties and is discussed already in detail in Sect. 2.1. Apart from bamboo, stainless steel (Grade-SS-304) and aluminum alloy (Grade-AA6061-T6) are used at locations with stress concentration. With the selection of material and the iterative design procedure used, the self-weight of the stretcher without the patient comes out to be 21 kg.

The stretcher consists of four essential elements called constructional features, namely backrest, seat, legrest, and footrest. The backrest is the part of the stretcher on which the portion of the body above the waist rests. The patient sits on the stretcher seat, which accommodates the lower torso and upper leg. The part of the body below the knee rests on the legrest and the footrest, on which the feet of the patient rest, is integrated within the legrest. The legrest also helps the patient step on the stretcher to be seated in the chair configuration.

The collapsible stretcher is a hybrid stretcher incorporating the features and advantages of both the wheeled recliner and ambulance stretcher, as shown in Fig. 4. According to the utility and functionality of the stretcher, there are four configurations in which the stretcher can operate: collapsed bed, elevated bed, recliner bed, and chair, as shown in Fig. 4a. The stretcher is supported by four legs: two rear legs and two front legs. These front and rear legs are connected through connector links of aluminum to make sure they move together when elevating or collapsing. As has been identified in the literature [26], during the handling of the stretcher, such as transferring the patient on/off the stretcher, loading into an ambulance leads to

injuries like sprain and fracture. The stretcher bed can collapse to the ground with a ground clearance of 185 mm, which ensures that the patient lying at the ground level can be moved into the stretcher with relative ease without risking of getting injured. Moreover, this configuration combined with the elevated bed allows the stretcher to be inducted into the ambulance easily and quickly. The upper part of the patient and backrest is first inserted into the ambulance, followed by the folding of the legs of the stretcher.

In the elevated bed configuration, the stretcher bed is at the height of 830 mm as prescribed by the medical industry regulations. This helps the stretcher be moved easily by employing minimal force and ensures that the patient can be moved to the hospital bed or other diagnosing machines and vice versa safely. The backrest

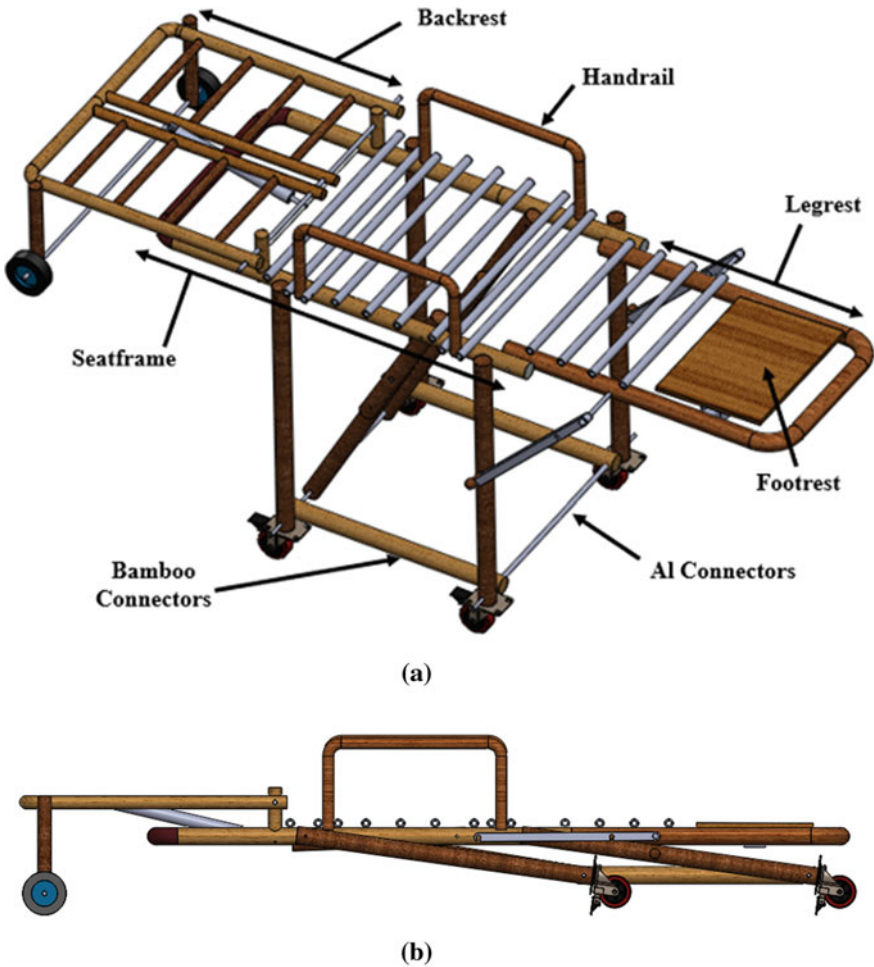


Fig. 4 CAD models of elevated and **b** Collapsed bed configuration

can lock at any intermediate position between the two extremes irrespective of the remaining portion of the stretcher. When the legrest of the stretcher is horizontal (0 degrees) and the backrest is slightly inclined (30–70 degrees) for comfortability, the stretcher is in recliner bed configuration. The stretcher performs the functions of the wheelchair, which enables the patient to be moved easily in the sitting position providing postural support and pressure relief for the patient.

Two critical criteria for the design are the length and weight of human body parts. To obtain an ergonomic design, anthropometric data is used to find out the length of the stretcher parts and the load distribution on the stretcher. Anthropometric data was obtained from work done by S Plagenhoef et al. [27]. It represents the proportion of weights of different segments as the percentage of the total body weight. This percentage-wise data provides a holistic approach and is best suited for the design. If the percentage of weight proportion is known, then the weight of segments can be calculated for any body weight as given in Fig. 4. The body is divided into four segments, namely head + neck, whole trunk, total arms, and total legs. These segments are further subdivided to obtain a more comprehensive weight distribution. This data collected forms the basis for finite element analysis conducted. Depending upon the configuration of the stretcher, different body segments are considered and summed up to find out the load on each part in each configuration.

A similar procedure is followed for determining the lengths of the three main portions of the stretcher, namely backrest, seat, and legrest. Taifa et al. [28] have given three sets of data, 5th percentile, 50th percentile, and 95th percentile. The 95th percentile data refers to the top 5% of the population and thus covers the average (50th percentile) and bottom 5% (5th percentile). The 95th percentile data was retrieved from the paper, and the lengths of the three main parts were decided to be: backrest = 780 mm, seat = 520 mm, legrest = 490 mm. The length of the three parts and the stretcher configurations is shown using line diagrams in Fig. 5b (Table 2).

The stretcher incorporates mechanisms for the movement of the three constructional features, i.e., backrest, legrest, and footrest. These mechanisms are crucial for transformation of the stretcher from one configuration to another. The elevating collapsing mechanism (ECM) shown in Fig. 6 is necessary to collapse the stretcher to

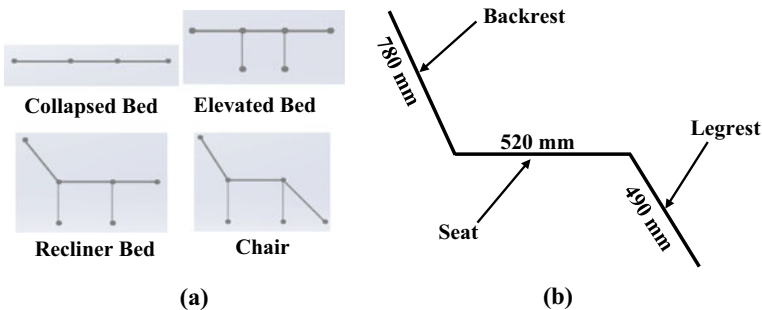


Fig. 5 Line diagram of configurations of the stretcher. **b** Length of backrest, seat and legrest

Table 2 Weight distribution of human body

	Division level 1		Subdivision level 2	Percentage	Weight distribution
A	Head + neck	A		8.26	
		A1	Head	6.15	9.225
		A2	Neck	2.11	3.165
B	Whole trunk (lower, middle, upper torso)	B		46.82	
		B3	Upper torso (thorax)	20.1	30.15
		B2	Middle torso (abdomen)	13.06	19.59
		B3	Lower torso (pelvis)	13.66	20.49
C	Total arms (upper arm, lower arm, hand)	C		11.54	
		C1	Upper arms (both)	6.5	9.75
		C2	Lower arm/forearms (both)	3.74	5.61
		C3	Hands (both)	1.3	1.95
D	Total legs	D		33.38	
		D1	Thighs (both)	21	31.5
		D2	Lower legs (both)	9.5	14.25
		D3	Feet (both)	2.88	4.32
	Total			100	150 kg

the ground and elevate it back to the standard height with assistance. This overcomes the limitation of a fixed height stretcher in which the patient runs an extremely high risk of being further injured while transferring. The elevated height of the stretcher is 830 mm, while the collapsed height of the stretcher is 185 mm. The ECM has four vertical links, two front legs (Link 4) and, two rear legs (Link 2), and four inclined links (Link 5 and Link 6), as shown in Fig. 6. The inclined links unequal in length are pivoted together. The pivot of the two links is so designed that it provides structural rigidity to the structure in the elevated position, and enables the structure to collapse and fold within a small space without compromising the functionality of the structure.

To transform efficiently from elevated position to collapsed position, the combination of the lengths of links exists only for a particular set of lengths of links. If any of the link is slightly changed, the mechanism fails. The sizes of ECM links (Link 5 and Link 6) that make the mechanism work smoothly are found out by geometrical construction. The mechanism is constructed in both elevated and collapsed positions using a suitable scale (Scale used is 1:10) as per the lengths of all the links. Links 1 and 3 are depicted in black as they are of the same length. Similarly, Links 4 and 2 depict the legs of the stretcher which are shown in red and are of same length. According to Grubler's criteria, the mechanism with 6 members/Links, 7 binary pairs (one tertiary converted to binary), and the mechanism's degree of freedom (DOF) is 1. DOF of 1 indicates that the minimum number of inputs required to have a constrained motion

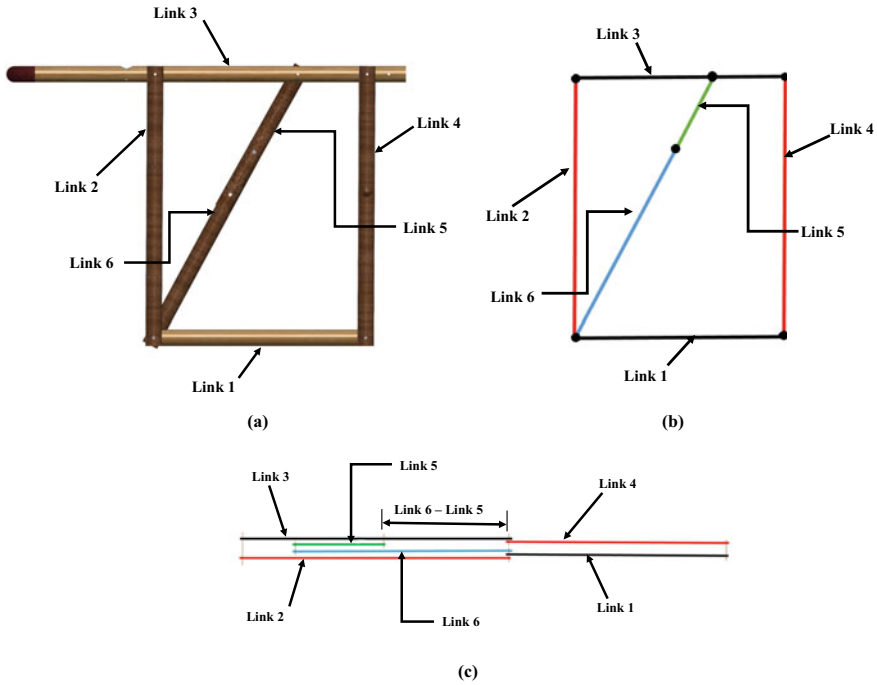


Fig. 6 Constructional diagrams for **a** Elevated, and **b** Collapsed configurations

of links of the mechanism is one for this mechanism. Here, it is the movement of the Link 5, which results in constrained movement of the other links for transforming the stretcher from the collapsed to elevated configuration and vice versa.

From the elevated and collapsed position construction diagrams, the lengths found out to be, Link 6 = 520 mm and Link 5 = 220 mm. The following ratios of link lengths were concluded to be the standard ratio for further design:

$$\text{Link 4/Link 3} = 1.25 \tag{1}$$

$$\text{Link 5/Link 4} = 0.34 \tag{2}$$

$$\text{Link 6/Link 5} = 2.36 \tag{3}$$

These ratios hold utmost importance and is not limited to collapsible stretcher mechanism and thus can be applied to other mechanisms, where the structure needs to be collapsed according to space constraints.

The stretcher, inherently being a chair, has a reclining backrest which, while in chair form, stays at an angle of 65–75° from the seat but in bed form lays flat aligned with the seat. A lockable gas spring of 400 N force was used to provide control

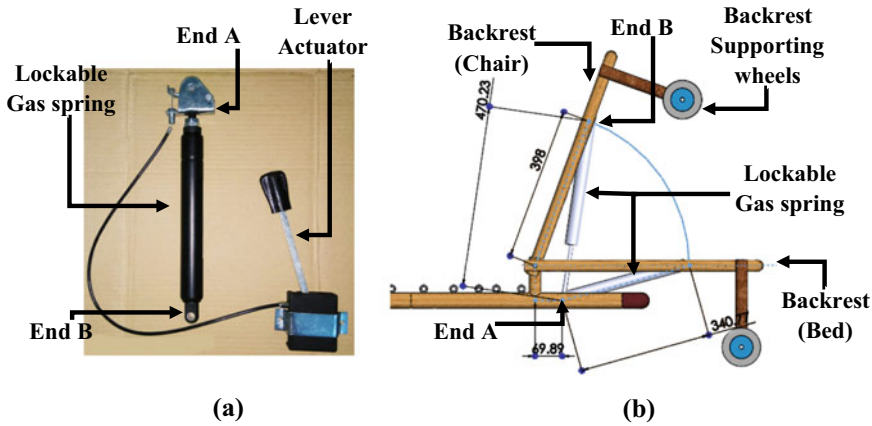


Fig. 7 a Lockable gas spring. b Backrest side view CAD model

between the backrest and the seat frame, as shown in Fig. 7. One end (End A) of the gas spring is attached to the seat frame, while the opposite end (End B) swivels about the backrest. The distance of the pivot point of end A on the seat frame and the distance of the pivot point of end B on the backrest are unknown and were found out using two constraints, i.e., the extreme angular positions of the backrest that are desired (70° and 0°) and the extended and stroke lengths of the lockable gas spring (470 and 398 mm, respectively). The actuation system of this gas spring has a lever and a cable, which is attached to the End A.

To ensure smooth movement of the parts of the stretcher, joinery techniques are designed in such a way that the fibrous nature of Moso bamboo does not increase friction and hinders the sliding between parts. Each joint is fabricated by drilling transversal holes through bamboo, followed by filing to remove Bamboo fibers from the hole. A metallic sleeve, which is a hollow cylinder of material SS-304 with outer diameter equal to the hole diameter, is inserted into the hole along with small amount of adhesive and interference fit. A metallic insert is inserted in the sleeve's hollow space whose length is greater than the diameters of the bamboo to be joined. Transversal holes are also drilled on the ends of the metallic insert and the clevis pin is used to prevent the transversal movement of the insert, as shown in Fig. 8.

3 Finite Element Analysis (FEA) Setup

Finite element analysis simulations were performed to obtain statistics on the load-bearing capacity and safety factor of the stretcher. The simulations were performed using ANSYS Mechanical 18.1, and a specific set of loading conditions was applied.

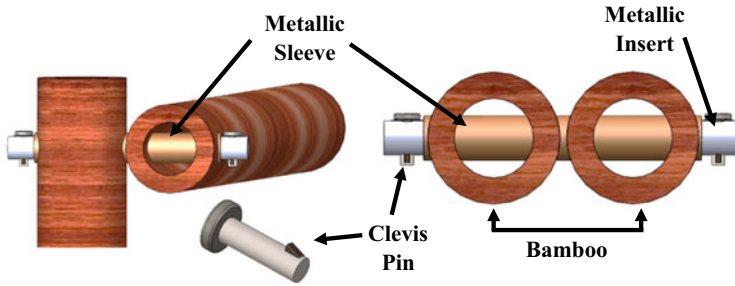


Fig. 8 Joinery technique used for joining the Moso bamboo sticks

3.1 *Material Model*

Bamboo is considered to be a layered material as discussed in the experimental testing, and the same methodology is used to prepare the material model of Bamboo for the FE simulation of the stretcher. Bamboo is composed of four layers: outermost layer, outer layer-1, inner layer-1, and innermost layer. For a bamboo pole with 40 mm external diameter, the radii of the layers from the center of the hollow portion are 38, 32, 24.8, and 22 mm, respectively. Bamboo is ideally an anisotropic material and has different values of elasticity, Poisson's ratio, and shear modulus in different directions. Bamboo laminates are often considered orthotropic materials with their properties defined in three different loading directions [29]; however, it is challenging to obtain specimens in different directions in raw bamboo poles. Thus, the material model for Moso Bamboo is taken as isotropic elasticity, and the stress–strain curves obtained from the experimental testing are used as input in a linear elastic material model in ANSYS workbench. The experimental tests discussed in previous sections as well as the prior research done on the mechanical properties of various bamboo portray that bamboo is a linear material [6, 30]. Bamboo is a composite material made up of fibers, and therefore, there is no permanent plastic deformation, i.e., yielding at any stress value. When exposed to uniaxial tensile testing, the material reaches ultimate tensile strength fails instantly with the splitting of fibers. This phenomenon is also observed in the uniaxial experimental tests done for the study. The material model was prepared using the APDL module from ANSYS and imported into ANSYS workbench (Fig. 9), where meshing was done and boundary conditions were applied.

3.2 *Loading Criteria for Analysis*

For FE analysis of the stretcher, a load of 150 kg was utilized and segmented according to the anthropometric data. Different analyses were performed and the factor of safety obtained from ANSYS mechanical is taken to be as a part of the overall safety of

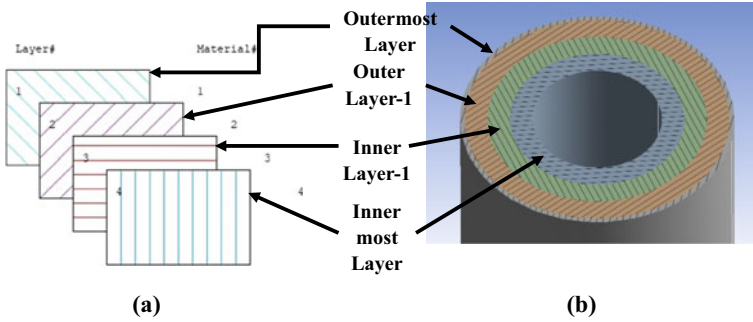


Fig. 9 Layer-wise material modeling on ANSYS APDL

factor determining the safety of the design for the worst-case scenario. A framework for static structural analysis was prepared and validated for simple boundary conditions, in which numerical deformation was compared with the experimental deformation, and acceptable results were achieved. This framework was used to analyze the stretcher to obtain accurate results. Table 3 summarizes which body part rests on which part of the stretcher. According to the body parts and stretcher part relation and the anthropometric data from Table 3, the load distribution on the stretcher is calculated for each configuration as listed in Table 3, which shows the details of the loading on the stretcher segmented for 150 kg body weight.

As mentioned in Table 4, FE simulation is carried out for three configurations, elevated bed, chair, and collapsed bed. Since almost every part of the stretcher is cylindrical in shape, 8 node brick elements are used for meshing the model. A mesh convergence study is also done to obtain the right mesh size without compromising computational load. The mesh sizes considered were 1.5, 0.85, and 0.5 mm. It was observed that for 0.85 and 0.5 mm, the stress and deformation values have a difference of less than 5%. The stretcher is fixed in position by constraining all degrees of freedom of all the nodes at the bottom surface of the legs of the stretcher. For simplicity of the linear static analysis, the contact formulated between various parts of the stretcher is bonded type with no sliding and no separation because the joints remain rigid in the static condition.

Table 3 Body parts resting on stretcher parts in different configurations of the stretcher

Analysis	Stretcher configuration	Body parts and stretcher part relation		
		Backrest	Seat	Legrest
I	Elevated bed	Head, neck, upper torso, middle torso, upper arms	Lower torso, lower arms and hands, thigh	Lower legs and feet
II	Chair	Head, neck, upper torso, middle torso	Lower torso, total arms, thigh	Lower legs and feet
III	Collapsed bed	Same as elevated bed		

Table 4 Load distribution of human body (150 kg)

Configuration	Part	Load (Kg)	Load (N)
Elevated/collapsed/recliner bed	Backrest	71.88	704
	Seat	59.55	584
	Legrest	18.57	182
Chair	Backrest	62.13	609
	Seat	69.3	680
	Footrest	18.57	182

4 Results and Discussions

4.1 Material Characterization

The engineering stress– strain plot for the specimens of thickness 1.5 mm taken at different depths in radial direction and tested in uniaxial direction is plotted and shown in Fig. 10. It is observed that the specimens taken from the outermost layer depict the highest tensile strength of 260 MPa and then fails by splitting transverse to the loading direction so that, the weakest fiber first leads to sharp reduction in strength to 225 MPa for a strain of 5%. This further leads to the failure of more fibers resulting in a stepped pattern in the plot before finally fracturing into two pieces apart as in the case of a brittle failure. The maximum strain achieved by the first specimen of outermost layer is only 10%. The highest tensile strength and lowest strain in the tensile specimen of outermost fiber are attributed to the highest grain density.

In the test specimen of the layer next to the outermost layer designated as outerlayer-1, the maximum tensile strength is reduced to 184 MPa at 12% strain, which further reduces to a fracture strength 130 MPa at 15% strain. The failure

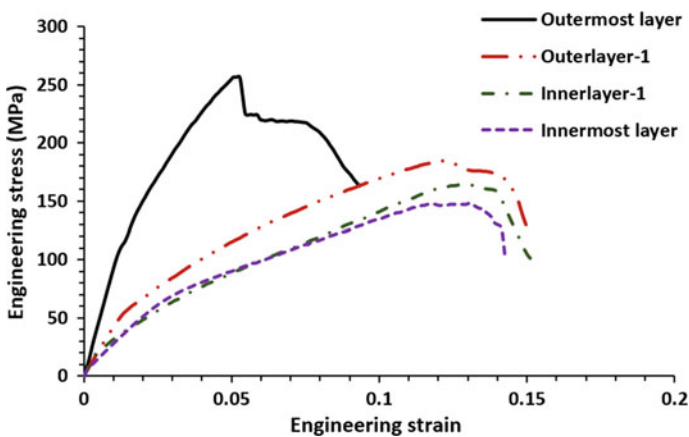


Fig. 10 Engineering stress—strain plot for tensile testing of different layers of Moso bamboo

by splitting is not quite explicit in this sample. The specimens show much lower elastic modulus, i.e., two-thirds, than the modulus depicted by the tensile specimen of outermost layer. In the test specimen of the layer next to the outlayer-1, i.e., the innerlayer-1, the maximum tensile strength is reduced further to 163 MPa at a tensile strain of 13.5% and shows a fracture strength of 100 MPa at a strain value of 15%.

A tensile strength of 150 MPa at a strain of 13.3% is observed in the tensile specimen taken from the innermost layer. Fracture strength of 100 MPa at a strain value of 14.5% is also observed. It is also seen that the initial slope of the curve, i.e., elastic modulus, shows negligible variation between the tensile specimens of innerlayer-1 and innermost layer.

Table 5 shows the elastic limits for the different layers of Moso bamboo. It can be concluded from the results of the tensile tests that the tensile strength increases with an increase in the grain density from inside to outside of the wall in a bamboo specimen, indicating a clear gradation in its strength in the radial direction. However, the gradation level decreases toward the bamboo's inner wall, suggesting a slight variation in the bamboo grain density.

The variation of flexural stress with respect to the central deflection of the punch is shown in Fig. 11. It is observed that the specimens for bending in which the high-density grains are oriented toward the punch show higher flexural strength than that of the specimens oriented with lower density grains facing the punch during the experiments.

The specimens designated as low-density grains facing the punch during bending show a flexural strength of 185–200 MPa but as the central deflection of the specimen reaches close to 10 mm, the specimen fractures in bending. The higher value of flexure is because the low-density grains are in compression, while the high-density grains are tension. The crack by splitting originates from the grains located on the exterior of tension side of the specimen, where the grains are much denser. The flexure strength on splitting of the grains falls quickly as only a few numbers of grains are available to sustain the bending load in tension.

In the case of the specimens oriented in such a way that the high-density grains facing the punch during bending, the flexure strength is observed to be in the range of 155–160 MPa when the central deflection of the specimen is approximately 12 mm maximum and the specimen fractures in bending in such a way that lower density grains fails first by splitting.

The lower flexure strength is because the high-density grains are on the compression side of the bending specimen and the low-density grains are on tension side and since the failure originates from the fibers located farther from the neutral axis

Table 5 Elastic limits of different layers of bamboo pole

Layer	Elastic limit (MPa)
Outermost layer	260
Outermost layer-1	190
Innermost layer-1	165
Innermost layer	150

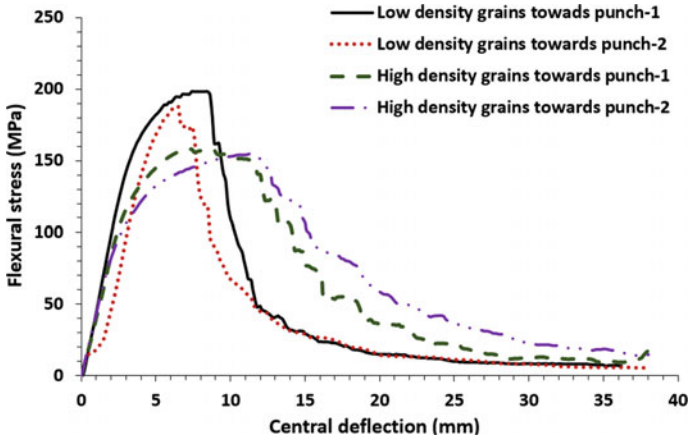


Fig. 11 Three-point bend test on Moso bamboo results

in tension. In this case, it is also observed that the flexure strength on splitting the grains of lower density drops quickly as only a few numbers of fibers are available to sustain the bending load in tension.

It can be concluded from the results of the flexural experiments that the bending strength increases when the specimens with high density of fibers or grains are located on tension side of the specimen during bending. This clearly indicates a gradation in its flexure strength which varies with grains location concerning the applied stress of tension or compression.

4.2 Simulation (FEA) Results

The results obtained from FEA of elevated bed configuration are shown in Fig. 12. The backrest is analyzed by treating it like a cantilever with load distribution closer to the hinges. As shown in Fig. 12a, the stress in the bamboo structure is very small when compared to the stress obtained at the hinges shown in Fig. 12b. These results depict that the max deformation of the backrest is 4.6 mm in the bed configuration when the weight of the upper torso is mostly on the backrest. The deformation is very small as compared to the dimensions of the stretcher and hence relatively will not affect the functioning of the backrest. Equivalent von Mises stress was taken into consideration as it gives the most accurate results compared to experimental results. The maximum stress was noted to be 162.27 MPa which is localized near the pivot of the backrest mechanism (lockable gas spring).

This stress value is much lower to the strength of the aluminum alloy (AA6061-T6) (yield strength of 255 MPa [24]) rod which is used to swivel the lockable gas spring and hence will not result in failure of the rod. The stress in the rest of the structure is much below the yield strength of bamboo and thus reduces the chances

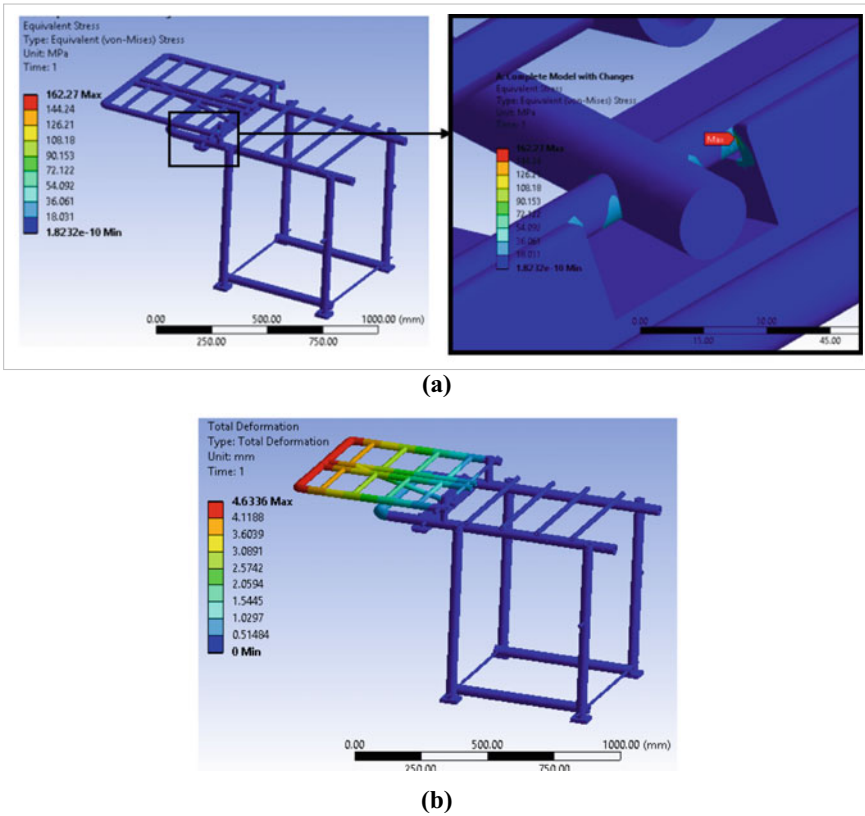


Fig. 12 Results for elevated bed. **a** Equivalent von Mises stress. **b** Total deformation

of failure. Therefore, it is observed from the FE analysis that both stress (162.27 MPa) and the deformation (4.6 mm) are in the acceptable range, hence, giving a safety of factor of 1.57.

The results obtained from FE analysis of chair configuration are shown in Fig. 13a and b. In this configuration, the load on the backrest is lower than the elevated bed configuration as the load shifts toward the seat of the chair. In the chair configuration, the load is divided so that the weight of the upper torso is not completely on the backrest compared to the bed configuration. In this case, the weight of the upper torso is divided into components and only the cosine component acts perpendicular to the backrest, and hence, the value of the maximum stress is limited to 117.3 MPa. Moreover, this time the location of maximum stress is in the rod on which the backrest pivots about the seat frame. Aluminum AA6061-T6 rod is used for swiveling the backrest, and hence, the stress obtained is under the permissible level, ensuring the design’s safety. The factor of safety achieved in this configuration is 2.17. The total deflection, in this case, is found out to 10 mm, which is more than the previous configuration because the angle of inclination of the backrest is larger, and hence,

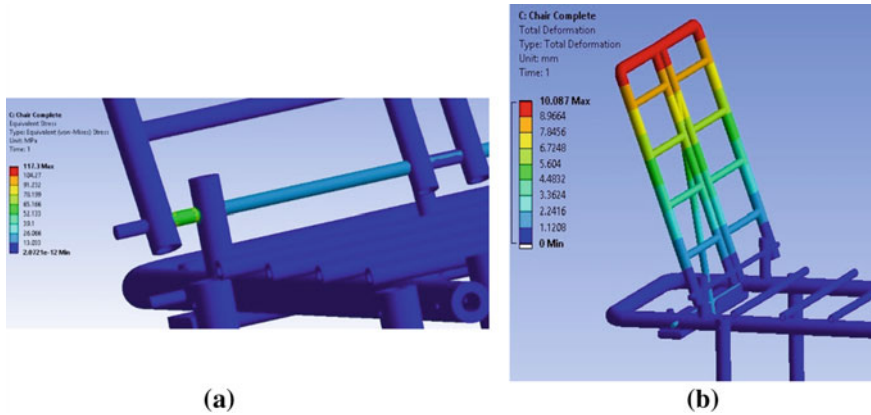


Fig. 13 Result for chair configuration. **a** Equivalent von Mises stress. **b** Total deformation

it will tend to lower the backrest. However, 10 mm deflection can be neglected considering the dimensions of the other parts.

The maximum stress in the collapsed configuration reached is about 139.78 MPa and lies much below the tensile strength of bamboo. The factor of safety in this case is 1.82.

The simulation results show that the stress concentration is generally obtained at areas where material stronger than Bamboo is being used. These results provide an insight to the behavior of the stretcher and thus helps in incorporating design modifications in order to minimize high stress points. After every analysis, the factor of safety is greater than one for every configuration under combined loading condition. However, some factors utilized for the safe design could not be included in the simulation due to the complexity in modeling. These factors include the joinery techniques and bamboo web on the part where the body rests. Additionally, the analysis is done for 150 kg body, whereas the stretcher is aimed for people with weight up to 100 kg. If these factors are included, the overall factor of safety of the design increases and lies in the range of 2–4 for every configuration which is the factor of safety considered by large-scale manufacturers.

4.3 Fabrication

The collapsible ambulance stretcher cum chair is fabricated to full scale to demonstrate the various mechanisms and configurations envisioned during design. The fabricated stretcher in elevated bed and chair configuration is shown in Fig. 14. Bamboo unlike other engineering material is hollow and has variable strength along different radial depths. All these characteristics pose a challenge as conventional fabrication techniques used for metals cannot be utilized to make any structure using

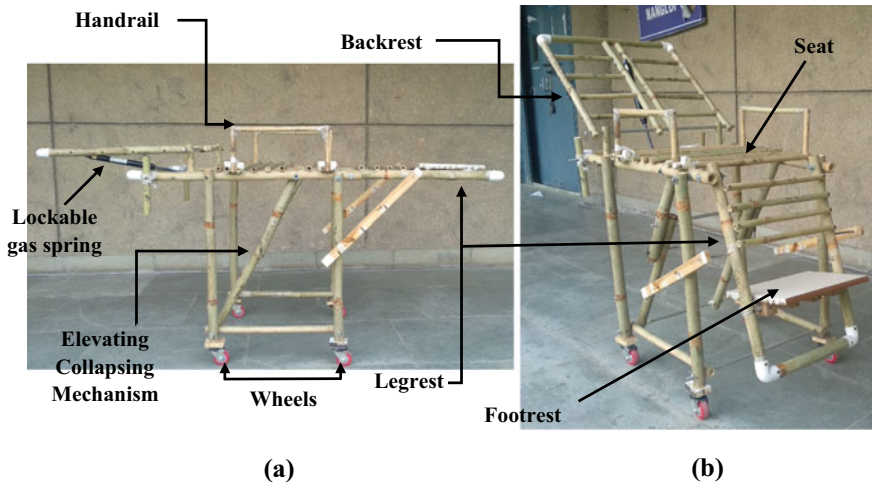


Fig. 14 Elevated and chair configurations of fabricated stretcher

bamboo. Hence, new fabrication and joinery techniques (discussed in Sect. 2.2) were incorporated to fabricate a full-scale stretcher. PVC elbows were used to make L-joints by scraping bamboo ends and then permanently fixing them with adhesives instead of heating the bamboo and bending it as it requires high level of expertise only available to bamboo craftsmen. Additionally, it was noticed during fabrication that the larger the wall thickness of the bamboo, the more easily its manufacturability was.

The bamboo stretcher was built as a prototype to bring out a fully functioning and safe stretcher that can compete with the other products in the market in terms of its functionality, i.e., save lives by providing quick, safe, and effective medical attention. However, the prototype requires several changes, primarily fabrication, to make it a market-ready product. Some of these changes include node and outer skin removal, straightening of bamboo pieces, preservation using caramelization against insects using insecticides, priming, and polishing, inserting rubber caps at the sharp ends, and adding cushioning pads, bending using heating application, etc.

5 Conclusions

Based on the study done for the mechanical characterization of Moso bamboo and the design of collapsible stretcher cum chair, the following conclusions have been drawn:

1. The current study used mechanical tests of Moso bamboo and finite element analysis to develop a full-scale collapsible stretcher that is easy to use, low in weight, and inexpensive.

2. A microscopic image of the bamboo intersection showed that Moso bamboo has a functionally graded structure. The tensile strength of Moso bamboo increases with an increase in the grain density from inside to outside of the wall in a bamboo specimen indicating a clear gradation in its strength in the radial direction but the gradation level decreases toward the inner wall of the bamboo suggesting a slight variation in the bamboo grain density.
3. The flexural strength increases when the specimens with high density of fibers are located on tension side of the specimen during bending. A gradation trend in its flexure strength is exhibited which varies with grains location with respect to the applied stress of tension or compression.
4. A quality function deployment (QFD) chart was used to understand the customer requirements and prioritize different design parameters. Safety, collapse capacity, engineering validation, and low-weight material utilization were highlighted in the QFD as the most critical design factors for the stretcher.
5. The designed stretcher has four constructional features: backrest, seatframe, legrest, and footrest. According to the utility and functionality of the stretcher, there are four configurations in which the stretcher can operate: collapsed bed, elevated bed, recliner bed, and chair.
6. The study portrays the importance of anthropometric data for the size and weight distribution of the human body, resulting in an ergonomic design of the stretcher. The 95th percentile data was utilized for the design, and the lengths of the three main parts were calculated to be: backrest = 780 mm, seat = 520 mm, legrest = 490 mm.
7. The collapsible ambulance stretcher cum chair designed weighs 21 kg and can sustain loads of 150 kg considering all safety factors. The stretcher has a standing (elevated position) height of 835 mm and a height of 185 mm when collapsed to the ground level. A novel elevating collapsing mechanism is designed to transform the stretcher from the elevated to collapsed position and vice versa.
8. The properties find out through mechanical tests were helpful in the finite element analysis, which was used to find the stress concentration locations in the stretcher under different loads. It was found that these stress concentration points were mostly at joints and to resolve it, material like steel and aluminum was used. The factor of safety (greater than 1) obtained in each configuration was satisfactory, and the stresses in bamboo were much lower than its tensile and bending strength values.
9. During the fabrication, it was also observed that the greater the wall thickness of the bamboo better will be the structure due to ease of manufacturability.
10. The stretcher requires two operators for the proper functioning of all the mechanisms, and the stretcher is simple, easy to use, and at par with the commercial stretchers that perform all the necessary functions at reduced costs.

6 Conflicts of Interest

The authors declare no conflict of interest.

Author Contributions Mohammad Ahmed Basri: Conceptualization, Methodology, Software, Validation, Formal analysis, Investigation, Data curation, Writing—original draft and editing, visualization. Vijay Gautam: Conceptualization, Methodology, Writing—Review and Editing, Supervision, Project administration Mukul Rai: Investigation, Methodology, Data curation, Writing—some portion and Editing. Nikhil Rajput: Investigation, Methodology, Data curation, Writing—some portion and Editing.

References

1. Richard MJ (2013) Assessing the performance of bamboo structural components. *J Chem Inf Model* 53:287
2. Janssen JJ, Boughton G, Adkoli NS, Ranjan MP, Sastry CB, Ganapathy PM, Ravindran K (1981) Bamboo as an engineering material. *IDRC Bamboo Ratt Res Netw Eindhoven Univ*
3. Tan T, Rahbar N, Allameh SM, Kwofie S, Dissmore D, Ghavami K, Soboyejo WO (2011) Mechanical properties of functionally graded hierarchical bamboo structures. *Acta Biomater* 7:3796–3803. <https://doi.org/10.1016/j.actbio.2011.06.008>
4. Bhalla S, Gupta S, Sudhakar P, Suresh R (2008) Bamboo as green alternative to concrete and steel for modern structures. *J Environ Res Dev* 3:362–370
5. Bhalla S, Sudhakar P, Gupta S, Kordke C (2008) Wind analysis of bamboo based shed structure and design of base connection for bambcrete column. In: *Proceedings of 1st international conference on modern bamboo structures, ICBS-2007*, pp 259–265. <https://doi.org/10.1201/9780203888926.ch29>
6. Dixon PG, Gibson LJ (2014) The structure and mechanics of Moso bamboo material. *J Royal Soc Interface* 11. <https://doi.org/10.1098/rsif.2014.0321>
7. Sharma B, Gat6o A, Ramage MH (2015) Effect of processing methods on the mechanical properties of engineered bamboo. *Constr Build Mater* 83:95–101. <https://doi.org/10.1016/j.conbuildmat.2015.02.048>
8. Reynolds T, Sharma B, Harries K, Ramage M (2016) Dowelled structural connections in laminated bamboo and timber. *Compos B Eng* 90:232–240. <https://doi.org/10.1016/j.compositesb.2015.11.045>
9. Xiao Y, Wu Y, Li J, Yang RZ (2017) An experimental study on shear strength of glulam. *Constr Build Mater* 150:490–500. <https://doi.org/10.1016/j.conbuildmat.2017.06.005>
10. Penellum M, Sharma B, Shah DU, Foster RM, Ramage MH (2018) Relationship of structure and stiffness in laminated bamboo composites. *Constr Build Mater* 165:241–246. <https://doi.org/10.1016/j.conbuildmat.2017.12.166>
11. Azwa ZN, Yousif BF (2019) Physical and mechanical properties of bamboo fibre/polyester composites subjected to moisture and hygrothermal conditions. *Proc Instit Mech Eng Part L: J Mater: Des Appl* 233:1065–1079
12. Godina M, Lorenzo R (2015) Calibrating a composite material model for analysis and design of bamboo structures. In: *10th world bamboo congress*
13. Bansal A, Zoolagud S (2002) Bamboo composites: material of the future. *J Bamboo Rattan* 1:119–130. <https://doi.org/10.1163/156915902760181595>
14. Kaur PJ, Pant KK, Satya S, Naik SN (2016) Bamboo: the material of future. *Int J Series Multidiscip Res (IJSMR)* 2:27–34. ISSN: 2455-2461
15. Wegst UGK (2011) Bending efficiency through property gradients in bamboo, palm, and wood-based composites. *J Mech Behav Biomed Mater* 4:744–755

16. Kumar D, Mandal S (2014) Uncertainty in improving durability aspects and mechanical properties of bamboo reinforced concrete. *Int J Adv Res Ideas Innov Technol* 1:1–5
17. Janssen JJA (2000) Designing and building with bamboo. *Int Netw Bamboo Rattan Netherlands*
18. Anokye R, Bakar ES, Ratnasingam J, Awang BK (2016) Bamboo properties and suitability as a replacement for wood. *PJSRR Pertanika J Scholarly Res Rev* 2:63–79. <https://doi.org/10.13140/RG.2.1.1939.3048>
19. Trujillo D, López LF (2016) Nonconventional and vernacular construction materials
20. Wang H, An X, Li W, Wang H, Yu Y (2014) Variation of mechanical properties of single bamboo fibers (*Dendrocalamus latiflorus* Munro) with respect to age and location in culms. *Holzforschung* 68:291–297
21. Vogtländer J, der Lugt P, Brezet H (2010) The sustainability of bamboo products for local and Western European applications. LCAs and land-use. *J Clean Prod* 18:1260–1269
22. Huang Z (2019) Application of bamboo in building envelope. Springer
23. Ramadan N, Boghdadi A (2020) Parametric optimization of TIG welding influence on tensile strength of dissimilar metals SS-304 and low carbon steel by using Taguchi approach. *Am J Eng Res (AJER)* 9:7–14
24. Yazdi SR, Beidokhti B, Haddad-Sabzevar M (2019) Pinless tool for FSSW of AA 6061–T6 aluminum alloy. *J Mater Process Technol* 267:44–51
25. Cavalcanti PM, Maciej W, Tetreault N, Graziosi JK (2010) Building an engineered complex stretcher
26. Wang HE, Weaver MD, Abo BN, Kaliappan R, Fairbanks RJ (2009) Ambulance stretcher adverse events. *Qual Saf Health Care* 18:213–216. <https://doi.org/10.1136/qshc.2007.024562>
27. Plagenhoef S, Evans FG, Abdelnour T (1983) Anatomical data for analyzing human motion. *Res Q Exerc Sport* 54:169–178
28. Taifa IW, Desai DA (2017) Anthropometric measurements for ergonomic design of students' furniture in India. *Eng Sci Technol Int J* 20:232–239. <https://doi.org/10.1016/j.jestch.2016.08.004>
29. Yang D, Li H, Xiong Z, Mimendi L, Lorenzo R, Corbi I, Corbi O, Hong C (2020) Mechanical properties of laminated bamboo under off-axis compression. *Compos Part A: Appl Sci Manuf* 138:106042. <https://doi.org/10.1016/j.compositesa.2020.106042>
30. Ghavami K (2008) Bamboo: low cost and energy saving construction materials. *Modern Bamboo Struct* 1:5–21